

Configuring post-lithium aqueous rechargeable zinc batteries using optimized electrolytes and electrode materials

by

Ms. Meena Ghosh
10CC16J26013

A thesis submitted to the
Academy of Scientific & Innovative Research
for the award of the degree of
DOCTOR OF PHILOSOPHY
in
SCIENCE

Under the supervision of
Dr. Sreekumar Kurungot



CSIR- National Chemical Laboratory, Pune



Academy of Scientific and Innovative Research
AcSIR Headquarters, CSIR-HRDC campus
Sector 19, Kamla Nehru Nagar,
Ghaziabad, U.P. – 201 002, India

May 2021

STATEMENTS OF ACADEMIC INTEGRITY

I Ms. Meena Ghosh, a Ph.D. student of the Academy of Scientific and Innovative Research (AcSIR) with Registration No. 10CC16J26013 hereby undertake that, the thesis entitled “Configuring post-lithium aqueous rechargeable zinc batteries using optimized electrolytes and electrode materials” has been prepared by me and that the document reports original work carried out by me and is free of any plagiarism in compliance with the UGC Regulations on “*Promotion of Academic Integrity and Prevention of Plagiarism in Higher Educational Institutions (2018)*” and the CSIR Guidelines for “*Ethics in Research and in Governance (2020)*”.



Signature of the Student

Date : 20/05/2021

Place : Pune

It is hereby certified that the work done by the student, under my supervision, is plagiarism-free in accordance with the UGC Regulations on “*Promotion of Academic Integrity and Prevention of Plagiarism in Higher Educational Institutions (2018)*” and the CSIR Guidelines for “*Ethics in Research and in Governance (2020)*”.



Signature of the Supervisor

Name : Dr. Sreekumar Kurungot

Date : 20/05/2021

Place : Pune

Certificate

This is to certify that the work incorporated in this Ph.D. thesis entitled, "Configuring post-lithium aqueous rechargeable zinc batteries using optimized electrolytes and electrode materials", submitted by Ms. Meena Ghosh to the Academy of Scientific and Innovative Research (AcSIR) in fulfillment of the requirements for the award of the Degree of Doctor of Philosophy in Science, embodies original research work carried-out by the student. We, further certify that this work has not been submitted to any other University or Institution in part or full for the award of any degree or diploma. Research materials obtained from other sources and used in this research work have been duly acknowledged in the thesis. Images, illustrations, figures, tables etc., used in the thesis from other sources, have also been duly cited and acknowledged.



(Signature of Student)

Meena Ghosh

Date: 20/05/2021



(Signature of Supervisor)

Dr. Sreekumar Kurungot

Date: 20/05/2021

Acknowledgment

At this moment of completing my doctoral thesis, I take this opportunity to thank everyone who has directly or indirectly given input and support throughout the past five years of my Ph.D. journey at CSIR-NCL.

First and foremost, I would like to express my heartiest gratitude to my research supervisor Dr. Sreekumar Kurungot for his persistent guidance and support during every stage of my doctoral research tenure. His constant motivation, positive criticism, timely suggestions, and encouragement helped build my confidence and skill to identify original research ideas with great passion and enthusiasm. I am very thankful to him for allowing me space and freedom while holding me on the right track, which shaped me as an independent researcher. His time management skills and the pace with which he corrects research articles always inspired me, and I wish I could imbibe these qualities throughout my research career. Once again, I warmly thank him for providing an excellent research atmosphere and all the essential research facilities during my stay at CSIR-NCL.

I devote my sincere acknowledgment to Prof. Rabah Boukherroub for hosting me as a Raman-Charpak Fellow at the University of Lille, France. His interest in scientific discussion and timely monitoring of work progress helped to complete my research project on time. I am thankful to all my labmates at the IEMN laboratory and friends for making my stay in France a memorable one.

I thank my doctoral advisory committee members Dr. Jayaraj Nithyanandhan, Dr. Vinod C. Prabhakaran, and Dr. H. V. Thulasiram, for their support, timely assessment, and valuable advice during the half-yearly meetings. I also thank Dr. Kumar Vanka, Dr. Rajesh Gonade, Dr. Sayan Bagchi, Dr. K. Krishnamoorthy, and Dr. S. K. Asha for their excellent lectures during coursework. I wish to thank the current and former directors of CSIR-NCL for establishing scientific infrastructure, instrumental facilities, and academic support for conducting high-quality research. I am profoundly thankful to the CMC division at CSIR-NCL for ensuring smooth execution of sample characterization, which is one of the essential parts of my research work. I would also like to thank the Student Academic Office Chirman, AcSIR Coordinator, Ms. Purnima Kohle, Mr. P. K. Purushothaman, Ms. Komal, Ms. Vaishali, and Ms. Vijaya, for the smooth processing of the official documents. I believe this an appropriate moment to remember all my former teachers as they built the foundation of knowledge toward achieving the doctoral degree.

I shall always remain grateful to my former labmates Dr. Harshitha B. A., Dr. Santosh Singh, Dr. Roby Soni, Dr. Varchaswal Kashyap, Dr. Vidyanand V., Dr. Pranav K.G., Dr. Rajith I.V., Dr. Siddheshwar Bhange, and Dr. Nadeema Ayasha for their mentoring and care during my days at CSIR-NCL. I especially thank Dr. Vidyanand, who patiently taught me electrochemical characterization, data analysis, device fabrication, and manuscript writing at several phases of my doctorate studies. I thank and appreciate my current labmates Manna, Sachin, Swati, Geeta, Ajmal, Maria, Priyanka and Sidharth for creating a friendly and cheerful atmosphere in the lab. Thanks to former and current post-docs in the lab, Dr. Raji, Dr. Gaurav, Dr. Debasree, and Dr. Shilpa. I also thank Dr. Abdul Khayum, Dr. Arjun Halder, Dr. Rahul Banerjee, Aryan Wavhal, Dr. S K Asha, Dr. Bihag Anothumakkool, Dr. Jijeesh Nair, and Dr. Amrita Jain for the collaborations. I must thank Dr. Vandana, Dr. Arun Torris, Dr. Shibin T, Poonam, Apurva, Kiran, and Fayiz, for their time to help me with many analyses and characterizations.

A special thanks to my friends Moumita, Vaishnavi, Shailja, Vipin, Shebeeb, and Prajitha for making my stay at CSIR-NCL pleasant and eventful. I also thank my other friends and well-wishers Pravin, Iswari, Vedi, Betsy, Ranjeesh, Vivek, Rajeshwari, Sayantan da, Rupa, Piyali, Shrikant, Mahendra, Ashwini, Amarnath Singham, Bharath, Tapas da, Jinesh Shah, Maya di, Shaibal da, Ajith, Abdul, and many others.

Above all, I find no words to express my gratitude to my parents for their struggle and sacrifice. Dedicating this thesis to Maa and Baba is a small recognition of their eternal love and blessings. I am grateful to Didi for her love and affection and for giving me support whenever needed. I thank Dadabhai for the care and encouragement. I remember cherished moments with my little niece Ishanvi.

Meena Ghosh

Table of Contents

Preface	1-3
Chapter 1	
Transition from Lithium to Post-Lithium Batteries: an Introduction to Aqueous Rechargeable Zinc Batteries	4-41
1.1 Introduction	5-9
1.2 General Insights on Battery	9-13
1.2.1 Definition of Battery	9
1.2.2 Components of Battery	10-11
1.2.3 Discovery of Battery: Brief Historical Context	11
1.2.4 Performance Parameters of Rechargeable Battery	12
1.2.5 Fundamental Factors Deciding the Working Voltage of Battery Cell	12-13
1.3 Transition from the Lithium Battery to Post-Lithium Battery	13-20
1.3.1 Lithium Batteries	13-18
1.3.2 Post-Lithium Batteries	18-20
1.4 Aqueous Zinc Batteries	20-22
1.5 Configurations, Components, and Charge Storage Mechanisms of ARZBs	22-32
1.5.1 Charge Storage Mechanism and Classification	22-24
1.5.2 Cathode Materials for ARZBs	24-28
1.5.3 Anode Material for ARZBs	28-29
1.5.4 Electrolyte Formulation	29-31
1.5.5 Separator	31-32
1.6 Conclusions, Scope, and Objective of the Thesis	33-35
1.7 References	35-41

Chapter 2

Dendrite Growth Suppression by Zn²⁺-Integrated Nafion Ionomer Membrane: Beyond Porous Separators towards Aqueous Zn V₂O₅ Battery with Extended Cycle Life	42-65
2.1 Introduction	43-44
2.2 Experimental Section	44-48
2.2.1 Materials	44
2.2.2 Fabrication of the V ₂ O ₅ Electrode	44-45
2.2.3 Pre-treatment of the Nafion Ionomer Membranes	45
2.2.4 Modification of the Conventional Porous Membranes	45
2.2.5 Assembly of Zn V ₂ O ₅ cells	45
2.2.6 Material Characterization	45-46
2.2.7 Electrochemical Measurements	46-48
2.3 Result and Discussion	48-60
2.3.1 Physical Characterization	48-49
2.3.2 Selection of the Separator	49-54
2.3.3 Electrochemical Characterization of the Zn V ₂ O ₅ Cells	54-56
2.3.4 Post-mortem Analysis of Anode	56-58
2.3.5 Post-Mortem Analysis of Cathode	58
2.3.6 Ragone Plot and Real-Life Demonstration	58-60
2.4 Conclusions	60-61
2.5 References	61-65

Chapter 3

Nafion Ionomer-Based Single Component Electrolytes for Aqueous Zn MnO₂ Battery with Long Cycle Life	66-96
3.1 Introduction	67-68
3.2 Experimental Section	68-71
3.2.1 Materials	68-69
3.2.2 Fabrication of the Cathode	69
3.3.3 Material Characterization	69

3.3.4	Electrochemical Measurements	69-71
3.3	Results and Discussion	71-89
3.3.1	Physical Characterizations	71-73
3.3.2	Selection of Electrolytes	73-75
3.3.3	Electrochemical Analysis of the Zn MnO ₂ Cell in 1M Zn(CF ₃ SO ₃) ₂	75-78
3.3.4	Electrochemical Analysis of the Zn MnO ₂ Cell in 1M ZnSO ₄	79
3.3.5	Cycling Stability and Impedance Analysis of Nafion-Based Zn MnO ₂ Cells	79-84
3.3.6	Cycling Stability and Impedance Analysis of Porous Separator-Based Zn MnO ₂ Cells	84-86
3.3.7	Physical Characterization of the Post-Stability Electrodes	86-89
3.4	Conclusions	89-90
3.5	References	96

Chapter 4

Scalable Synthesis of Manganese-Doped Hydrated Vanadium Oxide as a Cathode Material for Aqueous Zinc-Metal Battery		97-125
4.1	Introduction	98-99
4.2	Experimental Section	100-103
4.2.1	Materials	100
4.2.2	Synthesis of Hydrated Vanadium Oxide	100
4.2.3	Synthesis of Mn-doped Hydrated Vanadium Oxide	100
4.2.4	Preparation of Electrolyte	100-101
4.2.5	Fabrication of ARZMB Cells	101
4.2.6	Material Characterization	101-102
4.2.7	Electrochemical Measurements	102-103
4.3	Results and Discussion	103-118
4.3.1	Physical Characterization	103-110
4.3.2	Electrochemical characterization	110-118
4.4	Conclusions	118-119

4.5	References	119-125
-----	------------	---------

Chapter 5

Naphthalene Dianhydride Organic Anode for ‘Rocking-Chair’ Zinc-Proton Hybrid Ion Battery		126-144
5.1	Introduction	127-128
5.2	Experimental Sections	128-131
5.2.1	Materials	128
5.2.2	Fabrication of Electrodes	128
5.2.3	Fabrication of Electrochemical Cell	129-130
5.2.4	Electrochemical Measurements	130
5.2.5	Material Characterization	130-131
5.3	Result and Discussion	131-141
5.4	Conclusions	141
5.5	References	141-144

Chapter 6

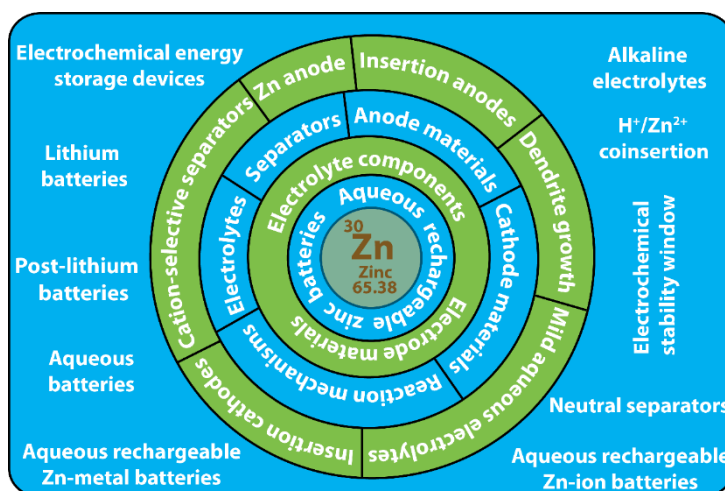
Summary & Future Perspectives		145-149
6.1	Summary	145-148
6.2	Future Perspectives	148-149
Abstract		150
List of Publications & Achievements		151-155
Erratum		156

Chapter 1

Transition from Lithium to Post-Lithium Batteries: an Introduction to Aqueous Rechargeable Zinc Batteries

The core theme of the present thesis is to explore efficient electrolytes, separators, and electrode materials for aqueous rechargeable zinc batteries (ARZBs), a safe and cost-effective alternative to state-of-the-art lithium-ion batteries (LIBs). The introductory chapter provides glimpses on the global energy scenario emphasizing the prospects of batteries for attaining energy sustainability. The historical background and working principle of various types of batteries are thoroughly discussed with individual sections dedicated to LIBs and lithium metal batteries (LMBs) employing nonaqueous electrolytes. Later, the concept of post-lithium batteries (PLBs) is introduced as one of the potential candidates over lithium batteries (LBs).

Among the PLBs, the fundamental benefits of employing Zn-based electrochemistry are discussed in the context of rechargeable aqueous batteries. For instance, the electrochemical behavior of Zn metal in aqueous electrolytes at alkaline, acidic, and nearly neutral pH conditions and its impacts on



the performance of aqueous Zn batteries are briefed. Ultimately the discussion sheds light on the necessity of developing Zn^{2+} ion-conducting mild aqueous electrolytes, tailor-made separators, and electrode materials for realizing rechargeable aqueous Zn-metal and Zn-ion batteries (ARZMBs and ARZIBs). This chapter further highlights the benefits of cation-selective separators in inhibiting the Zn-dendrite induced cell failure in ARZMBs. The final section of this chapter covers the scope and objectives of this thesis. In a nutshell, the current thesis put forwards interesting results in terms of encouraging the scope of aqueous Zn batteries through four dedicated working chapters.

1.1 Introduction

The increase in energy consumption and the environmental concerns caused by energy production from non-renewable fossil fuels have propelled the search for alternative and sustainable energy resources. Although renewable energy resources such as solar and wind are harvestable for commercial and household applications, their intermittent and localized nature remains a grave concern hindering widespread utilization. Therefore, efficient and eco-friendly energy storage technologies have become the key to overcome the practical intricacies associated with both renewable and non-renewable energy resources.¹ In this scenario, energy storage devices relying on electrochemistry principles, also known as electrochemical energy storage devices (EEDs), are widely considered the foremost contenders. Batteries are one of the most popular EEDs, ubiquitously used as a stand-alone power source in various electronic and electrical accessories, such as portable and wearable gadgets, medical equipment, home appliances, *etc.* Apart from the small-scale applications, batteries have infiltrated into multiple large-scale applications, including electric vehicles and electricity distribution grids.² It is apparent that battery technology has revolutionized many aspects of our lifestyle, and its further advancement is essential to transform the renewable energy sector affordable and reliable.

The chemistry of batteries is indeed vast and vivid. Various types of batteries can be designed based on strong interdisciplinary knowledge in chemistry, physics, and engineering. **Figure 1.1** shows the Ragone plot (energy density vs. power density) comparing the performance of various batteries available in the market to date. Generally, batteries are high energy density devices, which can power electronic devices for a long duration of time with a constant supply of energy. Examples of applications where batteries found of extreme importance include mobile phones, laptops, electric vehicles, *etc.* However, as shown in **Figure 1.1**, the maximum achievable energy and power densities of different batteries depend on the battery components and the associated electrochemical reactions. Lithium-ion batteries (LIBs) are well known for high energy density and by far the most popular EED technology of choice in the portable electronics and automotive sectors. However, the flammable and toxic organic electrolyte used in state-of-the-art LIBs imposes serious safety and environmental concerns against the large-scale application of LIBs. Also, the high price of raw materials (such as lithium, cobalt, and nickel), the requirement of stringent conditions during the manufacturing process, and sophisticated cell assembling norms increase the cost of LIB production.³ These setbacks make the use of LIBs rather impractical in large-scale stationary applications (*viz.*, electrical grid) where safety, cost, and long battery life become more important than energy density. Recently, a transition from LIBs to lithium-metal batteries (LMBs), which directly use

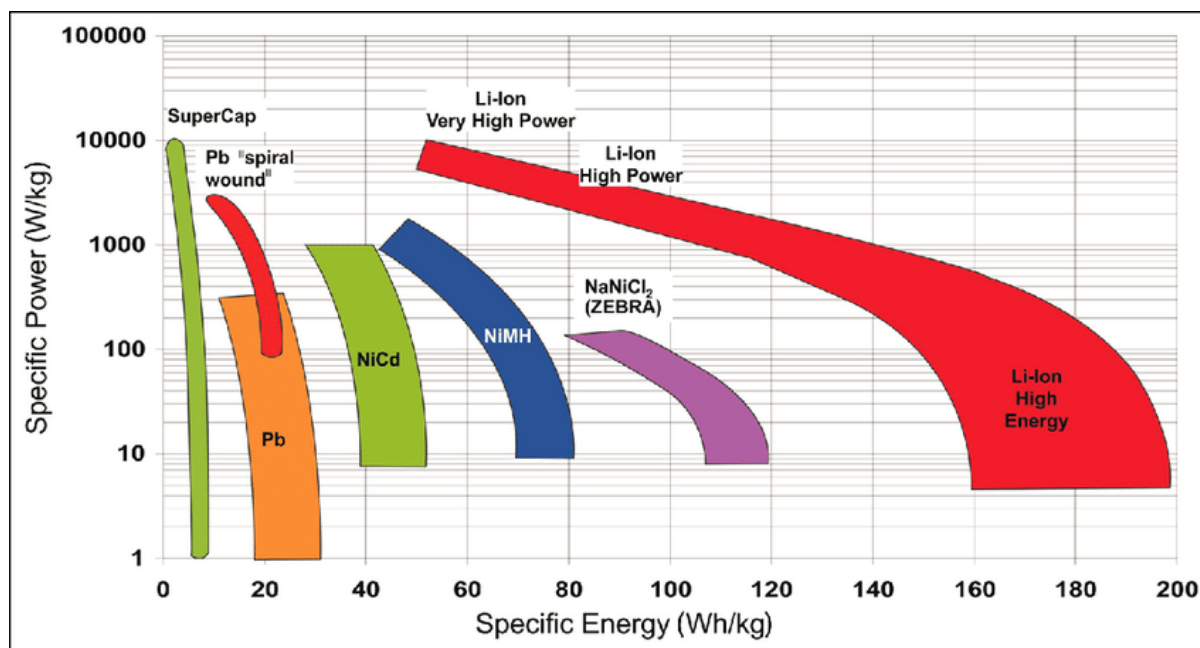


Figure 1.1. Ragone plot comparing the specific energy and specific power of supercapacitor (SuperCap), lead-acid battery (Pb), Ni-Cd battery (NiCd), Ni-metal hydride battery (NiMH), sodium-nickel chloride battery (NaNiCl₂), and lithium-ion battery (Li-ion). (Reproduced with permission from reference 2, SAGE Publications, Copyright © 2013, © SAGE Publications).

Li metal anode instead of graphite is also gaining attention among electrochemists as an alternative to LIBs (section 1.3.1). Li metal has a high theoretical capacity of about 3800 mAh g⁻¹, which is almost ten times that of graphite (380 mAh g⁻¹) in conventional LIBs.⁴ Therefore, LMBs may be potential candidates over LIBs in terms of improved energy density. However, the prospects of rechargeable LMBs are still in the early stages due to the risks related to dendrite-induced cell failure, fire hazards (due to the incompatibility between reactive Li metal and the nonaqueous electrolytes), and the requirement of solid-state electrolytes.⁵ In the context of this thesis, LIBs and LMBs are together represented by the term lithium batteries (LBs).

The shortcomings related to LBs bring opportunities to develop alternative battery systems coined by the term post-lithium batteries (PLBs). PLBs are indeed special as their working principle resembles that of LBs with the exception that the Li-based electrochemistry is replaced by the analogues Na, Mg, K, Zn, Ca, Al, *etc.*^{6,7} Similar to LIBs and LMBs, PLBs can also be classified into post-lithium-ion batteries (PLIBs) and their high-energy counterpart called post-lithium-metal batteries (PLMBs). Similar to LIBs, PLIBs also operate by the insertion/extraction mechanism, where the most common examples are sodium-ion batteries (SIBs) and magnesium-ion batteries (MIBs). On the other hand, PLMBs follow the plating/

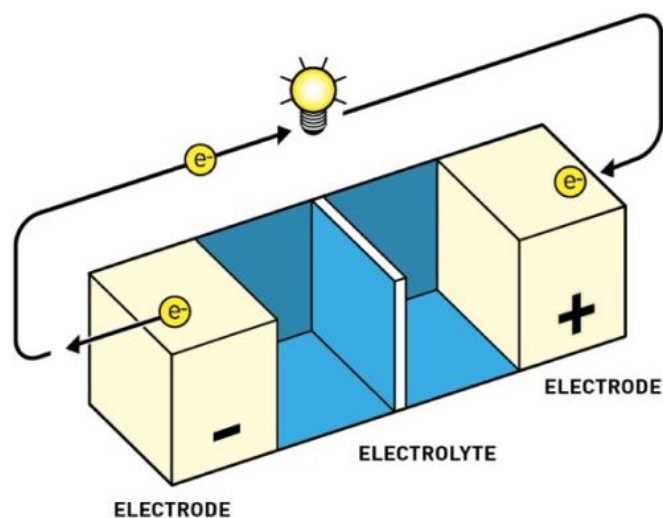


Figure 1.2. Schematic representation of a battery cell comprising two electrodes and an electrolyte component. (Reproduced from the press releases on the Nobel Prize in Chemistry 2019: © The Royal Swedish Academy of Sciences, <https://www.nobelprize.org/>).

stripping of the metal at the anode. PLIBs and PLMBs based on Ca, K, Zn, Al, *etc.* can be also envisaged. The similar working principles of LBs and PLBs allow the implementation of fundamental and technological know-how generated for LBs toward improving the performance of PLBs, which helps the industrial adoption of PLB technologies over the other alternatives mentioned in **Figure 1.1**. In any case, it should be noted that PLMBs are rarely explored due to the bottleneck associated with the dendrite growth at the metallic anode during the long-term operation of the battery similar to that of LMBs. However, considering the future landscape of battery technologies, serious efforts to improve the prospects of PLMBs should be considered.

In the context of PLBs (both PLIB and PLMB), revisiting the prospects of aqueous electrolytes offer non-flammability, easy handling, and cost-effectiveness.⁸ In addition, the high ionic conductivity of aqueous electrolytes makes them attractive, particularly for acquiring batteries with high power density. Earlier, aqueous electrolytes in extreme pH conditions are popularly used in the lead-acid battery (acidic electrolyte), Ni-Cd battery (alkaline electrolyte), Ni-metal hydride battery (alkaline electrolyte), so on and so forth in presence of metal anodes such as Ni, Pb, and even Zn (*e.g.*, Zn||MnO₂ alkaline battery). Application of these batteries, however, is limited due to the poor rechargeability, low energy density, toxicity, and environmental risk posed by them.⁹ Therefore, mild aqueous electrolytes (pH≈4) have received significant interest as they provide higher energy density, better durability, and improved safety compared to batteries employing strongly acidic and alkaline electrolytes. In this scenario, the development of PLIBs or PLMBs with mild aqueous

electrolytes (near-neutral pH) provides interesting opportunities and challenges. Among the PLBs using aqueous electrolytes, aqueous Zn batteries are of particular interest. The unique properties of Zn metal, *viz.*, the low redox potential of -0.76 V *vs.* standard hydrogen electrode (SHE) and high overpotential for hydrogen evolution reaction (HER), make it one of the most suitable anode materials to be used in aqueous electrolyte. Besides, Zn is relatively abundant and has a theoretical capacity of 820 mAh g^{-1} (volumetric capacity of 5854 mAh L^{-1}),¹⁰ a value is much high than that of graphite anode used in commercial LIBs. This signifies that the energy density of aqueous Zn batteries can surpass the LIBs provided that high-voltage cathode material with high theoretical capacity is available. In a few reports, the use of aqueous electrolytes has been attempted with LIBs and PLBs (SIBs, MIBs, *etc.*). However, the necessity of highly concentrated water-in-salt (WIS) electrolytes makes these systems very expensive, which offsets the advantages expected to gain from aqueous batteries. Moreover, due to the high reactivity with aqueous electrolytes, realizing aqueous PLMBs compatible with alkali metal anodes such as Li, Na, and K is also extremely challenging. Therefore, developing aqueous PLMBs using Zn as one of the readily available and water-compatible metals is important (section 1.3.2). The Zn electrochemistry in the aqueous electrolyte can be further extended for developing affordable PLIBs utilizing Zn^{2+} charge carrier (section 1.5.3). The advancement in aqueous rechargeable Zn batteries demands serious effort toward the exploration of electrode materials and electrolytes and understanding the associated electrochemical processes occurring in these batteries.

This thesis focuses on the development and optimization of electrolyte component (the term ‘electrolyte component’ refers to the combination of electrolyte and separator throughout this thesis) and electrode materials for aqueous rechargeable zinc batteries (ARZBs) emphasizing the two types of configurations, namely aqueous rechargeable zinc-metal battery (ARZMB) and zinc-ion battery (ARZIB). The second and third chapters aim to unveil the influence of separators to stabilize the Zn anode in ARZMBs for prolonging the cycling stability. For this purpose, ARZMB cells are fabricated with two types of separators (porous neutral separator and cation-selective separator), and their performance is compared. Followed by tuning the electrolyte component, the attention was moved toward the electrode material development. To prove the efficacy of the optimized electrolyte component in ARZMBs, the electrochemical cells are fabricated with V_2O_5 and MnO_2 cathodes in the second and third chapters, respectively. Utilizing the know-how generated from the above-mentioned chapters, the preparation and application of another cathode material for ARZMB based on hydrated vanadium oxide is discussed in the fourth chapter. The performance of ARZMB is also

demonstrated in a prototype homemade pouch cell using quasi-solid-state gel polymer electrolyte. Finally, to conceptualize the transition from ARZMB to ARZIB, the electrochemical properties of an organic anhydride molecule as the potential anode material is investigated in the fifth chapter. Furthermore, the systematic electrochemical studies presented in this chapter reveal that H^+ and Zn^{2+} coparticipate in the charge storage processes. In brief, the key findings of the present thesis encourage ongoing research on ARZBs.

1.2 General Insights on Batteries

1.2.1 Definition of Battery

Batteries are a collection of one or multiple electrochemical cells connected in series or parallel (the terms battery and battery cells are used interchangeably in this thesis to represent the same entity). The general configuration of a battery cell (in discharge mode) is shown in **Figure 1.2**. Each battery cell consists of two oppositely polarized electrodes immersed in an electrolyte. In batteries, electric charge storage and release evoke electron transfer at the electrode|electrolyte interface through redox reactions (or Faradaic reaction). Depending on the nature of electrochemical reactions (irreversible or reversible), batteries can be either non-rechargeable (primary battery) or rechargeable (secondary battery).¹¹ A rechargeable battery can operate both as a galvanic cell (that passes electrical energy to the external circuit) and an electrolytic cell (electrical energy supplied to the cell from an external power source) during the discharge and charge processes, respectively. During discharge, oxidation occurs at the negative electrode (anode), and the free electrons congregate around the anode resulting in a potential difference between the two terminals of the cell.¹² This potential difference drives the electrons to the positive electrode or cathode through the external circuit (as shown in **Figure 1.2**). Eventually, the cathode takes up the electron through a concurrent reduction reaction. The electron flow is counter-balanced by the flux of positively charged electrolyte ions from the anode to the cathode side. The aforementioned electrochemical processes follow a reverse manner (oxidation at the positive electrode and reduction at the negative electrode) during the charging process. Therefore, a rechargeable battery can facilitate the spontaneous conversion of stored chemical energy to electrical energy during discharge (similar to a galvanic cell) and non-spontaneous conversion of externally supplied electrical energy to be stored as chemical energy during charging (similar to an electrolytic cell). Unlike rechargeable batteries, the primary batteries are single-use galvanic cells that can only facilitate the spontaneous conversion of chemical energy to electrical energy.

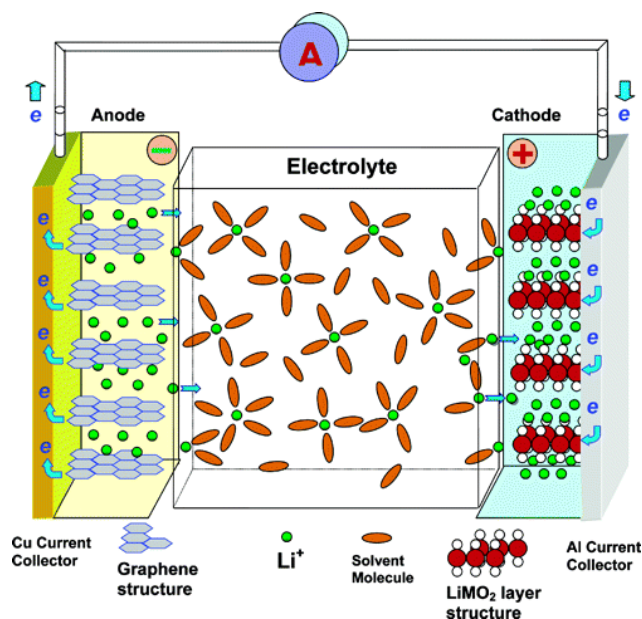


Figure 1.3. Illustration of state-of-the-art LIB employing layered transition metal oxide as cathode and lithiated graphitic carbon as the anode. The electrolyte component contains solvated Li^+ ions. The porous separator between the two electrodes is not shown here for simplicity. The spontaneous electrochemical process describes the discharge mode of the cell (deintercalation of Li^+ from the anode and simultaneous intercalation into the cathode). (Reproduced with permission from reference 13. Copyright © 2004 American Chemical Society).

1.2.2 Components of Battery

Typically, a battery cell consists of cathode and anode active material, cathode and anode current collectors, separator, and electrolyte. The aforementioned components are presented schematically in **Figure 1.3** by taking state-of-the-art LIB (in the discharge mode) as an example (LIBs are well-detailed in **Section 1.3**). The active materials (transitions metal oxides, conducting polymers, organic compounds, high surface area carbon) of a battery cell are responsible for storing/releasing the electrical charge through electrochemical reactions. The current collectors (Al, Cu, Ti foils, stainless steel, Grafoil sheet, carbon paper) collect the electric current generated at the electrodes and carry it to the external circuits, and vice versa. They are essentially non-active components and must be chemically stable in contact with the electrode material and electrolyte within a battery cell. In a classical way of battery electrode fabrication, the active materials are mixed with conducting additives (conducting carbon, carbon nanofibers, *etc.*) and binders (PVDF, Nafion, CMC) to improve the electronic conductivity and hold the electrode materials to the current collector, respectively. The

electrolytes are prepared by dissolving salts (LiCl , ZnSO_4 , LiCF_3SO_3), acids (H_2SO_4 , HCl), or bases (KOH , NaOH) in the water, organic solvents (ethylene carbonate, dimethyl carbonate, propylene carbonate), or ionic liquids. The electrodes are separated by a physical barrier, known as a separator, to facilitate ion conduction and avoidance of short-circuiting. The separators are soaked with a sufficient amount of liquid electrolyte before use, and the combination can be generally represented by the term ‘electrolyte component’. However, using a separator is not always necessary if the electrolyte itself can block direct physical contact between the electrodes (*e.g.*, solid-state/quasi-solid-state electrolytes can act as electrolyte cum separator). As shown in **Figure 1.3**, the cathode and anode are made of LiCoO_2 and lithiated graphite coated over Al and Cu current collectors, respectively. The electrolyte of state-of-the-art commercial LIBs is essentially an organic electrolyte, which is a solution of Li salt dissolved in aprotic organic solvents.¹³

1.2.3 Discovery of Battery: Brief Historical Context

Historically, the first electrochemical battery (known as voltaic pile) was demonstrated in 1800 by Italian physicist Alessandro Volta. The Voltaic Pile was made of Zn and Cu plates as the electrodes, which were separated by a piece of cardboard soaked with an acidic electrolyte. Following the basic principle of the Voltaic pile, many primary batteries are invented to date, which have received significant commercial success in the battery market. Therefore, Voltaic Pile is considered as the forerunner of modern batteries. Some of the examples are dry cell or Leclanché cell (consisting of Zn anode, carbon cathode, and NH_4Cl -based jellified electrolyte), alkaline cell (Zn anode, MnO_2 cathode, and KOH -based alkaline electrolyte), Li- MnO_2 (Li anode, MnO_2 cathode, and Li salt-containing nonaqueous electrolyte), Li- I_2 cell, *etc.* With the increasing popularity of rechargeable batteries and new battery chemistries, the market share of primary batteries is declining in recent years. However, primary batteries still play an important role in specific applications (*e.g.*, pacemaker, animal tracker, military combat, *etc.*), where rechargeability is impractical or impossible. The first rechargeable battery was invented in 1859 by French physicist Gaston Planté based on lead (Pb) and PbO_2 as the negative and positive electrodes, respectively (known as the lead-acid battery), and the same technology is still prevalent in several automobiles and stationary applications. Several other groundbreaking rechargeable batteries (*e.g.*, Ni-Cd, Ni-Zn, Ni-metal hydride, lithium-ion batteries) are discovered in the following decades.¹⁴ Among them, LIBs have the highest market share at present as they offer higher energy density compared to the Ni-based systems.

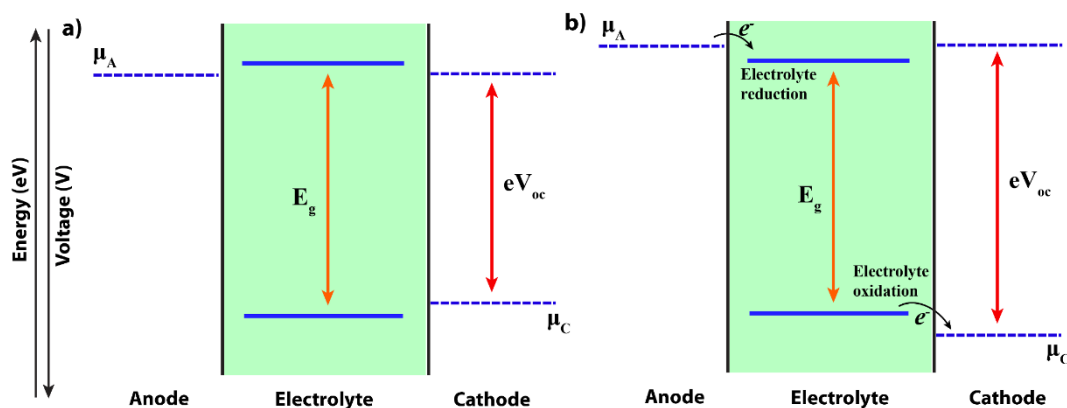


Figure 1.4. Schematic energy diagram of electrolyte stability: (a) in an ideal case where the potential of anode and cathode are within the ESW of electrolyte and (b) the potential of anode and cathode exceeds the ESW of electrolyte resulting in reduction and oxidation of electrolyte in the respective electrode.

1.2.4 Performance Parameters of Rechargeable Battery

The amount of electric charge stored in a battery is defined in terms of capacity (C), and it is quantified in ampere-hour (Ah) or mAh units. The capacity is calculated by multiplying the discharge time (in hours) by the discharge current (A or mA). The capacity of a cell decreases with increasing discharge current. The specific capacity values per unit mass, area, and volume are represented in mAh g^{-1} , mAh cm^{-2} , and mAh cm^{-3} . The other performance indicators of a battery are voltage, specific energy, specific power, and cycling stability. Voltage depends on the battery components, electrochemical reactions, and battery's internal resistance. The potential difference between the two electrodes when they are not electrically connected (no flow of charge) is called open-circuit voltage (OCV). The voltage of the cell changes as the electric charge flows through the outer circuit. Depending on the electrode material and electrolyte, each cell possesses maximum and minimum cut-off voltages. Operating beyond this limit may cause degradation of the electrode material and electrolytes, leading to permanent damage to a battery. The specific energy and specific power are obtained from the capacity, working voltage, and discharge time of the battery.

1.2.5 Fundamental Factors Deciding the Working Voltage of Battery Cell

The theoretical capacity and redox potential are the two important properties to be taken into account while selecting electrode material for battery application. At the open circuit condition (no flow of electrons), the voltage of a battery cell is determined by the equilibrium chemical potentials of the anode (μ_A) and cathode (μ_C). When the cell is subjected to charging

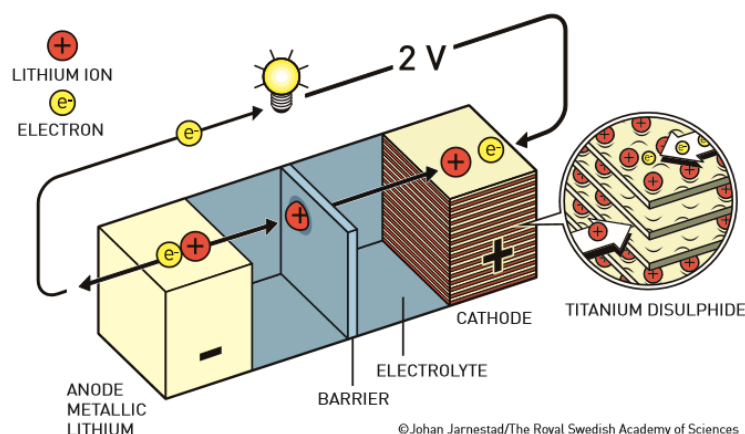


Figure 1.5. Schematic representation of LMB comprising Li metal as the anode, layered TiS_2 as intercalation cathode, and organic liquid electrolyte component invented by Whittingham et al. (Reproduced from the press releases on the Nobel Prize in Chemistry 2019: © The Royal Swedish Academy of Sciences, <https://www.nobelprize.org/>).

or discharging conditions, the electrochemical reactions displace the equilibrium potentials of the anode and cathode, resulting in a change in the cell voltage. For thermodynamic stability of the cell, μ_c is required to be above the lowest unoccupied molecular orbital (LUMO) and μ_A below the highest occupied molecular orbital (HOMO) of the electrolyte (Figure 1.4).¹⁵ The difference between HOMO-LUMO levels defines the electrochemical stability window (ESW) of the electrolyte.¹⁶ The maximum working voltage attainable for a battery cell is limited by the HOMO and LUMO energy levels of its electrolyte. If μ_A exceeds the electrolyte LUMO level, the electrolyte is reduced (e.g., hydrogen evolution in the aqueous electrolyte) by the electrons transferred from the anode. In an opposite scenario, the electrolyte transfers the electron to the cathode and gets oxidized (e.g., oxygen evolution in the aqueous electrolyte) when μ_c goes below the HOMO level. Therefore, judicious selection of electrode materials and electrolytes are important for achieving maximum working voltage without compromising the stability of the components and cycle life of the battery cell.

1.3 Transition from the Lithium Battery to Post-Lithium Battery

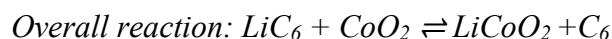
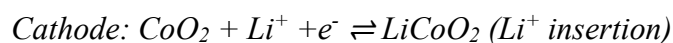
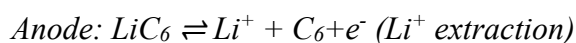
1.3.1 Lithium Batteries (LBs)

The foundation of lithium battery (LB) research was laid by M. Stanley Whittingham in 1970, who discovered the reversible storage/release of Li^+ ions in layered TiS_2 cathode paired with a Li metal anode in an organic liquid electrolyte (Figure 1.5).¹⁷ Since Li metal was directly used as the anode, the $\text{Li}||\text{TiS}_2$ battery can be called a lithium-metal battery (LMB). During the same period, a few other LMBs with different cathode chemistries (e.g., CuCl_2 ,

SOCl₂, SO₂, *etc.*) were also developed. Owing to the high reactivity, Li metal in liquid electrolyte-based LMBs exhibits serious morphological instability during the charging/discharging cycles.¹⁸ As a consequence, these LMBs are turned out to be non-rechargeable (primary battery) and unsafe. After a systematic search for alternate anode and cathode, the first rechargeable and potentially safe LB was discovered in 1980, which was made of a graphite-based anode, LiCoO₂ cathode, and liquid organic electrolyte. This configuration is called a lithium-ion battery (LIB). LIB was commercialized by SONY in 1990,¹⁹ and since then, the same remains as one of the most efficient power sources for a wide range of applications starting from portable electronics to electric vehicles. The recent and key developments made on both LIB and LMB technologies are briefly discussed here.

Lithium-ion batteries (LIBs)

As already mentioned, the anode and cathode materials in LIBs allow reversible insertion/extraction of Li⁺ ions shuttling between the two electrodes (as depicted in **Figure 1.3**). As the Li⁺ ions swing back and forth between the two insertion-type (intercalation) electrodes, the LIBs are also called 'swing batteries' or 'rocking chair batteries'.¹³ The electrochemical reactions happening at the anode (*e.g.*, lithiated graphite (LiC₆)) and cathode (*e.g.*, LiCoO₂) during the discharge of a LIB (LiC₆||LiCoO₂) can be presented as follows:²⁰



LiCoO₂ is extensively used in LIBs for digital cameras, mobile phones, and laptops. However, the material suffers from a short life span, low power capability, and low thermal stability. To improve the application range of LIBs, several layered transition metal oxides (*e.g.*, LiNi_xCo_yAl_zO₂ (NCA), LiMn_xNi_yCo_zO₂ (NMC), where x, y, and z represent the stoichiometries of the respective elements), spinel oxides (*e.g.*, LiMn₂O₄ (LMO)), and polyanion oxides (*e.g.*, LiFePO₄ (LFP)) are discovered over the years.^{21,22} These cathode materials with different structure-composition-property-performance relationships find application in one or another commercial LIBs. For example, NMC and NCA cathodes offer high energy density, making them suitable for electric vehicles, medical devices, and electric power trains. LFP cathode finds application in electric power tools. Similarly, apart from graphite, new anode materials with higher theoretical capacity have also been utilized for LIB fabrication. For example, the LiTiO₂ (LTO) anode shows the advantages of fast charge/discharge rate and long cycle life. Alloying anode such as Si and Sn are also promising

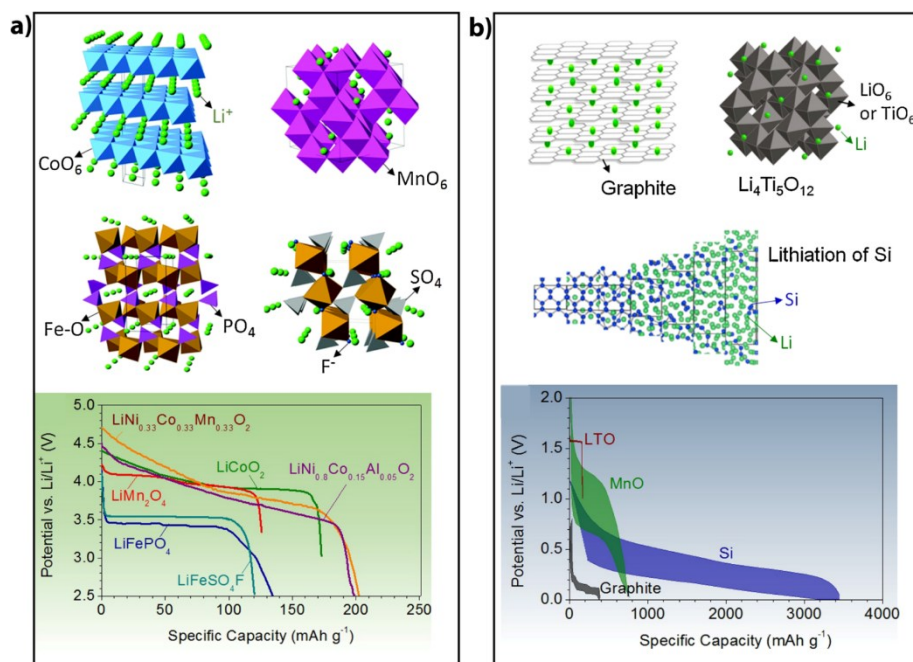


Figure 1.6. Crystal structures and discharge profiles (in half-cell) of some of the representative cathode and anode materials of LIBs: (a) layered LiCoO_2 , spinel LiMn_2O_4 , olivine LiFePO_4 , and tavorite LiFeSO_4F cathodes and (b) lithiated graphite, $\text{Li}_4\text{Ti}_5\text{O}_{12}$, and lithiated silicon anodes. (Reproduced with permission from reference 22. Copyright © 2014 The Authors. Published by Elsevier Ltd.).

as they offer high charge storage capacity.²² The crystal structure, electrochemical behaviour (voltage profile and discharge capacity) of some of the popular cathode and anode materials are summarized in **Figure 1.6a** and **b**.

Lithium-metal batteries (LMBs)

Despite the tremendous popularity of LIBs during the past several decades, metallic Li always remains the ultimate choice as anode material in lithium batteries. Being a strong reducing metal, Li easily sheds off free electrons and Li^+ ions. Li metal has a high theoretical capacity of 3842 mAh g^{-1} , a value ten times higher than that of graphite (380 mAh g^{-1}) anode used in state-of-the-art LIBs. Therefore, there is an opportunity to achieve a ten-fold increment in the energy density of commercial LIB if the graphite anode is replaced with a Li metal anode. However, the intricacies associated with LMBs arise because the conventional liquid electrolytes explored for LIBs are unstable in contact with highly reactive Li metal. In LMB, the plating and stripping of Li^+ ions take place at the Li anode during the charge and discharge cycles. The electrochemical processes at Li anode in LMBs are unique compared to all other anode materials (*viz.* graphite, Si, *etc.*) mentioned for LIBs. The anode reactions in LMB are

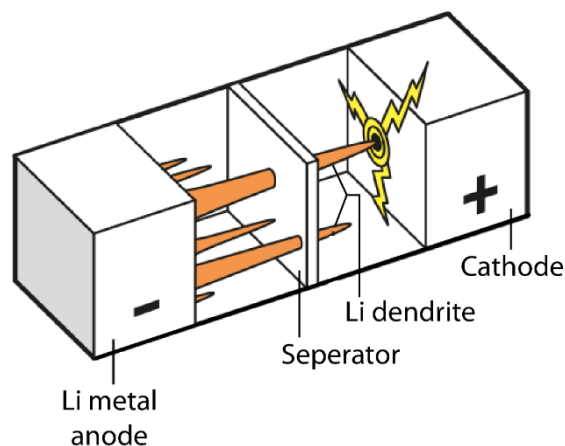


Figure 1.7. Scheme explaining the failure mechanism of LMB caused by uncontrolled growth of Li dendrites. (Reproduced from the press releases on the Nobel Prize in Chemistry 2019: © The Royal Swedish Academy of Sciences, <https://www.nobelprize.org/>).

are shown below:



The performance of LMBs is greatly affected by the morphology of the Li deposition layer (**Figure 1.7**) evolved during the electroplating and stripping process. Li deposition with uniform, smooth and dense morphology is one of the main criteria for realizing rechargeable LMBs. However, the non-regulated Li plating in conventional liquid electrolytes creates Li dendrites or high surface area lithium (HSAL).²³ The Li dendrites pierce through the separator and grow long enough to connect to the opposite electrode, short-circuiting the cell (**Figure 1.7**). During short-circuit, the heat generated inside the batteries can ignite the organic liquid electrolyte, which results in fire and explosion of LMBs.²⁴ Such catastrophic cell failure forbids the rechargeability of LMBs in liquid electrolytes.

The fundamental factor responsible for the uncontrolled Li dendrite growth in LMBs is the nature of the solid electrolyte interphase (SEI) layer. The SEI layer is formed due to the reductive decomposition of the liquid electrolyte (organic solvent and anions) in contact with the high electropositive Li anode. Once the SEI layer is created, it encases the anode from the surrounding liquid electrolyte, thereby preventing electrolyte degradation. A good SEI layer must be Li⁺ ion-conducting, electronically insulating, and mechanically stable. Unfortunately, the liquid carbonate electrolytes (common electrolytes for LIBs) could not form a stable SEI on the Li anode in LMBs. As a result of the unstable SEI layer, the liquid electrolyte comes in contact with the Li and decomposes with progressive cycles. This irreversible loss of the electrolyte and the inferior SEI layer favour the growth of Li dendrites and HSAL. The recent

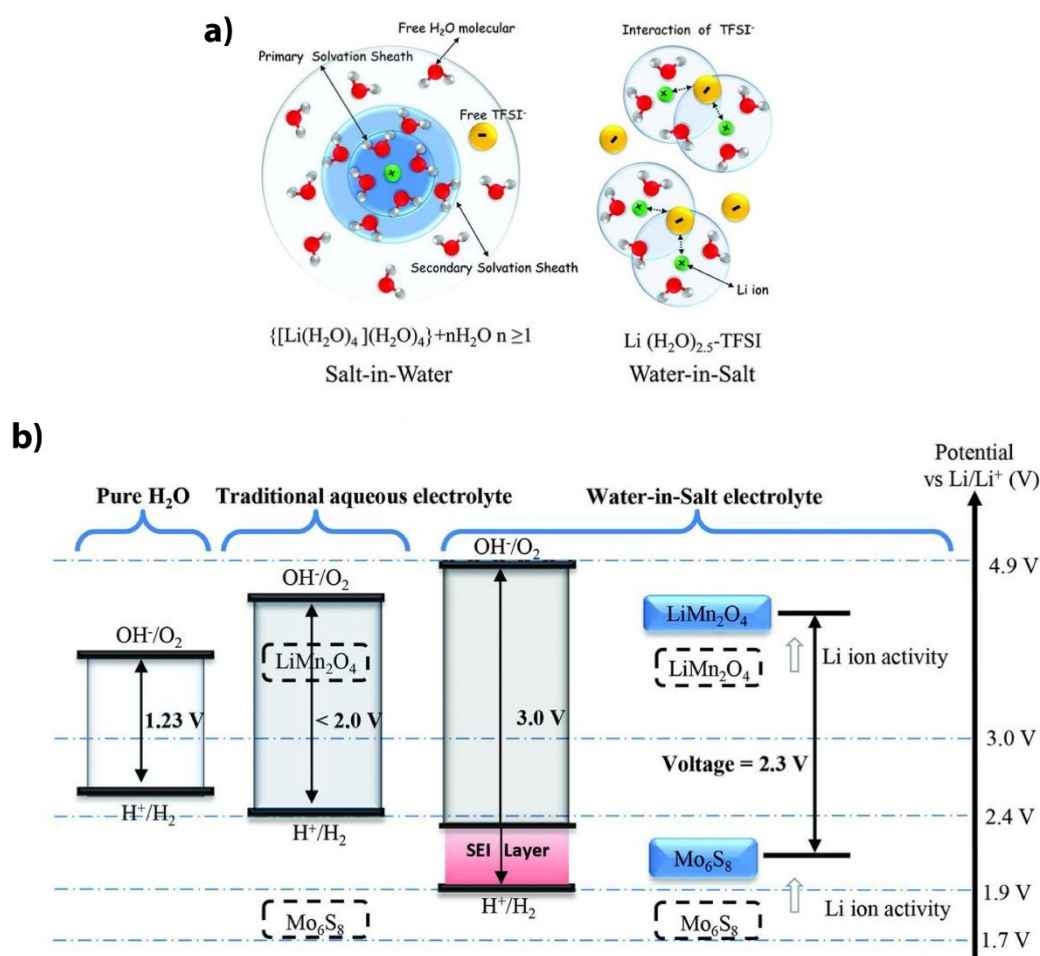


Figure 1.8. Schematic depiction of (a) Li^+ primary solvation sheath in diluted (salt-in-water) and WIS electrolyte, and (b) ESW of pure water, diluted electrolyte and WIS electrolyte. The expanded ESW of WIS electrolyte matches with the voltage requirement for LiMn_2O_4 cathode and Mo_6S_8 anode in aqueous LIB. (Reproduced with permission from reference 26. Copyright © 2015, American Association for the Advancement of Science).

advancements and breakthroughs in the LMB research have shown that Li^+ -conducting solid-state-electrolyte with high shear modulus than that of Li metal can suppress the HSAL or Li dendrite growth. The electrolytes offering a high preference toward Li^+ ion conduction (also known as single ion-conducting electrolytes) can also prevent such undesired Li deposition. The substitution of liquid electrolytes with the solid-state and single ion-conducting electrolytes have eliminated the risks of LMBs and enabled rechargeability for more than 1000 cycles.²⁵

Lithium batteries with aqueous electrolytes

As a safe alternative to the flammable organic electrolytes, the use of water-based electrolytes are also attempted in LIBs and a few LMBs. Aqueous electrolytes have distinct

merits such as high safety, high ionic conductivity, and low cost, making them appealing in many electrochemical applications. However, they are restricted by a narrow ESW of 1.23 V, which is far below the voltage required (> 3.0 V) for Li-battery electrodes. Nevertheless, the Li reacts vigorously with water and produces hydrogen and LiOH, which makes the fabrication of aqueous lithium batteries impossible. Interestingly, Suo *et al.* have shown that extremely concentrated aqueous electrolyte, typically with 20-21 m concentration, can overcome the drawbacks of aqueous electrolytes.^{26,27} This new class of aqueous electrolytes are referred to as water-in-salt (WIS) electrolyte. The physical and electrochemical properties of the WIS electrolyte are significantly different from the conventional electrolytes (with a salt concentration of 1-5 m). Because of the high salt/solvent ratio in WIS electrolytes, the dissolved salt outnumbered the water molecules. Therefore, most of the water molecules engage in the ion solvation shell, leaving no or a negligible number of free water molecules in the electrolyte. The ion solvation shell of WIS electrolyte and conventional aqueous electrolytes are schematically shown in **Figure 1.8a**. As a result, WIS electrolytes exhibit electrochemical behaviour similar to the organic electrolyte. The high salt concentration allows the WIS electrolyte to form a stable and protective SEI layer over the anode, which eventually increases the overpotential for the water-decomposition reactions at the electrode surface. The cumulative effects of higher overpotential and exclusion of free water molecules expand the ESW of WIS electrolyte up to ~ 3.0 V.²⁸ The ESW of conventional aqueous electrolyte, organic electrolyte, and WIS electrolytes are compared in **Figure 1.8b**. However, due to the requirement of a high concentration of expensive fluorine-rich electrolyte salt in WIS electrolyte, the concepts of aqueous LIB and LMB have not received much interest beyond the lab-level, and the technology is still at the early stage.

1.3.2 Post-Lithium Batteries (PLBs)

Unanimously, LIB technology has revolutionized our lifestyle. However, the advantage of using LIBs in large-scale applications is under debate due to the increasing consumption and rarity of raw material (Li, Co, Ni) resources along with environmental and economic concerns. Even in the case of LMBs, there are several challenges to overcome before projecting them to the commercial level. Therefore, it turns out to be essential and urgent to look for alternative battery technologies based on earth-abundant elements. In this context, the combination of low-cost, abundance, and environment-friendliness make the post-lithium batteries (PLBs) the leading contenders. Charge storage in PLBs employing multivalent charge carrier (Mg^{2+} , Zn^{2+} , and Al^{3+}) engage in more than one electron transfer, which leads to higher

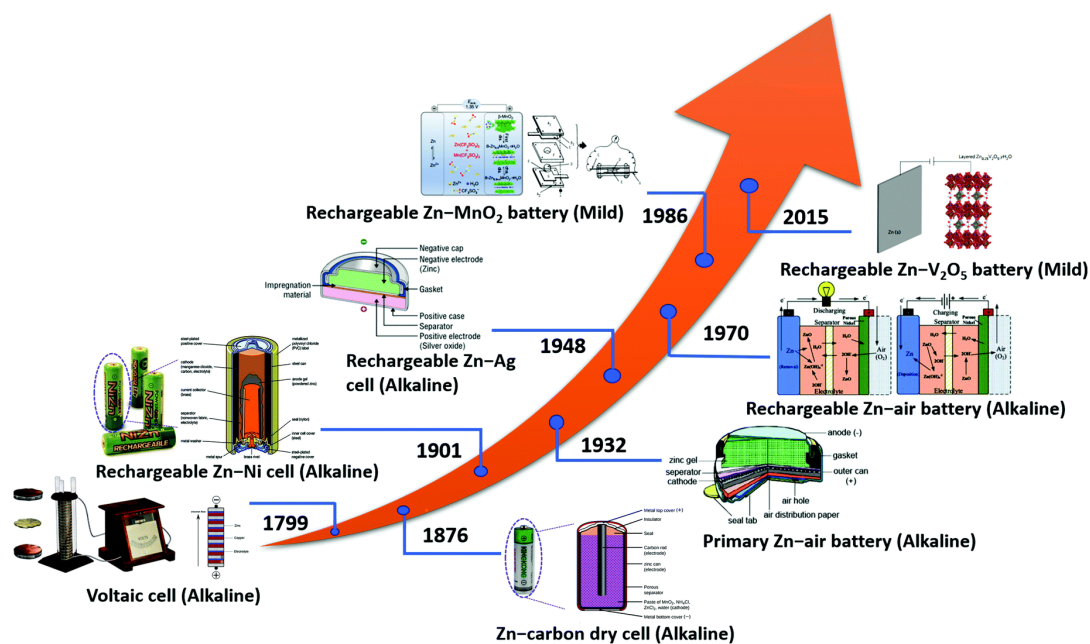


Figure 1.9. Schematic representation of the development of aqueous batteries employing Zn metal anode. (Reproduced with permission from reference 31. Copyright @ 2020 Royal Society of Chemistry).

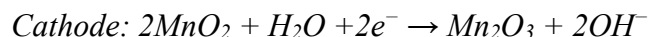
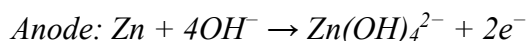
theoretical capacity. Therefore, multivalent PLBs excel in providing higher energy density compared to monovalent counterparts (Na^+ , K^+).²⁹ The use of aqueous electrolytes in PLBs can bring the additional advantages of improved safety and easy manufacturing. In the pursuit of high-performance battery chemistries, the standard reduction potentials of electrode materials and electrochemical stability of electrolytes are the most important aspects to consider. It is well-known that aqueous electrolytes provide a narrow voltage window of 1.23 V, which is the difference between the inherent oxidation potential (oxygen evolution reaction (OER)) and reduction potential (hydrogen evolution reaction (HER)) of water. The narrow ESW of water restrains the usage of many electronegative metals as the anode for high voltage aqueous rechargeable PLBs. For example, the redox potentials of Al (-1.66 V vs. SHE), Mg (-2.38 V vs. SHE), and Ca (-2.76 V vs. SHE) fall outside the stability limit of aqueous electrolyte. Consequently, aqueous batteries comprising Mg, Al, and Ca metal anode encounter HER as the predominant anodic reaction over the desired plating/stripping reactions of Mg/Al/Ca. Therefore, organic electrolytes are found to be the rational choice for PLMBs based on Mg, Al, and Ca anode. The use of aqueous electrolyte in these cases require additional treatment of the electrodes (*e.g.*, creating protective SEI) to avoid contact between the metallic anode and aqueous electrolyte.³⁰ On the contrary, metallic Zn anode with a standard reduction potential of -0.76 V vs. SHE can afford the reversible plating/stripping reaction in an aqueous electrolyte.

These virtues make Zn-metal the ideal anode for post-lithium aqueous batteries.⁸ The Zn-metal batteries with organic electrolytes are also reported to deliver a good cycle life; however, the organic electrolyte does not bring any significant advantage over the aqueous counterparts.

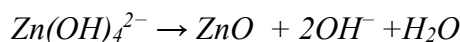
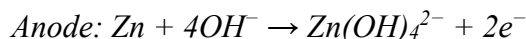
1.4 Aqueous Zinc Batteries

Being a low-cost, eco-friendly, and less reactive metal, Zn always attracted electrochemists and battery researchers. The first electrochemical battery, the Voltaic pile, employed Zn metal as the anode coupled with Cu cathode and separator soaked with salt-water electrolyte. Following this invention, Zn anode was utilized in Zn||Carbon dry cell, Zn||MnO₂ alkaline cell, Zn||Ag₂O cell, Zn||air, so on and so forth (**Figure 1.9**). However, except for the Zn||Carbon dry cell, the other examples utilize alkaline electrolyte (aqueous solution of NaOH or KOH), which is highly corrosive to the Zn metal. Although the cathode electrochemical reactions differ from one battery to another, the Zn anode undergoes similar electrochemical reactions in all these alkaline batteries. The electrochemical reactions in Zn||MnO₂ and Zn||air cells are provided below:

i. Zn||MnO₂ alkaline cell



ii. Zn||air cell



As shown above, in an alkaline electrolyte, Zn anode surrounded by OH⁻ gets oxidized to zincate ions (Zn(OH)₄²⁻), which is soluble in the electrolyte. The dissolved Zn(OH)₄²⁻ gradually diffuses to the bulk electrolyte leading to corrosion of the Zn anode. Nevertheless, as the concentration of Zn(OH)₄²⁻ species at the electrode|electrolyte interface reaches the saturation limit, the Zn(OH)₄²⁻ further reacts to form insoluble ZnO precipitation on the anode.³¹ Such precipitate passivates the anode surface and accelerates the dendritic growth damaging the scope of rechargeability in Zn-based alkaline batteries. Some of the recent research has demonstrated rechargeable Zn||Ni alkaline cell and Zn||air battery;^{32,33} however, several challenges are yet to be addressed to meet the benchmark performance and cycle life required for commercialization. Besides, the highly corrosive nature of alkaline electrolytes raises safety and environmental concerns.

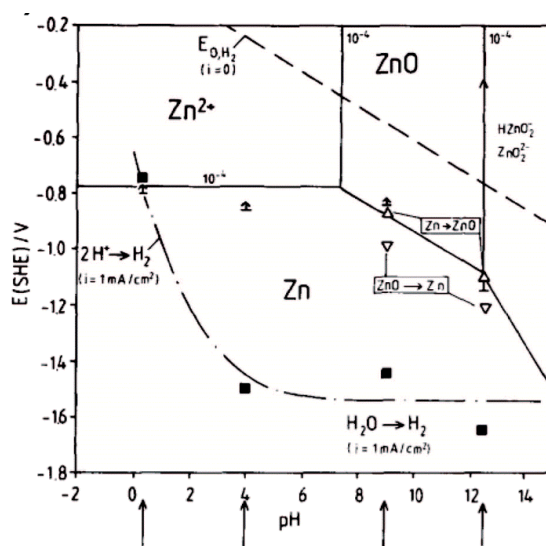


Figure 1.10. Pourbaix diagram of Zn/H₂O system including the hydrogen evolution reaction overpotential. (Reproduced with permission from reference 35, Copyright © 1990 Published by Elsevier Ltd.).

Interestingly, the electrochemical behaviour of Zn in an aqueous electrolyte can be regulated by varying the electrolyte pH and applied potential. This can be easily understood by looking at the Pourbaix diagram of the Zn/H₂O system in **Figure 1.10**.^{34,35} As shown in the diagram, Zn can be oxidized (electro-oxidation) to four different stable forms, Zn²⁺, Zn(OH)₂, HZnO₂⁻, and ZnO₂²⁻, depending on the pH of the water or electrolyte. At a higher electrolyte pH (pH > 6-7), the formation of Zn(OH)₂, HZnO₂⁻ and ZnO₂²⁻ gradually becomes more pronounced due to the high concentration of OH⁻ ions. On the contrary, oxidation of Zn to Zn²⁺ is predominant at pH = 4-6. This infers that Zn²⁺ ions can freely exist in an aqueous electrolyte with nearly neutral pH, and assist the reversible electrochemical Zn|Zn²⁺ conversion, similar to the plating/stripping of Li⁺ on Li metal anode in LMBs. Therefore, Zn|Zn²⁺ electrochemistry in neutral electrolytes accomplishes the rechargeability in Zn anode-based aqueous batteries.

The pH of aqueous electrolytes also influences the overpotential for HER. Theoretically, if the solution pH increases from pH = 4 to pH = 10, the HER potential shifts from -0.23 to -0.59 V vs. SHE, indicating high kinetic overpotential at high pH. As already mentioned, the reduction of Zn²⁺ to Zn occurs at a thermodynamic potential of -0.76 V vs. SHE. This means that the HER is thermodynamically more favourable than the reduction of Zn²⁺ to Zn (Zn plating) in an aqueous solution with pH = 4. However, Zn provides a unique advantage in deterring HER, resulting in a significant shift in the HER potential to the more negative potential than the theoretically predicted value (**Figure 1.10**).³⁴ As a result, Zn plating could happen well before the hydrogen evolution in mild acidic electrolytes. The high kinetic

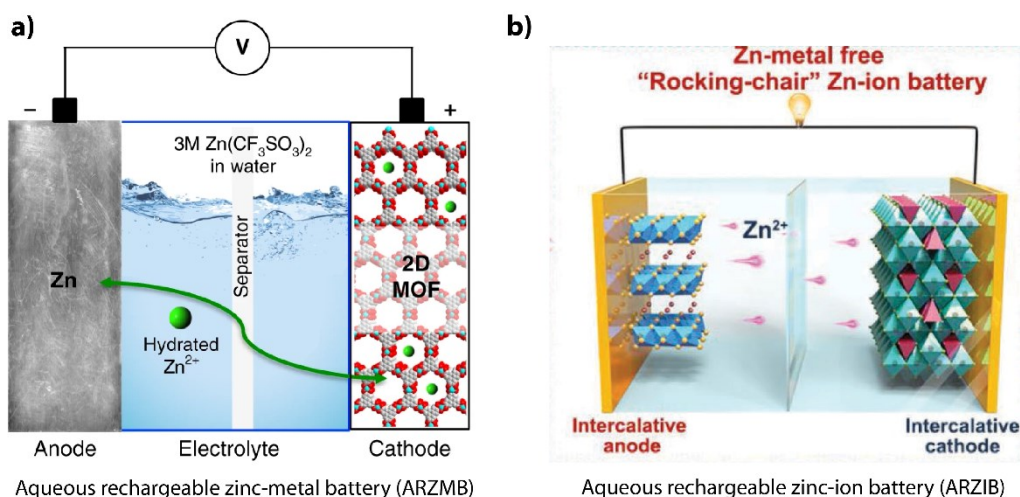


Figure 1.11. Schematic representations of (a) ARZMB and (b) ARZIB configurations employing Zn metal and Zn^{2+} -host material as the anodes, respectively. ((a) Reproduced from reference 47 with permission from Springer Nature, Copyright © 2019. Distributed under a Creative Commons Attribution License 4.0 International (CC BY 4.0) (<https://creativecommons.org/licenses/by/4.0/>)). (b) Reproduced with permission from reference 63. Copyright© 2020 Wiley-VCH GmbH).

overpotential for HER is the fundamental reason behind the effective functioning of aqueous rechargeable zinc batteries (ARZBs).

1.5 Configurations, Components, and Charge Storage Mechanisms of ARZBs

Similar to the LBs, the ARZBs can be assembled in two ways, zinc-metal battery (ARZMB) and zinc-ion battery (ARZIB) configurations (**Figure 1.11**). The ARZMB and ARZIB configurations are distinct by the electrode materials and electrochemical reactions on the anode side. ARZMBs employ Zn metal foil as the anode that experiences Zn plating/stripping during the charge/discharge process. On the contrary, the anode in ARZIB configuration consists of inorganic or organic materials that can reversibly host/release (or insert/extract) Zn^{2+} ions during the charge/discharge process. Meanwhile, the insertion/extraction of Zn^{2+} happens as the complimentary reaction at the cathode in both configurations.

1.5.1 Charge Storage Mechanism and Classification

The charge storage mechanisms in ARZBs depend on the intrinsic properties of the electrode materials. Two broad categories of energy storage mechanisms are faradaic redox reaction and electrical double layer (EDL) formation. The faradaic redox reaction mechanism indicates that the electrochemical reactions or oxidation/reduction (redox) reactions take place

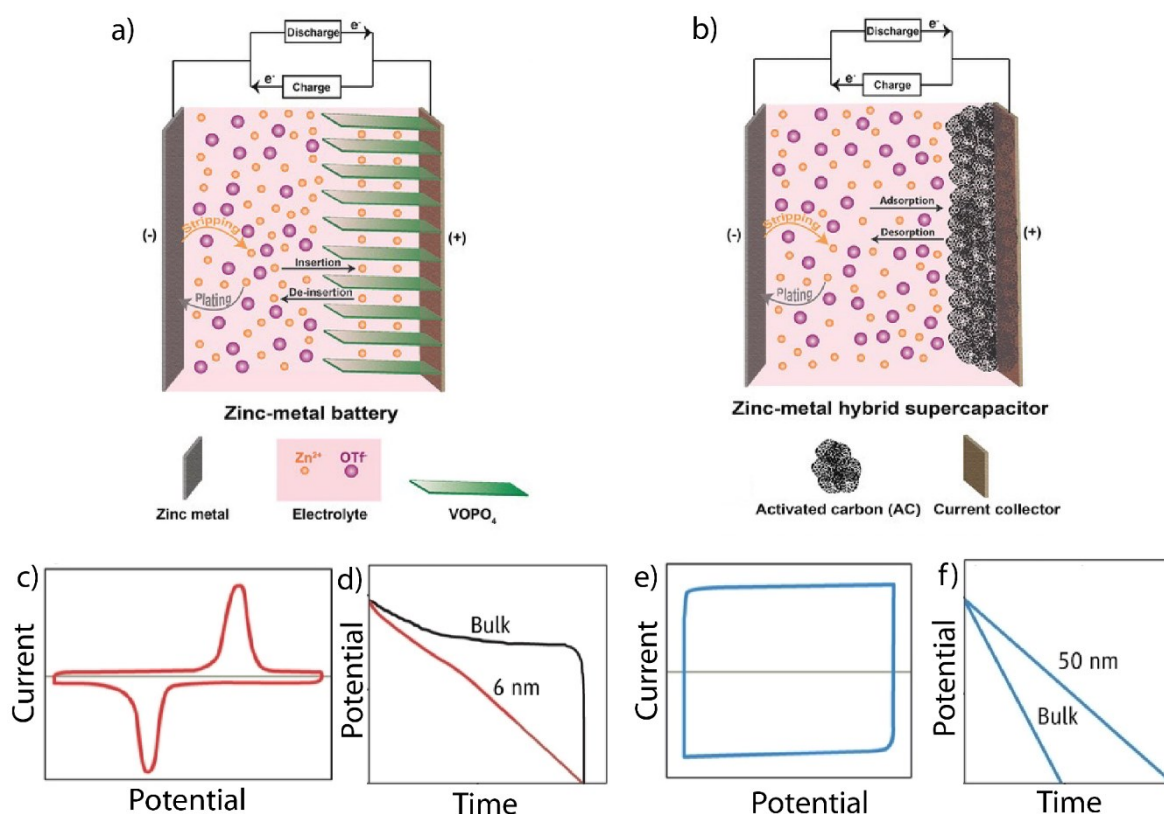


Figure 1.12. Schematic representation of (a) ARZMB and (b) ZMHS, where the negative electrodes are Zn metal in both cases and the positive electrodes are made of redox-active material and high surface area carbon, respectively; (c) cyclic voltammetry profile of a battery-type material; (d) GCD profiles representing the diffusion-controlled (black plot) and surface-controlled (red plot) mechanisms; (e) CV and (f) GCD plots corresponding to charge storage through EDL formation. ((a) and (b) Reproduced with permission from reference 38. Copyright © 2020 WILEY-VCH Verlag GmbH & Co. KGaA, Weinheim. (c)-(f) Reproduced/Adapted with permission from reference 40. Copyright © 2014 American Association for the Advancement of Science).

at the electrode during the charge storage process (**Figure 1.12a**). The redox-active materials go through different oxidation states to accommodate the Zn^{2+} ions within the electrode. The cycling voltammetry (CV) profiles of such materials exhibit sharp or broad oxidation and reduction peaks, signifying the change in their valence states. The redox-assisted charge storage is advantageous for achieving high capacity and energy density. Transition metal oxides (MnO_2 , V_2O_5), transition metal chalcogenides (VS_2), conducting polymers (polyaniline), etc., are examples of redox-active materials used in ARZB electrodes.^{36,37} Zn^{2+} ions can also be stored physically through the electrochemical double layer (EDL) formation at the interface between the electrode and electrolyte (**Figure 1.12b**). The CV profile for the

charge storage through EDL formation features a nearly rectangular behaviour without prominent redox peaks. The EDL formation process is highly reversible and provides ultralong cycling stability to the device. Generally, carbon materials with high surface area follow this mechanism. To distinguish this electrophysical charge storage mechanism, the corresponding electrochemical cells can be called zinc-metal hybrid supercapacitor (ZMHS, where the anode is Zn metal) or zinc-ion hybrid supercapacitor (ZIHS, where the anode is Zn^{2+} host material).^{38,39} As the charge storage in such carbon-based materials occurs purely through the electrostatic attraction between the charged electrode surface and electrolyte ions, the ZMHSs exhibit limited charge storage capacity and specific energy. Throughout the working chapters of this thesis, the Zn^{2+} ion storage by means of the faradaic redox reaction mechanism is emphasized, and the fundamentals are discussed in detail further.

According to the physical and chemical properties of the electrode material, the Faradaic redox reactions in ARZBs could be diffusion-controlled and surface-controlled. Generally, for bulk material (material with large particle size and low surface area), the Zn^{2+} ions are forced to diffuse into the bulk electrode material for accessing the redox-active centres. The kinetics of the redox reactions and the charge storage capacity depends on how facile the Zn^{2+} ions can diffuse into the bulk electrode; hence the process is called the diffusion-controlled process. The electrode materials following this mechanism are categorized as battery-type materials. The galvanostatic charge-discharge (GCD) profile with the well-defined discharge plateau is the characteristic of the diffusion-controlled mechanism (**Figure 1.12d**).⁴⁰ On the contrary, the redox-active centres of the electrode can be exposed at the surface or near-surface region by nanosizing the battery-type materials. As a result, the electrolyte ions can easily access the active centres, resulting in faster kinetics of the redox reactions. This charge storage mechanism is called the surface-controlled redox process. The voltage vs. time profile corresponding to the surface-controlled process does not show a distinct discharge plateau. Due to the fast kinetics, the surface-controlled process contributes to high rate performance and high power capability, whereas diffusion-controlled reactions are associated with high energy density.⁴⁰ It can be noted that the electrode materials in ARZBs often display electrochemical signature that implies both diffusion-controlled and surface-controlled kinetics, thereby offering high energy density along with high power density.⁴¹

1.5.2 Cathode Materials for ARZBs

In the last few years, a large variety of inorganic and organic cathode materials offering high capacity and long cycling stability are reported for ARZBs. Based on the crystal structure

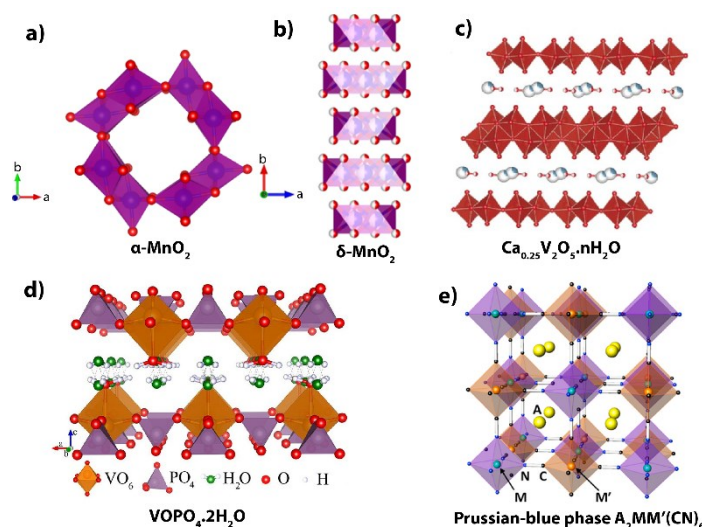


Figure 1.13. The crystal structure of some of the intercalation cathode materials used in RZBs: (a) tunnelled α - MnO_2 , (b) layered δ - MnO_2 , (c) layered vanadium oxide, (d) layered VOPO_4 , and (e) Prussian-blue analogue. ((a) and (b) Reproduced with permission from reference 45. Copyright © 2020, IOP. (c) Reproduced with permission from reference 49. Copyright © 2018 Wiley-VCH Verlag GmbH & Co. KGaA, Weinheim. (d) Reproduced with permission from reference 44. Copyright © 2019, American Chemical Society. (e) Reproduced with permission from reference 46. Copyright © 2016 Elsevier).

and nature of active sites, the host cathode can accommodate Zn^{2+} ions through intercalation, coordination, and conversion process. If not specified, a general terminology insertion/extraction can represent any of these three categories.

Intercalation cathode

Intercalation/deintercalation means the inclusion/exclusion of ions or molecules into the layered material. The Zn^{2+} ions intercalation is reported with tunnel structured α - MnO_2 , δ - MnO_2 , layered V_2O_5 , layered MoS_2 , copper hexacyanoferrate, metal-organic framework, *etc.*⁴²
⁴⁷ The crystal structure of some of the intercalation cathode materials in AZMBs is given in **Figure 1.13**. The open structure of these materials constructed from layers/channels/tunnels assists the to and fro movement of Zn^{2+} ions into the crystal lattice. The difficulties in designing intercalation cathodes for ARZBs stem from the high charge density of Zn^{2+} ions. Divalent Zn^{2+} ions firmly coordinate with six surrounding water molecules and form large size (~ 5.5 Å) clathrates in an aqueous solution.⁴² As a consequence, a cathode material with smaller interlayer spacing cannot intake the hydrated Zn^{2+} ions. In this case, the charge storage is accompanied by desolvation of Zn^{2+} from its solvation shell and breaking of Zn-H₂O bonds. This desolvation process causes a hefty energy penalty and hinders the diffusion of Zn^{2+} across

the electrode interface.⁴⁸ None the less, the Coulombic interaction between the divalent Zn^{2+} and the host crystal matrix makes the solid-state diffusion process even more challenging. These intricacies could lead to low specific capacity and rapid capacity fading during the long term cycling. Therefore, the host structures with large interlayer spacing are attractive for designing intercalation cathode for ARZBs. Encouragingly, tuning the interlayer spacing by incorporating water molecules and/or other cations between two layers of the crystal lattice is found to be an effective strategy to increase the Zn^{2+} diffusivity and ease the intercalation into the layered hosts.^{41,49} In **Chapter 4** of this thesis, enlarging the interlayer spacing of hydrated vanadium oxide cathode by manganese ion doping and its positive implications on the electrochemical performance of ARZMB are discussed.

Coordination cathode

Challenges associated with the intercalation materials also bring an opportunity to develop '*beyond-intercalation*' cathodes, among which coordination cathodes are important. The electronegative oxygen and nitrogen-rich small organic molecules (*viz.* perylene-3,4,9,10-tetracarboxylic diimide, p-Chloranil, pyrene-4,5,9,10-tetraone, *etc.*) or polymers (*viz.* poly(o-phenylenediamine)) belong to this class.^{50,51} Upon discharge, the oxygen and nitrogen centres present in the organic cathodes coordinate to the Zn^{2+} ions and release them in the reverse cycle.⁵² This redox-assisted coordination/uncoordination mechanism for charge storage reduces the risk of volume changes and pulverization within the electrode microstructure.⁵³

Conversion cathode

Conversion type materials are another class of '*beyond-intercalation*'-type cathode materials. So far, only a few materials are reported as conversion cathodes in ARZBs. For example, Co(III) rich Co_3O_4 cathode in a ZnSO_4 -based aqueous (2M ZnSO_4 +0.2M CoSO_4) electrolyte undergoes a conversion reaction between CoO and Co_3O_4 phase.⁵⁴ Similarly, the α - MnO_2 cathode in the ZnSO_4 electrolyte forms the MnOOH phase through conversion reaction.⁵⁵ It is interesting to note that the conversion of Co_3O_4 and MnO_2 cathodes in aqueous electrolytes entail H^+ as the charge carrier instead of Zn^{2+} . Moreover, the conversion reactions are reversible, and the ARZBs employing conversion cathodes exhibit good capacity and prolonged lifespan.

Zn^{2+} and H^+ coinsertion cathode

Aqueous solutions of Zn^{2+} salt show pH within the range of 3 to 5, indicating the slightly acidic nature. Therefore, the presence of H^+ in the aqueous solution of Zn salts is

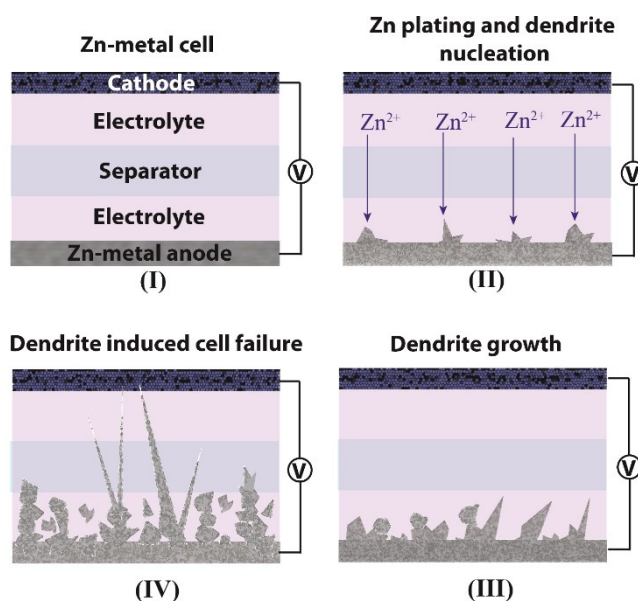


Figure 1.14. Schematic representation of the stepwise dendrite nucleation and growth on the Zn anode in ARZMB.

inevitable. As the free H^+ is small in size ($H^+ < Zn^{2+}$), they can quickly diffuse to the charge storage sites in the electrode materials and contribute to the electrochemical processes in ARZBs. The H^+ insertion has been proved with MnO_2 , diquinoxalino[2,3-a:2',3'-c]phenazine, polyaniline, and few other cathodes.^{55,56} Depending on the cathode materials, the H^+ uptake may or may not be associated with the subsequent Zn^{2+} uptake. The involvement of both H^+ and Zn^{2+} in the charge storage process is discussed in **Chapter 5**.

One important consequence of the H^+ insertion mechanism is the formation of layered double hydroxide (LDH)-type materials at the cathode during the discharge.⁵⁷ The insertion of H^+ increase OH^- concentration near the cathode|electrolyte interface resulting in a change in the local pH. The reactions between the excess OH^- ions and the dissolved Zn salts form LDHs. The composition and properties of the so formed LDHs mainly depend on the Zn salt used in the electrolyte. For instance, $ZnSO_4$ salt produces water-insoluble $Zn_4SO_4(OH)_6 \cdot nH_2O$ (zinc hydroxy sulfate, ZHS) LDH, whereas the $Zn(TFSI)_2[Zn(OH)_2]_3 \cdot xH_2O$ (zinc hydroxy trifluorosulfonylimide, ZHT) LDH formed with $Zn(TFSI)_2$ salt is water-soluble. The higher solubility of ZHT is proved to be advantageous in achieving low ohmic and charge transfer resistance in $Zn(TFSI)_2$ electrolyte compared to that in $ZnSO_4$ electrolyte.⁵⁸ Kundu *et al.* and few other groups reported the LDH precipitation is a reversible process, and the precipitate almost disappears upon charging.⁵⁷ The precipitation/dissolution of LDH helps maintain the pH in the mild acidic range, thereby assisting the H^+ insertion throughout the discharge process.

Apart from the inorganic materials, organic small molecules and polymers can also accommodate/release H^+ through the coordination mechanism. However, reports on the LDH precipitation mechanism in the context of the organic cathodes is rare. Moreover, how the LDHs created with different Zn-salts affects the performance and rechargeability of ARZB cathodes is still not completely understood, and further research is required in this direction.

1.5.3 Anode Material for ARZBs

Zn metal anode in ARZMB

Commercial Zn foil is directly used as the anode in ARZMBs. The electrochemical reactions associated with Zn metal anode are plating and stripping of Zn, as shown below;



Zn plating process in ARZMB forms disordered Zn deposits leading to the growth of high surface area Zn (HSAZ) and Zn dendrites (similar to Li plating in LMBs).⁵⁹ The steps involved in the nucleation and growth of Zn dendrite in ARZMB are schematically described in **Figure 1.14**. During the first charging cycle, Zn plating creates small protuberance on the anode surface. In the following plating cycles, these protrusions exhibit a strong electrical field compared to the other regions of the Zn anode. With the non-uniform distribution of the electrical field, Zn deposition preferably occurs around the tips instead of on the smooth regions of the anode. The prolonged electrochemical cycling of ARZMBs amplifies this process leading to Zn dendrites.⁶⁰ The HSAZ or dendrite growth is driven by nucleation overpotential, the concentration of Zn^{2+} , electrolyte pH, ionic conductivity of the electrolyte, *etc.*⁶¹ Zn dendrites in nearly neutral aqueous electrolytes generally exhibit hexagonal plate-like morphology with a sharp edge. However, the morphology may vary depending on the electrolyte, pH, temperature, and electrochemical conditions. As a general representation, the inhomogeneous depositions are referred to as Zn 'dendrite'. Regardless of the morphological variation, such disordered deposition is always undesired and detrimental to the overall electrochemical performance. Nevertheless, Zn protrusions can pierce the separator and bridge the gap between anode and cathode, leading to failure of the cell.

Facile transport of electrons and Zn^{2+} ion at the anode|electrolyte interface are the two necessary conditions for dendrite-free plating/stripping of Zn. Being metal, the Zn anode easily dissipates the electrons, which helps to control the deposition morphology and delay the dendrite growth. On the other hand, the Zn^{2+} ions go through a series of processes before meeting the electrons available at the Zn anode surface. At first, the hydrated Zn^{2+} ions diffuse

through the electrolyte toward the electron-rich anode. Zn^{2+} ions close to the electrode surface undergo stripping of the hydration sheath and participate in the subsequent electrochemical deposition process. However, the divalent Zn^{2+} ions strongly interact with the water molecules, which makes the diffusion and desolvation of hydrated ions challenging. Thus controlling the transport of Zn^{2+} ions and homogeneous Zn^{2+} flux is crucial for dendrite-free Zn deposition.⁶²

Insertion anode in ARZIB

The anode in ARZIB reversibly host/release Zn^{2+} ions during the charging/discharging process, which is similar to the charge storage process in LIBs.⁶³ High specific capacity, low redox potential (vs. $\text{Zn}|\text{Zn}^{2+}$), long cycling stability, and high Coulombic efficiency are prerequisites for efficient anode materials. As discussed for cathodes, the anode materials can accommodate Zn^{2+} ions through the intercalation or coordination process. For instance, ZnMo_6S_8 , Mo_6S_8 , and $\text{Na}_{0.14}\text{TiS}_2$ are intercalation-type anodes as their layered crystal structure could allow the reversible intercalation/deintercalation of Zn^{2+} ions.^{64,65} Organic anode material based on PTCDI is also reported in ARZIB.⁶⁶ However, the reports on anode materials are still minimal compared to the rapidly growing interest in the cathode materials of ARZMBs. **Chapter 5** of this thesis deals with the development of organic anode material for ARZIBs.

1.5.4 Electrolyte Formulation

Electrolyte salt

The electrochemical stability and ionic conductivity of the electrolyte have a remarkable impact on the performance of ARZBs. The most common electrolytes are ZnSO_4 and $\text{Zn}(\text{CF}_3\text{SO}_3)_2$. Among the other Zn salts ZnCl_2 , ZnClO_4 , *etc.*, are also being used for the electrolyte preparation. The solvation sheath structure of Zn^{2+} ions in aqueous electrolytes is a crucial feature that decides the Zn anode performance in ARZMBs. In a low-concentration electrolyte, water molecules in the solvation sheath are firmly coordinated with the Zn^{2+} ion. The hydrated Zn^{2+} in these diluted electrolytes are forced to overcome a high energy barrier to shed off the water molecules (desolvation) during the plating process. This incurs irregular Zn deposition over the anode. Increasing the electrolyte concentration is a practical approach to regulate the solvation sheath structure of Zn^{2+} ions. The solvation shell of Zn^{2+} in the concentrated electrolyte contains fewer water molecules than that in the diluted electrolyte. As a result, the desolvation of Zn^{2+} encounters a low energy penalty in the concentrated electrolyte, which is favourable for smooth and uniform deposition of Zn. Besides, a significantly high salt concentration can shift the oxidation potential of water to higher overpotential, widening the

electrochemical stability of the electrolyte (as depicted in **Figure 1.8**). For example, the aqueous solution of ZnCl_2 with 30 m concentration exhibits an ESW of 2.3 V, which is much higher than the ESW of ZnCl_2 electrolyte with 5 m concentration (1.6 V).⁶⁷ Zn salts with large counter anions such as $\text{Zn}(\text{TFSI})_2$ and $\text{Zn}(\text{CF}_3\text{SO}_3)_2$ also favour dendrite-free Zn deposition.

Electrolyte additive

The performance of ARZBs can be improved with the aid of organic and inorganic electrolyte additives, which can help in stabilizing both anode and cathode during electrochemical cycling. Organic additives such as SDBS, SDS, PEG, and triethyl phosphate in the aqueous electrolytes are capable of directing the crystallographic orientation of Zn deposits and control the growth of Zn protrusions.³⁴ Addition of Na-salts in the electrolyte help to regulate the local current distribution at the Zn anode surface.⁶⁸ Na^+ ions with substantially low reduction potential than Zn^{2+} can form a positively charged shield around the tips of Zn deposits. This electrostatic shield mechanism compels the Zn^{2+} ions to get reduced at the adjacent regions of the anode instead of the tip.⁶⁹ In effect, such mixed electrolytes can avoid the localized growth of Zn deposits compared to additive-free Zn-electrolyte. Use of dual salt electrolyte with very high salt concentration (e.g., 21 m $\text{LiTFSI}/1\text{M Zn}(\text{CF}_3\text{SO}_3)_2$), eutectic electrolyte (e.g., acetamide/ $\text{Zn}(\text{TFSI})_2$), and ionic liquid additives are also effective for controlling the uneven Zn plating.³⁴

Similarly, different salts are being used as electrolyte additives in the ARZBs to deal with undesired cathode dissolution. A small amount of MnSO_4 or $\text{Mn}(\text{CF}_3\text{SO}_3)_2$ salt in ZnSO_4 or $\text{Zn}(\text{CF}_3\text{SO}_3)_2$ electrolyte can reduce the dissolution of Mn^{2+} ions from the manganese oxide cathodes in ARZBs.⁷⁰ An optimum concentration of Na_2SO_4 additive in the ZnSO_4 electrolyte prevents the loss of Na^+ from the crystal structure of $\text{NaV}_3\text{O}_8 \cdot 1.5\text{H}_2\text{O}$ cathode and stabilizes the Zn anode in ARZMB.⁶⁸ Apart from salt, phosphoric acid (H_3PO_4) is also being used as an additive to stabilize the $\text{VOPO}_4 \cdot x\text{H}_2\text{O}$ cathode. The presence of PO_4^{3-} ions in the electrolyte shifts the decomposition equilibrium of the VOPO_4 and prolongs the battery life.⁷¹

Gel electrolyte

The transition from liquid electrolytes to gel polymer electrolytes (GPEs) is approached in the ARZBs in recent years. The use of GPEs simplifies the cell packaging process and provides flexibility to the battery. GPEs for ARZBs are prepared by dissolving a polymer (e.g., PVA, polyacrylamide, cellulose, etc.) into the aqueous solutions of Zn-salts. During the preparation of GPEs, a large amount of liquid electrolyte can be trapped inside the polymer matrix without compromising the ionic conductivity. GPEs with good mechanical stability

protect the Zn anode from the dendrite nucleation. The low liquid content in GPEs can also be beneficial to mitigate the dissolution of electrode material in ARZBs.

1.5.5 Separator

Unlike the electrode materials and electrolytes, the separators do not directly participate in the electrochemical reactions; however, the microstructure and intrinsic properties of separators have strong implications on the battery performance. Separators must have the characteristics of good mechanical stability, low thickness, high affinity (wettability) to the electrolyte, and facile permeability to the electrolyte ions.

Porous separator

Most of the separators used in ARZBs are made of polyolefin polymers (*e.g.*, polypropylene), glass fiber paper, and cellulose membrane.⁷² All these separators have porous microstructure with various pore size. The pore spaces hold the liquid electrolyte, and these regions are responsible for the easy transport of electrolyte ions. Therefore, the ion conduction in a battery cell also relies on the interaction between the separator surface and electrolyte. For aqueous electrolyte, a porous separator with good wettability in water ensures the complete filling of the pores with the electrolyte, which is crucial for achieving homogeneous ion transport. If the separator is hydrophobic, the partial filling of the pores blocks the ion transport pathways. This increases the electrolyte resistance within the cell and imposes a high overpotential to the electrochemical reactions.

The commercial porous separators do not contain any functional groups and are chemically neutral. This means both cation and anions can freely pass through the pores filled with electrolytes. Therefore, the transport of ions through the porous separators is much like the ion transport in a liquid electrolyte. The transference number of cation (t_+) varies within the range of 0.2-0.3 in the liquid electrolyte. This signifies that the fraction of current carried by the cations is less compared to the current carried by the anions. The porous separator soaked with liquid electrolyte also shows similar t_+ value. A low t_+ value of the electrolyte component hampers the distribution of Zn^{2+} flux over the Zn anode and creates a gradient in Zn^{2+} concentration at the anode|electrolyte interface. The concentration gradient leads to the nucleation of Zn dendrite in porous separator-based ARZMBs (**Figure 1.15a**). Therefore, the electrolyte component offering t_+ value close to ~ 1 is ideal for ARZMBs and any other rechargeable metal-ion batteries (*e.g.*, ARZIBs, LBs, magnesium batteries, *etc.*).

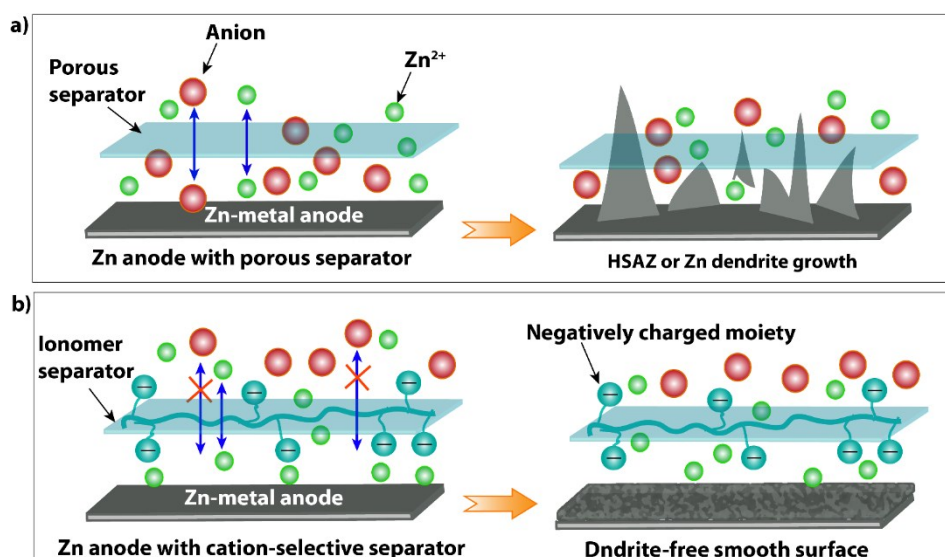


Figure 1.15. Schematic illustration of the influence of separators in ARZMB: (a) porous separator allows the transport of both cations and anions and favours the dendrite growth on the Zn metal anode; (b) cation-selective ionomer separator allows only the cation transport and favours the smooth, dense and uniform deposition of Zn.

Cation-selective separator

Interestingly, the separators can be equipped with suitable functional groups to accomplish the selectivity toward cation conduction. One way to design a cation-selective separator is to modify the existing microporous separators by creating thin layers of negatively charged materials (e.g., graphene oxide) over them. This negatively charged layer allows the cations to pass through and repels the anions.⁷³ As an alternate way, negatively charged polymer membrane (viz., Nafion) can be utilized as the separator for improving the t_+ of the electrolyte component. These polymers possess anionic functional groups tethered to the polymer backbone. The negatively charged units build cation transport channels throughout the separator, which imparts a high transference number for cation conduction. Therefore, the modified porous separators and ionomer separators with polyanionic attributes can serve dual roles in ARZMBs. One is to keep the physical barrier between the electrodes, which is the general function of a separator. At the same time, the cation-selective separator suppresses the nonuniform deposition of Zn over the Zn anode and eliminates the risk of HSAZ and Zn dendrite growth. For better understanding, the effect of the porous separator and charged polymer separator on the morphology of Zn deposits in ARZMBs is schematically in **Figure 1.15a** and **b**, respectively. The advantage of cation-selective separator over the porous neutral separators in aqueous ARZMBs is discussed in **Chapter 2** and **Chapter 3**.

1.6 Conclusions, Scope, and Objectives of the Thesis

In summary, this introductory chapter of the current thesis provides a brief overview of the current energy scenario and the importance of batteries as electrochemical energy storage devices (EEDs). This chapter explains the fundamentals of batteries and their components, which play a vital role in the charge storage process. The benefits and concerns associated with the state-of-the-art LIBs and the necessary transition from LIBs to LMBs and post-lithium batteries (PLBs) are thoroughly discussed. In the context of PLBs, the importance of post-lithium-ion batteries (PLIBs) and post-lithium-metal batteries (PLMBs) are discussed with an emphasis on the advantages of aqueous electrolytes. It is envisaged that rechargeable Zn batteries employing neutral aqueous electrolyte could be one of the promising PLB technologies. The aqueous rechargeable zinc batteries (ARZBs) are intrinsically safe, cost-effective, and environmental-friendly in nature. Despite these advantages, the Zn metal anode in ARZMBs persistently suffers from low reversibility and poor Coulombic efficiency in the aqueous electrolyte due to the growth of HSAZ and Zn dendrite, restraining the advancement ARZMBs beyond the lab-level. Unfortunately, if the existing literature reports are considered, most of them are focused on exploring the cathode materials and little attention has been paid to address the issues related to the Zn anode. Tuning the electrolyte component (combination of electrolyte and separator) can improve the electrochemical performance of the Zn anode by suppressing the HSAZ and Zn dendrite growth. Besides, the inherent limitations associated with the Zn anode can be overcome by switching from Zn to insertion-type anode material to device aqueous rechargeable zinc-ion batteries (ARZIBs). Therefore, this thesis emphasizes the development of both the electrolyte component and electrode materials for improving the overall performance of ARZBs.

In most of the ARZMB literature, porous separators are extensively used in combination with Zn^{2+} -conducting liquid electrolytes. However, Zn anode coupled with porous separator exhibits the dendrite growth, which causes severe capacity fading and cell failure by leading to short-circuit. The use of a cation-selective separator integrated with Zn^{2+} -conducting electrolyte can improve the performance of ARZMBs.

- *In the second chapter (Chapter 2) of this thesis, the prospect of Nafion ionomer membrane as an effective alternative to the conventional porous separator in ARZMB is demonstrated by taking the example of the $\text{Zn}||\text{V}_2\text{O}_5$ cell. The Zn^{2+} -integrated Nafion separator improves the cycling stability of ARZMB by suppressing the dendrite growth on the Zn metal anode. The ionomer character and cation-selective nature of Nafion help maintain a uniform flux of Zn^{2+} ions near the anode|electrolyte interface, ensuring*

low overpotential for reversible plating/stripping of Zn. The superiority of the Nafion separator over the porous separator is proven through physical and electrochemical characterizations of the Zn||V₂O₅ cells.

MnO₂ is recognized as high voltage cathode material for ARZMB. The dissolution of MnO₂ in the aqueous electrolyte causes active material loss from the cathode side during electrochemical cycling, thereby hampering the long-term cycling stability of the Zn||MnO₂ cells. The use of Mn²⁺ salt additive in the aqueous electrolyte is proved to be a viable solution to mitigate the performance drop in many reports. However, the optimization of Mn²⁺ concentration adds additional steps to the cell fabrication and the additive can lead to the overestimation of cell capacity.

- *In the third chapter (Chapter 3), the benefits of the Nafion separator is further exploited in Zn||MnO₂ cells. The electrochemical analyses reveal that the use of the Nafion separator can improve the cycling stability of the Zn||MnO₂ cell without requiring the Mn²⁺ additive. The influence of the type of electrolyte salt and concentration of the liquid electrolyte on the performance is also investigated. Moreover, the Nafion-based Zn||MnO₂ cells with single-component electrolyte outperform the cells prepared with porous separators. The ionomer character of the Nafion membrane is found to be effective in controlling the morphology of the Zn anode, which further validates the cation-selective separator will be a better choice over the porous separator of ARZMBs, as already evidenced in Chapter 2.*

The development of efficient cathode material to facilitate the reversible insertion/extraction of Zn²⁺ ions is also important for improving the overall performance of ARZMBs. Being a divalent cation with high charge density, insertion/extraction of hydrated Zn²⁺ ions is challenging and destabilize the crystal structure of the cathode. Layered hydrated vanadium oxide with large interlayer spacing and multiple oxidation states have attracted prominent interest as the cathode material in ARZMBs.

- *The fourth chapter (Chapter 4) of this thesis deals with the facile synthesis of manganese-doped hydrated vanadium oxide as the cathode material in ARZMB. The porous morphology of the material designed by using anionic surfactant during the preparation, enhances the diffusion of electrolyte ions and electrons, resulting in high charge storage capacity of the ARZMB cell. The doping of Mn-ion helps expand the interlayer spacing of the material compared to the undoped counterpart. The advantage of manganese-doped is evidenced in the improved capacity retention*

during the long-term cycling stability of the ARZMB cell. The performance of manganese-doped hydrated vanadium oxide is also demonstrated in a quasi-solid-state ARZMB pouch cell.

Along with the zinc-metal battery, the development of zinc-ion battery configuration utilizing insertion-type anode material is also important. However, reports on anode material for ARZIBs is rare. Therefore, exploring anode material with high capacity, suitable redox potential, and good cycling stability is interesting and essential for advancing the ARZIBs.

- *The fifth chapter (Chapter 5) of this thesis introduces the applicability of organic anhydride molecule as the anode material in ARZIB. The electrochemical analysis of the anhydride molecule shows reversible redox behaviour at a low potential region (vs. Zn|Zn²⁺). The electrochemical studies also reveal the involvement of Zn²⁺ and H⁺ in the charge storage process. The ARZIB cell fabricated with the anhydride anode and MnO₂ cathode participates in the reversible charge/discharge cycles. As both Zn²⁺ and H⁺ are found to be active charge carriers, the full-cell is coined as zinc-proton hybrid ion battery.*

In brief, this thesis highlights the importance of post-lithium aqueous batteries with a special emphasis on rechargeable zinc batteries. The key results presented in this thesis show that the research on electrode material and electrolyte component should go hand-in-hand to achieve a significant leap in the performance of ARZBs. Ultimately, the connection between emerging electrochemistry and advanced materials is the key to develop efficient and reliable batteries.

1.7. References

- (1) Gür, T. M. Review of electrical energy storage technologies, materials and systems: challenges and prospects for large-scale grid storage. *Energy & Environmental Science* **2018**, *11*, 2696-2767.
- (2) Budde-Meiwes, H.; Drillkens, J.; Lunz, B.; Muennix, J.; Rothgang, S.; Kowal, J.; Sauer, D. U. A review of current automotive battery technology and future prospects. *Proceedings of the Institution of Mechanical Engineers, Part D: Journal of Automobile Engineering* **2013**, *227*, 761-776.
- (3) Kim, H.; Hong, J.; Park, K.-Y.; Kim, H.; Kim, S.-W.; Kang, K. Aqueous rechargeable Li and Na ion batteries. *Chemical reviews* **2014**, *114*, 11788-11827.
- (4) Cheng, X.-B.; Zhang, R.; Zhao, C.-Z.; Zhang, Q. Toward safe lithium metal anode in rechargeable batteries: a review. *Chemical reviews* **2017**, *117*, 10403-10473.

- (5) Cheng, X. B.; Zhang, R.; Zhao, C. Z.; Wei, F.; Zhang, J. G.; Zhang, Q. A review of solid electrolyte interphases on lithium metal anode. *Advanced science* **2016**, *3*, 1500213.
- (6) Choi, J. W.; Aurbach, D. Promise and reality of post-lithium-ion batteries with high energy densities. *Nature Reviews Materials* **2016**, *1*, 1-16.
- (7) Liang, Y.; Dong, H.; Aurbach, D.; Yao, Y. Current status and future directions of multivalent metal-ion batteries. *Nature Energy* **2020**, *5*, 646-656.
- (8) Chao, D.; Zhou, W.; Xie, F.; Ye, C.; Li, H.; Jaroniec, M.; Qiao, S.-Z. Roadmap for advanced aqueous batteries: From design of materials to applications. *Science advances* **2020**, *6*, eaba4098.
- (9) Liu, J.; Xu, C.; Chen, Z.; Ni, S.; Shen, Z. X. Progress in aqueous rechargeable batteries. *Green Energy & Environment* **2018**, *3*, 20-41.
- (10) Konarov, A.; Voronina, N.; Jo, J. H.; Bakenov, Z.; Sun, Y.-K.; Myung, S.-T. Present and future perspective on electrode materials for rechargeable zinc-ion batteries. *ACS Energy Letters* **2018**, *3*, 2620-2640.
- (11) Winter, M.; Brodd, R. J. What are batteries, fuel cells, and supercapacitors? *Chemical reviews* **2004**, *104*, 4245-4270.
- (12) Schmidt-Rohr, K. How batteries store and release energy: explaining basic electrochemistry. *Journal of Chemical Education* **2018**, *95*, 1801-1810.
- (13) Xu, K. Nonaqueous liquid electrolytes for lithium-based rechargeable batteries. *Chemical reviews* **2004**, *104*, 4303-4418.
- (14) Placke, T.; Kloepsch, R.; Dühnen, S.; Winter, M. Lithium ion, lithium metal, and alternative rechargeable battery technologies: the odyssey for high energy density. *Journal of Solid State Electrochemistry* **2017**, *21*, 1939-1964.
- (15) Liu, C.; Neale, Z. G.; Cao, G. Understanding electrochemical potentials of cathode materials in rechargeable batteries. *Materials Today* **2016**, *19*, 109-123.
- (16) Goodenough, J. B.; Kim, Y. Challenges for rechargeable Li batteries. *Chemistry of materials* **2010**, *22*, 587-603.
- (17) Whittingham, M. S. The role of ternary phases in cathode reactions. *Journal of The Electrochemical Society* **1976**, *123*, 315.
- (18) Vijayakumar, V.; Anothumakkool, B.; Kurungot, S.; Winter, M.; Nair, J. R. In situ polymerization process: an essential design tool for lithium polymer batteries. *Energy & Environmental Science*, **2021**, *14*, 2708-2788.

- (19) Xie, J.; Lu, Y.-C. A retrospective on lithium-ion batteries. *Nature Communications* **2020**, *11*, 1-4.
- (20) Walter, M.; Kovalenko, M. V.; Kravchyk, K. V. Challenges and benefits of post-lithium-ion batteries. *New Journal of Chemistry* **2020**, *44*, 1677-1683.
- (21) Whittingham, M. S. Lithium batteries and cathode materials. *Chemical reviews* **2004**, *104*, 4271-4302.
- (22) Nitta, N.; Wu, F.; Lee, J. T.; Yushin, G. Li-ion battery materials: present and future. *Materials today* **2015**, *18*, 252-264.
- (23) Bieker, G.; Winter, M.; Bieker, P. Electrochemical in situ investigations of SEI and dendrite formation on the lithium metal anode. *Physical Chemistry Chemical Physics* **2015**, *17*, 8670-8679.
- (24) Zhang, Y.; Zuo, T.-T.; Popovic, J.; Lim, K.; Yin, Y.-X.; Maier, J.; Guo, Y.-G. Towards better Li metal anodes: challenges and strategies. *Materials Today* **2020**, *33*, 56-74.
- (25) Vijayakumar, V.; Diddens, D.; Heuer, A.; Kurungot, S.; Winter, M.; Nair, J. R. Dioxolanone-Anchored Poly (allyl ether)-Based Cross-Linked Dual-Salt Polymer Electrolytes for High-Voltage Lithium Metal Batteries. *ACS applied materials & interfaces* **2019**, *12*, 567-579.
- (26) Suo, L.; Borodin, O.; Gao, T.; Olguin, M.; Ho, J.; Fan, X.; Luo, C.; Wang, C.; Xu, K. "Water-in-salt" electrolyte enables high-voltage aqueous lithium-ion chemistries. *Science* **2015**, *350*, 938-943.
- (27) Yang, C.; Chen, J.; Qing, T.; Fan, X.; Sun, W.; von Cresce, A.; Ding, M. S.; Borodin, O.; Vatamanu, J.; Schroeder, M. A. 4.0 V aqueous Li-ion batteries. *Joule* **2017**, *1*, 122-132.
- (28) Wang, Y.; Meng, X.; Sun, J.; Liu, Y.; Hou, L. Recent Progress in "Water-in-Salt" Electrolytes Toward Non-lithium Based Rechargeable Batteries. *Frontiers in Chemistry* **2020**, *8*.
- (29) Yuan, D.; Zhao, J.; Manalastas Jr, W.; Kumar, S.; Srinivasan, M. Emerging rechargeable aqueous aluminum ion battery: Status, challenges, and outlooks. *Nano Materials Science* **2020**, *2*, 248-263.
- (30) Zhao, Q.; Zachman, M. J.; Al Sadat, W. I.; Zheng, J.; Kourkoutis, L. F.; Archer, L. Solid electrolyte interphases for high-energy aqueous aluminum electrochemical cells. *Science Advances* **2018**, *4*, eaau8131.

- (31) Hao, J.; Li, X.; Zeng, X.; Li, D.; Mao, J.; Guo, Z. Deeply understanding the Zn anode behaviour and corresponding improvement strategies in different aqueous Zn-based batteries. *Energy & Environmental Science* **2020**, *13*, 3917-3949.
- (32) Lai, S.-B.; James, M.-I.; Wu, X.-C.; Dong, Y.-L.; Wang, J.-H.; Gao, M.; Liu, J.- F.; Sun, X.-M. A promising energy storage system: rechargeable Ni–Zn battery. *Rare Metals* **2017**, *36*, 381-396.
- (33) Xu, M.; Ivey, D.; Xie, Z.; Qu, W. Rechargeable Zn-air batteries: Progress in electrolyte development and cell configuration advancement. *Journal of Power Sources* **2015**, *283*, 358-371.
- (34) Shin, J.; Lee, J.; Park, Y.; Choi, J. W. Aqueous zinc ion batteries: focus on zinc metal anodes. *Chemical science* **2020**, *11*, 2028-2044.
- (35) Wippermann, K.; Schultze, J.; Kessel, R.; Penninger, J. The inhibition of zinc corrosion by bisaminotriazole and other triazole derivatives. *Corrosion Science* **1991**, *32*, 205-230.
- (36) Zhang, N.; Cheng, F.; Liu, Y.; Zhao, Q.; Lei, K.; Chen, C.; Liu, X.; Chen, J. Cation-deficient spinel ZnMn₂O₄ cathode in Zn (CF₃SO₃)₂ electrolyte for rechargeable aqueous Zn-ion battery. *Journal of the American Chemical Society* **2016**, *138*, 12894-12901.
- (37) Wan, F.; Zhang, L.; Wang, X.; Bi, S.; Niu, Z.; Chen, J. An aqueous rechargeable zinc-organic battery with hybrid mechanism. *Advanced Functional Materials* **2018**, *28*, 1804975.
- (38) Vijayakumar, V.; Ghosh, M.; Kurian, M.; Torris, A.; Dilwale, S.; Badiger, M. V.; Winter, M.; Nair, J. R.; Kurungot, S. An In Situ Cross-Linked Nonaqueous Polymer Electrolyte for Zinc-Metal Polymer Batteries and Hybrid Supercapacitors. *Small* **2020**, *16*, 2002528.
- (39) Wang, Q.; Wang, S.; Li, J.; Ruan, L.; Wei, N.; Huang, L.; Dong, Z.; Cheng, Q.; Xiong, Y.; Zeng, W. A Novel Aqueous Zinc-Ion Hybrid Supercapacitor Based on TiS₂ (De) Intercalation Battery-Type Anode. *Advanced Electronic Materials* **2020**, *6*, 2000388.
- (40) Simon, P.; Gogotsi, Y.; Dunn, B. Where do batteries end and supercapacitors begin? *Science* **2014**, *343*, 1210-1211.
- (41) Yan, M.; He, P.; Chen, Y.; Wang, S.; Wei, Q.; Zhao, K.; Xu, X.; An, Q.; Shuang, Y.; Shao, Y. Water-lubricated intercalation in V₂O₅· nH₂O for high-capacity and high-rate aqueous rechargeable zinc batteries. *Advanced Materials* **2018**, *30*, 1703725.

- (42) Liang, H.; Cao, Z.; Ming, F.; Zhang, W.; Anjum, D. H.; Cui, Y.; Cavallo, L.; Alshareef, H. N. Aqueous zinc-ion storage in MoS₂ by tuning the intercalation energy. *Nano letters* **2019**, *19*, 3199-3206.
- (43) Trócoli, R.; Kasiri, G.; La Mantia, F. Phase transformation of copper hexacyanoferrate (KCuFe(CN)₆) during zinc insertion: effect of co-ion intercalation. *Journal of Power Sources* **2018**, *400*, 167-171.
- (44) Verma, V.; Kumar, S.; Manalastas Jr, W.; Zhao, J.; Chua, R.; Meng, S.; Kidkhunthod, P.; Srinivasan, M. Layered VOPO₄ as a cathode material for rechargeable zinc-ion battery: effect of polypyrrole intercalation in the host and water concentration in the electrolyte. *ACS Applied Energy Materials* **2019**, *2*, 8667-8674.
- (45) Liu, X.; Yi, J.; Wu, K.; Jiang, Y.; Liu, Y.; Zhao, B.; Li, W.; Zhang, J. Rechargeable Zn-MnO₂ batteries: advances, challenges and perspectives. *Nanotechnology* **2020**, *31*, 122001.
- (46) Chae, M. S.; Heo, J. W.; Kwak, H. H.; Lee, H.; Hong, S.-T. Organic electrolyte-based rechargeable zinc-ion batteries using potassium nickel hexacyanoferrate as a cathode material. *Journal of Power Sources* **2017**, *337*, 204-211.
- (47) Nam, K. W.; Park, S. S.; Dos Reis, R.; Dravid, V. P.; Kim, H.; Mirkin, C. A.; Stoddart, J. F. Conductive 2D metal-organic framework for high-performance cathodes in aqueous rechargeable zinc batteries. *Nature communications* **2019**, *10*, 1-10.
- (48) Kundu, D.; Vajargah, S. H.; Wan, L.; Adams, B.; Prendergast, D.; Nazar, L. F. Aqueous vs. nonaqueous Zn-ion batteries: consequences of the desolvation penalty at the interface. *Energy & Environmental Science* **2018**, *11*, 881-892.
- (49) Xia, C.; Guo, J.; Li, P.; Zhang, X.; Alshareef, H. N. Highly stable aqueous zinc-ion storage using a layered calcium vanadium oxide bronze cathode. *Angewandte Chemie International Edition* **2018**, *57*, 3943-3948.
- (50) Xu, D.; Cao, Z.; Ye, Z.; Zhang, H.; Wang, L.; John, M.; Dong, P.; Gao, S.; Shen, J.; Ye, M. Electrochemical oxidation of π - π coupling organic cathode for enhanced zinc ion storage. *Chemical Engineering Journal* **2021**, *417*, 129245.
- (51) Kundu, D.; Oberholzer, P.; Glaros, C.; Bouzid, A.; Tervoort, E.; Pasquarello, A.; Niederberger, M. Organic cathode for aqueous Zn-ion batteries: taming a unique phase evolution toward stable electrochemical cycling. *Chemistry of materials* **2018**, *30*, 3874-3881.

- (52) Zhang, S.; Long, S.; Li, H.; Xu, Q. A high-capacity organic cathode based on active N atoms for aqueous zinc-ion batteries. *Chemical Engineering Journal* **2020**, *400*, 125898.
- (53) Zhao-Karger, Z.; Fichtner, M. Beyond intercalation chemistry for rechargeable Mg batteries: a short review and perspective. *Frontiers in Chemistry* **2019**, *6*, 656.
- (54) Ma, L.; Chen, S.; Li, H.; Ruan, Z.; Tang, Z.; Liu, Z.; Wang, Z.; Huang, Y.; Pei, Z.; Zapien, J. A. Initiating a mild aqueous electrolyte Co₃O₄/Zn battery with 2.2 V-high voltage and 5000-cycle lifespan by a Co (iii) rich-electrode. *Energy & Environmental Science* **2018**, *11*, 2521-2530.
- (55) Pan, H.; Shao, Y.; Yan, P.; Cheng, Y.; Han, K. S.; Nie, Z.; Wang, C.; Yang, J.; Li, X.; Bhattacharya, P. Reversible aqueous zinc/manganese oxide energy storage from conversion reactions. *Nature Energy* **2016**, *1*, 1-7.
- (56) Tie, Z.; Liu, L.; Deng, S.; Zhao, D.; Niu, Z. Proton insertion chemistry of a zinc–organic battery. *Angewandte Chemie International Edition* **2020**, *59*, 4920-4924.
- (57) Oberholzer, P.; Tervoort, E.; Bouzid, A.; Pasquarello, A.; Kundu, D. Oxide versus nonoxide cathode materials for aqueous Zn batteries: an insight into the charge storage mechanism and consequences thereof. *ACS applied materials & interfaces* **2018**, *11*, 674-682.
- (58) Jin, Y.; Zou, L.; Liu, L.; Engelhard, M. H.; Patel, R. L.; Nie, Z.; Han, K. S.; Shao, Y.; Wang, C.; Zhu, J. Joint Charge Storage for High-Rate Aqueous Zinc–Manganese Dioxide Batteries. *Advanced Materials* **2019**, *31*, 1900567.
- (59) Liu, M.; Yang, L.; Liu, H.; Amine, A.; Zhao, Q.; Song, Y.; Yang, J.; Wang, K.; Pan, F. Artificial solid-electrolyte interface facilitating dendrite-free zinc metal anodes via nanowetting effect. *ACS applied materials & interfaces* **2019**, *11*, 32046-32051.
- (60) Wang, A.; Zhou, W.; Huang, A.; Chen, M.; Chen, J.; Tian, Q.; Xu, J. Modifying the Zn anode with carbon black coating and nanofibrillated cellulose binder: A strategy to realize dendrite-free Zn-MnO₂ batteries. *Journal of colloid and interface science* **2020**, *577*, 256-264.
- (61) Glatz, H.; Tervoort, E.; Kundu, D. Unveiling critical insight into the Zn metal anode cyclability in mildly acidic aqueous electrolytes: implications for aqueous zinc batteries. *ACS applied materials & interfaces* **2019**, *12*, 3522-3530.
- (62) Wang, C.; Wang, A.; Ren, L.; Guan, X.; Wang, D.; Dong, A.; Zhang, C.; Li, G.; Luo, J. Controlling Li Ion Flux through Materials Innovation for Dendrite-Free Lithium Metal Anodes. *Advanced Functional Materials* **2019**, *29*, 1905940.

- (63) Tian, Y.; An, Y.; Wei, C.; Xi, B.; Xiong, S.; Feng, J.; Qian, Y. Recent Advances and Perspectives of Zn-Metal Free “Rocking-Chair”-Type Zn-Ion Batteries. *Advanced Energy Materials* **2021**, *11*, 2002529.
- (64) Kaveevivitchai, W.; Manthiram, A. High-capacity zinc-ion storage in an open-tunnel oxide for aqueous and nonaqueous Zn-ion batteries. *Journal of Materials Chemistry A* **2016**, *4*, 18737-18741.
- (65) Li, W.; Wang, K.; Cheng, S.; Jiang, K. An Ultrastable Presodiated Titanium Disulfide Anode for Aqueous “Rocking-Chair” Zinc Ion Battery. *Advanced Energy Materials* **2019**, *9*, 1900993.
- (66) Liu, N.; Wu, X.; Zhang, Y.; Yin, Y.; Sun, C.; Mao, Y.; Fan, L.; Zhang, N. Building High Rate Capability and Ultrastable Dendrite-Free Organic Anode for Rechargeable Aqueous Zinc Batteries. *Advanced Science* **2020**, *7*, 2000146.
- (67) Zhang, C.; Holoubek, J.; Wu, X.; Daniyar, A.; Zhu, L.; Chen, C.; Leonard, D. P.; Rodríguez-Pérez, I. A.; Jiang, J.-X.; Fang, C. A ZnCl₂ water-in-salt electrolyte for a reversible Zn metal anode. *Chemical communications* **2018**, *54*, 14097-14099.
- (68) Wan, F.; Zhang, L.; Dai, X.; Wang, X.; Niu, Z.; Chen, J. Aqueous rechargeable zinc/sodium vanadate batteries with enhanced performance from simultaneous insertion of dual carriers. *Nature communications* **2018**, *9*, 1-11.
- (69) Ding, F.; Xu, W.; Graff, G. L.; Zhang, J.; Sushko, M. L.; Chen, X.; Shao, Y.; Engelhard, M. H.; Nie, Z.; Xiao, J. Dendrite-free lithium deposition via self-healing electrostatic shield mechanism. *Journal of the American Chemical Society* **2013**, *135*, 4450-4456.
- (70) Zhang, N.; Cheng, F.; Liu, J.; Wang, L.; Long, X.; Liu, X.; Li, F.; Chen, J. Rechargeable aqueous zinc-manganese dioxide batteries with high energy and power densities. *Nature communications* **2017**, *8*, 1-9.
- (71) Shi, H. Y.; Song, Y.; Qin, Z.; Li, C.; Guo, D.; Liu, X. X.; Sun, X. Inhibiting VOPO₄·x H₂O Decomposition and Dissolution in Rechargeable Aqueous Zinc Batteries to Promote Voltage and Capacity Stabilities. *Angewandte Chemie International Edition* **2019**, *58*, 16057-16061.
- (72) Xu, W.; Wang, Y. Recent progress on zinc-ion rechargeable batteries. *Nano-Micro Letters* **2019**, *11*, 1-30.
- (73) Pan, Y.; Hao, J.; Zhu, X.; Zhou, Y.; Chou, S.-L. Ion selective separators based on graphene oxide for stabilizing lithium organic batteries. *Inorganic Chemistry Frontiers* **2018**, *5*, 1869-1875.

ABSTRACT

Name of the Student: Ms. Meena Ghosh
Faculty of Study: Chemical Sciences
AcSIR academic centre/CSIR Lab:
CSIR-National Chemical Laboratory

Registration No. : 10CC16J26013
Year of Submission: 2021
Name of the Supervisor: Dr. Sreekumar
Kurungot

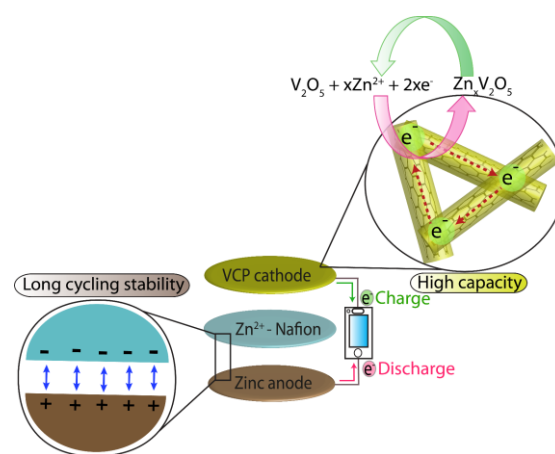
Title of the thesis: Configuring post-lithium aqueous rechargeable zinc batteries using optimized electrolytes and electrode materials

The quest for alternative energy storage systems to complement the lithium-ion batteries (LIBs) is of utmost importance. Aqueous electrolyte-based post-lithium batteries aiming at improved safety, low cost, and environmental benignity have received significant attention in recent years as one of the promising alternatives to LIBs. Among the numerous candidates, aqueous rechargeable zinc batteries (ARZBs) comprising a near-neutral aqueous electrolyte offer the advantages such as high capacity, long-term cycling stability, and adequate energy density. The present thesis deals with optimizing electrolyte components (combination of electrolyte and separator) and developing electrode materials to advance the ARZB technology. The dissertation begins with (**Chapter 1**) a brief overview of the importance of ARZBs in the context of the current energy scenario. **Chapter 1** further introduces the components and working principles of two different ARZB configurations, namely aqueous rechargeable zinc-metal batteries (ARZMBs) and aqueous rechargeable zinc-ion batteries (ARZIBs). The challenges associated with ARZMBs include the growth of irregular dendrite-like Zn deposits over the Zn metal anode, sluggish diffusion kinetics of hydrated Zn^{2+} ions in the electrolyte, and lack of efficient cathode materials, which are explained in **Chapter 1**. The introductory chapter also discusses the limitations and opportunities toward developing insertion-type anode materials for ARZIBs. The following chapter (**Chapter 2**) introduces a novel concept of using a cation-selective Nafion membrane integrated with Zn^{2+} -conducting aqueous electrolyte as the dendrite-suppressing separator in ARZMB, taking $Zn||V_2O_5$ cell as an example. Herein, the negatively charged Nafion separator outperforms the classical porous separator counterparts. The advantage of Nafion is exploited further in **Chapter 3** in another ARZMB cell comprising MnO_2 cathode. The $Zn||MnO_2$ cell benefitted from the dendrite-suppressing Nafion ionomer endows outstanding cycling stability without the requirement of any foreign electrolyte additives such as manganese salts. Besides, the same chapter sheds light on the influence of different Zn salts and their concentration on the electrochemical processes occurring at the electrode|electrolyte interface. **Chapter 4** is dedicated to developing a facile and scalable synthesis route for hydrated vanadium oxides (HVO) as the cathode materials in ARZMB. **Chapter 4** also discusses the positive implications of the preinsertion of Mn ions in the HVO lattice, which in turn improves cycling stability. Utilizing the know-how generated in these chapters, **Chapter 5** explores the possibility of replacing the Zn metal with a Zn^{2+} insertion anode based on an organic anhydride molecule to realize the ARZIB configuration. Herein, the role of H^+ and Zn^{2+} in the charge-storage mechanism is discussed by introducing a new concept of *zinc-proton hybrid ion battery*. **Chapter 6** summarizes the key findings presented in each working chapter of this thesis and provides future directives for further improving the performance of ARZBs.

Chapter 2

Dendrite Growth Suppression by Zn²⁺-Integrated Nafion Ionomer Membrane: Beyond Porous Separators toward Aqueous Zn||V₂O₅ Battery with Extended Cycle Life

The dendritic/irregular growth of Zn deposits in the anode surface is often considered as a major intricacy limiting the lifespan of the aqueous zinc-metal batteries. The effect of separators on the evolution of the surface morphology of the metallic Zn anode has been rarely studied. In this chapter, we demonstrate the efficacy of the Zn²⁺-integrated Nafion ionomer membrane as the separator to effectively suppress the growth of irregular Zn deposits in the metallic anode of an aqueous Zn||V₂O₅ battery. The Zn²⁺ ions coordinated with the SO₃⁻ moieties in Nafion result in a high transference number for the Zn²⁺ ion conduction all the while facilitating high ionic conductivity. The Zn²⁺-integrated Nafion membrane enables the Zn||V₂O₅ cell to deliver a high specific discharge capacity of ~510 mAh g⁻¹ at a current of 0.25 A g⁻¹, which is close to the theoretical capacity of the anhydrous V₂O₅ (589 mAh g⁻¹). Moreover, the same cell exhibits excellent cycling stability with 88% retention of the initial capacity even after 1800 charge-discharge cycles, superior to that of the Zn||V₂O₅ cells comprising conventional porous separators.



Contents of this chapter is published in the article: DOI: 10.1002/ente.201900442. Reprinted (adapted) with permission from Energy Technology, 2019, 7, 1900442. Copyright © 2019 WILEY-VCH Verlag GmbH & Co. KGaA, Weinheim.

2.1 Introduction

The widespread utilization of renewable energy sources and their intermittent nature demands the concomitant development of cost-effective and high performing energy storage devices.^{1,2} The lithium-ion batteries (LIBs) are the benchmark energy storage aid owing to their wide range of applications extending from micro-electronics to electric vehicles. However, their high cost and the use of flammable organic electrolytes raise several concerns on the safety and environmental benignity.^{3,4} These drawbacks propel the research toward the development of low-cost rechargeable aqueous batteries.⁵⁻⁷ Although aqueous electrolyte prototypes are available for LIBs,⁸ the use of highly concentrated expensive electrolytes make the aqueous LIBs unsuited for commercial applications. The reactive Li metals cannot generate a stable interface with an aqueous electrolyte, damaging the prospects of realizing futuristic metal battery designs.⁹⁻¹¹ Therefore, aqueous battery chemistries beyond Li-ion are evolving as an important area in the energy storage research.^{12,13}

Recently, Xu *et al.* reported an aqueous rechargeable zinc-metal battery (ARZMB) prototype using metallic Zn, MnO₂, and aqueous ZnSO₄ as the anode, cathode, and electrolyte, respectively.¹⁴ Compared to the previously known Zn||MnO₂ non-rechargeable aqueous batteries based on corrosive alkaline electrolytes, discussions regarding the aforementioned system have dominated research in recent years. This has opened up new challenges as well as opportunities in the realisation of more efficient ARZMBs with variety of other cathode materials.¹⁵⁻²¹ Despite the availability of efficient cathode materials, the ARZMBs often suffer from severe performance deterioration during prolonged cycling. The inferior lifespan of ARZMBs originates due to the dendritic growth of Zn deposits and formation of high surface area Zn (HSAZ) on the metallic anode during cycling.^{22,23} The use of electrodeposited Zn on foreign substrates instead of commercial Zn foil is found to be an effective way to suppress the formation of the Zn dendrite.²⁴ Pre-treatment of the Zn surface with carbon-based materials is also found to minimize the dendrite growth.^{23,25} However, such complicated procedures preclude the use of these strategies beyond the lab-level. Therefore, exploring practical strategies to impede the formation of Zn dendrites and HSAZ is indeed important despite the challenges involved. In this context, the separators may have a decisive role in the structural evolution of the anode surface. Unfortunately, no study has been carried out to decipher the influence of different separators in the cycling stability of ARZMBs.

Here, for the first time, we demonstrate the fabrication of an aqueous Zn||V₂O₅ battery combining Zn metal, cation-selective Zn²⁺-integrated Nafion ionomer membrane, and electrodeposited V₂O₅ as the anode, separator, and cathode, respectively. The Nafion ionomer

membrane separator is found to effectively suppress the formation of Zn dendrites compared to the conventional porous separators (glass fiber, filter paper, and polypropylene) based ARZMBs. The non-porous cation-selective Nafion membrane offers preferential transport of Zn^{2+} , which helps to maintain uniform ion flux close to the anode surface. This is reflected in the augmented lifespan of the Nafion based $\text{Zn}||\text{V}_2\text{O}_5$ cell, all-the-while, the electrochemically synthesized cathode (nano-structured V_2O_5 over a pre-functionalized carbon fiber paper) helps in achieving high capacity. A specific discharge capacity of 510 mAh g^{-1} is delivered by the Zn^{2+} -integrated Nafion based $\text{Zn}||\text{V}_2\text{O}_5$ cell, which is close to the theoretical Zn^{2+} storage capacity of anhydrous V_2O_5 (589 mAh g^{-1}).²⁶ Apart from the high discharge capacity, the system is found to retain 88% of the initial capacity even after prolonged cycling for 1800 cycles at a current rate of 10 A g^{-1} . This study reveals the drawbacks of the porous separators and proposes a viable way to suppress the dendrite growth in ARZMBs.

2.2 Experimental Section

2.2.1 Materials

Vanadium sulfate oxide hydrate ($\text{VOSO}_4 \cdot x\text{H}_2\text{O}$) was procured from Alfa-Aesar. Lithium perchlorate (LiClO_4) was purchased from Sigma-Aldrich. Zinc sulfate ($\text{ZnSO}_4 \cdot 7\text{H}_2\text{O}$) was purchased from HiMedia Laboratories Pvt. Limited. Toray carbon paper, Glass fiber paper (grade GF/F), Celgard® separator (polypropylene membrane), and Whatman cellulose filter paper were supplied by Global Nanotech. Nafion 212 was purchased from Du Pont, USA.

2.2.2 Fabrication of the V_2O_5 electrode

The free-standing V_2O_5 electrode was prepared by the electrodeposition method.²⁷ A piece of Toray carbon fiber paper (pCP) was electrochemically functionalized (fCP) in an aqueous electrolyte (by applying a bias voltage of 10 V in 0.1 M Na_2SO_4 electrolyte) and washed with deionized (DI) water. After that, the fCP paper was dried and used as the working electrode for chronopotentiometric electrodeposition of V_2O_5 in a three-electrode cell. The precursor solution for the electrodeposition contains 0.2 M VOSO_4 salt and 0.25 M LiClO_4 as the supporting electrolyte in a mixture of DI water and ethanol with a 1:1 ratio. Following Faraday's Law (**Equation 2.1**) a constant current of 3 mA cm^{-2} was applied for 177 secs to obtain a loading of 1 mg of V_2O_5 in 1 cm^2 area of fCP.

$$\text{Loading (mg)} = \frac{I (\text{mA}) \times \text{Mol.wt. of } \text{V}_2\text{O}_5 (\text{g/mol}) \times t (\text{sec})}{n \times F} \quad (\text{Equation 2.1})$$

Here, 'I', 't', 'n', and 'F' are the applied current, deposition time, number of electron transfer, and Faraday's constant, respectively. After careful washing with DI water, the obtained electrode was subjected to annealing at 250° C for 2 h and marked as VCP.

2.2.3 Pre-treatment of the Nafion ionomer membranes

Prior to use, the Nafion (abbreviated as NAF) ionomer membrane (Nafion 212), was treated sequentially at 80°C for 30 min. in (1) 4 wt% H₂O₂, (2) DI water, (3) 0.8M H₂SO₄, and (4) DI water, respectively, with the numbers representing the order of treatment.²⁸ The coupons of the as-obtained activated Nafion ionomer membrane (thickness 60 μm) were dipped in the desired electrolyte (aqueous ZnSO₄.7H₂O) with a salt concentration of 0 and 3M, for three days. The respective membranes are marked as NAF-Y, where 'Y' stands for the concentration of the electrolytes solution used.

2.3.4 Modification of the conventional porous membranes

To study the effect of conventional porous separators on the performance of the ARZMB, three different porous membranes (Celgard (CEL), Whatman filter paper (FP), and glass fiber paper (GFP) with a thickness of 40, 175, and 270 μm, respectively) were used. All the porous membranes were also soaked in 3M ZnSO₄.7H₂O before the use. The electrolyte soaked separators were labelled as CEL-3, FP-3, and GFP-3.

2.3.5 Assembly of Zn||V₂O₅ cells

All the Zn||V₂O₅ cells were assembled in CR2032 coin cell in a traditional fashion where a Zn foil (area 1 cm²), a freshly prepared VCP electrode (area 1 cm²), and desired Nafion membrane (NAF-0 or NAF-3) were used as the anode, cathode, and separator, respectively. Here, the terms anode and cathode are used for the negative and positive electrodes, respectively, considering the discharge state of the cell. For the purpose of comparison, the Zn||V₂O₅ cells were also assembled in a similar fashion (CR2032 coin cell) using the CEL-3, FP-3, and GFP-3 separators. In accordance with the various separators used, the respective cells are designated as Zn|X-Y|VCP. Here also, 'X' stands for the type of the separator used and 'Y' for the concentration of the ZnSO₄.7H₂O electrolyte used.

2.3.6 Material characterization

Morphological investigations of the VCP samples were carried out with field emission scanning electron microscope (FESEM) Nova Nano SEM 450 and FEI-Quanta 450-FEG instrument. The morphology of the various separators was obtained with ESEM-Quanta 200-3D instrument. Energy dispersive X-ray spectroscopy (EDS) elemental mapping was

performed with the ESEM-Quanta 200-3D instrument. Transmission electron microscopy (TEM) imaging was carried out using a Tecnai T-20 instrument at an accelerating voltage of 200 kV. Fourier transform infrared (FTIR) analysis of the sample was carried out with a Bruker Tensor27 FTIR instrument. A Thermo K-alpha+ X-ray spectrometer was used for the X-ray photoelectron spectroscopy (XPS) analysis. X-ray diffraction (XRD) analysis was carried out using Rigaku, MicroMax-007HF with high-intensity Microfocus rotating anode X-ray generator (Cu K α ($\lambda = 1.54 \text{ \AA}$)).

2.3.7 Electrochemical measurements

The electrochemical analyses were carried out in a BioLogic VMP3 Potentiostat-Galvanostat instrument. Electrochemical impedance spectroscopy (EIS) analysis was used to determine the ionic conductivity of Zn²⁺ in various membranes. The frequency for the EIS analysis was varied from 1 MHz to 1 Hz against an open circuit potential with a sinus amplitude of 10 mV ($V_{\text{rms}} = 7.07 \text{ mV}$). The conductivity cells were fabricated in the CR2032 coin cell by keeping the desired membranes in between two stainless steel plates with 1 mm thickness. The conductivity measurements were carried out between 20 to 60°C at every 10°C interval. The temperature was controlled by using an Espec environmental test chamber. Finally, the ionic conductivity and activation energy values were calculated from **Equation 2.2** and **Equation 2.3**, respectively.

$$\sigma \text{ (S cm}^{-1}\text{)} = \frac{l}{RA} \quad \text{(Equation 2.2)}$$

σ = Conductivity of the electrolyte soaked separator

R = bulk resistance obtained from the Nyquist plot

A = Area of the electrolyte soaked separator

l = Thickness of the electrolyte soaked separator

The Arrhenius relationship is given in **Equation 2.3**,

$$\sigma = \sigma^{\circ} \exp(-E_a/RT) \quad \text{(Equation 2.3)}$$

In **Equation 2.3**, σ , σ° , E_a , R, and T represent the ionic conductivity, the pre-exponential factor, the activation energy for ion transport, the gas constant, and the absolute temperature, respectively. The activation energy of the electrolyte soaked separator is obtained from the linear fitting of the $\ln \sigma$ vs. $1/T$ plot.

Zn plating/stripping experiments in the presence of various separators were carried out in symmetric cell configuration with two Zn foils separated by desired separators. The cells are designated as Zn|X-Y|Zn, where 'X' and 'Y' carry the same information as mentioned in the

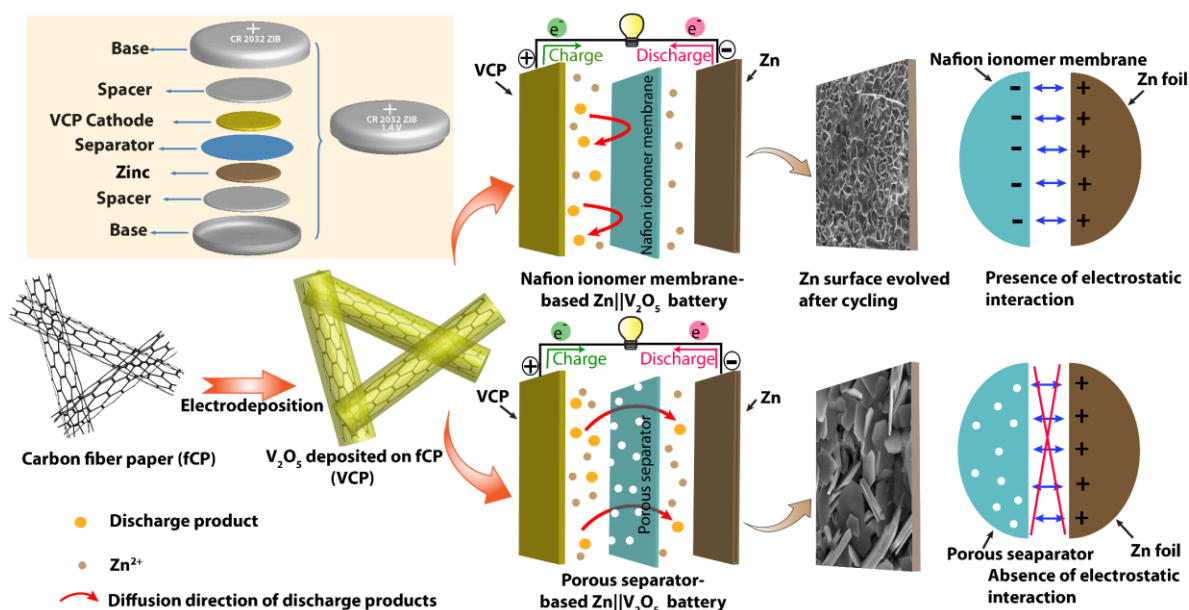


Figure 2.1. Schematic representation of the different $\text{Zn}||\text{V}_2\text{O}_5$ cells containing the Zn^{2+} -integrated Nafion ionomer membrane and the conventional porous separator. (Reprinted (adapted) with permission from *Energy Technology*, 2019, 7, 1900442. Copyright © 2019 WILEY-VCH Verlag GmbH & Co. KGaA, Weinheim).

previous section. These cells were characterized by galvanostatic cycling at a current rate of 0.1 mA cm^{-2} (30 min Zn-plating and 30 min Zn-stripping). The oxidation stability (anodic stability) and reduction stability (cathodic stability) of the electrolytes soaked in various separators were studied by cyclic voltammetry at a scan rate of 5 mV s^{-1} . For this purpose, the electrochemical cells ($\text{Zn}|X\text{-}Y|\text{CP}$) were assembled using pCP (1 cm^2 area) as a working electrode, a piece of Zn foil (1 cm^2 area) as a counter and reference electrode, and the desired separator in the CR2032 coin cell.

For measuring the transference number of Zn^{2+} ($t_{\text{Zn}^{2+}}$) in the presence of various separators, the chronoamperometry experiments were carried out at 25 mV potential in $\text{Zn}|X\text{-}Y|\text{Zn}$ symmetric cell configuration. The resistance values before and after the DC polarization were obtained from the EIS analyses and $t_{\text{Zn}^{2+}}$ values for the different separators were calculated from **Equation 2.4** proposed by Abhraham *et al.*^{29,30}:

$$t_{\text{Zn}^{2+}} = \frac{I_{\text{SS}}R_{\Omega, \text{SS}}(\Delta V - I_0 R_{\text{ct}, 0})}{I_0 R_{\Omega, 0}(\Delta V - I_{\text{SS}} R_{\text{ct}, \text{SS}})} \quad (\text{Equation 2.4})$$

Here, V is the DC polarization voltage, I_0 and I_{SS} are the initial and steady-state current response during the DC polarization, R_{Ω} and R_{ct} stand for the ESR and charge transfer resistance obtained from the Nyquist plot.³⁰

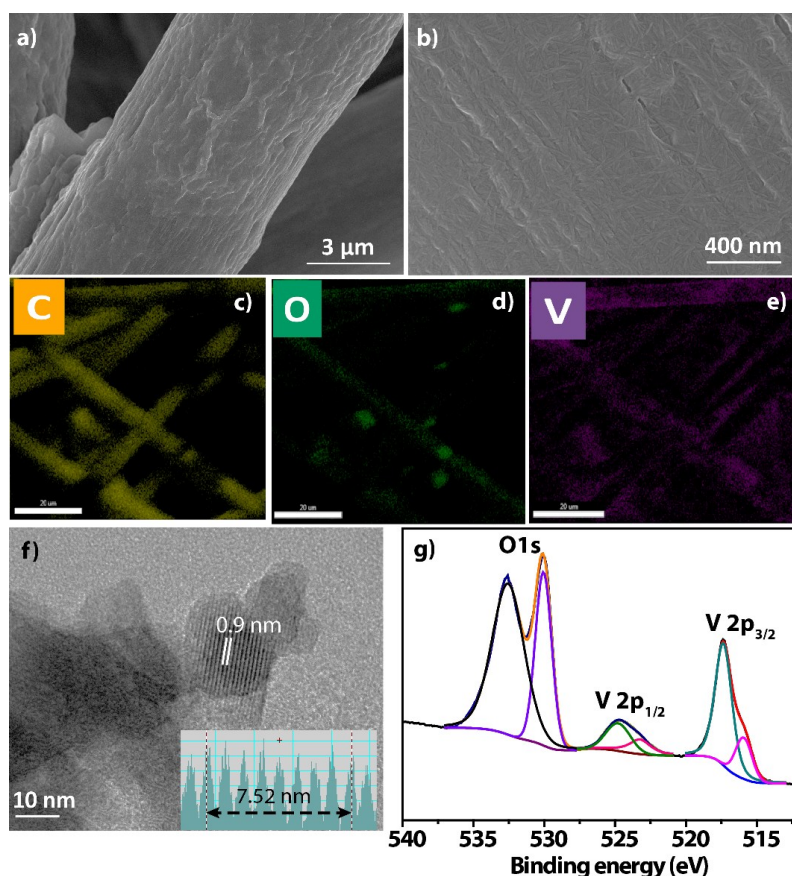


Figure 2.2. (a)-(b) FESEM images, (c)-(e) elemental mapping of C, O, and V, and (f) TEM image of VCP sample; (g) deconvoluted XPS spectra of V and O present in the VCP specimen. (Reprinted (adapted) with permission from Energy Technology, 2019, 7, 1900442. Copyright © 2019 WILEY-VCH Verlag GmbH & Co. KGaA, Weinheim).

To check the performance of the Zn||V₂O₅ cells, CV (at scan rates of 1.0, 0.5, 0.3, and 0.1 mV s⁻¹) and galvanostatic charge-discharge (GCD) (at constant current rates of 0.25, 0.5, 1, 3, 5, 7 and 10 A g⁻¹) analyses were carried out in the voltage window of 1.6 V-0.2 V. The cycling stability tests were performed by GCD experiment at current rates of 5 A g⁻¹ and 10 A g⁻¹.

2.3 Result and discussion

2.3.1 Physical characterization

The preparation of the VCP electrode and fabrication of the Zn||V₂O₅ cells using the Nafion and porous separators are schematically presented in **Figure 2.1**. For the preparation of the VCP cathode, a Toray carbon fiber paper (pCP) was electrochemically functionalized for improving the hydrophilic nature of the paper. Generally, the pCP is hydrophobic in nature (contact angle for water >120°), which prevents the infiltration of the precursor solution during

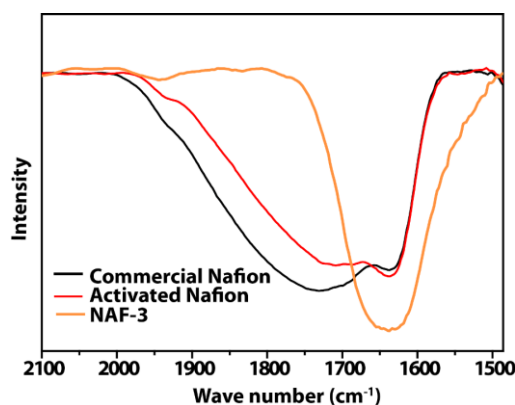


Figure 2.3. FTIR spectra of the commercial Nafion, activated Nafion, and Zn^{2+} -integrated Nafion (NAF-3). (Reprinted (adapted) with permission from *Energy Technology*, 2019, 7, 1900442. Copyright © 2019 WILEY-VCH Verlag GmbH & Co. KGaA, Weinheim).

the electrodeposition process leading to nonuniform deposition of the desired material. The electrochemical functionalization under 10 V applied voltage introduces OH^- functional groups on the carbon fibers without damaging the interconnected microstructure of pCP. The enhanced wettability of functionalized carbon fiber paper (fCP) assures the uniform coating of V_2O_5 on the carbon fibers of fCP during the electrochemical deposition.²⁷

The FESEM images of the VCP specimens (**Figure 2.2a** and **b**) display the growth of the V_2O_5 nano-structure on the carbon fibers. The elemental mapping analysis (**Figure 2.2c-e**) confirms the distribution of V and O on the carbon fibers. As evidenced from the TEM image of VCP in **Figure 2.2f**, the electrodeposited material possesses an interlayer spacing of ~ 0.9 nm, which can facilitate the insertion/extraction of Zn^{2+} and/or H^+ during the electrochemical cycling of the cell.^{31,32} In the XPS data (**Figure 2.2g**), the peaks located at the binding energies of 517.3 and 525.2 eV correspond to the +5 oxidation state of $\text{V}2\text{p}_{3/2}$ and $\text{V}2\text{p}_{1/2}$ doublets. The presence of the +4 oxidation state is also observed at the binding energies of 515.9 and 523.8 eV.^{33,34} In the $\text{O}1\text{s}$ XPS spectra, the peaks located at 530.0 and 532.6 eV are attributed to the oxygen coordinated with vanadium (O-V) and carbon (O-C) in the VCP specimen, respectively.³⁵

2.3.2 Selection of the separator

The coordination of Zn^{2+} with the Nafion ionomer is confirmed from the FTIR analysis (**Figure 2.3**). Followed by the impregnation of Zn^{2+} in the Nafion membrane, the FTIR peak in the commercial Nafion and activated Nafion at 1730 cm^{-1} shows a red shift to 1640 cm^{-1} . This observation suggests the exchange of H^+ in the activated Nafion membrane with Zn^{2+} ions from ZnSO_4 electrolyte.^{36,37} In **Figure 2.4a**, the $\ln \sigma$ vs. $1/T$ plots for the electrolyte soaked

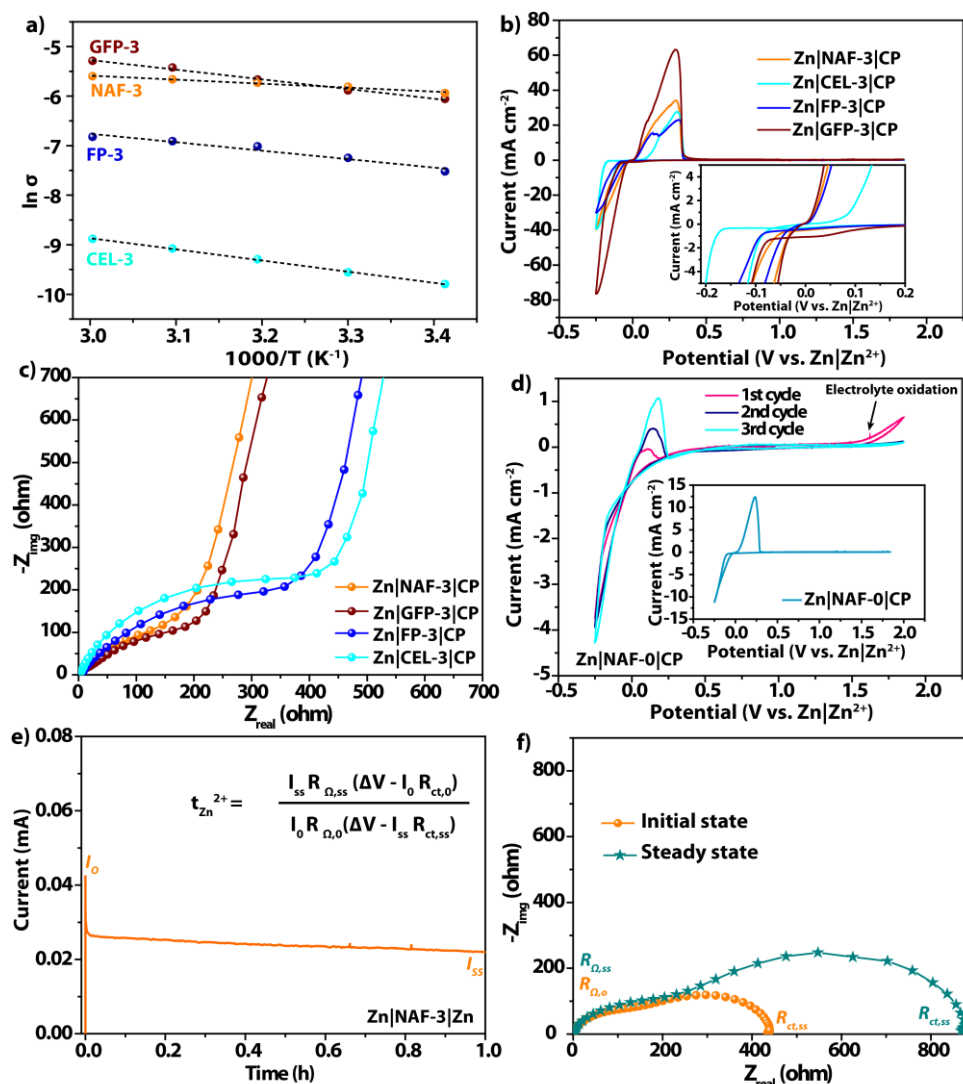


Figure 2.4. (a) $\ln \sigma$ vs $1/T$ plots for the NAF-3, GFP-3, FP-3, and CEL-3 separators; (b) CV profiles, (c) Nyquist plots for Zn|X-Y|CP cells; (d) CV profiles for Zn|NAF-0|CP cell in the initial cycles and at 15th cycle (inset); (e) chronoamperometry data of Zn|NAF-3|Zn cell; (f) the Nyquist plots of Zn|NAF-3|Zn cell at the initial state and after chronoamperometry. (Reprinted (adapted) with permission from Energy Technology, 2019, 7, 1900442. Copyright © 2019 WILEY-VCH Verlag GmbH & Co. KGaA, Weinheim).

separators are compared. As shown in the figure, the NAF-3 and GFP-3 separators exhibit better ionic conductivity compared to FP-3 and CEL-3 counterparts. At 30°C, the conductivity value obtained with NAF-3 is $2.6\ mS\ cm^{-1}$. The interaction of Zn^{2+} with the SO_3^- moieties present in Nafion can enhance the dissociation of $ZnSO_4$, which could facilitate the transport of Zn^{2+} . The slightly higher ionic conductivity ($2.8\ mS\ cm^{-1}$) in GFP-3 may be due to its better wettability and intrinsic porous nature. The activation energy toward ion conduction is also

calculated from the slope of the $\ln \sigma$ vs. $1/T$ plots. Compared to the porous separators, NAF-3 exhibits the lowest activation energy (0.069 eV).

The anodic and cathodic stability of the electrolyte impregnated in various separators are analyzed by CV experiments in Zn|X-Y|CP cells. As shown in **Figure 2.4b**, all the cells display negligible current response during the anodic scan revealing good oxidation stability of the ZnSO₄ electrolyte beyond 1.85 V (vs. Zn|Zn²⁺). The clear and sharp redox peaks observed in the lower potential region (below 0.4 V vs. Zn|Zn²⁺) correspond to the plating and stripping processes of Zn. The voltage gap between the onset potentials of redox peaks corresponding to plating and stripping of Zn in Zn|NAF-3|CP cell is only 75 mV (**Figure 2.4b inset**), which is lower compared to the porous separator based counterparts. The values obtained for Zn|GFP-3|CP, Zn|FP-3|CP, and Zn|CEL-3|CP cells are 84, 92, and 263 mV, respectively. Nevertheless, as shown in the Nyquist plots in **Figure 2.4c**, Zn|NAF-3|CP cell exhibits low charge transfer resistance (R_{ct}) compared to the other Zn|X-Y|CP cells. Therefore, the higher ionic conductivity, low activation energy, and low R_{ct} value along with the better interface formed by the Nafion ionomer membrane with the Zn anode and working electrode are the reasons for the better plating/stripping behavior of Zn in the case of the NAF-3 separator (**Figure 2.4b**).

Several literatures highlight that the charge storage in ARZMBs can be due to the intercalation of Zn²⁺ or H⁺ or by the co-intercalation of both Zn²⁺ and H⁺.^{31,38} The existence of H⁺ in the electrolyte of the ARZMBs is expected due to the low pH (pH \approx 4) of the ZnSO₄ aqueous solution. Therefore, it is indeed important to understand the effect of H⁺ ions alone in the charge storage mechanism of ARZMB. For this purpose, we have fabricated Zn|NAF-0|CP cell using ZnSO₄-free Nafion ionomer membrane (NAF-0). As observed in **Figure 2.4d**, there is no significant positive current response during the oxidation of Zn in the first cycle of the CV. However, as we move from the first to third cycle, the current corresponding to Zn oxidation is found to increase gradually. This can directly indicate the occurrence of some sort of Zn plating/stripping, even in the absence of ZnSO₄ in the system. The acidic nature of the activated Nafion ionomer in the NAF-0 membrane causes the dissolution of the Zn electrode, which eventually takes part in the plating/stripping reaction on the working electrode. After several cycles, the CV profile of the Zn|NAF-0|CP cell (**Figure 2.4d inset**) appears similar to that of Zn|NAF-3|CP cell. However, the low current density and higher overpotential (149 mV) in the CV plot indicate the inferior kinetics of the Zn plating/stripping in Zn|NAF-0|CP cell. In addition to the above observation, an oxidation peak is observed beyond 1.5 V in the first CV cycle (**Figure 2.4d**) related to the water decomposition. However, this peak diminishes with

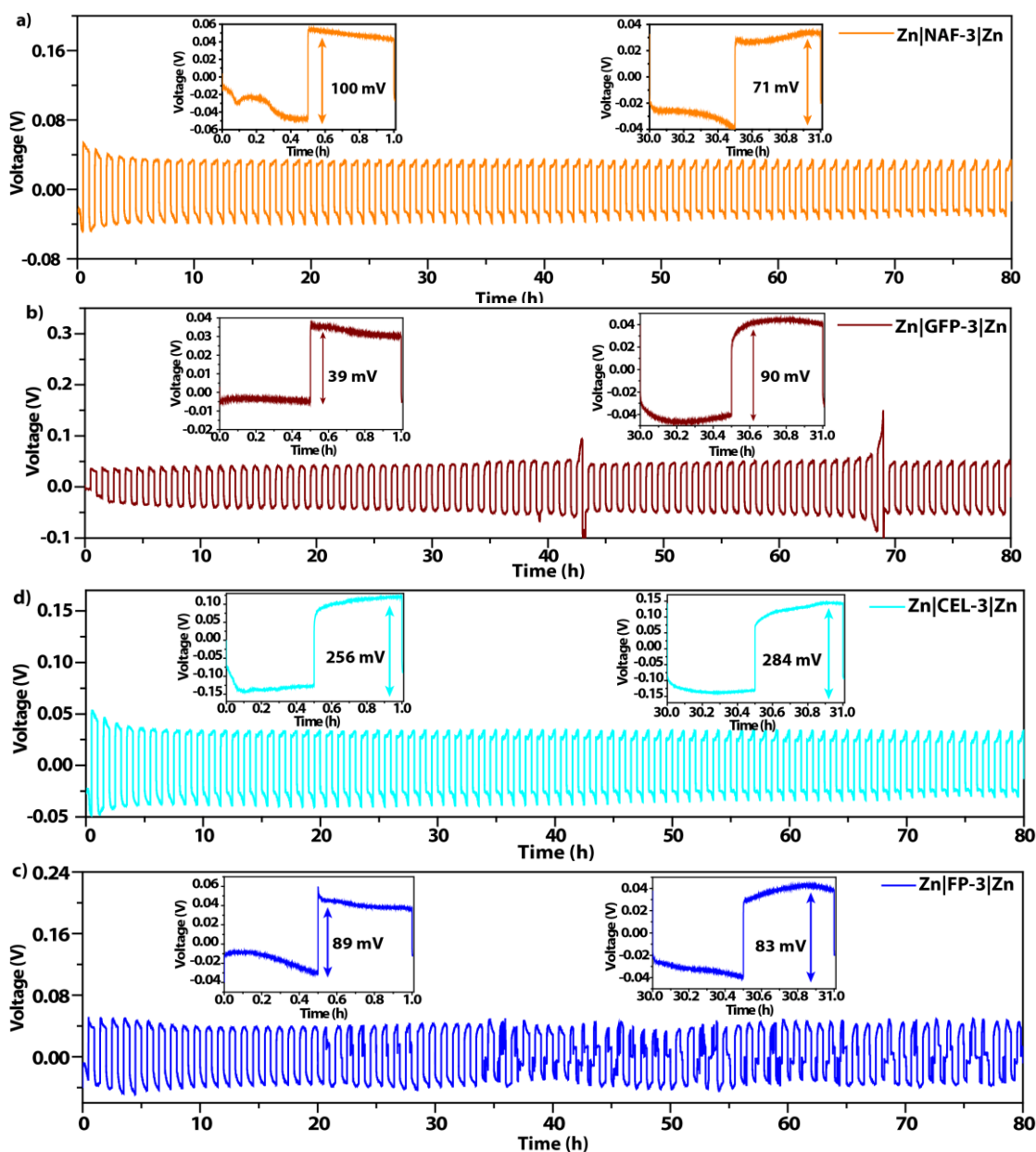


Figure 2.5. Galvanostatic cycling of the Zn|X-Y|Zn cells fabricated with (a) NAF-3, (b) GFP-3, (c) CEL-3, and (d) FP-3 separators. (Reprinted (adapted) with permission from Energy Technology, 2019, 7, 1900442. Copyright © 2019 WILEY-VCH Verlag GmbH & Co. KGaA, Weinheim).

the evolution of the oxidation peak corresponding to Zn. This confirms that the presence of Zn^{2+} in the electrolyte not only provides better reversibility but also increases the anodic stability of the electrolyte. These observations prove the importance of Zn^{2+} integration in the Nafion membrane.

The $t_{\text{Zn}^{2+}}$ for the NAF-3 is calculated to be 0.52 (Figure 2.4e and f), which is higher than the same obtained for the porous separators ($t_{\text{Zn}^{2+}}$ obtained for GFP-3 and FP-3 are 0.32

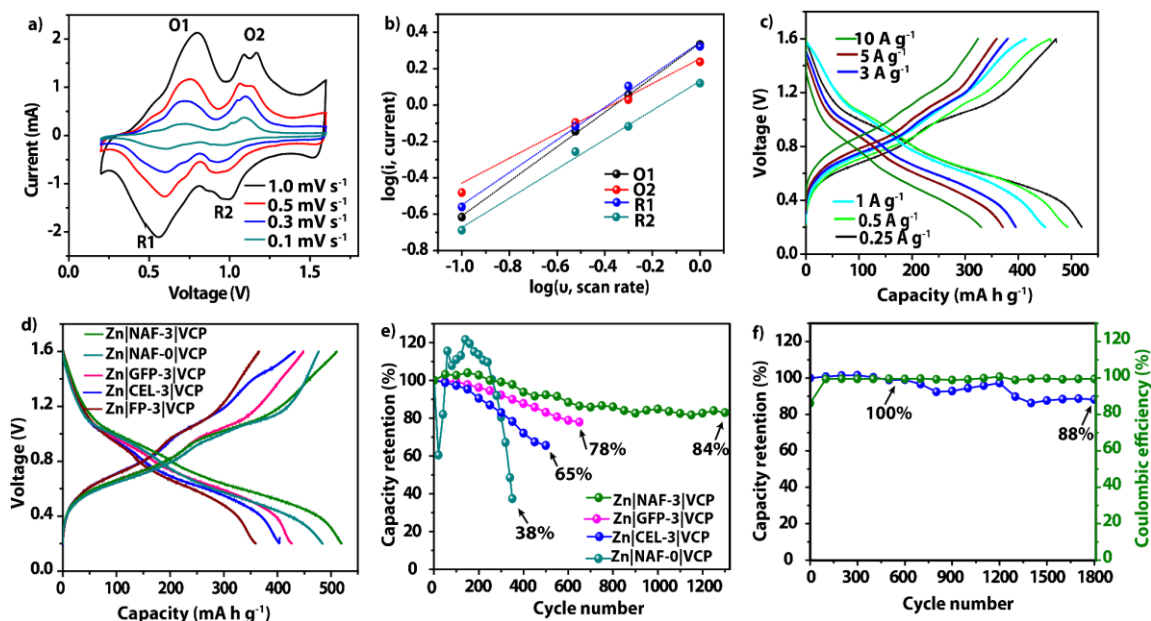


Figure 2.6. (a) The CV at various scan rates, (b) $\log i$ vs. $\log v$ plots, and (c) GCD profiles of the Zn|NAF-3|VCP cell at the various current rates; (d) GCD profiles of Zn|X-Y|VCP cells at 0.25 A g^{-1} current rate; (e) cycling stability comparison of Zn|X-Y|VCP cells at current rate of 5 A g^{-1} ; (f) cycling stability and Coulombic efficiency of Zn|NAF-3|VCP cell at current density of 10 A g^{-1} . (Reprinted (adapted) with permission from *Energy Technology*, 2019, 7, 1900442. Copyright © 2019 WILEY-VCH Verlag GmbH & Co. KGaA, Weinheim).

and 0.30, respectively). The higher $t_{\text{Zn}^{2+}}$ in NAF-3 indicates the preferential role of Zn^{2+} transport in maintaining the ionic current. The coordination of the Zn^{2+} with the SO_3^- moieties in the Nafion ionomer helps in selective migration of the cation in the direction of the electric field, resulting in higher $t_{\text{Zn}^{2+}}$ value.³⁹ On the other hand, in the case of the porous separators, the low $t_{\text{Zn}^{2+}}$ indicates the lesser extent of contribution toward the ionic conductivity by the cation owing to the lack of negatively charged moieties as in the case of Nafion. The higher value of $t_{\text{Zn}^{2+}}$ in Nafion can reduce the ion concentration gradient near the anode surface, which is one of the important factors for preventing the nonuniform deposition of Zn metal. Therefore, the preferential transport of Zn^{2+} offered by the NAF-3 separator makes it a potential candidate to be used in ARZMBs.

The performance of the various separators soaked in $3\text{M ZnSO}_4 \cdot 7\text{H}_2\text{O}$ electrolyte was further evaluated in symmetric cell configuration (Zn|X-Y|Zn). **Figure 2.5a-d** display the voltage vs. time profiles recorded during galvanostatic cycling at a constant current of 0.1 mA cm^{-2} . As evident from the enlarged part (**Figure 2.5a-d**) at various cycles, the Zn|NAF-3|Zn cell (**Figure 2.5a**) displays a significant decrease of overpotential (71 mV at 30th cycle) upon cycling. On the contrary, the gradual enhancement in the voltage separation between plating

and stripping in case of the porous separator-based Zn|X-Y|Zn cells (at 30th cycle the corresponding overpotential of Zn|GFP-3|Zn, Zn|CEL-3|Zn, and Zn|FP-3|Zn are 90 mV, 284 mV, and 83 mV, respectively, **Figure 2.5b-d**) indicates the superiority of the NAF-3 ionomer separator.

2.3.3 Electrochemical characterization of the Zn||V₂O₅ cells

Figure 2.6a displays the current response in the CV profiles of Zn|NAF-3|VCP cell recorded at different scan rates ranging from 0.10 to 1.0 mV s⁻¹. The appearance of the multiple anodic and cathodic peaks can be attributed to the multistep reversible insertion of Zn²⁺ into the VCP cathode. The plot of log (i) vs. log (v) in **Figure 2.6b** shows the current dependence on the scan rate, and the charge storage behavior is investigated using the following equation:

$$i = a v^b \quad (\text{Equation 2.5})$$

where, 'i' is the current, 'v' is the scan rate and 'a' and 'b' represent adjustable parameters.⁴⁰ The b-values corresponding to the peaks O1, O2, R1, and R2 are obtained as 0.94, 0.71, 0.89, and 0.80, respectively. The b-values significantly higher than 0.5 indicate that the Faradaic reactions in the VCP cathode are predominantly surface-controlled.^{41,42} This indicates fast insertion/extraction kinetics of Zn²⁺, enabling high power output of the device.

Zn|NAF-3|VCP cell is characterized by GCD experiment at current rates of 0.25 to 10 A g⁻¹. A high specific discharge capacity of ~510 mAh g⁻¹ is obtained at a current of 0.25 A g⁻¹ (**Figure 2.6c**). The discharge capacity is calculated considering the loading of active material on the cathode side. In **Table 2.1**, the charge storage capacity of the Zn|NAF-3|VCP cell is compared with some of the previously reported ARZMBs.^{15-18,25,26,31,42-49} The Zn|NAF-3|VCP cell shows a specific discharge capacity of ~330 mAh g⁻¹ (65 % retention of the capacity obtained at 0.25 A g⁻¹) at a high current rate of 10 A g⁻¹. The attractive rate performance and high discharge capacity of the Zn|NAF-3|VCP cell is credited to the rationally designed binder-free VCP cathode. The conventional methods for the cathode fabrication involve the use of electrically insulating polymer binder and multistep coating of the active material over the current collectors, contributing to the high resistance of the electrochemical cell. However, in this work, the electrodeposition of V₂O₅ directly onto fCP (**Figure 2.1**) provides an interconnected pathway for facilitating the transport of electrons throughout the electrode. Therefore, the contact resistance is reduced with the added advantage of the increased number of accessible redox-active sites, which promotes the Zn²⁺ uptake capacity leading to the high capacity of the cell. The GCD profiles of the other Zn||V₂O₅ cells under study are compared in

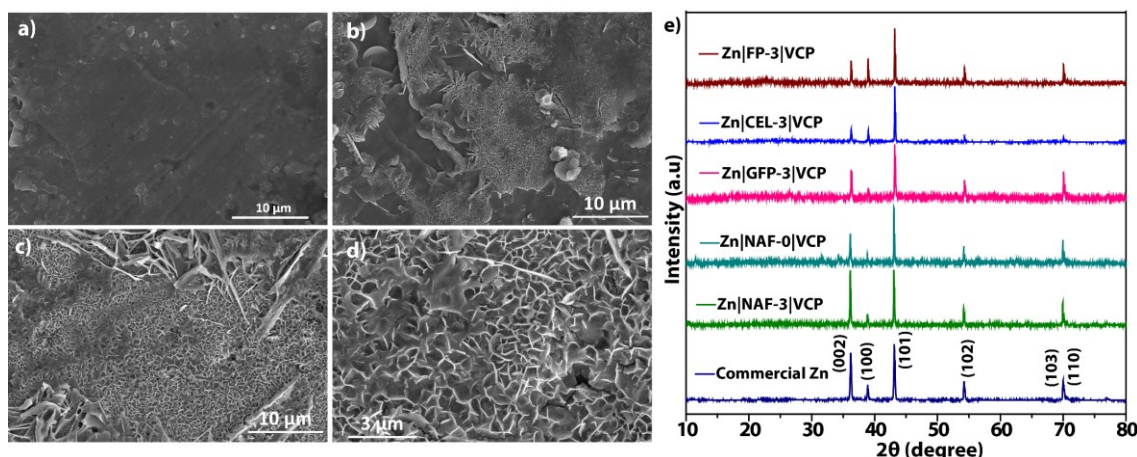


Figure 2.7. (a) FESEM image of the commercial Zn foil; FESEM image of the Zn anode recovered from the Zn|NAF-3|VCP cell after (b) 500 and (c)-(d) 1300 charge discharge cycles; (e) XRD profiles of the commercial Zn and Zn anodes recovered from the various Zn|X-Y|VCP cells after the cycling stability test. (Reprinted (adapted) with permission from Energy Technology, 2019, 7, 1900442. Copyright © 2019 WILEY-VCH Verlag GmbH & Co. KGaA, Weinheim).

Figure 2.6d. At a current rate of 0.25 A g^{-1} , the discharge capacity obtained for the Zn|NAF-0|VCP (480 mAh g^{-1}), Zn|GFP-3|VCP (430 mAh g^{-1}), Zn|CEL-3|VCP (400 mAh g^{-1}), and Zn|FP-3|VCP (360 mAh g^{-1}) cells are significantly lower compared to that of the Zn|NAF-3|VCP cell.

The long term cycling stability data of all the Zn||V₂O₅ cells at a current rate of 5 A g^{-1} are compared in **Figure 2.6e**. The Zn|NAF-3|VCP cell exhibits outstanding cycling stability with 84% retention of the initial capacity over 1300 cycles. Besides, at a high current rate of 10 A g^{-1} (**Figure 2.6f**), the same cell could retain 88% of its initial capacity after 1800 cycles with 99% Coulombic efficiency. On the other hand, the Zn|GFP-3|VCP and Zn|CEL-3|VCP show only 78% retention of the initial capacity after 650 cycles and 65% retention of the initial capacity after 500 cycles, respectively (**Figure 2.6e**). The cycling stability data for Zn|FP-3|VCP cell is not provided here as the cell is found to be failed just after few initial cycles. Therefore, the above discussion indeed points out the superiority of the NAF-3 separator for realizing high-performance ARZMB. The cycling stability performance of the Zn|NAF-0|VCP cell is also included in **Figure 2.6e**. From the data, it is evident that irrespective of a sharp increase in capacity during the initial few cycles, a sudden drop is observed in the region of 200 cycles. After 250 cycles, only 38% of the initial capacity is retained. This further supports the claim that the integration of Zn²⁺ into the Nafion separator is the key to achieve the long cyclability of ARZMBs. Moreover, the concomitant delivery of long cycle life and high

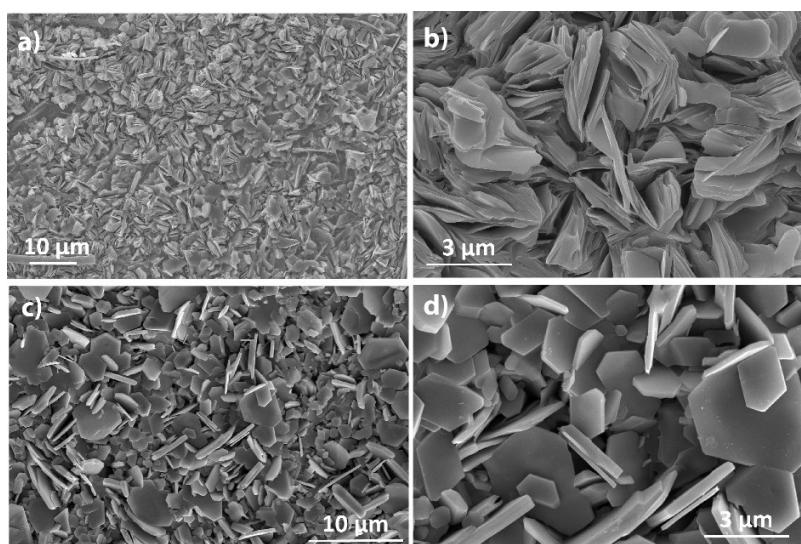


Figure 2.8. FESEM images of post-stability Zn anode recovered from (a)-(b) Zn|GFP-3|VCP cell after 650 cycles and (g)-(h) Zn|CEL-3|VCP cell after 500 cycles. (Reprinted (adapted) with permission from *Energy Technology*, 2019, 7, 1900442. Copyright © 2019 WILEY-VCH Verlag GmbH & Co. KGaA, Weinheim).

discharge capacity is rarely found in ARZMB literature (**Table 2.1**), which highlights the importance of the Zn|NAF-3|VCP cell in a futuristic perspective. The underlying reasons pertaining to the difference in the cycling stability in the presence of different membranes are further deciphered through the post-mortem analyses of the anode and cathode. The results are explained in the following sections.

2.3.4 Post-mortem analysis of anode

The FESEM images of the commercial Zn foil and the post-stability Zn anodes recovered from the Zn|X-Y|VCP cells are analyzed. Apparently, the commercial Zn foil (**Figure 2.7a**) possesses a very smooth and flat surface. On the other hand, different morphological evolution can be observed over the post-cycling Zn anode, which indicates the nucleation and growth of Zn deposits on the anode side during the prolonged cycling of the Zn||V₂O₅ cells. The Zn anode recovered from Zn|NAF-3|VCP cell after 500 cycles (**Figure 2.7b**) manifests a surface more or less similar to that of the commercial Zn foil, although with a few regions of random/irregular morphology. After 1300 cycles, the morphological evolution on the Zn anode is found to be more pronounced (**Figure 2.7c** and **d**), covering the Zn surface more evenly. At higher magnification (**Figure 2.7d**), this morphology is found to possess a nanowall-like growth pattern, which is confirmed to be composed of the Zn deposits from the XRD data given in **Figure 2.7e**. The Zn nanowalls can be considered embedded in the nearly flat surface of the original Zn foil. The two-dimensional, thin, uniform and interconnected

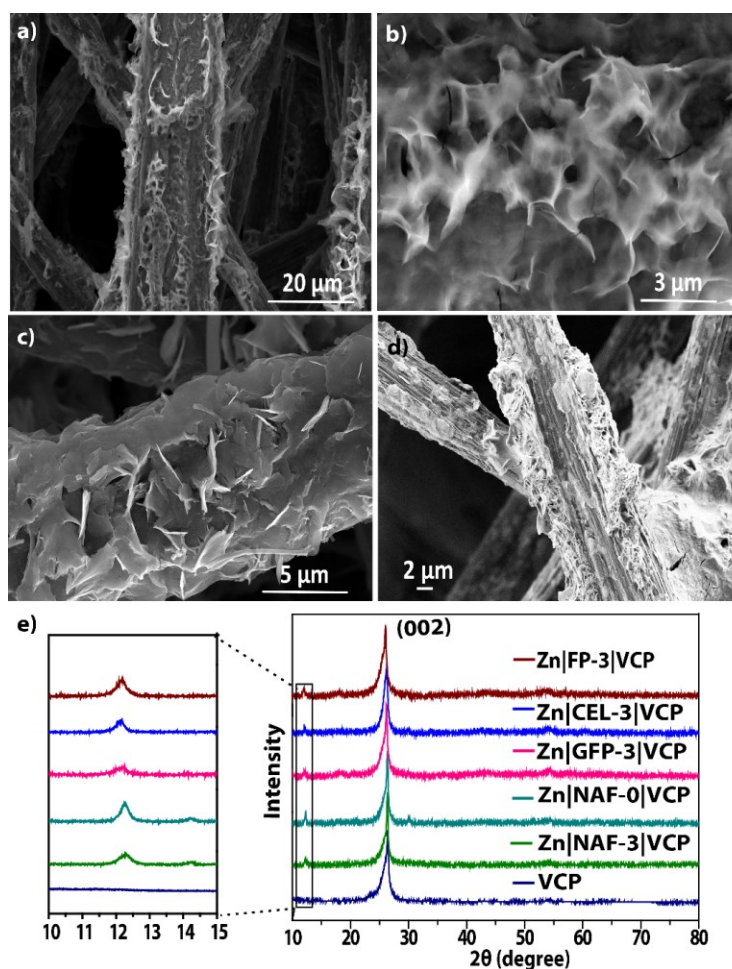


Figure 2.9. FESEM images of the cycled cathode recovered from the (a)-(b) Zn|NAF-3|VCP, (c) Zn|GFP-3|VCP, and Zn|CEL-3|VCP cells; (e) XRD profiles of the cycled cathodes recovered from the Zn|X-Y|VCP cells under study. (Reprinted (adapted) with permission from *Energy Technology*, 2019, 7, 1900442. Copyright © 2019 WILEY-VCH Verlag GmbH & Co. KGaA, Weinheim).

nanowall pattern (**Figure 2.7d**) favours the homogeneous distribution of the electric field in the anode even after long cycling. This inhibits the polarization of the electrode and the growth of the irregular bulk Zn deposits. Moreover, in the XRD profile of the Zn anode in the Zn|NAF-0|VCP cell (after 1300 cycles), the higher intensity of the (002) plane strongly suggests that the dendritic growth in the respective anode is less likely.²⁴

The suppressed bulk/dendritic deposition of Zn in Zn|NAF-3|VCP can be due to the combined contribution from the inherent single-ion conducting property and the presence of the anionic $-\text{SO}_3^-$ group in the Nafion ionomer. The electrostatic interaction between electron-rich SO_3^- groups in the Nafion ionomer and the positively charged Zn can provide a strong interfacial interaction, which suppresses the dendritic growth during the long-term cycling and

facilitates the uniform deposition of Zn.^{50,51} This interfacial interaction assists in maintaining an efficient contact between the Zn anode and the Nafion ionomer membrane. This is schematically represented in **Figure 2.1**. The dendrite suppressing nature of the single ion-conducting electrolytes is already proved in literature.^{52,53} Interestingly, the Zn deposits in the anode coupled with the GFP-3 separator is found to be composed of highly dense 3D-scales of Zn with sharp edges and irregular morphology (**Figure 2.8a and b**). On the other hand, the CEL-3 separator leads to the 3D hexagonal growth of micrometre-sized bulk Zn deposits (**Figure 2.8c and d**). The sharp edges of these protruding Zn deposits can damage the porous separators. Such bulk deposits can be due to the absence of electrostatic interaction between the anode and porous separators. Moreover, the morphological evolution of the Zn anode during cycling is in line with the results obtained from the plating/stripping and cycling stability tests in the presence of the NAF-3 separator.

2.3.5 Post-mortem analysis of cathode

The FESEM images of the post-cycling VCP cathodes are given in **Figure 2.9a-d**. The VCP cathode of the Zn|NAF-3|VCP cell possesses a thin and uniform coating of exfoliated nanosheets over the porous carbon paper (**Figure 2.9a and b**). This is different from the dense and agglomerated morphology of the VCP cathodes in the Zn|GFP-3|VCP (**Figure 2.9c**) and Zn|CEL-3|VCP (**Figure 2.9d**) cells. From the XRD analysis (**Figure 2.9e**), it is apparent that the appearance of a new peak at a 2θ value of 12.3° is consistent in all the VCP cathodes, which corresponds to the formation of a $Zn_xV_2O_5$ phase.⁴⁴ It can also be noted that the XRD plots of all cathodes are more or less similar. This draws the conclusion that the plausible limiting factor for the cyclic stability of ARZMB is the morphological evolution of both the anode and cathode during cycling.

2.3.6 Ragone plot and real-life demonstration

The average voltage of the Zn|NAF-3|VCP cell is found to be ~ 0.80 V (**Figure 2.10a**). The Ragone plot representing the energy and power density of the Zn|NAF-3|VCP cell is given in **Figure 2.10b**. At the different power densities of 195 and 7800 W kg⁻¹, the device delivers high energy densities of 398 and 257 Wh kg⁻¹, respectively (energy density of the cell is evaluated considering the loading of V₂O₅ on the cathode). The combination of high energy and power densities of the Zn|NAF-3|VCP cell can narrow the gap between the supercapacitors and batteries. The application of ARZMBs in various real-life situations is also demonstrated. **Figure 2.10c** shows the image of the two cells connected in series being used for powering a

Table 2.1. The discharge capacity and cyclic stability data of the Zn|NAF-3|VCP cell are compared with some of the high-performance ARZMBs reported in the literature, where various separators and electrolytes are used. (Reprinted (adapted) with permission from Energy Technology, 2019, 7, 1900442. Copyright © 2019 WILEY-VCH Verlag GmbH & Co. KGaA, Weinheim).

Cathode material	Electrolyte	Separator	Capacity @ current rate	Cycling stability	Ref.
V ₂ O ₅	21 m LiTFSI and 1 m Zn(CF ₃ SO ₃) ₂	FP	242 mAh g ⁻¹ @ 0.05 A g ⁻¹	83% retention after 2000 cycles	15
V ₂ O ₅ .nH ₂ O	3 M Zn(CF ₃ SO ₃) ₂	GFP	381 mAh g ⁻¹ @ 0.06 A g ⁻¹	71% retention after 900 cycles	42
Zn ₂ V ₂ O ₇	1M ZnSO ₄	GFP	227.8 mAh g ⁻¹ @0.3 A g ⁻¹	85% retention after 1000 cycles	43
Zn _{0.25} V ₂ O ₅ ·nH ₂ O	1M ZnSO ₄	-	220 mAh g ⁻¹ @4.5 A g ⁻¹	80% retention after 1000 cycles	49
V ₂ O ₅	3M ZnSO ₄	GFP	224 mAh g ⁻¹ @0.1 A g ⁻¹	54% retention after 400 cycles	44
VO ₂	3 M Zn(CF ₃ SO ₃) ₂	GFP	357 mAh g ⁻¹ @0.1 A g ⁻¹	100% retention after 50 cycles	45
H ₂ V ₃ O ₈ NW/graphene	3 M Zn(CF ₃ SO ₃) ₂	GFP	394 mAh g ⁻¹ @ 0.1 A g ⁻¹	87% retention after 2000 cycles	46
V ₂ O ₅	3 M Zn(CF ₃ SO ₃) ₂	GFP	470 mAh g ⁻¹ @0.2 A g ⁻¹	91.1% retention after 4000 cycles	26
VO ₂	3 M Zn(CF ₃ SO ₃) ₂	GFP	274 mAh g ⁻¹ @0.1 A g ⁻¹	79% retention after 10000 cycles	17
V ₃ O ₇ ·H ₂ O/rGO	1 M ZnSO ₄	-	271 mAh g ⁻¹ @0.3 A g ⁻¹	79% retention after 1000 cycles	47
Na ₂ V ₆ O ₁₆ ·3H ₂ O	1 M ZnSO ₄	GFP	361 mAh g ⁻¹ @0.1 A g ⁻¹	84.5% retention after 1000 cycles	18
Zn ₃ V ₂ O ₇ (OH) ₂ ·2H ₂ O	1 M ZnSO ₄	CEL	213 mAh g ⁻¹ @0.05 A g ⁻¹	68% retention after 300 cycles	48
NaV ₃ O ₈ ·1.5H ₂ O	1 M ZnSO ₄ /1 M Na ₂ SO ₄	FP	380 mAh g ⁻¹ @0.05 A g ⁻¹	82% retention after 1000 cycles	31
Ca _{0.24} V ₂ O ₅ ·0.83H ₂ O	1 M ZnSO ₄	GFP	72 mAh g ⁻¹ @ 80C	96% retention after 3000 cycles	16
Na ₃ V ₂ (PO ₄) ₂ F ₃	2 M Zn(CF ₃ SO ₃) ₂	GFP	47 mAh g ⁻¹ @1.0 A g ⁻¹	95% retention after 4000 cycles	25
V ₂ O ₅	3M ZnSO ₄	NAF	510 mAh g ⁻¹ @ 0.25 A g ⁻¹	88% retention after 1800 cycles	This work

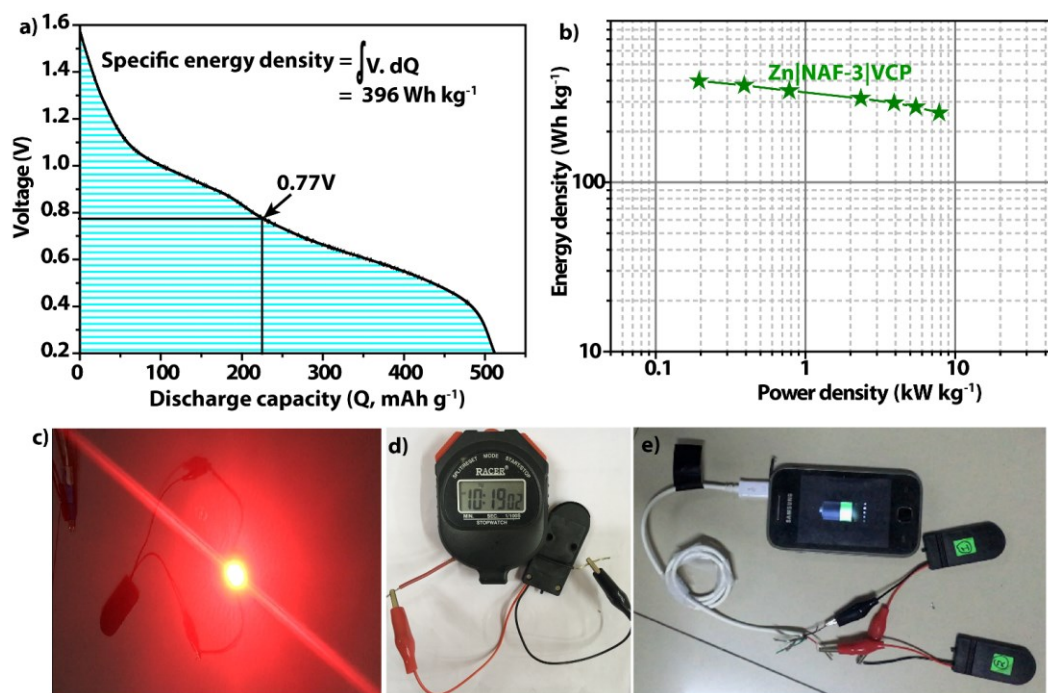


Figure 2.10. (a) Voltage vs. discharge capacity plot of the Zn|NAF-3|VCP cell recorded at a current rate of 0.25 A g^{-1} , (b) Ragone plot (energy density vs. power density) of the Zn|NAF-3|VCP cell; (b)-(d) real-life demonstration of the Zn||V₂O₅ battery (c) by lighting a red LED bulb, (d) by powering a 1.5 V stopwatch and (e) by powering a smartphone. (Figure 7c). (Reprinted (adapted) with permission from *Energy Technology*, 2019, 7, 1900442. Copyright © 2019 WILEY-VCH Verlag GmbH & Co. KGaA, Weinheim).

red LED bulb with a nominal voltage of 1.8 V. The setup is used for powering a digital clock continuously for 96 h (**Figure 2.10d**). **Figure 2.10e** demonstrates powering of a smartphone by using four Zn||V₂O₅ cells connected in series.

2.4 Conclusions

This work demonstrates the advantage of using a Zn²⁺-integrated Nafion ionomer separator over the conventional porous separators (glass fiber, filter paper, polypropylene, *etc.*) to realize high-performance ARZMBs. The use of a Nafion ionomer separator stabilizes the anode in a Zn||V₂O₅ cell (Zn|NAF-3|VCP) by suppressing the growth of bulk/dendritic Zn deposits during cycling. The unique thin and nanowall-like morphology of the Zn surface is found to promote the cycling stability of the cell compared to the micrometre sized sharp edged deposit obtained with the porous separators. The cathode morphology is also found to have the favourable thin Zn_xV₂O₅ phase in the case of the Zn²⁺-integrated Nafion separator. The high Zn²⁺ transference number and low activation energy offered by the NAF-3 separator reduce the overpotential of Zn plating/stripping, which is an added advantage compared to the other

separators. The high discharge capacity of $\sim 510 \text{ mAh g}^{-1}$ at a current density of 0.25 A g^{-1} is obtained for Zn|NAF-3|VCP, which is facilitated by the rationally designed V_2O_5 cathode. The Nafion-based cell is found to retain a capacity of 84% even after 1300 continuous charge-discharge cycles at 5 A g^{-1} current density. Therefore, it can be concluded that the strategy of using the Zn^{2+} -integrated Nafion ionomer separator has several advantages, which are essential for achieving the high capacity as well as long cycling life of ARZMBs.

2.5 References

- (1) Dunn, B.; Kamath, H.; Tarascon, J.-M. Electrical energy storage for the grid: a battery of choices. *Science* **2011**, *334*, 928-935.
- (2) Yang, Z.; Zhang, J.; Kintner-Meyer, M. C.; Lu, X.; Choi, D.; Lemmon, J. P.; Liu, J. Electrochemical energy storage for green grid. *Chemical reviews* **2011**, *111*, 3577-3613.
- (3) Kim, H.; Hong, J.; Park, K.-Y.; Kim, H.; Kim, S.-W.; Kang, K. Aqueous rechargeable Li and Na ion batteries. *Chemical reviews* **2014**, *114*, 11788-11827.
- (4) Wang, G.; Fu, L.; Zhao, N.; Yang, L.; Wu, Y.; Wu, H. An aqueous rechargeable lithium battery with good cycling performance. *Angewandte Chemie* **2007**, *119*, 299-301.
- (5) Luo, J. Y.; Xia, Y. Y. Aqueous lithium-ion battery $\text{LiTi}_2(\text{PO}_4)_3/\text{LiMn}_2\text{O}_4$ with high power and energy densities as well as superior cycling stability. *Advanced Functional Materials* **2007**, *17*, 3877-3884.
- (6) Wang, Y.; Yi, J.; Xia, Y. Recent Progress in Aqueous Lithium-Ion Batteries. *Advanced Energy Materials* **2012**, *2*, 830-840.
- (7) Li, W.; Dahn, J. R.; Wainwright, D. S. Rechargeable lithium batteries with aqueous electrolytes. *Science* **1994**, *264*, 1115-1118.
- (8) Chang, Z.; Li, C.; Wang, Y.; Chen, B.; Fu, L.; Zhu, Y.; Zhang, L.; Wu, Y.; Huang, W. A lithium ion battery using an aqueous electrolyte solution. *Scientific reports* **2016**, *6*, 28421.
- (9) Suo, L.; Borodin, O.; Gao, T.; Olguin, M.; Ho, J.; Fan, X.; Luo, C.; Wang, C.; Xu, K. "Water-in-salt" electrolyte enables high-voltage aqueous lithium-ion chemistries. *Science* **2015**, *350*, 938-943.
- (10) Kühnel, R.-S.; Reber, D.; Battaglia, C. A high-voltage aqueous electrolyte for sodium-ion batteries. *ACS Energy Letters* **2017**, *2*, 2005-2006.

- (11) Suo, L.; Borodin, O.; Wang, Y.; Rong, X.; Sun, W.; Fan, X.; Xu, S.; Schroeder, M. A.; Cresce, A. V.; Wang, F. "Water-in-salt" electrolyte makes aqueous sodium-ion battery safe, green, and long-lasting. *Advanced Energy Materials* **2017**, *7*, 1701189.
- (12) Wang, X.; Wang, F.; Wang, L.; Li, M.; Wang, Y.; Chen, B.; Zhu, Y.; Fu, L.; Zha, L.; Zhang, L. An aqueous rechargeable Zn//Co₃O₄ battery with high energy density and good cycling behavior. *Advanced Materials* **2016**, *28*, 4904-4911.
- (13) Wang, X.; Li, M.; Wang, Y.; Chen, B.; Zhu, Y.; Wu, Y. A Zn–NiO rechargeable battery with long lifespan and high energy density. *Journal of Materials Chemistry A* **2015**, *3*, 8280-8283.
- (14) Xu, C.; Li, B.; Du, H.; Kang, F. Energetic zinc ion chemistry: the rechargeable zinc ion battery. *Angewandte Chemie* **2012**, *124*, 957-959.
- (15) Hu, P.; Yan, M.; Zhu, T.; Wang, X.; Wei, X.; Li, J.; Zhou, L.; Li, Z.; Chen, L.; Mai, L. Zn/V₂O₅ aqueous hybrid-ion battery with high voltage platform and long cycle life. *ACS applied materials & interfaces* **2017**, *9*, 42717-42722.
- (16) Xia, C.; Guo, J.; Li, P.; Zhang, X.; Alshareef, H. N. Highly stable aqueous zinc-ion storage using a layered calcium vanadium oxide bronze cathode. *Angewandte Chemie International Edition* **2018**, *57*, 3943-3948.
- (17) Wei, T.; Li, Q.; Yang, G.; Wang, C. An electrochemically induced bilayered structure facilitates long-life zinc storage of vanadium dioxide. *Journal of Materials Chemistry A* **2018**, *6*, 8006-8012.
- (18) Soundharrajan, V.; Sambandam, B.; Kim, S.; Alfaruqi, M. H.; Putro, D. Y.; Jo, J.; Kim, S.; Mathew, V.; Sun, Y.-K.; Kim, J. Na₂V₆O₁₆·3H₂O barnesite nanorod: an open door to display a stable and high energy for aqueous rechargeable Zn-ion batteries as cathodes. *Nano letters* **2018**, *18*, 2402-2410.
- (19) He, P.; Yan, M.; Zhang, G.; Sun, R.; Chen, L.; An, Q.; Mai, L. Layered VS₂ nanosheet-based aqueous Zn ion battery cathode. *Advanced Energy Materials* **2017**, *7*, 1601920.
- (20) Zhang, L.; Chen, L.; Zhou, X.; Liu, Z. Towards high-voltage aqueous metal-ion batteries beyond 1.5 V: the zinc/zinc hexacyanoferrate system. *Advanced Energy Materials* **2015**, *5*, 1400930.
- (21) Trócoli, R.; La Mantia, F. An aqueous zinc-ion battery based on copper hexacyanoferrate. *ChemSusChem* **2015**, *8*, 481-485.
- (22) Song, Y.; Hu, J.; Tang, J.; Gu, W.; He, L.; Ji, X. Real-time X-ray imaging reveals interfacial growth, suppression, and dissolution of zinc dendrites dependent on anions

- of ionic liquid additives for rechargeable battery applications. *ACS Applied Materials & Interfaces* **2016**, *8*, 32031-32040.
- (23) Li, W.; Wang, K.; Zhou, M.; Zhan, H.; Cheng, S.; Jiang, K. Advanced low-cost, high-voltage, long-life aqueous hybrid sodium/zinc batteries enabled by a dendrite-free zinc anode and concentrated electrolyte. *ACS applied materials & interfaces* **2018**, *10*, 22059-22066.
- (24) Sun, K. E.; Hoang, T. K.; Doan, T. N. L.; Yu, Y.; Zhu, X.; Tian, Y.; Chen, P. Suppression of dendrite formation and corrosion on zinc anode of secondary aqueous batteries. *ACS applied materials & interfaces* **2017**, *9*, 9681-9687.
- (25) Li, W.; Wang, K.; Cheng, S.; Jiang, K. A long-life aqueous Zn-ion battery based on Na₃V₂(PO₄)₂F₃ cathode. *Energy Storage Materials* **2018**, *15*, 14-21.
- (26) Zhang, N.; Dong, Y.; Jia, M.; Bian, X.; Wang, Y.; Qiu, M.; Xu, J.; Liu, Y.; Jiao, L.; Cheng, F. Rechargeable aqueous Zn–V₂O₅ battery with high energy density and long cycle life. *ACS Energy Letters* **2018**, *3*, 1366-1372.
- (27) Ghosh, M.; Vijayakumar, V.; Soni, R.; Kurungot, S. A rationally designed self-standing V₂O₅ electrode for high voltage non-aqueous all-solid-state symmetric (2.0 V) and asymmetric (2.8 V) supercapacitors. *Nanoscale* **2018**, *10*, 8741-8751.
- (28) Zhao, Q.; Huang, W.; Luo, Z.; Liu, L.; Lu, Y.; Li, Y.; Li, L.; Hu, J.; Ma, H.; Chen, J. High-capacity aqueous zinc batteries using sustainable quinone electrodes. *Science advances* **2018**, *4*, eaao1761.
- (29) Abraham, K.; Jiang, Z.; Carroll, B. Highly conductive PEO-like polymer electrolytes. *Chemistry of materials* **1997**, *9*, 1978-1988.
- (30) Porcarelli, L.; Vlasov, P. S.; Ponkratov, D. O.; Lozinskaya, E. I.; Antonov, D. Y.; Nair, J. R.; Gerbaldi, C.; Mecerreyes, D.; Shaplov, A. S. Design of ionic liquid like monomers towards easy-accessible single-ion conducting polymer electrolytes. *European Polymer Journal* **2018**, *107*, 218-228.
- (31) Wan, F.; Zhang, L.; Dai, X.; Wang, X.; Niu, Z.; Chen, J. Aqueous rechargeable zinc/sodium vanadate batteries with enhanced performance from simultaneous insertion of dual carriers. *Nature communications* **2018**, *9*, 1-11.
- (32) Channu, V. R.; Holze, R.; Yeo, I.-H.; Mho, S.-i.; Kalluru, R. R. Electrochemical properties of polyaniline-modified sodium vanadate nanomaterials. *Applied Physics A* **2011**, *104*, 707-711.
- (33) Wang, X.; Jia, W.; Wang, L.; Huang, Y.; Guo, Y.; Sun, Y.; Jia, D.; Pang, W.; Guo, Z.; Tang, X. Simple in situ synthesis of carbon-supported and nanosheet-assembled

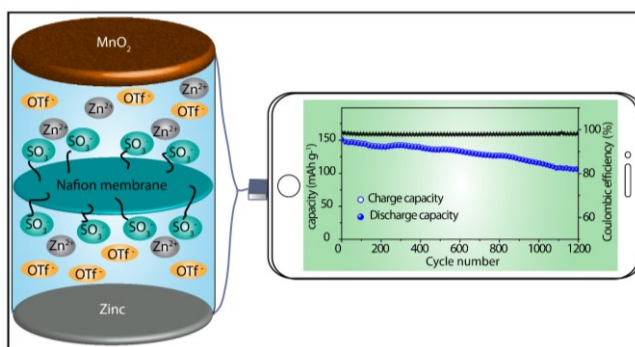
- vanadium oxide for ultra-high rate anode and cathode materials of lithium ion batteries. *Journal of Materials Chemistry A* **2016**, *4*, 13907-13915.
- (34) Zheng, Y.-Z.; Ding, H.; Uchaker, E.; Tao, X.; Chen, J.-F.; Zhang, Q.; Cao, G. Nickel-mediated polyol synthesis of hierarchical V₂O₅ hollow microspheres with enhanced lithium storage properties. *Journal of Materials Chemistry A* **2015**, *3*, 1979-1985.
- (35) Venkatesan, A.; Chandar, N. R. K.; Kandasamy, A.; Chinnu, M. K.; Marimuthu, K. N.; Kumar, R. M.; Jayavel, R. Luminescence and electrochemical properties of rare earth (Gd, Nd) doped V₂O₅ nanostructures synthesized by a non-aqueous sol-gel route. *RSC Advances* **2015**, *5*, 21778-21785.
- (36) Yu, X.; Joseph, J.; Manthiram, A. Polymer lithium-sulfur batteries with a Nafion membrane and an advanced sulfur electrode. *Journal of Materials Chemistry A* **2015**, *3*, 15683-15691.
- (37) Bauer, I.; Thieme, S.; Brückner, J.; Althues, H.; Kaskel, S. Reduced polysulfide shuttle in lithium-sulfur batteries using Nafion-based separators. *Journal of Power Sources* **2014**, *251*, 417-422.
- (38) Sun, W.; Wang, F.; Hou, S.; Yang, C.; Fan, X.; Ma, Z.; Gao, T.; Han, F.; Hu, R.; Zhu, M. Zn/MnO₂ battery chemistry with H⁺ and Zn²⁺ coinsertion. *Journal of the American Chemical Society* **2017**, *139*, 9775-9778.
- (39) Cai, Z.; Liu, Y.; Liu, S.; Li, L.; Zhang, Y. High performance of lithium-ion polymer battery based on non-aqueous lithiated perfluorinated sulfonic ion-exchange membranes. *Energy & Environmental Science* **2012**, *5*, 5690-5693.
- (40) Kim, H.-S.; Cook, J. B.; Lin, H.; Ko, J. S.; Tolbert, S. H.; Ozolins, V.; Dunn, B. Oxygen vacancies enhance pseudocapacitive charge storage properties of MoO_{3-x}. *Nature materials* **2017**, *16*, 454-460.
- (41) Wang, J.; Polleux, J.; Lim, J.; Dunn, B. Pseudocapacitive contributions to electrochemical energy storage in TiO₂ (anatase) nanoparticles. *The Journal of Physical Chemistry C* **2007**, *111*, 14925-14931.
- (42) Yan, M.; He, P.; Chen, Y.; Wang, S.; Wei, Q.; Zhao, K.; Xu, X.; An, Q.; Shuang, Y.; Shao, Y. Water-lubricated intercalation in V₂O₅·nH₂O for high-capacity and high-rate aqueous rechargeable zinc batteries. *Advanced materials* **2018**, *30*, 1703725.
- (43) Sambandam, B.; Soundharajan, V.; Kim, S.; Alfaruqi, M. H.; Jo, J.; Kim, S.; Mathew, V.; Sun, Y.-k.; Kim, J. Aqueous rechargeable Zn-ion batteries: an imperishable and high-energy Zn₂V₂O₇ nanowire cathode through intercalation regulation. *Journal of Materials Chemistry A* **2018**, *6*, 3850-3856.

- (44) Zhou, J.; Shan, L.; Wu, Z.; Guo, X.; Fang, G.; Liang, S. Investigation of V₂O₅ as a low-cost rechargeable aqueous zinc ion battery cathode. *Chemical Communications* **2018**, *54*, 4457-4460.
- (45) Ding, J.; Du, Z.; Gu, L.; Li, B.; Wang, L.; Wang, S.; Gong, Y.; Yang, S. Ultrafast Zn²⁺ Intercalation and Deintercalation in Vanadium Dioxide. *Advanced Materials* **2018**, *30*, 1800762.
- (46) Pang, Q.; Sun, C.; Yu, Y.; Zhao, K.; Zhang, Z.; Voyles, P. M.; Chen, G.; Wei, Y.; Wang, X. H₂V₃O₈ Nanowire/Graphene Electrodes for Aqueous Rechargeable Zinc Ion Batteries with High Rate Capability and Large Capacity. *Advanced Energy Materials* **2018**, *8*, 1800144.
- (47) Shen, C.; Li, X.; Li, N.; Xie, K.; Wang, J.-g.; Liu, X.; Wei, B. Graphene-Boosted, High-Performance Aqueous Zn-Ion Battery. *ACS Applied Materials & Interfaces* **2018**, *10*, 25446-25453.
- (48) Xia, C.; Guo, J.; Lei, Y.; Liang, H.; Zhao, C.; Alshareef, H. N. Rechargeable Aqueous Zinc-Ion Battery Based on Porous Framework Zinc Pyrovanadate Intercalation Cathode. *Advanced Materials* **2018**, *30*, 1705580.
- (49) Kundu, D.; Adams, B. D.; Duffort, V.; Vajargah, S. H.; Nazar, L. F. A high-capacity and long-life aqueous rechargeable zinc battery using a metal oxide intercalation cathode. *Nature Energy* **2016**, *1*, 16119.
- (50) Shin, W.-K.; Kannan, A. G.; Kim, D.-W. Effective Suppression of Dendritic Lithium Growth Using an Ultrathin Coating of Nitrogen and Sulfur Codoped Graphene Nanosheets on Polymer Separator for Lithium Metal Batteries. *ACS Applied Materials & Interfaces* **2015**, *7*, 23700-23707.
- (51) Gao, J.; Sun, C.; Xu, L.; Chen, J.; Wang, C.; Guo, D.; Chen, H. Lithiated Nafion as polymer electrolyte for solid-state lithium sulfur batteries using carbon-sulfur composite cathode. *Journal of Power Sources* **2018**, *382*, 179-189.
- (52) Lu, Y.; Tikekar, M.; Mohanty, R.; Hendrickson, K.; Ma, L.; Archer, L. A. Stable Cycling of Lithium Metal Batteries Using High Transference Number Electrolytes. *Advanced Energy Materials* **2015**, *5*, 1402073.
- (53) Zhang, W.; Tu, Z.; Qian, J.; Choudhury, S.; Archer, L. A.; Lu, Y. Design Principles of Functional Polymer Separators for High-Energy, Metal-Based Batteries. *Small* **2018**, *14*, 1703001.

Chapter 3

Nafion Ionomer-Based Single Component Electrolytes for Aqueous Zn||MnO₂ Battery with Long Cycle Life

Recently, aqueous rechargeable Zn||MnO₂ batteries are emerging as promising energy storage aids owing to their improved safety, low cost of fabrication, and high energy density. However, the rapid decay of capacity during extended charge-discharge cycles hinders the prospect of this technology beyond lab-scale. In the conventional Zn||MnO₂ cell, additives such as Mn²⁺ have been used to tackle the stability issue. Here, we demonstrate that cycling performance of the Zn||MnO₂ cell can be improved substantially by using Nafion ionomer as the separator in combination with Zn²⁺ ion conducting electrolytes. The Nafion ionomer-based Zn||MnO₂ cells do not require any Mn²⁺ additive in the electrolyte and hence termed as ‘single component’ electrolytes. The post-mortem study of the post-cycled electrodes reveals that



the structural evolution of both the anode and cathode in various electrolytes (1M Zn(CF₃SO₃)₂, 1M ZnSO₄·7H₂O and 3M ZnSO₄·7H₂O) during prolonged cycling significantly influences the cycle life of the respective cells. Optimizing the Nafion ionomer membrane with a suitable electrolyte could render the desired combination of high capacity and high cycle life for a Zn||MnO₂ cell.

Contents of this chapter is published in the article: DOI: 10.1021/acssuschemeng.9b06798. Reprinted (adapted) with permission from (ACS Sustainable Chem. Eng. 2020, 8, 13, 5040–5049). Copyright (2020) American Chemical Society.

3.1 Introduction

State-of-the-art lithium-ion batteries (LIBs) use a graphite anode in combination with flammable organic electrolytes inciting several safety concerns.^{1, 2} Although the prospect of aqueous electrolyte and solid-state electrolyte based LIBs is heavily researched,^{3, 4} their commercial potential is debated due to the poor interfaces and stability issues. In this scenario, post-lithium rechargeable battery chemistries are receiving significant attention. Among them, aqueous rechargeable zinc (Zn)-metal batteries (ARZMBs) conceiving the reversible shuttling of Zn-ion (Zn^{2+}) between a metallic Zn anode and an insertion cathode are of particular interest.^{5,6} Zn is naturally abundant and possesses a low reduction potential of -0.76 V vs. standard hydrogen electrode.⁷ It is expected that the use of a high capacity Zn anode (820 mAh g^{-1}) in combination with a suitable high-voltage cathode could make the ARZMBs reach up to 190 Wh kg^{-1} ; however, due to poor cathode performance, values are around 80 - 90 Wh kg^{-1} .⁸

MnO_2 is considered as one of the promising cathode materials for the reversible insertion of Zn^{2+} .^{9,10} MnO_2 cathode exhibits high average potential (~ 1.4 V) along with high capacity (> 200 mAh g^{-1}), which enhances the possible energy output of ARZMB.¹¹ However, despite the above-mentioned advantages, the further development of rechargeable Zn|| MnO_2 batteries is still constrained due to severe capacity fading during cycling. As per the current understanding, this shortcoming originates from the dissolution of Mn^{2+} into the electrolyte.¹² In this aspect, Mn(II) salts such as MnSO_4 and $\text{Mn}(\text{CF}_3\text{SO}_3)_2$ are employed as additives in the Zn^{2+} -conducting electrolytes and are proved to improve the cycle life of the Zn|| MnO_2 battery.¹³ The presence of a Mn(II) salt in the electrolyte maintains an equilibrium concentration of Mn^{2+} at the electrode|electrolyte interface suppressing the dissolution of the electrode material.^{14, 15} Also, the Mn(II) salt could be electrodeposited on the cathode during electrochemical cycling of the cell, leading to higher loading of the active material.^{16, 17} This leads to the overestimation of the cell performance, which is often not taken into account. Despite the know-how regarding the Mn^{2+} dissolution leading to capacity fading in the Zn|| MnO_2 battery, the other factors contributing to the same still remain ambiguous. Therefore, an alternate strategy to improve the cycle life of the Zn|| MnO_2 battery without a pre-added Mn(II) salt is desirable.

Few recent reports have demonstrated that accumulation of an irreversible byproduct (such as $\text{ZnMn}_3\text{O}_7 \cdot 2\text{H}_2\text{O}$ or woodruffite structure) on the cathode impedes the reversibility of the Zn^{2+} shuttling, deteriorating the overall performance of the battery.¹⁸⁻²⁰ Besides, ARZMBs suffer from low cycle life owing to the dendrite-like structural evolution on the surface of the metallic Zn anode.²¹⁻²³ In addition to this, recently Zhao *et al.* have shown the poisoning of the anode by means of diffused discharge byproducts from the cathode to be detrimental to the

cycling stability of ARZMBs.²⁴ Therefore, in the case of the Zn||MnO₂ battery, the poisoning of the Zn surface by Mn(II) deposition could possibly be another factor contributing toward the observed performance degradation. In fact, reports on a manganese-based LIB cathode have proved that dissolved Mn-species diffuse, migrate, and eventually get deposited on the anode, leading to poisoning of the solid electrolyte interphase (SEI) on the anode.²⁵ The aforementioned intricacies can be mitigated by using a cation selective ionomer membrane such as Nafion as the separator. Recently, our group has explored this strategy with two different cathodes *viz.*, V₂O₅ and covalent organic framework (COF).^{26,27}

Here, we investigate the electrochemical performance of lab-scale Zn||MnO₂ cells with Nafion ionomer membrane as the separator in combination with Zn²⁺ ion conducting liquid electrolytes. Unlike the plethora of available reports on ARZMBs, no additional Mn(II) salt is added into the electrolytes, and hence they are called ‘*single component*’ electrolytes. Specific attention is dedicated to the Nafion membrane-based Zn||MnO₂ cells comprising Zn(CF₃SO₃)₂ or ZnSO₄ electrolytes, which offer a more favourable electrode|electrolyte interface and wide electrochemical stability window compared to other salts such as ZnCl₂, Zn(OOCCH₃)₂, and Zn(NO₃)₂. In 1M Zn(CF₃SO₃)₂, the Nafion-based Zn||MnO₂ cell exhibits a high capacity of 350 mAh g⁻¹ at 0.1 A g⁻¹ and excellent cycling stability (89% of the initial capacity is retained after 500 cycles at 3 A g⁻¹ current rate) compared to all the other electrolytes. On the other hand, in 1M ZnSO₄·7H₂O, the Zn||MnO₂ cell delivers a high initial capacity; however, the capacity drops drastically to 110 mAh g⁻¹ after 500 cycles. Such capacity fading is found to be reduced in a concentrated electrolyte (3M ZnSO₄·7H₂O). Most importantly, the current study emphasizes that, irrespective of the type of the liquid electrolyte used, all the Nafion-based Zn||MnO₂ cells outperform the porous separator (glass fiber paper and polypropylene)-based counterparts. This highlights the utility of the Nafion-based single component electrolyte to eliminate the necessity of Mn(II) additives in the electrolyte in the Zn||MnO₂ cells. Additionally, through detailed structural analyses of the post-cycling electrodes, we have also elucidated the underlying factors contributing to the improved performance of the Nafion-based Zn||MnO₂ cells as a function of different electrolytes.

3.2 Experimental Section

3.2.1 Materials

Manganese acetate (Mn(OOCCH₃)₂), ammonium acetate (NH₄OOCCH₃), zinc trifluoromethanesulfonate (Zn(CF₃SO₃)₂), zinc nitrate hexahydrate (Zn(NO₃)₂·6H₂O), zinc chloride (ZnCl₂), and zinc sulphate heptahydrate (ZnSO₄·7H₂O) were procured from Sigma

Aldrich. Zinc acetate ($\text{Zn}(\text{OOCCH}_3)_2$) was purchased from Rankem Chemicals. Toray carbon fiber paper was supplied by Global Nanotech. Nafion® membrane (212) was procured from DuPont, USA. Glass fiber (Grade GF/F) and polypropylene-based Celgard® were supplied by Global Nanotech.

3.2.2 Fabrication of the Cathode

The precursor solution was prepared by dissolving 432 mg of $\text{Mn}(\text{OOCCH}_3)_2$ (0.1 M) and 193 mg of $(\text{NH}_4\text{OOCCH}_3)$ (0.1 M) in 25 ml of deionized water. Electrochemical deposition of MnO_2 was carried out in a three-electrode setup using commercial Toray carbon paper (CP, 1 cm^2 area) as the working electrode, a platinum mesh as the counter electrode, and a platinum wire as the quasi reference electrode in a Biologic VMP3 potentiostat instrument. A constant current of 4 mA cm^{-2} was applied for different time intervals of 560, 1663, and 2772 sec to obtain the MnO_2 loading values of 1, 3, and 5 mg, respectively. Followed by the electrodeposition, all the electrodes were rinsed thoroughly with water and dried at 60°C. The as-prepared electrodes are marked as MnCP-X, where 'X' stands for the loading of the MnO_2 on CP.

3.2.3 Material Characterization

Morphology of the MnCP-X samples was investigated with field emission scanning electron microscope (FESEM) Nova Nano SEM 450. Energy-dispersive X-ray spectroscopy (EDAX) analysis and EDAX elemental mapping were performed with an ESEM-Quanta 200-3D instrument. A Tecnai T-20 instrument at an accelerating voltage of 200 kV was used for transmission electron microscopy (TEM) imaging. Fourier transform infrared (FTIR) analysis was carried out with a Bruker Tensor 27 FTIR instrument. X-ray photoelectron spectroscopy (XPS) analysis was performed using a Thermo K-alpha+ X-ray spectrometer. Rigaku, MicroMax-007HF with high-intensity Microfocus rotating anode X-ray generator ($\text{Cu K}\alpha$ ($\alpha = 1.54 \text{ \AA}$) was used for X-ray diffraction (XRD) analysis.

3.2.4 Electrochemical Measurements

BioLogic VMP3 Potentio-Galvanostat instrument was used for all the electrochemical analyses. All the electrochemical cells were fabricated in CR2032 coin cell configuration using Nafion membrane as the separator. Prior to use, the Nafion membranes were pre-treated by following the previously reported method.²⁶ In this work, aqueous solution of 1M $\text{Zn}(\text{CF}_3\text{SO}_3)_2$, 1M $\text{ZnSO}_4 \cdot 7\text{H}_2\text{O}$, 1M ZnCl_2 , 1M $\text{Zn}(\text{NO}_3)_2 \cdot 6\text{H}_2\text{O}$, 1M $\text{Zn}(\text{OOCCH}_3)_2$ or 3M $\text{ZnSO}_4 \cdot 7\text{H}_2\text{O}$ were used as the electrolytes. The electrolytes in combination with Nafion

membrane are represented as NAF-T-1, NAF-S-1, NAF-C-1, NAF-N-1, NAF-A-1, and NAF-S-3, respectively, where ‘NAF’ stands for Nafion, the letter followed by ‘NAF’ indicates the type of conducting salt (‘T’= $\text{Zn}(\text{CF}_3\text{SO}_3)_2$, ‘S’= $\text{Zn}(\text{SO}_4)_2$, ‘C’= ZnCl_2 , ‘N’= $\text{Zn}(\text{NO}_3)_2$ and ‘A’= $\text{Zn}(\text{OOCCH}_3)_2$) and the digits ‘1’ and ‘3’ represent the concentration of the electrolytes. Cyclic voltammetry (CV) analyses were carried out in Zn|Y|CP cell configuration using CP and Zn foil as the working and reference electrodes, respectively. Here the letter ‘Y’ is used as a general representation for the aforementioned electrolyte-soaked Nafion membranes (e.g., NAF-T-1, NAF-S-1, etc.). Similarly, the galvanostatic Zn plating/stripping experiments were carried out at a current rate of 0.1 mA cm^{-2} (30 min Zn plating and 30 min Zn stripping) in a Zn|Y|Zn symmetric cell configuration.

Ionic conductivity values of the electrolytes were determined by the electrochemical impedance spectroscopy (EIS) technique. The conductivity cells were fabricated in the CR2032 coin cell by keeping the desired electrolyte-soaked Nafion membrane in between two stainless steel plates with 1 mm thickness. The conductivity measurements were carried out between 20 to 60° C at every 10° C interval. The temperature was controlled by using an Espec environmental test chamber. The transference number of Zn^{2+} ($t_{\text{Zn}^{2+}}$) in the electrolyte-infused Nafion membranes was also analyzed in the Zn|Y|Zn symmetric cell configuration, and $t_{\text{Zn}^{2+}}$ values were calculated from the following equation (**Equation 3.1**) proposed by Abraham *et al.*^{28,29}

$$t_{\text{Zn}^{2+}} = \frac{I_{SS}R_{\Omega,SS}(\Delta V - I_0R_{ct,0})}{I_0R_{\Omega,0}(\Delta V - I_{SS}R_{ct,SS})} \quad (\text{Equation 3.1})$$

where, V stands for the DC polarization voltage, I_0 and I_{SS} are the initial and steady state current response during the polarization, respectively, and R_{Ω} and R_{ct} are the equivalent series resistance (ESR) and charge transfer resistance obtained from the impedance data at initial and steady state, respectively.

The electrochemical performance of the MnCP-X cathodes was studied in the CR2032 coin cell (Zn|Y|MnCP-X), where ‘X’ and ‘Y’ indicate the amount of MnO_2 loading on CP and the type of electrolyte used. The CV (at scan rates of 1.0, 0.5, 0.3, and 0.1 mV s^{-1}) and galvanostatic charge-discharge (GCD) (at constant current rates of 0.1, 0.25, 0.5, 1, and 3 A g^{-1}) techniques were employed to characterize the Zn|| MnO_2 cells within the voltage window of 0.80–2.0 V vs. Zn| Zn^{2+} . The cycling stability tests were performed by the GCD experiment at a current rate of 3 A g^{-1} . The specific discharge capacity values of the Zn|| MnO_2 cells are calculated from the GCD plots considering the loading of the active material (MnO_2) in the

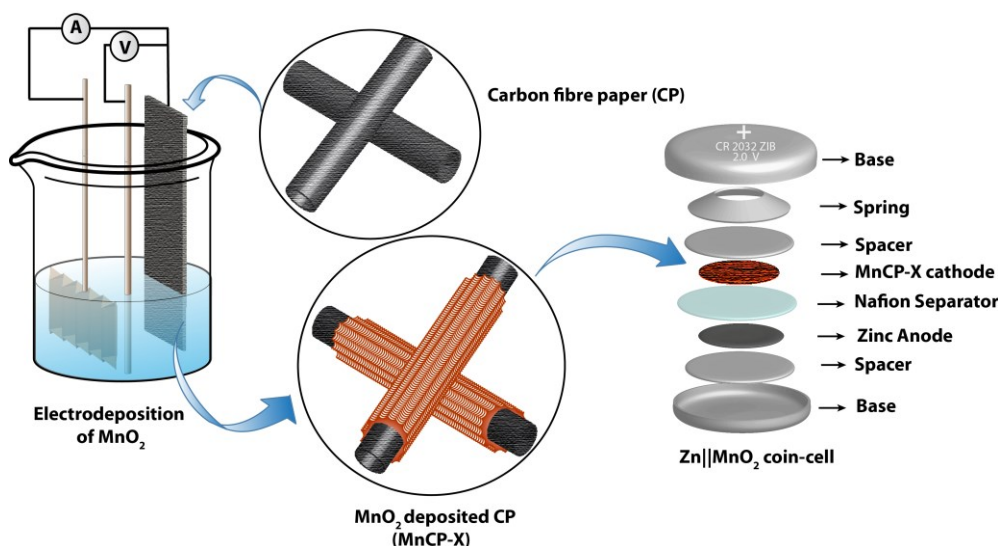


Figure 3.1. Schematic presentation of the fabrication of the MnCP-X electrode. (Reprinted (adapted) with permission from *ACS Sustainable Chem. Eng.* 2020, 8, 13, 5040–5049). Copyright (2020) American Chemical Society).

cathode. The overall resistance of the Zn|Y|MnCP-X cells was monitored by impedance analyses within the 1 MHz to 50 mHz frequency range with a sinus amplitude of 10 mV ($V_{\text{rms}} = 7.07 \text{ mV}$). The spectra were recorded during the 1st and 100th discharge cycles at a potential of 1.25 V vs. Zn|Zn²⁺. For comparison purpose, Zn||MnO₂ cells are also fabricated with glass fiber paper (GFP) and polypropylene-based Celgard (CEL) as the porous separator using 1M Zn(CF₃SO₃)₂, 1M ZnSO₄·7H₂O, and 3M ZnSO₄·7H₂O electrolytes. The cells with GFP are represented as Zn|GFP-T-1|MnCP-1, Zn|GFP-S-1|MnCP-1, and Zn|GFP-S-3|MnCP-1, respectively. The CEL-based cells are marked as Zn|CEL-T-1|MnCP-1, Zn|CEL-S-1|MnCP-1, and Zn|CEL-S-3|MnCP-1, respectively.

3.3 Results and Discussion

3.3.1 Physical Characterizations

The fabrication of the MnO₂ electrode (MnCP-X) and its use as cathode for assembling Zn||MnO₂ cell are schematically presented in **Figure 3.1**. The FESEM images in **Figure 3.2a** and **b** reveal that the surface of the carbon fibers in MnCP-1 sample is uniformly covered with the vertically aligned MnO₂ nanosheets. The nanosheets are interconnected with each other to form a uniform porous network over the carbon fibers. The uniform distribution of manganese (Mn) and oxygen (O) over the carbon (C) fibers is confirmed by elemental mapping analysis of MnCP-1 (**Figure 3.2c**). In order to understand the effect of deposition time on the MnO₂

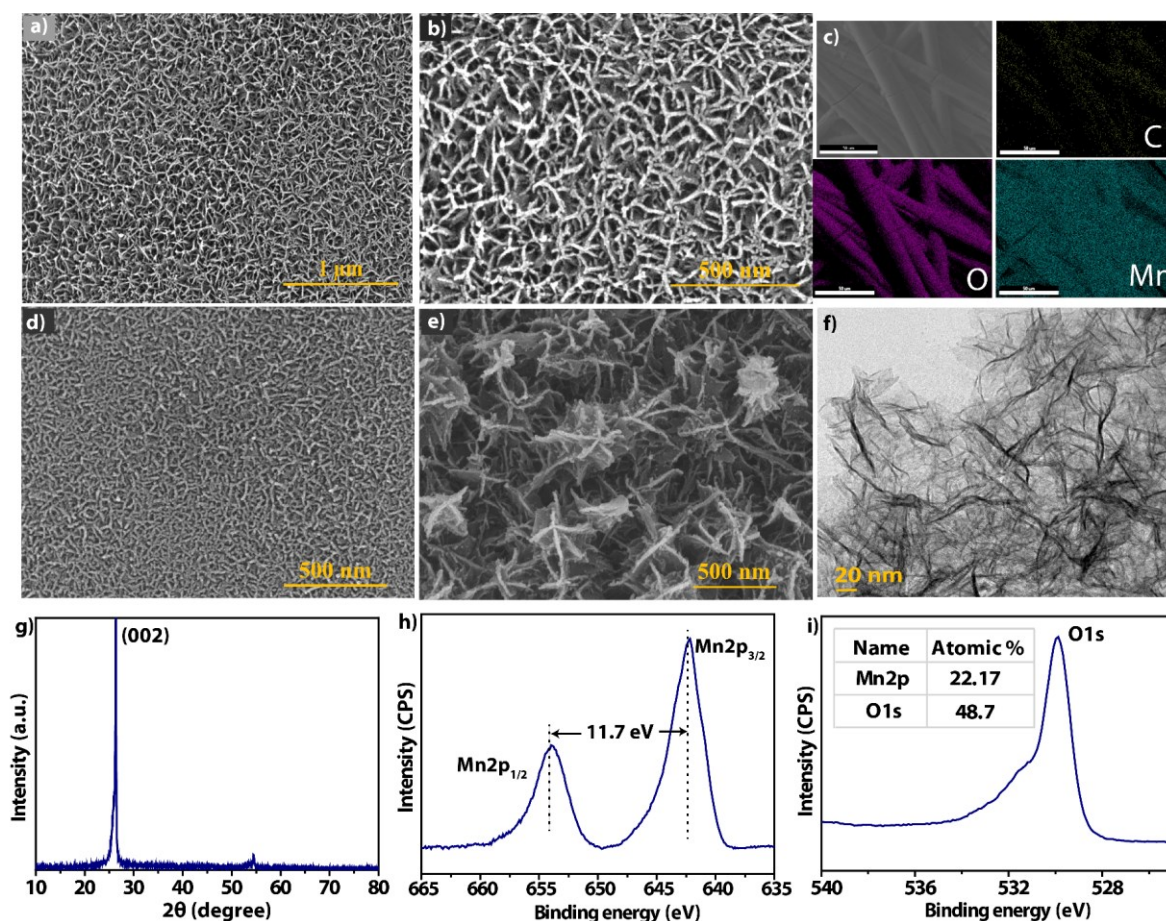


Figure 3.2. (a)-(b) FESEM images and (c) elemental mapping of C, O, and Mn of the MnCP-1 sample; FESEM image of the (d) MnCP-3, and (e) MnCP-5 samples; (f) TEM image, (g) XRD profile, (h) Mn2p XPS profile, and (i) O1s XPS profile of the MnCP-1 sample. (Reprinted (adapted) with permission from *ACS Sustainable Chem. Eng.* 2020, 8, 13, 5040–5049). Copyright (2020) American Chemical Society).

morphology, the morphology of MnCP-3 and MnCP-5 samples is also studied. **Figure 3.2d** and **e** exhibit the formation of dense MnO₂ nanosheets in MnCP-3 and MnCP-5.

Later, the MnCP-1 sample was subjected to further characterization. The TEM image of MnCP-1 (**Figure 3.2f**) reveals the growth of thin and interconnected MnO₂ nanosheets. In the XRD data of the MnCP-1 sample (**Figure 3.2g**), the absence of prominent characteristic peaks for MnO₂ may be due to the amorphous nature of the sample. The formation of the MnO₂ phase is supported through XPS analysis. In **Figure 3.2h**, the appearance of two peaks at the binding energies of 642.4 and 654.0 eV correspond to the Mn 2p_{3/2} and Mn 2p_{1/2} doublet of the +4 oxidation state of Mn, respectively. The spacing of 11.7 eV between the doublets validates the +4 oxidation state of Mn.³⁰ The O1s spectra at the binding energy of 529.0 eV correspond to the Mn-O-Mn coordination in the MnO₂ lattice (**Figure 3.2i**).³¹ Moreover, the

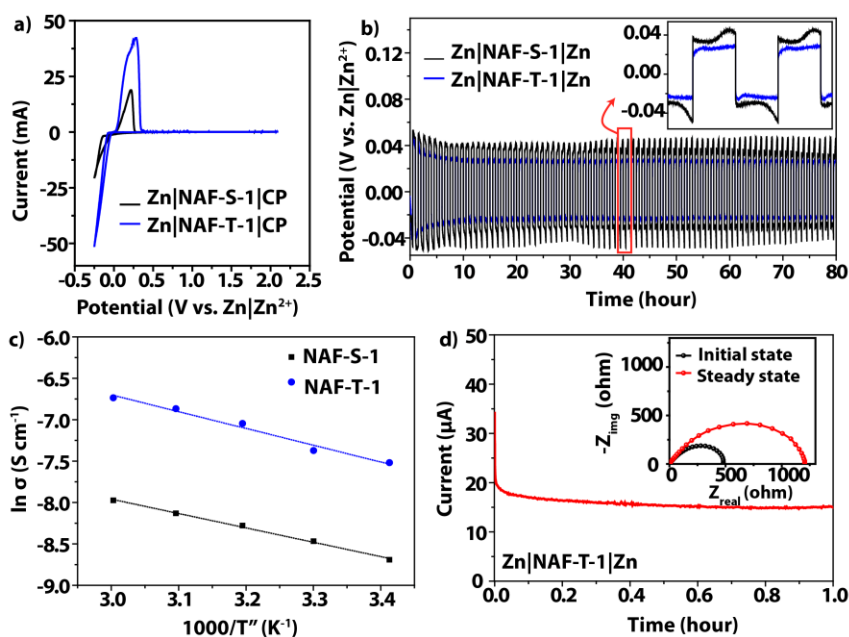


Figure 3.3. (a) CV plots of the Zn|NAF-T-1|CP and Zn|NAF-S-1|CP cells recorded at a scan rate of 5 mV s^{-1} ; (b) voltage vs. time profiles of the Zn|NAF-T-1|Zn and Zn|NAF-S-1|Zn cells; (c) Arrhenius plot representing the linear relationship between Ionic conductivity (σ) and temperature (T'') for the NAF-T-1 and NAF-S-1 electrolytes; (d) chronoamperometry data of the Zn|NAF-T-1|Zn cell recorded at a bias potential of 25 mV, where the corresponding impedance plots are given in the inset. (Reprinted (adapted) with permission from (ACS Sustainable Chem. Eng. 2020, 8, 13, 5040–5049). Copyright (2020) American Chemical Society).

atomic percentage of the elements in MnCP-1 confirms the presence of Mn and O with a stoichiometric ratio of $\approx 1:2$.

3.3.2 Selection of Electrolytes

The reversibility of the Zn plating/stripping process in different electrolytes and the electrochemical stability of the respective electrolytes are primarily investigated by CV analyses at a scan rate of 5 mV s^{-1} . In **Figure 3.3a**, the pair of the redox peaks corresponds to the plating and stripping of Zn in the Zn|NAF-S-1|CP and Zn|NAF-T-1|CP cells. Apart from these two peaks, no significant current response is observed in the anodic region up to a potential of 2.1 V vs. Zn|Zn^{2+} . The wide potential window suggests the compatibility of the aforementioned electrolytes to be employed with a high voltage cathode such as MnO_2 . However, the difference between the onset potential for the plating and stripping processes is more in the case of the Zn|NAF-S-1|CP cell. This indicates the lower overpotential and better reversibility of Zn plating/stripping in 1M $\text{Zn}(\text{CF}_3\text{SO}_3)_2$.

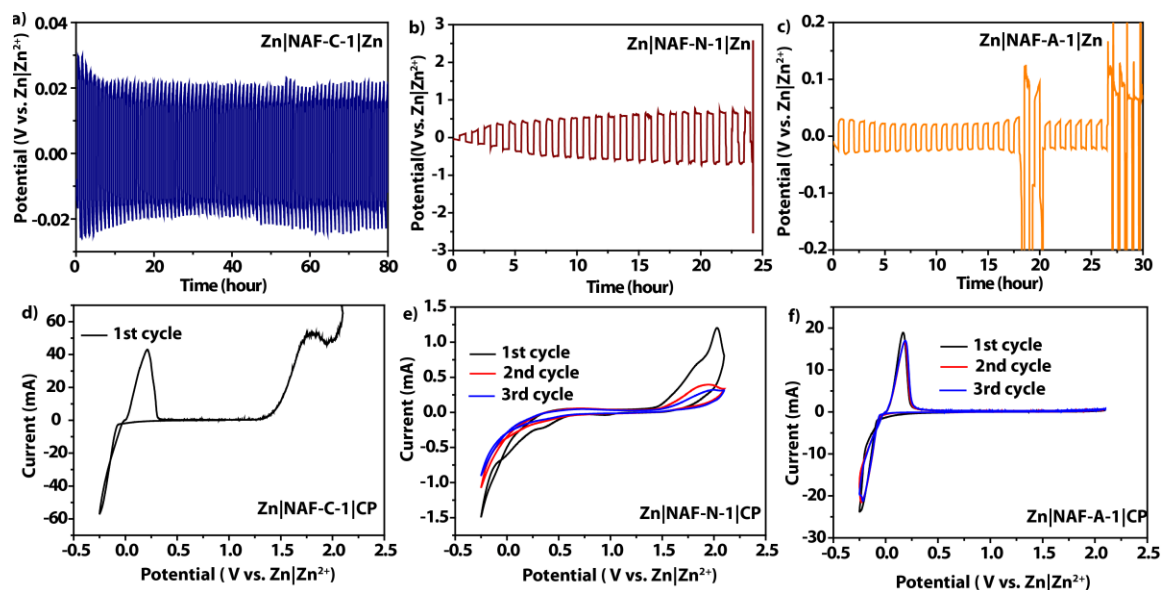


Figure 3.4. Voltage vs. time profiles of the (a) Zn|NAF-C-1|Zn, (b) Zn|NAF-N-1|Zn, and (c) Zn|NAF-A-1|Zn cells; CV plots of the (d) Zn|NAF-C-1|CP, (e) Zn|NAF-N-1|CP, and (f) Zn|NAF-A-1|CP cells recorded at the scan rate of 5 mV s^{-1} . (Reprinted (adapted) with permission from (ACS Sustainable Chem. Eng. 2020, 8, 13, 5040–5049). Copyright (2020) American Chemical Society).

The reversibility of the Zn plating/stripping is further confirmed from the long-time plating/stripping behavior in the Zn|NAF-S-1|Zn and Zn|NAF-T-1|Zn symmetric cell configurations (**Figure 3.3b**). In both the cells, a gradual drop in the voltage polarization during the initial cycles indicates the formation of a stable electrode|electrolyte interface. As given in the enlarged image (**Figure 3.3b**), the plating/stripping overpotential obtained for the Zn|NAF-T-1|Zn cell is lower (52 mV) than that of the Zn|NAF-S-1|Zn cell (94 mV). Nevertheless, compared to the flat voltage profile in $1 \text{ M Zn}(\text{CF}_3\text{SO}_3)_2$, both plating and stripping processes in $1 \text{ M ZnSO}_4 \cdot 7\text{H}_2\text{O}$ experience small voltage shoot up, which is a characteristic of porous and non-uniform electrode surface evolved during repeated cycling.³² However, in the previous chapter (**Chapter 2**), a favourable plating and stripping process with a lower overpotential value of 71 mV in a concentrated ZnSO_4 electrolyte ($3 \text{ M ZnSO}_4 \cdot 7\text{H}_2\text{O}$) has already been proved.²⁶ The superior electrochemical behavior of the Zn|NAF-T-1|Zn cell can be ascribed to the bulky CF_3SO_3^- counterpart present in the $\text{Zn}(\text{CF}_3\text{SO}_3)_2$ electrolyte.³³ The large size of the anion reduces the number of solvating water molecules surrounding the Zn^{2+} ions, which facilitates the mobility of the Zn^{2+} under the applied potential. This could lead to uniform plating of Zn during the electrochemical cycling.³⁴

The ion transport properties of the NAF-T-1 and NAF-S-1 membranes are investigated through ionic conductivity and Zn^{2+} ion transference number analysis. The temperature-dependent ionic conductivities of the NAF-T-1 and NAF-S-1 membranes were measured, and the corresponding data are summarized in the form of the Arrhenius plot in **Figure 3.3c**.^{35, 36} At 40°C, NAF-T-1 and NAF-S-1 membranes offer more or less similar ionic conductivity (0.87 and 0.25 mS cm⁻¹, respectively) and activation energy (0.17 and 0.15 eV, respectively). In order to check the cationic contribution toward the total ionic transport, the Zn^{2+} ion transference numbers ($t_{Zn^{2+}}$) are evaluated for Zn|NAF-T-1|Zn and Zn|NAF-S-1|Zn cells. The $t_{Zn^{2+}}$ values obtained for 1M Zn(CF₃SO₃)₂ (**Figure 3.3d**) and 1M ZnSO₄·7H₂O based membranes are 0.54 and 0.51, respectively. The $t_{Zn^{2+}}$ values higher than 0.50 are credited to the cation selective Nafion ionomer membrane as the separator in both the cells.³⁷

Later, electrochemical properties of three other Zn^{2+} ion conducting aqueous electrolytes (1M Zn(NO₃)₂·6H₂O, 1M Zn(OOCCH₃)₂, and 1M ZnCl₂) in combination with Nafion membrane are studied. The associated electrochemical data are displayed in **Figure 3.4a-f**. Among them, only the Zn|NAF-C-1|Zn cell could sustain stable plating/stripping for 80 h with an overpotential of 80 mV (**Figure 3.4a**). However, in the CV plot of the Zn|NAF-C-1|CP cell (**Figure 3.4d**), the steep increase in the current at 1.2 V vs. Zn|Zn²⁺ originates from the low electrochemical stability of the ZnCl₂ electrolyte.³⁸ On the other hand, the cycling data of the Zn|NAF-N-1|Zn and Zn|NAF-A-1|Zn cells (**Figure 3.4b and c**) shows a gradual increase in voltage polarization with respect to time. The appearance of spikes in the plating and stripping half indicates the internal short circuits by means of the inferior electrode|electrolyte interface.³⁹ Such interfacial instability leads to cell failure just after 30 h of operation. Nevertheless, the reversible peaks for the Zn plating/stripping process are not observed in the CV profile of the Zn|NAF-N-1|CP cell (**Figure 3.4e**) due to corrosion of Zn in the presence of the strong oxidizing NO₃⁻ ions in the electrolyte.⁴⁰ Therefore, considering the wide electrochemical stability, low plating/stripping overpotential, and long cycling stability obtained in 1M Zn(CF₃SO₃)₂ and 1M ZnSO₄·7H₂O electrolytes, we have opted for these two electrolytes for the fabrication of Zn||MnO₂ cells.

3.3.3 Electrochemical Analysis of the Zn||MnO₂ Cell in 1M Zn(CF₃SO₃)₂

The Zn^{2+} storage property of the MnCP-1 electrode in the 1M Zn(CF₃SO₃)₂ electrolyte (Zn|NAF-T-1|MnCP-1 cell) is primarily investigated by CV analysis within a voltage range of 0.80 to 2.0 V vs. Zn|Zn²⁺. In **Figure 3.5a**, the CV plots at different scan rates exhibit a pair of redox peaks at potentials of 1.3 V/1.6 V vs. Zn|Zn²⁺, implying the reversible insertion of Zn^{2+}

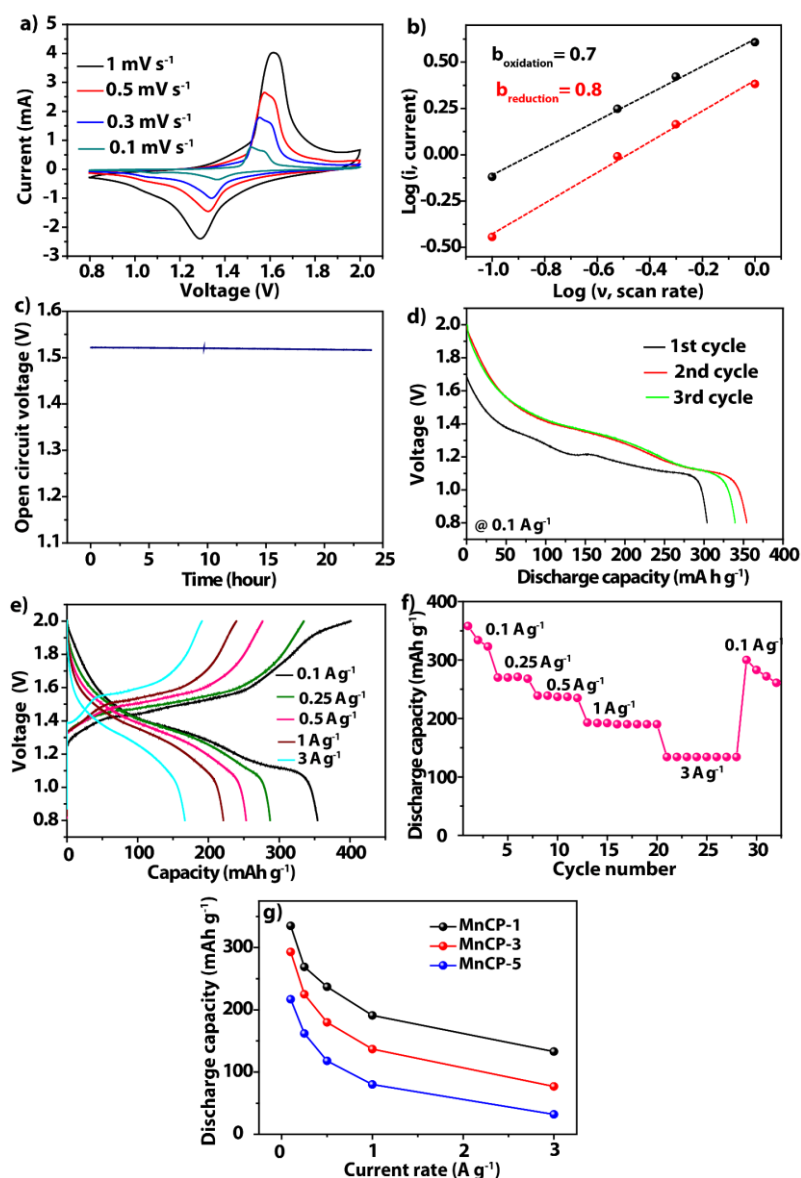


Figure 3.5. (a) CV plots of the Zn|NAF-T-1|MnCP-1 cell recorded at various scan rates; (b) $\text{Log}(i)$ vs. $\text{Log}(v)$ plots of the oxidation and reduction peaks as appeared in Figure(a); (c) the open-circuit voltage (OCV) vs. time profile, (d) discharge profiles in the initial cycles at a current rate of 0.1 A g^{-1} , (e) GCD profiles at various current rates, (f) rate performance of the Zn|NAF-T-1|MnCP-1 cell; (g) discharge capacities of the Zn|NAF-T-1|MnCP-X cells measured at various current rates. (Reprinted (adapted) with permission from *ACS Sustainable Chem. Eng.* 2020, 8, 13, 5040–5049). Copyright (2020) American Chemical Society).

ions into the MnO_2 lattice. The charge storage mechanism is investigated by analyzing the dependence of the peak current (i) on the scan rate (v) using the following equation:

$$i = a v^b \quad (\text{Equation 3.2})$$

where ‘ a ’ and ‘ b ’ are the adjustable parameters.⁴¹ In particular, $b = 0.5$ and $b = 1.0$ signify the contribution from the diffusion-controlled and surface-controlled faradaic processes, respectively.^{42,43} b values for the anodic and cathodic peaks of the Zn|NAF-T-1|MnCP-1 cells are obtained from the Log (i) vs. Log (v) relationship (**Figure 3.5b**). A b value higher than 0.5 (0.73 for the oxidation peak and 0.82 for the reduction peak) indicates that the Zn²⁺ storage in the MnCP-1 cathode is hybrid with dominant contribution from the surface-controlled process.⁴⁴ Besides, the Zn|NAF-T-1|MnCP-1 cell could maintain the open-circuit voltage (~ 1.5 V vs. Zn|Zn²⁺) for more than 24 h, indicating negligible self-discharge (**Figure 3.5c**).

The charge storage capacity of the MnCP-1 sample in the 1M Zn(CF₃SO₃)₂ electrolyte is analyzed by the GCD method. At a current rate of 0.1 A g⁻¹, the cell achieves high discharge capacities of 300 and 350 mAh g⁻¹ in the 1st and 2nd cycles, respectively (**Figure 3.5d**). To assess the rate capability of the Zn|NAF-T-1|MnCP-1 cell, the capacities at various current rates are recorded. The cell delivers average discharge capacities of 350, 300, 250, 225, and 175 mAh g⁻¹ at current rates of 0.1, 0.25, 0.5, 1, and 3 A g⁻¹, respectively (**Figure 3.5e and f**). The obtained capacity values indicate a good rate capability of the cell with 50% retention of the capacity when the current rate is varied from 0.1 to 3 A g⁻¹. Notably, when the current rate is abruptly decreased to 0.1 A g⁻¹, the cell could recover a discharge capacity of 290 mAh g⁻¹ (**Figure 3.5f**). A slight decrease in the capacity at 0.1 A g⁻¹ during the following cycles can be due to the degradation of the cathode at a very low current rate. Moreover, the symmetric appearance of the charge-discharge profiles at all the current rates (**Figure 3.5e**) suggests the reversible Zn²⁺ insertion/extraction process occurring in the MnCP-1 cathode.

The remarkable capacity and rate performance of the Zn|NAF-T-1|MnCP-1 cell can be credited to the unique architecture of the MnCP-1 cathode. The vertically aligned MnO₂ nanosheets (**Figure 3.2a**) over the carbon fibers can expose more number of redox sites and facilitate the access of the electrolyte to the interior of the electrode. This extended electrode|electrolyte interfacial contact reduces the diffusion path for the electrolyte ions.⁴⁵ Besides, the carbon fiber backbone of the MnCP-1 cathode ensures the easy transport of electrons even when the electrochemical reactions are performed at higher current rates. The synergic effect of the aforementioned factors maximizes the number of accessible active sites for accommodating the Zn²⁺ ions in the MnCP-1 cathode.

The discharge capacities of the other MnCP-X electrodes are also measured as a function the MnO₂ loading (**Figure 3.5g**). At a current rate of 0.1 A g⁻¹, the MnCP-3 and MnCP-5 samples exhibit discharge capacities of 292 and 216 mAh g⁻¹, respectively. The drop

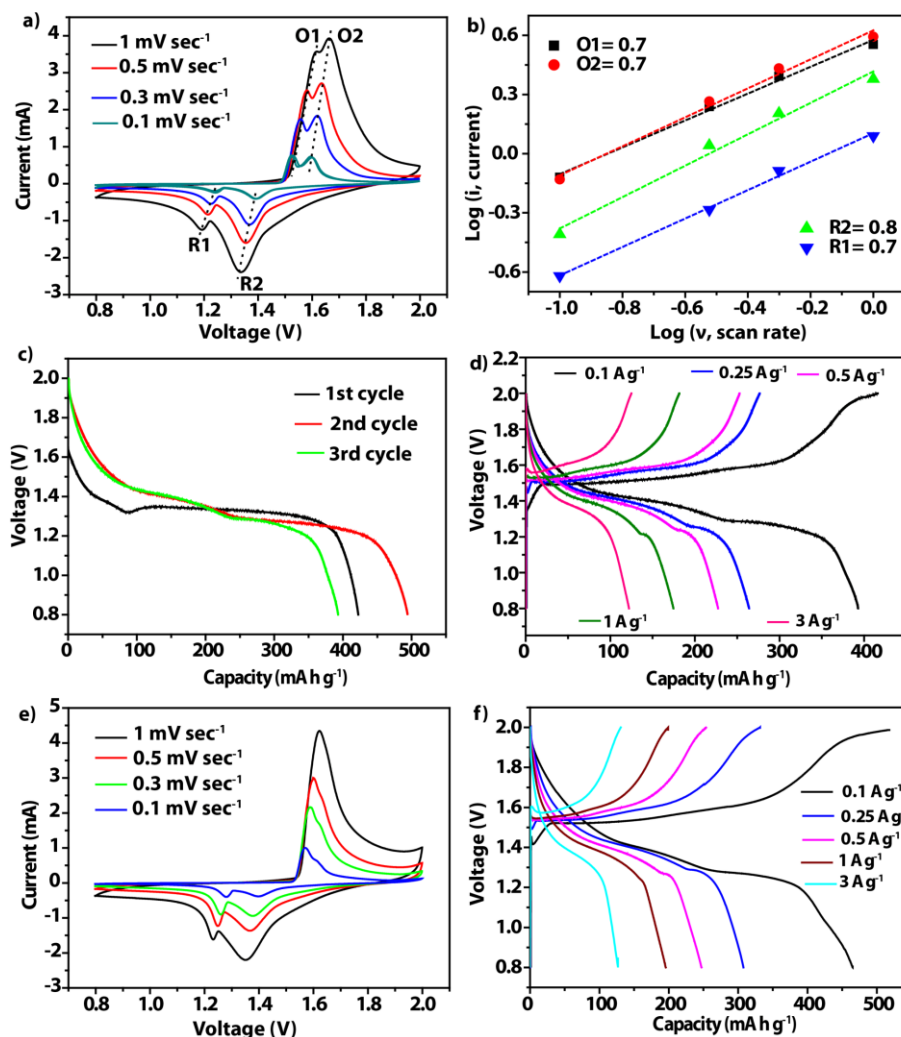


Figure 3.6. (a) CV plots of the Zn|NAF-S-1|MnCP-1 cell recorded at various scan rates; (b) $\text{Log}(i)$ vs. $\text{Log}(v)$ plots of the redox peaks as shown in (a); (c) discharge profiles in the initial cycles recorded at a current rate of 0.1 A g^{-1} ; (d) GCD profiles obtained at various current rates of the Zn|NAF-S-1|MnCP-1 cell; (e) CV profiles recorded at various scan rates and (f) GCD profiles recorded at various current rates of the Zn|NAF-S-3|MnCP-1 cell. (Reprinted (adapted) with permission from (ACS Sustainable Chem. Eng. 2020, 8, 13, 5040–5049). Copyright (2020) American Chemical Society).

in the discharge capacity with higher loading is obvious as observed in the other charge storage devices based on semiconducting MnO_2 .^{46, 47} Due to the thick coating of MnO_2 in MnCP-3 and MnCP-5, the electrolyte ions can access only a fraction of the active material, which could further take part in the associated redox reactions. Still, considering the high loading, the specific capacity of MnCP-5 is appreciable in comparison to the other MnO_2 -based ARZMB cathodes reported previously.⁴⁸⁻⁵⁰

3.3.4 Electrochemical Analysis of the Zn||MnO₂ Cell in 1M ZnSO₄

The electrochemical performance of MnCP-1 is further explored in the 1M ZnSO₄·7H₂O electrolyte (Zn|NAF-S-1|MnCP-1 cell). The CV profiles (**Figure 3.6a**) of the Zn|NAF-S-1|MnCP-1 cell display two distinct pairs of reversible redox peaks, which could be related to the insertion/extraction of H⁺ (1.5 V/1.39 V) and Zn²⁺ (1.59 V/1.24 V) ions into the MnO₂ lattice. The charge storage mechanism of the Zn|NAF-S-1|MnCP-1 cell is also analyzed from the current vs. scan rate relationship (**Equation 3.2, Figure 3.6b**). Similar to the Mn|NAF-T-1|Zn cell, the *b* values for the oxidation and reduction peaks are in the range of 0.70-0.80, signifying the dominant contribution of the surface-controlled redox reactions.

The initial discharge profiles displayed in **Figure 3.6c** shows that the Zn|NAF-S-1|MnCP-1 cell achieves a discharge capacity of 420 mAh g⁻¹ (at 0.1 A g⁻¹) in the first cycle, a value that is superior to that of the Zn|NAF-T-1|MnCP-1 cell (**Figure 3.5e**). The charge-discharge profiles of the Zn|NAF-S-1|MnCP-1 cell recorded at different current rates are given in **Figure 3.6d**. At a current rate of 3 A g⁻¹, the same cell could retain 120 mAh g⁻¹ discharge capacity (30% of the obtained capacity at 0.1 A g⁻¹; **Figure 3.6d**). Unlike the 1M Zn(CF₃SO₃)₂, the 1st discharge profile of the Zn|NAF-S-1|MnCP-1 cell appears with a sharp voltage plateau, while two sloping voltage curves are observed in the subsequent cycles (**Figure 3.6d**). According to the recent reports, the single discharge platform in the 1st cycle associates with the phase transformation in the MnO₂ cathode followed by H⁺/Zn²⁺ insertion.^{51, 52} The electrochemical performance of Zn||MnO₂ cell is also recorded in 3M ZnSO₄·7H₂O electrolyte. Note that the preparation of the Zn(CF₃SO₃)₂ electrolyte with the same concentration (3M) is difficult due to the low water solubility of the Zn(CF₃SO₃)₂ salt. Also, considering the high cost, the use of the concentrated electrolyte with Zn(CF₃SO₃)₂ (~18 times more costly than the ZnSO₄ salt) is not economically viable. The CV and GCD plots of the Zn|NAF-S-3|MnCP-1 cell are presented in **Figure 3.6e** and **f**, featuring similar charge storage properties as like in 1M ZnSO₄·7H₂O.

3.3.5 Cycling Stability and Impedance Analysis of Nafion-Based Zn||MnO₂ Cells

The cycling stability of Zn|NAF-T-1|MnCP-1 and Zn|NAF-S-1|MnCP-1 cells was investigated at a current rate of 3 A g⁻¹ (**Figure 3.7a**). The Zn|NAF-T-1|MnCP-1 cell exhibits a discharge capacity of 151 mAh g⁻¹ and retains 89% of the initial capacity after 500 cycles. With continuous cycling, the same cell could still deliver 75% and 69% retention of the initial capacity over 1000 and 1200 stability cycles, respectively. To the best of our knowledge, the Zn|NAF-T-1|MnCP-1 cell surpasses the cycling performance of all the previously reported

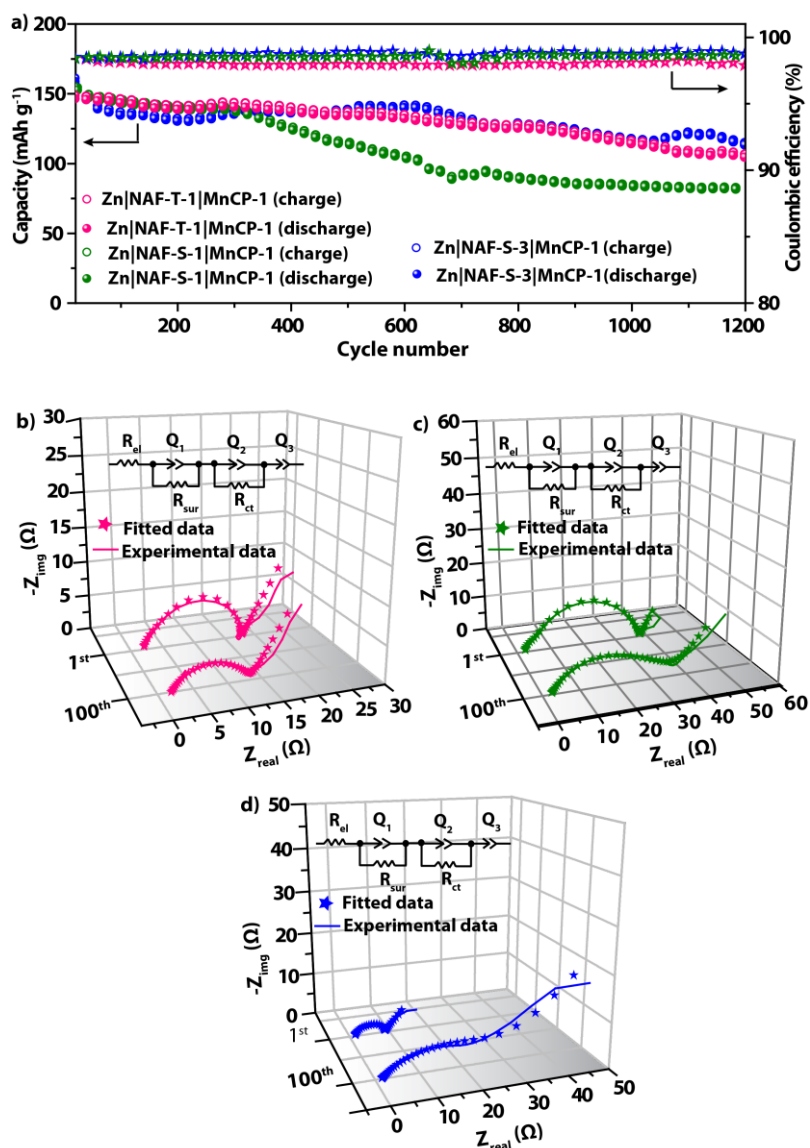


Figure 3.7. (a) Comparison of the cycling stability; impedance plots of the (b) Zn|NAF-T-1|MnCP-1, (c) Zn|NAF-S-1|MnCP-1, and (d) Zn|NAF-S-3|MnCP-1 cells recorded at a discharge voltage of 1.25 V vs. Zn|Zn²⁺ during the 1st and 100th discharge cycles. (Reprinted (adapted) with permission from *ACS Sustainable Chem. Eng.* 2020, 8, 13, 5040–5049). Copyright (2020) American Chemical Society).

single component electrolyte-based Zn||MnO₂ cells (see **Table 3.1**).^{48, 53-55} It can also be noted that the obtained discharge capacity and cyclability of the Zn|NAF-T-1|MnCP-1 cell are superior to many of the reported Mn(II) additive-based Zn||MnO₂ cells, as shown in **Table 3.1**.^{50, 56-59}

At the same time, the discharge capacity obtained for the Zn|NAF-S-1|MnCP-1 cell is 185 mAh g⁻¹. Despite the high initial capacity, in the subsequent cycles, the capacity fading is

Table 3.1. The discharge capacity and cyclic stability of the Zn|NAF-T-1|MnCP-1 cell are compared with some of the manganese oxide based cathodes reported in the literature. (Reprinted (adapted) with permission from (ACS Sustainable Chem. Eng. 2020, 8, 13, 5040–5049). Copyright (2020) American Chemical Society).

Cathode Material	Electrolyte	Discharge capacity	Cycling stability	Ref.
δ -MnO ₂	1M ZnSO ₄	252 mAh g ⁻¹ at 0.083 A g ⁻¹	44% after 100 cycles at 0.083 A g ⁻¹	54
b-MnO ₂	1M ZnSO ₄ (with MnSO ₄)	193 mAh g ⁻¹ at 0.132 A g ⁻¹	75% after 200 cycles at 0.2 A g ⁻¹	57
Ramsdellite MnO ₂	2M ZnSO ₄	200 mAh g ⁻¹ at 0.02 A g ⁻¹	65% after 1000 cycles at 0.1 A g ⁻¹	55
ZnMn ₂ O ₄	3M Zn(CF ₃ SO ₃) ₂	150 mAh g ⁻¹ at 0.05 A g ⁻¹	94% after 500 cycles at 0.5 A g ⁻¹	48
Mn ₃ O ₄	1 M ZnSO ₄ + 1 M MnSO ₄	221 mAh g ⁻¹ at 0.1 A g ⁻¹	92% after 500 cycles at 0.5 A g ⁻¹	56
α -MnO ₂ /graphene scrolls	2 M ZnSO ₄ + 0.2 M MnSO ₄	382.2 mAh g ⁻¹ at 0.3 A g ⁻¹	94% after 3000 cycles at 3 A g ⁻¹	14
MnO ₂ /rGO	2 M ZnSO ₄ + 0.1 M MnSO ₄	332.2 mAh g ⁻¹ at 0.3 A g ⁻¹	96% after 500 cycles at 6 A g ⁻¹	59
ZnMn ₂ O ₄	1 M ZnSO ₄ + 0.05 M MnSO ₄	106.5 mAh g ⁻¹ at 0.1 A g ⁻¹	100% after 300 cycles at 0.1 A g ⁻¹	50
α -MnO ₂	2 M ZnSO ₄ + 0.1 M MnSO ₄	275.2 mAh g ⁻¹ at 1/3 C	86.8% after 140 cycles at 1C	58
CNT-MnO _x @PEDOT	PVA/LiCl–ZnCl ₂ –MnSO ₄ gel	289 mAh g ⁻¹ at 2 mA cm ⁻²	88.7% after 1000 cycles at 20 mA cm ⁻²	23
MnO ₂ @PEDOT	PVA/LiCl–ZnCl ₂ –MnSO ₄ gel	282.4 mA h g ⁻¹ at 0.37 A g ⁻¹	77.7% after 300 cycles at 1.86 A g ⁻¹	10
MnCP-1	NAF-T-1	350 mAh g ⁻¹ at 0.1 A g ⁻¹	69% after 1200 cycles at 3 A g ⁻¹	This work

Table 3.2. Electrolyte resistance, surface resistance and charge transfer resistance of the Zn||MnO₂ cells during the 1st and 100th discharge cycles. (Reprinted (adapted) with permission from (ACS Sustainable Chem. Eng. 2020, 8, 13, 5040–5049). Copyright (2020) American Chemical Society).

Zn MnO ₂ cell	Cycle	R _{el} (Ω)	R _{sur} (Ω)	R _{ct} (Ω)
Zn NAF-T-1 MnCP-1	1 st	1.9	4.1	11.7
Zn NAF-T-1 MnCP-1	100 th	1.8	0.5	11.5
Zn NAF-S-1 MnCP-1	1 st	2.1	2.4	33.1
Zn NAF-S-1 MnCP-1	100 th	2.0	20.0	14.7
Zn NAF-S-3 MnCP-1	1 st	1.2	2.6	4.9
Zn NAF-S-3 MnCP-1	100 th	1.3	4.4	15.9

found to be more prominent, resulting in 61% retention of the initial capacity after the 500 cycles. Nevertheless, followed by the 1200 cycles, the Zn|NAF-S-1|MnCP-1 cell exhibits only 43% of the initial capacity. Interestingly, the Zn||MnO₂ cell with concentrated electrolyte exhibits substantial improvement in capacity retention at the current rate of 3 A g⁻¹. The initial discharge capacity obtained for the Zn|NAF-S-3|MnCP-1 cell is 205 mAh g⁻¹ and it gradually stabilizes to 150 mAh g⁻¹ within 30 charge-discharge cycles. In the following cycles, the capacity drop is reduced, resulting in 112 mAh g⁻¹ capacity after the 1200 charge-discharge cycles (55% retention of its initial capacity and 75% retention of the capacity obtained at the 30th cycle). Despite the initial drop, the overall capacity retention of the Zn|NAF-S-3|MnCP-1 cell is superior compared to that of its 1M ZnSO₄·7H₂O counterpart (**Figure 3.7a**).

EIS analyses are carried out to understand the influence of various electrolytes on the cycle life of the Zn||MnO₂ cells. Impedance spectra are recorded at 1.25 V vs. Zn|Zn²⁺ in the 1st and 100th discharge cycles (**Figure 3.7b-d**). A simple equivalent circuit (**Figure 3.7b-d** inset) is used to fit the impedance spectra, and the obtained resistance values are tabulated in **Table 3.2**. The equivalent circuit consists of the three main components denoted as the bulk resistance (R_{el}), surface resistance (R_{sur}), and charge transfer resistance (R_{ct}). R_{el} is the equivalent series resistance (ESR) of the cell, which is mainly contributed from the ohmic resistance of the electrolyte and cell components. R_{sur} and R_{ct} represent the nature of the SEI layer and resistance to the charge transfer reactions occurring at the electrode|electrolyte

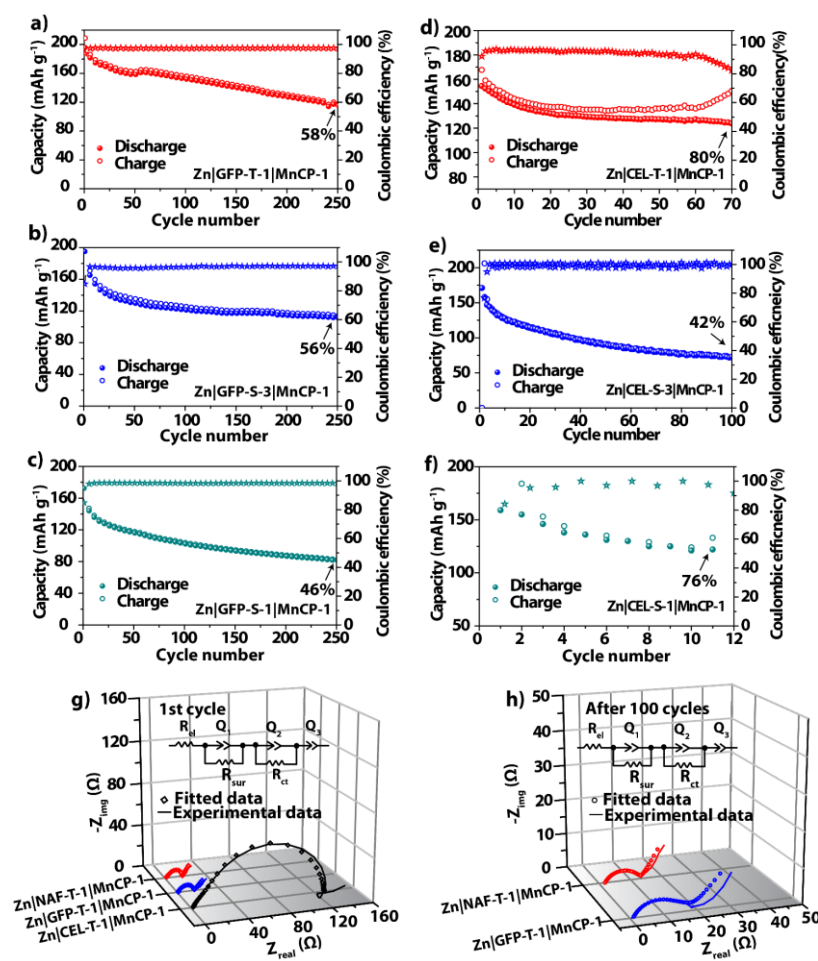


Figure 3.8. Cycling stability data of the (a) Zn|GFP-T-1|MnCP-1, (b) Zn|GFP-S-1|MnCP-1, (c) Zn|GFP-S-3|MnCP-1, (d) Zn|CEL-T-1|MnCP-1, (e) Zn|CEL-S-1|MnCP-1, and (f) Zn|CEL-S-3|MnCP-1 cells; impedance plots of the (g) Zn|NAF-T-1|MnCP-1, Zn|GFP-T-1|MnCP-1 and Zn|CEL-T-1|MnCP-1 cells recorded at 1.25 V vs. Zn|Zn²⁺ during the 1st discharge and (h) impedance plots of the Zn|NAF-T-1|MnCP-1 and Zn|GFP-T-1|MnCP-1 cells after the 100th discharge cycles. (Reprinted (adapted) with permission from *ACS Sustainable Chem. Eng.* 2020, 8, 13, 5040–5049). Copyright (2020) American Chemical Society).

interface, respectively.^{60,61} The overall resistance of the cells ($R_{el} + R_{sur} + R_{ct}$) is represented as R_t .

As given in **Table 3.2**, in the 1st discharge, the R_t values of Zn|NAF-T-1|MnCP-1 (17.7 Ω) and Zn|NAF-S-3|MnCP-1 (8.7 Ω) cell are much lower than that of the Zn|NAF-S-1|MnCP-1 cell (37.6 Ω). Followed by cycling, the R_{sur} of the Zn|NAF-S-1|MnCP-1 cell is increased to 20.0 Ω , a value much higher than those of Zn|NAF-T-1|MnCP-1 (0.5 Ω) and Zn|NAF-S-3|MnCP-1 (4.4 Ω). The higher R_{sur} value indicates the inferior SEI resulting from the low

Table 3.3. Electrolyte resistance, surface resistance and charge transfer resistance of the Zn||MnO₂ cells with porous separators during the 1st and 100th discharge cycles. (Reprinted (adapted) with permission from (ACS Sustainable Chem. Eng. 2020, 8, 13, 5040–5049). Copyright (2020) American Chemical Society).

Zn MnO ₂ cell	Cycle	R _{el} (Ω)	R _{sur} (Ω)	R _{ct} (Ω)
Zn GFP-T-1 MnCP-1	1 st	0.9	5.2	10.0
Zn GFP-T-1 MnCP-1	100 th	0.9	10.5	7.2
Zn CEL-T-1 MnCP-1	1 st	2.1	18.2	109.5

Zn|electrolyte interface stability in 1M ZnSO₄.7H₂O, causing faster degradation of the cell performance (**Figure 3.7a**). The slightly high R_{sur} of the Zn|NAF-S-3|MnCP-1 cell could be responsible for the initial capacity drop in the Zn|NAF-S-3|MnCP-1 cell; however, the percentage increase in the R_{sur} from the 1st to 100th cycles is less than that of 1M ZnSO₄.7H₂O. Hence, the R_{sur} and R_t values suggest that 1M Zn(CF₃SO₃)₂ and 3M ZnSO₄.7H₂O electrolytes offer much better interfacial compatibility with the Zn anode contributing to the stability of the Nafion-based Zn||MnO₂ cells. These results further agree with the plating/stripping overpotential of Zn in the Zn|Zn configuration in the respective electrolytes (**Figure 3.3b**).

3.3.6 Cycling Stability and Impedance Analysis of Porous Separator-Based Zn||MnO₂ Cells

To understand the influence of the Nafion separator, we have carried out the cycling stability experiment of the Zn||MnO₂ cells using two types of porous separators, GFP and CEL (**Figure 3.8a-f**). The initial capacities of the Zn||MnO₂ cells with various separators are more or less comparable. However, compared to the Nafion-based cells, all the porous separators exhibit dramatic deterioration in terms of capacity retention. Over 250 stability cycles, the Zn|GFP-S-1|MnCP-1 cell retains only 46% of its initial capacity, whereas the Zn|GFP-T-1|MnCP-1 and Zn|GFP-S-3|MnCP-1 cells display 58 and 56% capacity retention, respectively (**Figure 3.8a-c**). Nevertheless, capacity retention in the CEL cells are found to be even lower, and all the cells failed after few initial cycles due to the internal short circuit. The Zn|CEL-T-1|MnCP-1, Zn|CEL-S-1|MnCP-1, and Zn|CEL-S-3|MnCP-1 cells deliver 80, 76, and 42% of their initial capacity after the 70, 12, and 100 charge-discharge cycles, respectively (**Figure**

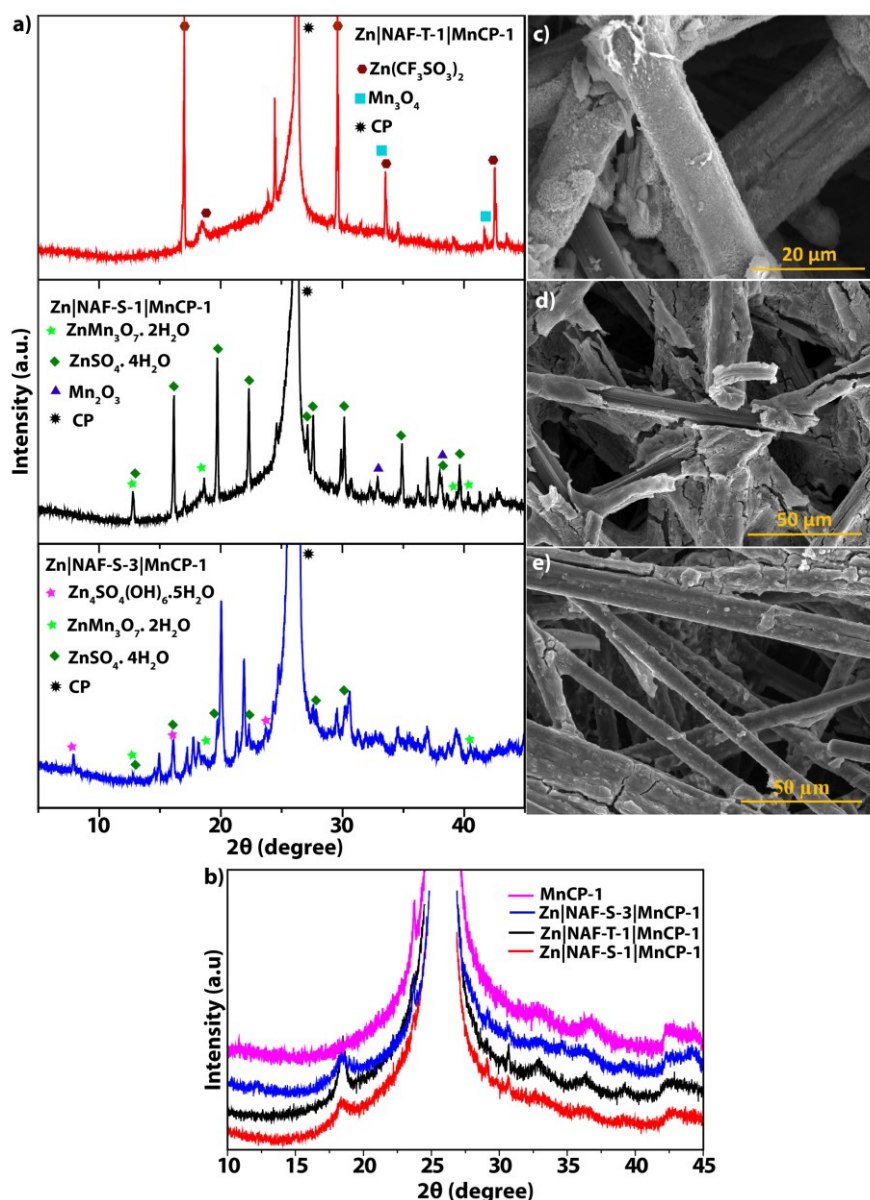


Figure 3.9. (a) XRD profiles of the cycled cathodes recorded before washing; (b) XRD profiles of the cycled cathodes recorded after washing; FESEM image of (c) the Zn|NAF-T-1|MnCP-1 cathode, (d) the Zn|NAF-S-1|MnCP-1 cathode, and (e) the Zn|NAF-S-3|MnCP-1 cathode recorded after the cycling stability test. (Reprinted (adapted) with permission from *ACS Sustainable Chem. Eng.* 2020, 8, 13, 5040–5049). Copyright (2020) American Chemical Society).

3.8d-f). Hence, the above discussion points out the critical role of the ionomer membrane in maintaining the performance of the Zn||MnO₂ cell in the Mn(II) additive-free electrolyte.

The impedance analysis for the Zn||MnO₂ cells is extended to the GFP and CEL separators. As the Zn(CF₃SO₃)₂ electrolyte provides better cycling stability in all the cases, the impedance data with porous separators are taken in 1M Zn(CF₃SO₃)₂, and the related EIS data

are compared in **Figure 3.8g-h** and **Table 3.3**. The R_t of the Zn|GFP-T-1|MnCP-1 cell (16.9 Ω) in the 1st cycle is close to that of the Zn|NAF-T-1|MnCP-1 cell. However, at the 100th cycle, the R_{sur} of the GFP cell is increased to 10.5 Ω , suggesting the formation of the inferior SEI that hampers the transport of Zn^{2+} ions at the Zn|electrolyte interface. On the other hand, the Nyquist plot of the Zn|CEL-T-1|MnCP-1 cell shows an exceptionally high resistance ($R_t = 129 \Omega$) in the 1st cycle. This could be due to the low electrolyte retention capacity of the CEL separator. Nevertheless, we could not compare the change in impedance after cycling of Zn|CEL-T-1|MnCP-1 due to failure of the cell within 80 cycles.

Based on the aforementioned observations, the extraordinary cycle life of the Zn|NAF-T-1|MnCP-1 and Zn|NAF-S-3|MnCP-1 cells is attributed to the influence of the Nafion ionomer separator. In contrast to the conventionally used porous separators, Nafion membrane offers improved interfacial stability to the anode and cathode of the respective cells, which can potentially improve the capacity retention. Additionally, the ionomer separator arrests the diffusion of the undesired discharge side products from the cathode and mitigates the surface poisoning on the anode.

3.3.7 Physical Characterization of the Post-Stability Electrodes

We have investigated the composition of the post-stability cathodes of the Nafion-based Zn||MnO₂ cells using XRD analyses. The XRD data presented in **Figure 3.9a** are taken without any prior washing of the recovered cathodes under consideration. Compared to the pristine MnCP-1 sample (**Figure 3.2g**), the XRD data of the cycled cathodes exhibit several intense peaks, apparently formed due to associated structural changes occurred during the prolonged cycling of the cells. In the case of Zn|NAF-T-1|MnCP-1, the XRD peaks are found to match with that of the $Zn(CF_3SO_3)_2$ salt and Mn₃O₄ (JCPDS 01-075-0765) phase. On the other hand, in the case of Zn|NAF-S-1|MnCP-1, along with the characteristic peaks of the ZnSO₄ salt (JCPDS 00-031-0818), the new peaks found at 12.7, 18.6, 39.4, and 40.3° could be indexed to the woodruffite phase (ZnMn₃O₇·2H₂O, JCPDS 00-047-1825). Few peaks corresponding to the Mn₂O₃ (JCPDS 00-041-1442) phase are also detected in the XRD data.¹⁵ The formation of the woodruffite phase is also evidenced in the XRD profile retrieved from the cathode of the Zn|NAF-S-3|MnCP-1 cell (**Figure 3.9a**). In addition to this, few new peaks appeared at 7.9, 16.0, and 24.3° could be assigned to Zn₄SO₄(OH)₆·5H₂O layered double hydroxide (LDH).⁶² Recently, Kundu *et al.* proposed that the LDH formed on the cathode surface plays a favourable role in maintaining the stable capacity of the Zn||MnO₂ cells, which could be responsible for

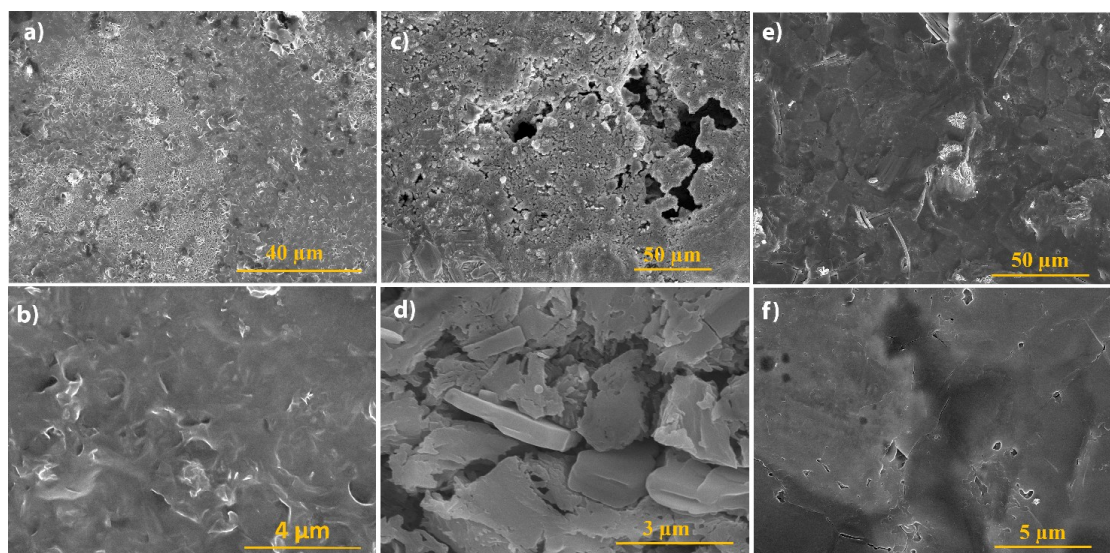


Figure 3.10. FESEM image of the (a)-(b) Zn|NAF-T-1|MnCP-1 anode, (c)-(d) Zn|NAF-S-1|MnCP-1 anode, and (e)-(f) Zn|NAF-S-3|MnCP-1 anode after the cycling stability test. (Reprinted (adapted) with permission from (ACS Sustainable Chem. Eng. 2020, 8, 13, 5040–5049). Copyright (2020) American Chemical Society).

better cycling stability of the Zn|NAF-S-3|MnCP-1 cell.⁶³ It is interesting to note that the peaks related to the woodruffite phase are absent in the Zn|NAF-T-1|MnCP-1 cell. This indicates the influence of the electrolytes in directing the structural changes in the cathode of the Zn||MnO₂ cells.

The XRD data associated with the post-stability cathodes followed by washing (with water) are also collected and compared with the pristine MnCP-1 sample (**Figure 3.9b**). Interestingly, in the case of ZnSO₄ and Zn(CF₃SO₃)₂ salt-based cells, the XRD profiles overlap with each other. This in turn indicates that the structural changes mostly took place at the surface of the electrode material, whereas the bulk remains more or less similar to the pristine electrode, except for the three new peaks observed at 18.5, 30.5, and 39.1°. Despite the aforementioned similarity, the difference in the electrochemical performance indicates that the side reactions occurring at the electrode surface are rather important in line with determining the stability of the Zn||MnO₂ cells.

Apart from the change in the electrode composition, the morphological changes on the electrode surface are also an important factor influencing the cycling stability of the electrochemical cells. In the following sections, we have discussed the change in morphology of both the cathode (**Figure 3.9c-e**) and anode (**Figure 3.10a-f**) of the post-stability cells through FESEM analyses. The FESEM images are taken after washing the respective

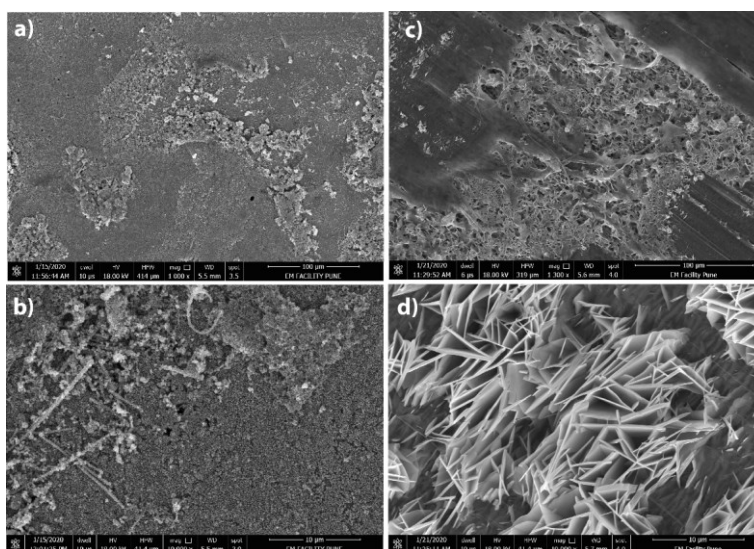


Figure 3.11. FESEM images of the post-stability zinc anodes recovered from the (a)-(b) Zn|GFP-T-1|MnCP-1 and (c)-(d) Zn|CEL-T-1|MnCP-1 cells. (Reprinted (adapted) with permission from (ACS Sustainable Chem. Eng. 2020, 8, 13, 5040–5049). Copyright (2020) American Chemical Society).

electrodes to avoid any interference from the precipitated electrolyte salt or other side reaction products present on the surface. As seen in **Figure 3.9c**, no obvious structural change is observed in the Zn|NAF-T-1|MnCP-1 cathode, and the contact between the electrode material and carbon fibers remains unaffected during the cycling. On the contrary, the FESEM image of the Zn|NAF-S-1|MnCP-1 cathode (**Figure 3.9d**) reveals a significant number of cracks and fractures causing detachment of the active material from the carbon fiber skeleton. The disconnection between the active material and conductive support hinders the Zn^{2+} uptake in the cathode of the Zn|NAF-S-1|MnCP-1 cell, which could deteriorate the battery life. The cathode morphology in the concentrated ZnSO_4 electrolyte (Zn|NAF-S-3|MnCP-1 cathode) looks (**Figure 3.9e**) more or less similar to that of the Zn|NAF-T-1|MnCP-1 cell. This suggests the superiority of $\text{Zn}(\text{CF}_3\text{SO}_3)_2$ and concentrated ZnSO_4 electrolytes over the low-concentrated ZnSO_4 counterpart.

Later, the morphology of the post-cycled Zn anode of all the three cells is also compared. As shown in **Figure 3.10a** and **b**, the surface of the Zn|NAF-T-1|MnCP-1 anode looks smooth and dense, which is similar to the commercial Zn foil (**Chapter 2, Figure 2.7a**). The absence of any obvious protrusion indicates the uniform plating of Zn during cycling in 1M $\text{Zn}(\text{CF}_3\text{SO}_3)_2$, whereas the Zn|NAF-S-1|MnCP-1 anode consists of a significant number of protruded Zn deposits (**Figure 3.10c** and **d**) and microscale cracks, which are responsible for the origin of the porous Zn surface with large holes (**Figure 3.10c**). The evolution of such a

non-uniform surface and numerous grain boundaries impedes the reversible electrochemical reactions occurring at the Zn|electrolyte interface.

Despite the presence of the Nafion ionomer separator, the undesired morphology (**Figure 3.10d**) of the Zn anode as observed in Zn|NAF-S-1|MnCP-1 cell is responsible for the higher voltage polarization during the plating/stripping of Zn (**Figure 3.3b**). Also, a low concentration of the electrolyte induces the Zn^{2+} ion concentration gradient near to the anode surface, resulting in localized deposition of Zn. This effect is believed to be mitigated in the concentrated electrolyte,⁶⁴ which is indeed confirmed from the smooth and dendrite-free surface of the Zn|NAF-S-3|MnCP-1 anode (**Figure 3.10e** and **f**). Therefore, it is reasonable to say that the difference in the electrode morphology evolved during the prolong cycling is the critical reason for the different cycle life displayed by the Nafion-based Zn||MnO₂ cells under study.

For comparison, post-cycling morphology of the Zn metal surface coupled with GFP and CEL separators are also characterized by FESEM analyses. The uneven and rough surface of Zn is clearly evident in **Figure 3.11a-d**. It is worth mentioning that, in the case of the porous separators, such a morphology evolved just after few initial charge-discharge cycles. While the Zn anode coupled with the NAF-T-1 or NAF-S-3 electrolyte maintains an almost flat surface, the flake-like deposits with sharp edges are observed with the CEL-T-1 and CEL-S-3 electrolytes (**Figure 3.11c** and **d**). At the same time, the granular and flaky morphology on the Zn surface of the GFP-based cells is also evident (**Figure 3.11a** and **b**). This indicates that the favourable surface structure evolution on the anode surface, as in the case of Nafion, promotes the improved cycle life and reduced cell resistance compared to the GFP and CEL separator-based Zn||MnO₂ cells.

3.4 Conclusions

In conclusion, this study shows the remarkable performance of the Zn||MnO₂ cells in single component electrolytes or, in other words, Mn(II) salt-free electrolytes by utilizing the Nafion ionomer separator. The improved stability of the Nafion-based cells originates from the suppression of the Zn dendrite growth compared to the traditional GFP or CEL separators. Also, compared to 1M ZnSO₄·7H₂O, 1M Zn(CF₃SO₃)₂, and 3M ZnSO₄·7H₂O offer the evolution of dendrite-free anode morphology and at the same time preserving the structural integrity of cathode. This in turn helps in achieving longer cycle life of the Zn||MnO₂ cell with 75% retention of capacity over 1000 cycles. Unlike the existing ARZMB reports emphasizing the importance of Mn(II) salts in the Zn||MnO₂ cells, this work directs an alternate way to

realize the long cycle life of the Zn||MnO₂ cells in the absence of any electrolyte additive. The results provide significant evidence that an ionomer membrane along with an appropriate Zn²⁺ ion conducting electrolyte is effective in maintaining the desired structural evolution of the electrodes and preventing the capacity loss of the Zn||MnO₂ cell.

3.5 References

- (1) Balakrishnan, P. G.; Ramesh, R.; Prem Kumar, T. Safety mechanisms in lithium-ion batteries. *Journal of Power Sources* **2006**, *155*, 401-414.
- (2) Yang, C.; Chen, J.; Qing, T.; Fan, X.; Sun, W.; von Cresce, A.; Ding, M. S.; Borodin, O.; Vatamanu, J.; Schroeder, M. A.; Eidson, N.; Wang, C.; Xu, K. 4.0 V Aqueous Li-Ion Batteries. *Joule* **2017**, *1*, 122-132.
- (3) Suo, L.; Borodin, O.; Gao, T.; Olguin, M.; Ho, J.; Fan, X.; Luo, C.; Wang, C.; Xu, K. “Water-in-salt” electrolyte enables high-voltage aqueous lithium-ion chemistries. *Science* **2015**, *350*, 938-943.
- (4) Suo, L.; Borodin, O.; Wang, Y.; Rong, X.; Sun, W.; Fan, X.; Xu, S.; Schroeder, M. A.; Cresce, A. V.; Wang, F.; Yang, C.; Hu, Y.-S.; Xu, K.; Wang, C. “Water-in-Salt” Electrolyte Makes Aqueous Sodium-Ion Battery Safe, Green, and Long-Lasting. *Advanced Energy Materials* **2017**, *7*, 1701189.
- (5) Selvakumaran, D.; Pan, A.; Liang, S.; Cao, G. A review on recent developments and challenges of cathode materials for rechargeable aqueous Zn-ion batteries. *Journal of Materials Chemistry A* **2019**, *7*, 18209-18236.
- (6) Chen, S.; Zhang, Y.; Geng, H.; Yang, Y.; Rui, X.; Li, C. C. Zinc ions pillared vanadate cathodes by chemical pre-intercalation towards long cycling life and low-temperature zinc ion batteries. *Journal of Power Sources* **2019**, *441*, 227192.
- (7) Hu, P.; Zhu, T.; Wang, X.; Wei, X.; Yan, M.; Li, J.; Luo, W.; Yang, W.; Zhang, W.; Zhou, L.; Zhou, Z.; Mai, L. Highly Durable Na₂V₆O₁₆·1.63H₂O Nanowire Cathode for Aqueous Zinc-Ion Battery. *Nano Letters* **2018**, *18*, 1758-1763.
- (8) Ming, J.; Guo, J.; Xia, C.; Wang, W.; Alshareef, H. N. Zinc-ion batteries: Materials, mechanisms, and applications. *Materials Science and Engineering: R: Reports* **2019**, *135*, 58-84.
- (9) Xu, C.; Li, B.; Du, H.; Kang, F. Energetic Zinc Ion Chemistry: The Rechargeable Zinc Ion Battery. *Angewandte Chemie International Edition* **2012**, *51*, 933-935.

- (10) Zeng, Y.; Zhang, X.; Meng, Y.; Yu, M.; Yi, J.; Wu, Y.; Lu, X.; Tong, Y. Achieving Ultrahigh Energy Density and Long Durability in a Flexible Rechargeable Quasi-Solid-State Zn–MnO₂ Battery. *Advanced Materials* **2017**, *29*, 1700274.
- (11) Fang, G.; Zhou, J.; Pan, A.; Liang, S. Recent Advances in Aqueous Zinc-Ion Batteries. *ACS Energy Letters* **2018**, *3*, 2480-2501.
- (12) Pan, H.; Shao, Y.; Yan, P.; Cheng, Y.; Han, K. S.; Nie, Z.; Wang, C.; Yang, J.; Li, X.; Bhattacharya, P.; Mueller, K. T.; Liu, J. Reversible aqueous zinc/manganese oxide energy storage from conversion reactions. *Nature Energy* **2016**, *1*, 16039.
- (13) Zhang, N.; Cheng, F.; Liu, J.; Wang, L.; Long, X.; Liu, X.; Li, F.; Chen, J. Rechargeable aqueous zinc-manganese dioxide batteries with high energy and power densities. *Nature Communications* **2017**, *8*, 405.
- (14) Wu, B.; Zhang, G.; Yan, M.; Xiong, T.; He, P.; He, L.; Xu, X.; Mai, L. Graphene Scroll-Coated α -MnO₂ Nanowires as High-Performance Cathode Materials for Aqueous Zn-Ion Battery. *Small* **2018**, *14*, 1703850.
- (15) Huang, Y.; Mou, J.; Liu, W.; Wang, X.; Dong, L.; Kang, F.; Xu, C. Novel Insights into Energy Storage Mechanism of Aqueous Rechargeable Zn/MnO₂ Batteries with Participation of Mn²⁺. *Nano-Micro Letters* **2019**, *11*, 49.
- (16) Li, H.; Ma, L.; Han, C.; Wang, Z.; Liu, Z.; Tang, Z.; Zhi, C. Advanced rechargeable zinc-based batteries: Recent progress and future perspectives. *Nano Energy* **2019**, *62*, 550-587.
- (17) Qiu, N.; Chen, H.; Yang, Z.; Sun, S.; Wang, Y. Synthesis of manganese-based complex as cathode material for aqueous rechargeable batteries. *RSC Advances* **2018**, *8*, 15703-15708.
- (18) Li, Y.; Wang, S.; Salvador, J. R.; Wu, J.; Liu, B.; Yang, W.; Yang, J.; Zhang, W.; Liu, J.; Yang, J. Reaction Mechanisms for Long-Life Rechargeable Zn/MnO₂ Batteries. *Chemistry of Materials* **2019**, *31*, 2036-2047.
- (19) Poyraz, A. S.; Laughlin, J.; Zec, Z. Improving the cycle life of cryptomelane type manganese dioxides in aqueous rechargeable zinc ion batteries: The effect of electrolyte concentration. *Electrochimica Acta* **2019**, *305*, 423-432.
- (20) Zhao, S.; Han, B.; Zhang, D.; Huang, Q.; Xiao, L.; Chen, L.; Ivey, D. G.; Deng, Y.; Wei, W. Unravelling the reaction chemistry and degradation mechanism in aqueous Zn/MnO₂ rechargeable batteries. *Journal of Materials Chemistry A* **2018**, *6*, 5733-5739.

- (21) Kang, L.; Cui, M.; Jiang, F.; Gao, Y.; Luo, H.; Liu, J.; Liang, W.; Zhi, C. Nanoporous CaCO_3 Coatings Enabled Uniform Zn Stripping/Plating for Long-Life Zinc Rechargeable Aqueous Batteries. *Advanced Energy Materials* **2018**, *8*, 1801090.
- (22) Wang, L.-P.; Li, N.-W.; Wang, T.-S.; Yin, Y.-X.; Guo, Y.-G.; Wang, C.-R. Conductive graphite fiber as a stable host for zinc metal anodes. *Electrochimica Acta* **2017**, *244*, 172-177.
- (23) Zeng, Y.; Zhang, X.; Qin, R.; Liu, X.; Fang, P.; Zheng, D.; Tong, Y.; Lu, X. Dendrite-Free Zinc Deposition Induced by Multifunctional CNT Frameworks for Stable Flexible Zn-Ion Batteries. *Advanced Materials* **2019**, *31*, 1903675.
- (24) Zhao, Q.; Huang, W.; Luo, Z.; Liu, L.; Lu, Y.; Li, Y.; Li, L.; Hu, J.; Ma, H.; Chen, J. High-capacity aqueous zinc batteries using sustainable quinone electrodes. *Science Advances* **2018**, *4*, eaao1761.
- (25) Zhan, C.; Lu, J.; Jeremy Kropf, A.; Wu, T.; Jansen, A. N.; Sun, Y.-K.; Qiu, X.; Amine, K. Mn(II) deposition on anodes and its effects on capacity fade in spinel lithium manganate–carbon systems. *Nature Communications* **2013**, *4*, 2437.
- (26) Ghosh, M.; Vijayakumar, V.; Kurungot, S. Dendrite Growth Suppression by Zn^{2+} -Integrated Nafion Ionomer Membranes: Beyond Porous Separators toward Aqueous Zn/ V_2O_5 Batteries with Extended Cycle Life. *Energy Technology* **2019**, *7*, 1900442.
- (27) Banerjee, R.; Khayum M, A.; Ghosh, M.; Vijayakumar, V.; Halder, A.; Nurhuda, M.; Addicoat, M. A.; Kurungot, S.; Kumar, S. Zinc Ion Interactions in a Two-Dimensional Covalent Organic Framework based Aqueous Zinc Ion Battery. *Chemical Science* **2019**, *10*, 8889-8894.
- (28) Abraham, K. M.; Jiang, Z.; Carroll, B. Highly Conductive PEO-like Polymer Electrolytes. *Chemistry of Materials* **1997**, *9*, 1978-1988.
- (29) Vijayakumar, V.; Diddens, D.; Heuer, A.; Kurungot, S.; Winter, M.; Nair, J. R. Dioxolanone-Anchored Poly(allyl ether)-Based Cross-Linked Dual-Salt Polymer Electrolytes for High-Voltage Lithium Metal Batteries. *ACS Applied Materials & Interfaces* **2020**, *12*, 567-579.
- (30) Li, Z.; Wang, J.; Liu, X.; Liu, S.; Ou, J.; Yang, S. Electrostatic layer-by-layer self-assembly multilayer films based on graphene and manganese dioxide sheets as novel electrode materials for supercapacitors. *Journal of Materials Chemistry* **2011**, *21*, 3397-3403.

- (31) Toupin, M.; Brousse, T.; Bélanger, D. Charge Storage Mechanism of MnO₂ Electrode Used in Aqueous Electrochemical Capacitor. *Chemistry of Materials* **2004**, *16*, 3184-3190.
- (32) Li, N.-W.; Yin, Y.-X.; Li, J.-Y.; Zhang, C.-H.; Guo, Y.-G. Passivation of Lithium Metal Anode via Hybrid Ionic Liquid Electrolyte toward Stable Li Plating/Stripping. *Advanced Science* **2017**, *4*, 1600400.
- (33) Song, M.; Tan, H.; Chao, D.; Fan, H. J. Recent Advances in Zn-Ion Batteries. *Advanced Functional Materials* **2018**, *28*, 1802564.
- (34) Shah, D. B.; Olson, K. R.; Karny, A.; Mecham, S. J.; DeSimone, J. M.; Balsara, N. P. Effect of anion size on conductivity and transference number of perfluoroether electrolytes with lithium salts. *Journal of The Electrochemical Society* **2017**, *164*, A3511-A3517.
- (35) Vijayakumar, V.; Ghosh, M.; Torris A. T, A.; M. K, N. C.; Nair, S. B.; Badiger, M. V.; Kurungot, S. Water-in-Acid Gel Polymer Electrolyte Realized through a Phosphoric Acid-Enriched Polyelectrolyte Matrix toward Solid-State Supercapacitors. *ACS Sustainable Chemistry & Engineering* **2018**, *6*, 12630-12640.
- (36) Aziz, S. B.; Woo, T. J.; Kadir, M. F. Z.; Ahmed, H. M. A conceptual review on polymer electrolytes and ion transport models. *Journal of Science: Advanced Materials and Devices* **2018**, *3*, 1-17.
- (37) Lu, Y.; Tikekar, M.; Mohanty, R.; Hendrickson, K.; Ma, L.; Archer, L. A. Stable Cycling of Lithium Metal Batteries Using High Transference Number Electrolytes. *Advanced Energy Materials* **2015**, *5*, 1402073.
- (38) Zhang, L.; Rodríguez-Pérez, I. A.; Jiang, H.; Zhang, C.; Leonard, D. P.; Guo, Q.; Wang, W.; Han, S.; Wang, L.; Ji, X. ZnCl₂ “Water-in-Salt” Electrolyte Transforms the Performance of Vanadium Oxide as a Zn Battery Cathode. *Advanced Functional Materials* **2019**, *29*, 1902653.
- (39) Bieker, G.; Winter, M.; Bieker, P. Electrochemical in situ investigations of SEI and dendrite formation on the lithium metal anode. *Physical Chemistry Chemical Physics* **2015**, *17*, 8670-8679.
- (40) Hoang, T. K. A.; Doan, T. N. L.; Sun, K. E. K.; Chen, P. Corrosion chemistry and protection of zinc & zinc alloys by polymer-containing materials for potential use in rechargeable aqueous batteries. *RSC Advances* **2015**, *5*, 41677-41691.

- (41) Wang, J.; Polleux, J.; Lim, J.; Dunn, B. Pseudocapacitive Contributions to Electrochemical Energy Storage in TiO₂ (Anatase) Nanoparticles. *The Journal of Physical Chemistry C* **2007**, *111*, 14925-14931.
- (42) Lindström, H.; Södergren, S.; Solbrand, A.; Rensmo, H.; Hjelm, J.; Hagfeldt, A.; Lindquist, S.-E. Li⁺ Ion Insertion in TiO₂ (Anatase). 2. Voltammetry on Nanoporous Films. *The Journal of Physical Chemistry B* **1997**, *101*, 7717-7722.
- (43) Geng, H.; Cheng, M.; Wang, B.; Yang, Y.; Zhang, Y.; Li, C. C. Electronic Structure Regulation of Layered Vanadium Oxide via Interlayer Doping Strategy toward Superior High-Rate and Low-Temperature Zinc-Ion Batteries. *Advanced Functional Materials*, *n/a*, 1907684.
- (44) Yu, P.; Li, C.; Guo, X. Sodium Storage and Pseudocapacitive Charge in Textured Li₄Ti₅O₁₂ Thin Films. *The Journal of Physical Chemistry C* **2014**, *118*, 10616-10624.
- (45) Anothumakkool, B.; Kurungot, S. Electrochemically grown nanoporous MnO₂ nanowalls on a porous carbon substrate with enhanced capacitance through faster ionic and electrical mobility. *Chemical Communications* **2014**, *50*, 7188-7190.
- (46) Huang, M.; Li, F.; Dong, F.; Zhang, Y. X.; Zhang, L. L. MnO₂-based nanostructures for high-performance supercapacitors. *Journal of Materials Chemistry A* **2015**, *3*, 21380-21423.
- (47) Wang, J.-G.; Yang, Y.; Huang, Z.-H.; Kang, F. Coaxial carbon nanofibers/MnO₂ nanocomposites as freestanding electrodes for high-performance electrochemical capacitors. *Electrochimica Acta* **2011**, *56*, 9240-9247.
- (48) Zhang, N.; Cheng, F.; Liu, Y.; Zhao, Q.; Lei, K.; Chen, C.; Liu, X.; Chen, J. Cation-Deficient Spinel ZnMn₂O₄ Cathode in Zn(CF₃SO₃)₂ Electrolyte for Rechargeable Aqueous Zn-Ion Battery. *Journal of the American Chemical Society* **2016**, *138*, 12894-12901.
- (49) Guo, X.; Li, J.; Jin, X.; Han, Y.; Lin, Y.; Lei, Z.; Wang, S.; Qin, L.; Jiao, S.; Cao, R. A Hollow-Structured Manganese Oxide Cathode for Stable Zn-MnO₂ Batteries. *Nanomaterials (Basel)* **2018**, *8*, 301.
- (50) Wu, X.; Xiang, Y.; Peng, Q.; Wu, X.; Li, Y.; Tang, F.; Song, R.; Liu, Z.; He, Z.; Wu, X. Green-low-cost rechargeable aqueous zinc-ion batteries using hollow porous spinel ZnMn₂O₄ as the cathode material. *Journal of Materials Chemistry A* **2017**, *5*, 17990-17997.

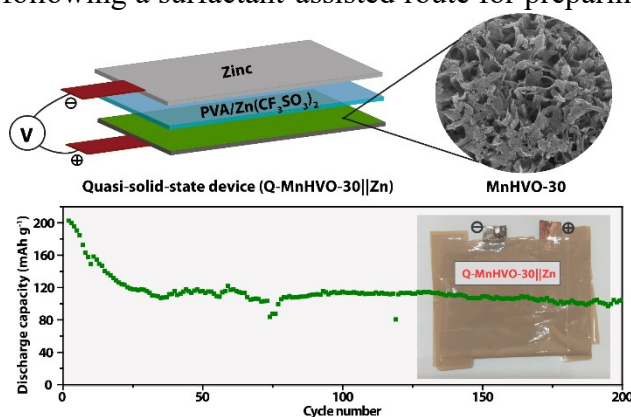
- (51) Lee, B.; Lee, H. R.; Kim, H.; Chung, K. Y.; Cho, B. W.; Oh, S. H. Elucidating the intercalation mechanism of zinc ions into α -MnO₂ for rechargeable zinc batteries. *Chemical Communications* **2015**, *51*, 9265-9268.
- (52) Alfaruqi, M. H.; Mathew, V.; Gim, J.; Kim, S.; Song, J.; Baboo, J. P.; Choi, S. H.; Kim, J. Electrochemically Induced Structural Transformation in a γ -MnO₂ Cathode of a High Capacity Zinc-Ion Battery System. *Chemistry of Materials* **2015**, *27*, 3609-3620.
- (53) Alfaruqi, M. H.; Islam, S.; Putro, D. Y.; Mathew, V.; Kim, S.; Jo, J.; Kim, S.; Sun, Y.-K.; Kim, K.; Kim, J. Structural transformation and electrochemical study of layered MnO₂ in rechargeable aqueous zinc-ion battery. *Electrochimica Acta* **2018**, *276*, 1-11.
- (54) Alfaruqi, M. H.; Gim, J.; Kim, S.; Song, J.; Pham, D. T.; Jo, J.; Xiu, Z.; Mathew, V.; Kim, J. A layered δ -MnO₂ nanoflake cathode with high zinc-storage capacities for eco-friendly battery applications. *Electrochemistry Communications* **2015**, *60*, 121-125.
- (55) Stoševski, I.; Bonakdarpour, A.; Cuadra, F.; Wilkinson, D. P. Highly crystalline ramsdellite as a cathode material for near-neutral aqueous MnO₂/Zn batteries. *Chemical Communications* **2019**, *55*, 2082-2085.
- (56) Wang, L.; Cao, X.; Xu, L.; Chen, J.; Zheng, J. Transformed Akhtenskite MnO₂ from Mn₃O₄ as Cathode for a Rechargeable Aqueous Zinc Ion Battery. *ACS Sustainable Chemistry & Engineering* **2018**, *6*, 16055-16063.
- (57) Islam, S.; Alfaruqi, M. H.; Mathew, V.; Song, J.; Kim, S.; Kim, S.; Jo, J.; Baboo, J. P.; Pham, D. T.; Putro, D. Y.; Sun, Y.-K.; Kim, J. Facile synthesis and the exploration of the zinc storage mechanism of β -MnO₂ nanorods with exposed (101) planes as a novel cathode material for high performance eco-friendly zinc-ion batteries. *Journal of Materials Chemistry A* **2017**, *5*, 23299-23309.
- (58) Dong, W.; Shi, J.-L.; Wang, T.-S.; Yin, Y.-X.; Wang, C.-R.; Guo, Y.-G. 3D zinc@carbon fiber composite framework anode for aqueous Zn–MnO₂ batteries. *RSC Advances* **2018**, *8*, 19157-19163.
- (59) Huang, Y.; Liu, J.; Huang, Q.; Zheng, Z.; Hiralal, P.; Zheng, F.; Ozgit, D.; Su, S.; Chen, S.; Tan, P.-H.; Zhang, S.; Zhou, H. Flexible high energy density zinc-ion batteries enabled by binder-free MnO₂/reduced graphene oxide electrode. *npj Flexible Electronics* **2018**, *2*, 21.
- (60) Gao, X.-W.; Deng, Y.-F.; Wexler, D.; Chen, G.-H.; Chou, S.-L.; Liu, H.-K.; Shi, Z.-C.; Wang, J.-Z. Improving the electrochemical performance of the LiNi_{0.5}Mn_{1.5}O₄ spinel by polypyrrole coating as a cathode material for the lithium-ion battery. *Journal of Materials Chemistry A* **2015**, *3*, 404-411.

-
- (61) Liu, F.; Chen, Z.; Fang, G.; Wang, Z.; Cai, Y.; Tang, B.; Zhou, J.; Liang, S. V_2O_5 nanospheres with mixed vanadium valences as high electrochemically active aqueous zinc-ion battery cathode. *Nano-Micro Letters* **2019**, *11*, 25.
- (62) Jin, Y.; Zou, L.; Liu, L.; Engelhard, M. H.; Patel, R. L.; Nie, Z.; Han, K. S.; Shao, Y.; Wang, C.; Zhu, J.; Pan, H.; Liu, J. Joint Charge Storage for High-Rate Aqueous Zinc–Manganese Dioxide Batteries. *Advanced Materials* **2019**, *31*, 1900567.
- (63) Oberholzer, P.; Tervoort, E.; Bouzid, A.; Pasquarello, A.; Kundu, D. Oxide versus Nonoxide Cathode Materials for Aqueous Zn Batteries: An Insight into the Charge Storage Mechanism and Consequences Thereof. *ACS Applied Materials & Interfaces* **2019**, *11*, 674-682, DOI: 10.1021/acsami.8b16284.
- (64) Jeong, S.-K.; Seo, H.-Y.; Kim, D.-H.; Han, H.-K.; Kim, J.-G.; Lee, Y. B.; Iriyama, Y.; Abe, T.; Ogumi, Z. Suppression of dendritic lithium formation by using concentrated electrolyte solutions. *Electrochemistry Communications* **2008**, *10*, 635-638.

Chapter 4

Scalable Synthesis of Manganese-Doped Hydrated Vanadium Oxide as a Cathode Material for Aqueous Zinc-Metal Battery

Aqueous rechargeable aqueous zinc-metal batteries (ARZMBs) are considered as the potential energy storage devices for stationary applications. Despite the significant developments in recent years, the performance of ARZMBs is still limited due to the lack of advanced cathode materials delivering high capacity and long cycle life. In this work, we report a low-temperature and scalable synthesis method following a surfactant-assisted route for preparing manganese-doped hydrated vanadium oxide (MnHVO-30) and its application as the cathode material for ARZMB. The as-prepared material possesses a porous architecture and expanded interlayer spacing. Therefore, MnHVO-30 cathode offers fast and reversible insertion of Zn^{2+} ions during the charge/discharge process and delivers 341 mAh g^{-1} capacity at 0.1 A g^{-1} . Moreover, the $\text{Zn}||\text{MnHVO-30}$ cell retains 82% of its initial capacity over 1200 stability cycles, which is higher compared to that of the undoped system. Besides, a quasi-solid-state home-made pouch cell with an area of $3.3 \times 1.6 \text{ cm}^2$ and 3.6 mg cm^{-2} loading is assembled, achieving 115 mAh g^{-1} capacity over 100 stability cycles. Therefore, this work provides an easy and attractive way for preparing efficient cathode materials for aqueous ARZMBs.



Contents of this chapter is published in the article: DOI: 10.1021/acsami.0c13221.

Reprinted (adapted) with permission from ACS Appl. Mater. Interfaces 2020, 12, 43, 48542–48552. Copyright (2020) American Chemical Society.

4.1 Introduction

In recent years, multivalent ion-based aqueous batteries (such as Zn^{2+} , Mg^{2+} , and Al^{3+}) are receiving immense research interest because of their high capacity, easy fabrication, and inherent safety.^{1,2} Aqueous rechargeable zinc-metal batteries (ARZMBs) comprising metallic zinc as the anode and a Zn^{2+} ion insertion cathode in mild aqueous zinc-ion conducting electrolytes are at the forefront of next-generation aqueous batteries. Considering the high theoretical capacity of metallic zinc (820 mAh g^{-1}), ARZMBs have the potential to surpass the energy density of graphite anode (theoretical capacity of $\approx 380 \text{ mAh g}^{-1}$)-based commercial lithium-ion batteries.³⁻⁵ However, like the other electrochemical devices, the advancement of ARZMBs requires the development of suitable electrolyte, electrode materials, separator, and cell-fabrication techniques. Although significant efforts have already been made toward this direction, unfortunately, the overall performance of ARZMBs in terms of capacity, cell voltage, and cycle life is still inadequate to meet the commercial need.

To date, several inorganic and organic compounds have been demonstrated as efficient hosts for the Zn^{2+} ion, *viz.*, vanadium oxide, manganese oxide, Prussian blue analogues, conducting polymers, and so on.⁶⁻¹⁰ The performance of ARZMBs constructed with different cathodes depends on the nature of the redox centre, the number of electron transfer during the faradaic reactions, reaction kinetics, and the associated reaction mechanism involving the participation of Zn^{2+} and/or H^+ ions.¹¹ For instance, the average discharge-voltage plateau for manganese oxide often appears at $1.25 \text{ V vs. Zn|Zn}^{2+}$ with a specific capacity of $200\text{--}300 \text{ mAh g}^{-1}$.⁴ Despite the high capacity and average voltage, manganese oxide experiences low capacity retention due to the dissolution of active material and irreversible phase transition during battery cycling.¹² Zn^{2+} insertion in the Prussian blue analogue occurs at an even higher voltage ($\sim 1.5 \text{ V vs. Zn|Zn}^{2+}$); however, the maximum discharge capacity obtained with this material is only around 65 mAh g^{-1} .⁹ Furthermore, the cathode materials based on vanadium oxides exhibit an average voltage at $0.80 \text{ V vs. Zn|Zn}^{2+}$.¹³ However, the high specific capacity offered by the multiple oxidation states of vanadium (+5, +4, and +3) as well as the excellent structural stability for >1000 charge/discharge cycles makes them attractive cathodes for ARZMBs.¹⁴ Similarly, polyaniline and organic molecules are also found to deliver good capacity. Still, they often suffer from a low voltage plateau and inferior cycle life.^{15,16} In short, designing of a ARZMB cathode with high capacity, cell voltage, and long lifespan is still challenging.

Hydrated vanadium oxides (HVOs), which are layered-type compounds, have been recently employed as cathode materials in ARZMBs. The HVO structure consists of water molecules intercalated between the two-dimensional V_2O_5 layers with large interlayer spacing

ranging from 8.8 Å to 13.8 Å.¹⁷ These water molecules reduce the electrostatic interaction between the bivalent Zn^{2+} and the host lattice, ensuring the resilience of the electrode material against the back and forth movement of Zn^{2+} ions across the layered framework. In a recent report, Yan *et al.* have demonstrated that the intercalated water molecules in the $\text{V}_2\text{O}_5 \cdot n\text{H}_2\text{O}$ lattice lubricate the insertion of the Zn^{2+} ion, showing excellent electrochemical stability.¹⁸ Various strategies have been developed to reinforce the electrochemical performance of HVOs. These include designing nanostructured HVOs, tuning the interlayer spacing, and integrating with carbon materials. Zhang *et al.* have reported electrodeposition of $\text{V}_5\text{O}_{12} \cdot 6\text{H}_2\text{O}$ with 1.18 nm interlayer spacing delivering a Zn^{2+} storage capacity of 354.8 mAh g^{-1} .¹⁹ The preinsertion of foreign cations (*viz.*, Mn^{2+} , Co^{2+} , Na^+ , Ca^{2+} , Al^{3+} , *etc.*) into the HVO lattice could tune the interlayer spacing, resulting in better stability of the host framework.²⁰⁻²³ It is observed that the Al-doped $\text{V}_{10}\text{O}_{24} \cdot 12\text{H}_2\text{O}$ cathode could retain 98% of the initial capacity of over 3000 cycles, which is significantly higher than that of the undoped $\text{V}_{10}\text{O}_{24} \cdot 12\text{H}_2\text{O}$ (68% retention).²⁴ Cao *et al.* have reported remarkable improvement in the cycling stability of the HVO cathode by chemically inserting Mn^{2+} ions into the HVO lattice.²⁵ However, the complex and multistep synthesis methods involving hydrothermal treatment, high-temperature annealing, *etc.*, make them unsuited for large-scale production. Therefore, the development of the facile and green synthesis of nanostructured HVOs is indeed important.

Herein, we report a low-temperature one-pot synthesis of HVO by an evaporation-assisted method from an aqueous solution of V_2O_5 in the presence of anionic dodecyl sulfate as a surfactant. The synthesis method is facile and scalable, producing a high yield of HVO. The lab-scale ARZMB cell fabricated with the HVO cathode delivers a specific capacity of 330 mAh g^{-1} with excellent rate performance. To improve the cycling stability of the HVO sample, we introduced Mn doping into the HVO lattice during the synthesis step. The final Mn-doped HVO shows a homogeneous distribution of Mn, and no separate manganese oxide phase was detected. Moreover, compared to the undoped sample (78% retention of the initial capacity after 800 cycles), the Mn-doped HVO sample shows a profound improvement in capacity retention (91% of the initial capacity over 800 cycles). The physical analyses of both the doped- and undoped HVO samples justify the observed change in the electrochemical performance. Finally, we have demonstrated the scalability of the synthesis strategy by fabricating a large electrode with $3.3 \times 1.6 \text{ cm}^2$ area and 3.6 mg cm^{-2} loading, and the electrochemical performance was demonstrated in a home-made pouch cell.

4.2 Experimental Section

4.2.1 Materials

Vanadium pentoxide (V_2O_5), manganese chloride tetrahydrate ($MnCl_2 \cdot 4H_2O$), zinc trifluoromethanesulfonate ($Zn(CF_3SO_3)_2$), sodium dodecyl sulfate (SDS) and poly(vinylalcohol) (PVA, molecular weight 85000) were procured from Sigma-Aldrich. Nafion (212) membrane separator was supplied by DuPont. Grafoil roll was supplied by Global Nanotech.

4.2.2 Synthesis of Hydrated Vanadium Oxide

In a typical process, at first, 150 mg of the SDS surfactant was dissolved in 15 ml of deionized water followed by the addition of 180 mg of commercial bulk V_2O_5 powder. Later, 2.5 ml of 30% H_2O_2 was added into the solution for the complete dissolution of V_2O_5 . The solution was stirred for 1 h at room temperature. Finally, the solution (Solution A) was transferred into a Petri dish and kept at 40-45°C for 3 days for complete evaporation of the water. The obtained green-colored powder material was washed with a copious amount of water to remove the SDS surfactant, and this was finally dried at 60°C. The sample was labeled as HVO-30, where the number '30' represents the concentration of SDS (in mM) in the reaction mixture. Also, different amounts of SDS (30 and 500 mg) were added while preparing the reaction mixture, and the corresponding samples were marked as HVO-6, and HVO-100, respectively. The numbers 6, and 100 also represent the concentration of SDS in the precursor solution. For comparison purposes, the HVO sample without the SDS surfactant (HVO-0) was prepared, and the sample was dark-orange in color.

4.2.3 Synthesis of Mn-doped Hydrated Vanadium Oxide

100 mg of $MnCl_2 \cdot 4H_2O$ salt was added into Solution A (as mentioned in the previous section) and was stirred for another 15 min. (Solution B). Solution B was transferred into a Petri dish, the temperature of which was maintained at 40-45°C for 3 days leading to complete evaporation of the water. The final sample was obtained after washing with water and dried at 60°C. This sample was marked as MnHVO-30. The average yields of all the HVO samples were 80-85% of the total weight of the solid-state commercial bulk V_2O_5 precursor used in the synthesis.

4.2.4 Preparation of Electrolyte

The electrolyte used in this study is an aqueous solution of 1M $Zn(CF_3SO_3)_2$ salt. A piece of preactivated Nafion membrane²⁶ was soaked in this liquid electrolyte for 2 days, and

the electrolyte-impregnated Nafion membrane was employed as a separator. For the fabrication of a scaled-up cell, PVA/Zn(CF₃SO₃)₂ gel electrolyte was prepared by dissolving 0.7 g of PVA in 4 ml of water at 110°C. In the next step, 1 g of Zn(CF₃SO₃)₂ salt was dissolved into the transparent PVA solution.

4.2.5 Fabrication of ARZMB Cells

The electrochemical cells were fabricated in CR2032 coin cell in an open atmosphere. To prepare the cathode, the HVO-0, HVO-30 or MnHVO-30 sample, conducting carbon, and poly(vinylidene fluoride) (PVDF) binder were taken with a weight ratio of 80:15:5, and the mixture was blended in N-methylpyrrolidone (NMP) for 5 h. The uniform slurry was coated on a Grafoil sheet to obtain 1 mg cm⁻² loading. Finally, the electrode was dried overnight at 70°C. CR2032 coin cells were fabricated with metallic zinc anode, liquid electrolyte-soaked Nafion membrane separator, the Grafoil loaded with the desired material as the cathode, and 1M Zn(CF₃SO₃)₂ liquid electrolyte. The coin cells were marked as Zn||HVO-0, Zn||HVO-30, and Zn||MnHVO-30. In a similar way, the electrochemical cells were fabricated for analyzing the performance of HVOs prepared with different amounts of SDS, and the cells were marked as Zn||HVO-6 and Zn||HVO-100.

For fabricating the scaled-up prototype home-made pouch cell, a thick slurry was prepared by mixing the MnHVO-30 sample, conducting carbon and PVDF binder in 80:15:5-weight ratio in NMP. The slurry was probe-sonicated for 15 min and coated over a Grafoil sheet with the help of a bar coater, and the MnHVO-30 coated Grafoil sheet was dried at 80°C for 12 h. The coated Grafoil sheet was cut into a 3.3×1.6 cm² area, and the required amount of the PVA/Zn(CF₃SO₃)₂ gel electrolyte was spread over the electrode. A thin layer of the gel electrolyte was also coated over a piece of zinc foil with the same area. Two small-sized copper tapes were attached to the respective electrodes, which serve as the anode and cathode current collectors. Later, the electrodes were sandwiched together by keeping the Nafion separator for preventing contact between the electrodes. The cell was correctly sealed with adhesive tape to minimize the electrolyte evaporation. This quasi-solid-state pouch cell was labeled as Q-Zn||MnHVO-30.

4.2.6 Material Characterization

A Rigaku, MicroMax-007HF with a high-intensity microfocus rotating anode X-ray generator (Cu K α ($\alpha = 1.54 \text{ \AA}$)) was used for X-ray diffraction (XRD) analysis. The morphology

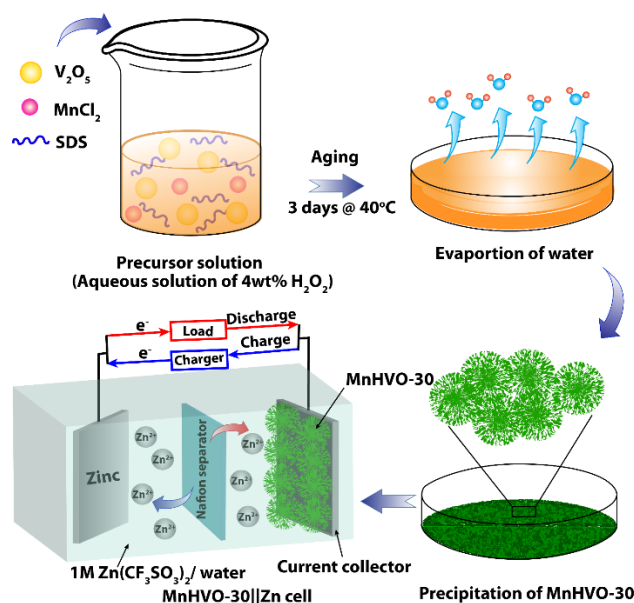


Figure 4.1. Schematic representation for the synthesis and application of the MnHVO-30 sample. For simplicity, the anionic counterpart of the electrolyte is not shown in the figure. (Reprinted (adapted) with permission from *ACS Appl. Mater. Interfaces* 2020, 12, 43, 48542–48552. Copyright (2020) American Chemical Society).

of the HVO-0, HVO-30, and MnHVO-30 samples was analyzed with a field emission scanning electron microscope (FESEM) Nova Nano SEM 450. The elemental composition was investigated through energy-dispersive X-ray spectroscopy (EDAX) analysis, and EDAX elemental mapping was performed with an ESEM-Quanta 200-3D instrument. The transmission electron microscopy (TEM) imaging was recorded with a Tecnai T-20 instrument at an accelerating voltage of 200 kV. A Bruker Tensor 27 FTIR instrument was used to perform Fourier transform infrared (FTIR) analysis. X-ray photoelectron spectroscopy (XPS) analysis was performed using a Thermo K-Alpha+ X-ray spectrometer. Thermogravimetric analysis (TGA) was performed with an SDT Q600 DSC-TGA instrument under an air atmosphere with a temperature ramp of 10 °C per min. Brunauer-Emmett-Teller (BET) analysis was carried out in a Quantachrome Quadrasorb instrument for studying the N₂ adsorption/desorption properties and pore size distribution patterns of the samples.

4.2.7 Electrochemical Measurements

The electrochemical performance of the cathode samples HVO-0, HVO-30, and MnHVO-30 was studied in a CR2032 coin cell. The cells were characterized by cyclic voltammetry (CV) (at scan rates of 1.0, 0.5, 0.3, and 0.1 mV s⁻¹) and galvanostatic charge-discharge (GCD) (at constant current rates of 0.1, 0.25, 0.5, 1.0, and 3.0 A g⁻¹) techniques

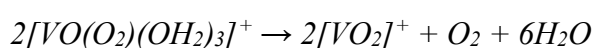
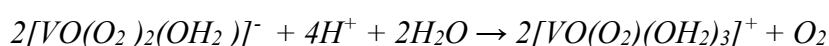
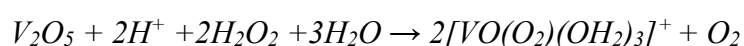
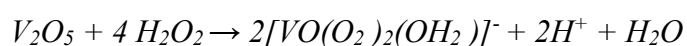
within the voltage window of 0.2 V- 1.6 V vs. Zn|Zn²⁺. The capacity of the cells was calculated considering the loading of the active material in the cathode. The cycling stability tests were performed by a GCD experiment at a current rate of 3.0 A g⁻¹. The impedance analyses were carried out in the frequency range of 1 MHz to 100 mHz frequency range with a sinus amplitude of 10 mV (V_{rms} = 7.07 mV). The Q-Zn||MnHVO-30 cell was tested by CV at the scan rate of 1.0 mV s⁻¹ and the GCD technique at a current rate of 1.3 A g⁻¹. For the *ex situ* characterization of the Zn||MnHVO-30 cell, the cathodes were recovered from the cells after the 1st complete discharge to 0.20 V and complete charge to 1.6 V, respectively, at 0.1 A g⁻¹ current rate.

4.3 Results and Discussion

4.3.1 Physical Characterization

The synthesis of the MnHVO-30 sample is schematically presented in **Figure 4.1**. The desired material is obtained from an aqueous solution of the commercial V₂O₅ and MnCl₂ additive in the presence of the SDS surfactant and 4 wt% H₂O₂. The adopted synthesis protocol is cost-effective and eco-friendly, and the process does not require any additional high-temperature treatment. Here, we have selected anionic surfactant so that it can strongly interact with the cationic species generated in the reaction mixture to form a surfactant-metal cation composite.²⁷

The processes occurring during the evolution of the aforementioned reaction mixture can be briefly explained as follows. In the diluted solution of H₂O₂, the bulk V₂O₅ powder undergoes a vigorous reaction forming O₂ gas and the diperoxo anion [VO(O₂)₂(OH₂)]⁻, which later decomposes into the monoperoxo cation [VO(O₂)(OH₂)₃]⁺.²⁸ These complexes further react to form [VO₂]⁺ ions in the solution, liberating O₂ bubbles;²⁹ the change in solution color from yellow to dark-orange indicates the formation of different intermediates during the reaction. The associated chemical reactions are given below:



In the presence of SDS with 30 mM concentration (>> critical micelle concentration of SDS), the surfactant molecules are likely to form micellar structures, which could serve as soft templates. The [VO₂]⁺ ions can get absorbed over these micelles through the electrostatic interaction with the SDS. During aging, [VO₂]⁺ ions start to nucleate and undergo the

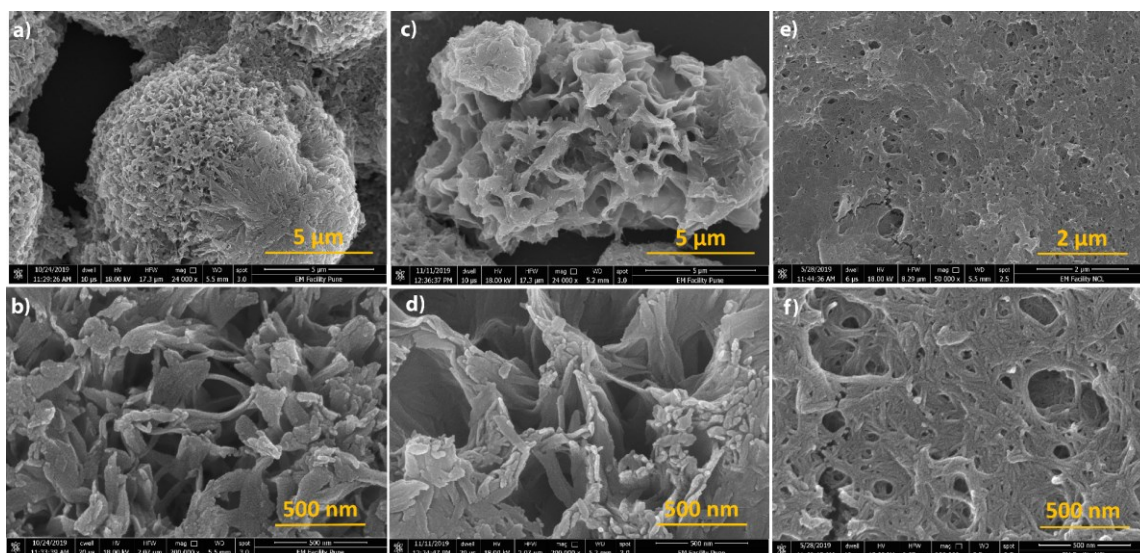


Figure 4.2. FESEM images of (a)-(b) MnHVO-30, (c)-(d) HVO-30, and (e)-(f) HVO-0. (Reprinted (adapted) with permission from *ACS Appl. Mater. Interfaces* 2020, 12, 43, 48542–48552. Copyright (2020) American Chemical Society).

crystallization process to form $V_2O_5 \cdot nH_2O$. During the crystal growth, the preadded Mn^{2+} species in the reaction mixture could intercalate between the layers of $V_2O_5 \cdot nH_2O$, resulting in the doping of Mn into the HVO lattice.

As given in **Figure 4.2a** and **b**, the MnHVO-30 sample exhibits porous 3D architecture consisting of randomly assembled nanoflake structures. For comparison, we have prepared a control sample without introducing Mn doping (HVO-30). The HVO-30 sample also possesses (**Figure 4.2c** and **d**) self-assembled microstructures similar to that of the Mn-doped material. This implies that the addition of Mn^{2+} salt in the precursor reaction mixture does not induce significant morphological change except for the doping of Mn. Contrarily, the sample prepared in the absence of SDS surfactant (HVO-0) agglomerated and showed less porous (**Figure 4.2e** and **f**) morphology. Hence, it is evident that the SDS surfactant present in the solution acts as a pore-creating as well as a structure-directing agent during the synthesis.

The elemental mapping profile validates the uniform dispersion of the V, Mn, and O in the MnHVO-30 sample, proving the Mn-doping (**Figure 4.3a-c**). The morphology of MnHVO-30 is further characterized by TEM analyses. **Figure 4.3d** shows the aggregation of the nanoflakes in a randomly orientated manner. **Figure 4.3e** reveals that the nanoflakes possess an average interlayer spacing of ~ 0.8 nm, possibly resulted from the insertion of water molecules and Mn^{2+} ions into the interlayer space of the lattice structure. In fact, such higher interlayer spacing could favour the fast and reversible diffusion of the Zn^{2+} ions when employed as the cathode material in ARZMBs. The TEM image of HVO-30 also points out a

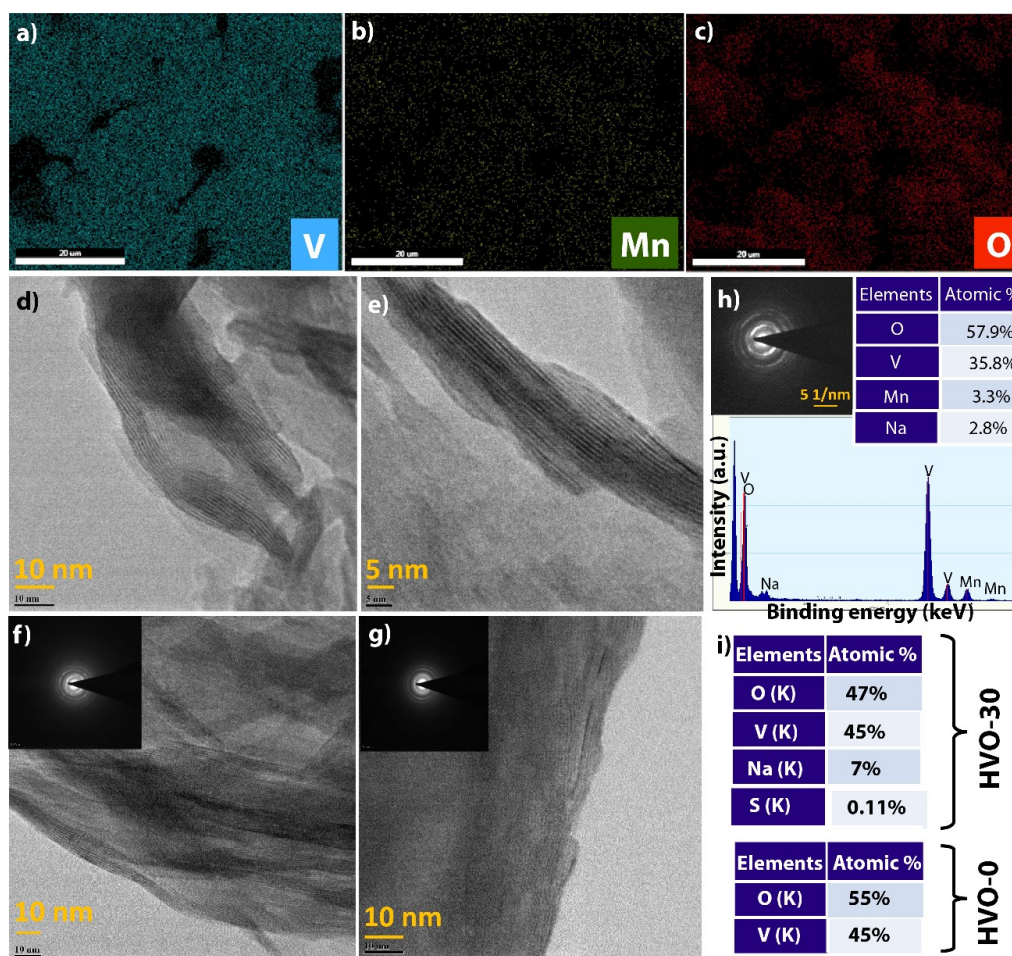


Figure 4.3. Elemental mapping of (a) V, (b) Mn, and (c) O in MnHVO-30; TEM images of (d)-(e) MnHVO-30, (f) HVO-30, and (g) HVO-0; (h) EDAX data of the MnHVO-30 sample; Selected area electron diffraction (SAED) patterns of the MnHVO-30, HVO-30, and HVO-0 samples are shown in the inset of (h), (f), and (g), respectively; (i) the atomic percentage of the elements in HVO-30 and HVO-0 samples obtained from EDAX analysis. (Reprinted (adapted) with permission from ACS Appl. Mater. Interfaces 2020, 12, 43, 48542–48552. Copyright (2020) American Chemical Society).

layered structure with an interlayer spacing of ~ 0.8 nm (Figure 4.3f). It may be noted that the interlayer spacing in both the samples is obtained after averaging the measurements from the different sections of the TEM sample. For comparison, the TEM image of HVO-0 is provided in Figure 4.3g. The SAED patterns of MnHVO-30 (Figure 4.3h inset), HVO-30 (Figure 4.3f inset), and HVO-0 (Figure 4.3g inset) show the polycrystalline nature of the samples.³⁰ The EDAX data of MnHVO-30 (Figure 4.3h) displays the presence of O, V, and Mn in the sample. The sample also contains a small amount of Na coming from the cationic counterpart of the SDS surfactant.

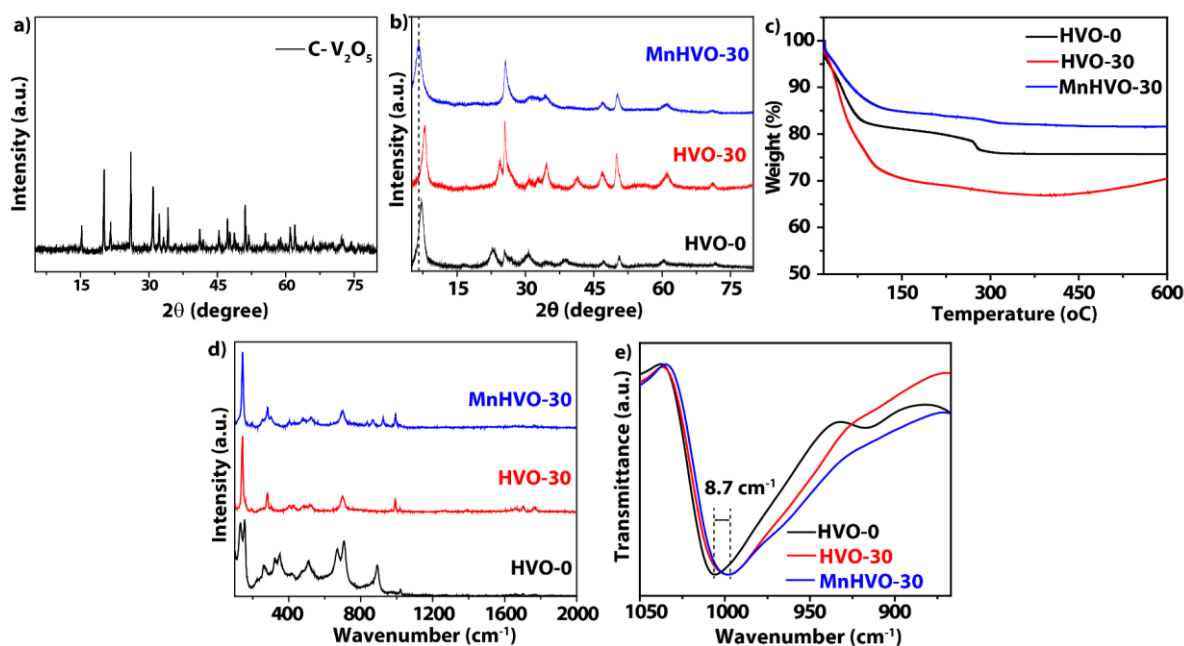


Figure 4.4. (a) XRD profile of commercial V_2O_5 ; (b) XRD profiles, (c) TGA profiles, (d) Raman data, and (e) FTIR data of the MnHVO-30, HVO-30, and HVO-0 samples. (Reprinted (adapted) with permission from *ACS Appl. Mater. Interfaces* 2020, 12, 43, 48542–48552. Copyright (2020) American Chemical Society).

Similarly, the elemental composition of the HVO-30 and HVO-0 samples obtained from EDAX analysis is given in **Figure 4.3i**.

Later, the crystal structure of the samples was studied by XRD analyses (**Figure 4.4a-b**). The XRD patterns of all the samples (**Figure 4.4b**) appear different from that of the commercial bulk V_2O_5 (C- V_2O_5 , **Figure 4.4a**), indicating the changes that occurred in the original crystal structure of the C- V_2O_5 after the reaction with H_2O_2 . The XRD data of the HVO-0 sample matches with the diffraction pattern of $V_2O_5 \cdot nH_2O$ (JCPDS 40-1296), as reported earlier.^{31,32} The strong peak at the 2θ value of 7.2° is assigned to the (001) plane of $V_2O_5 \cdot nH_2O$. The additional peaks at 22.9° , 30.8° , and 38.7° correspond to (003), (004), and (005) planes of $V_2O_5 \cdot nH_2O$, which indicate the layered structure of HVO-0, showing a preferred orientation along the (001) planes. In addition to the above (001) planes, the small peak appearing at the 2θ value of 25.4° relates to the in-plane (hkl) reflection of the HVO, as mentioned in the previous reports.³¹

The XRD patterns of HVO-30 and MnHVO-30 exhibit a strong peak at $2\theta < 10^\circ$ related to the (001) plane of $V_2O_5 \cdot nH_2O$, suggesting that the layered crystal structure is preserved. The increased intensity of the (hkl) reflection compared to HVO-0 is due to the reduced stacking of the vanadium oxide layers.³³ Moreover, the XRD patterns of HVO-30 and MnHVO-30 match

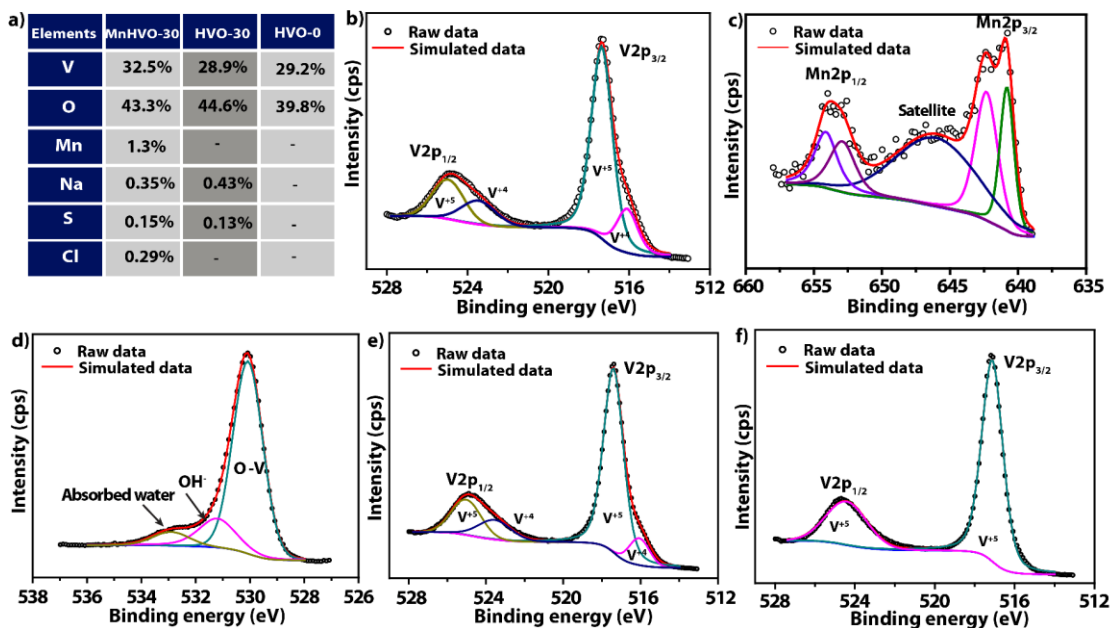


Figure 4.5 (a) Elemental composition of the MnHVO-30, HVO-30, and HVO-0 samples obtained from the XPS analysis sample; (b) V2p, (c) Mn2p, (d) O1s XPS profiles of MnHVO-30 sample; V2p XPS profiles of (e) HVO-30 and (f) HVO-0 samples. (Reprinted (adapted) with permission from *ACS Appl. Mater. Interfaces* 2020, 12, 43, 48542–48552. Copyright (2020) American Chemical Society).

with the previously reported cation inserted (*viz.* Na^+ , Mn^{2+} , Ni^{2+} , K^+ , *etc.*) $\text{V}_2\text{O}_5 \cdot n\text{H}_2\text{O}$.^{25,34,35} Besides, no significant diffraction peaks corresponding to the crystalline phase of the manganese oxide are observed in MnHVO-30. Interestingly, the strongest peak at $2\theta < 10^\circ$ for MnHVO-30 relates to an expanded interlayer spacing of 13.3 Å, a value higher than 11.2 Å calculated for HVO-30. The observed shift indicates the incorporation of Mn^{2+} ions into the interlayer space of MnHVO-30.^{22,25} However, the interplanar spacing calculated from the XRD data is slightly higher than the values obtained from the corresponding TEM data. This could be due to the shrinkage of the interlayer spacing during the TEM experiment as a consequence of the evaporation of the interlayer water molecules under the intense electron beam in vacuum.^{36,37} The presence of water molecules in the samples is also supported through TGA analysis. In **Figure 4.4c**, the TGA profiles of all the three samples show a rapid weight loss before 100°C due to the removal of loosely bound water molecules. After that, the gradual removal of crystalline water molecules is observed in the temperature range of 100–200°C.^{38,39} These water molecules residing in the interlayer space of HVO could act as ‘lubricant’ and facilitate the electrochemical insertion/extraction of the divalent Zn^{2+} ions.¹⁸

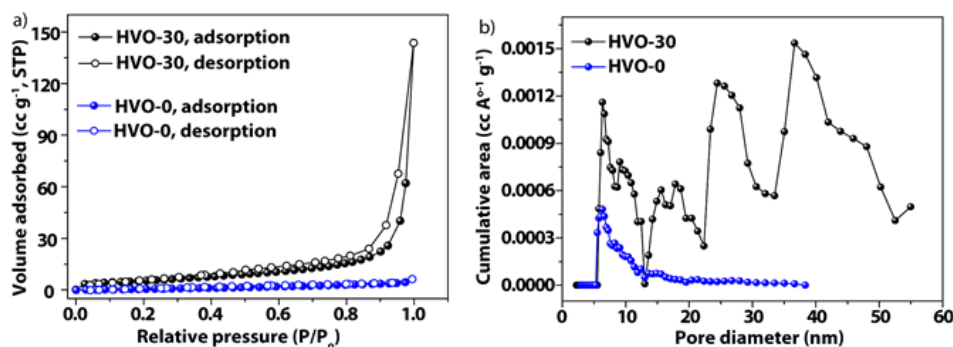


Figure 4.6. (a) BET isotherm data and (b) pore size distribution profiles for the HVO-30 and HVO-0 samples. (Reprinted (adapted) with permission from *ACS Appl. Mater. Interfaces* 2020, 12, 43, 48542–48552). Copyright (2020) American Chemical Society.

In the Raman spectra of HVO-0 (**Figure 4.4d**), the peak at 155 cm^{-1} is related to the vibration of the V-O-V chain in the layered $\text{V}_2\text{O}_5 \cdot n\text{H}_2\text{O}$.^{31,35} A similar lattice vibrational mode in HVO-30 and MnHVO-30 is observed at 143 cm^{-1} .⁴⁰ Besides, other peaks located at 282, 404, 698, and 993 cm^{-1} match with that of the different vibrational modes of the cation inserted $\text{V}_2\text{O}_5 \cdot n\text{H}_2\text{O}$. The FTIR data of all of the samples in the frequency range of $997\text{--}1006\text{ cm}^{-1}$ are compared in **Figure 4.4e**. The observed FTIR peak at this region originates from the characteristic V=O stretching vibration in the samples.⁴¹ **Figure 4.4e** shows a red shift of the V=O stretching in the cases of HVO-30 and MnHVO-30 (997 cm^{-1}) compared to that of HVO-0 (1006 cm^{-1}). This observed shift signifies a weakening of the V=O bond in the former due to the reduction of a small amount of the V^{5+} to the V^{4+} state.²⁵

The oxidation states of the elements in the respective HVO samples are analyzed by XPS. From the XPS elemental analysis of MnHVO-30, the contents of V and Mn are obtained as 32.5 and 1.3%, respectively (**Figure 4.5a**), suggesting the low doping level of Mn. The deconvoluted XPS profiles of V, Mn, and O in the MnHVO-30 sample are given in **Figure 4.5b-f**. In O1s XPS data of MnHVO-30 (**Figure 4.5d**), the characteristic strong peak at the binding energy of 530 eV corresponds to the surface O atom coordinated with V.⁴² The other peaks at the higher binding energy values (531.2 and 532.9 eV) with low intensity come from the hydroxyl group bonded with V atom and surface-absorbed water molecules, respectively.^{40,43} The characteristic signal of $\text{Mn}2p_{3/2}$ at 640.9 and 642.6 eV (**Figure 4.5c**) implies that the preinserted Mn ions are present in both the divalent as well as the higher valent oxidation states. The ionic radius of Mn^{4+} is similar to that of V^{5+} , and Mn^{2+} possesses a higher radius; therefore, the latter accounts for the observed structural changes in MnHVO-30 upon Mn doping.⁴⁴ The intense $\text{V}2p_{3/2}$ spectra (**Figure 4.5b**) are deconvoluted into two peaks at

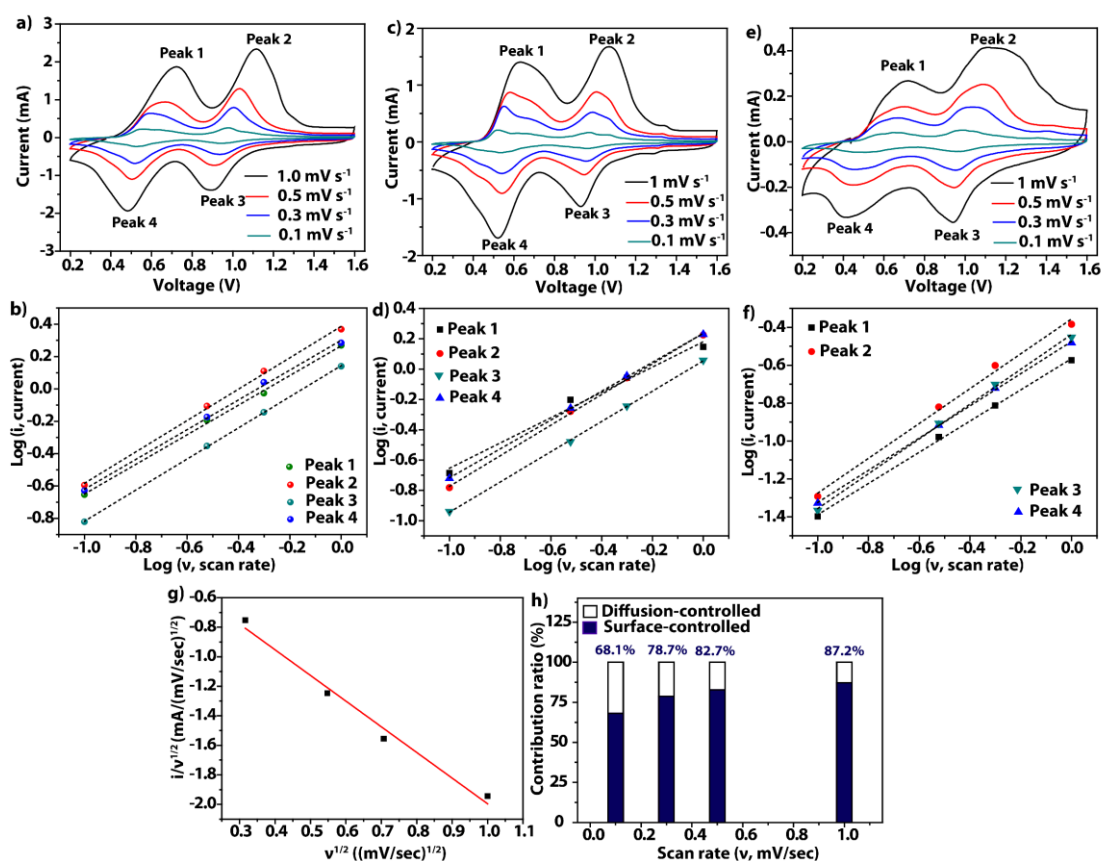


Figure 4.7. (a), (c), and (e) CV profiles recorded at various scan rates for MnHVO-30, HVO-30, and HVO-0 samples, respectively; (b), (d), and (f) Log i vs. Log v plots for the MnHVO-30, HVO-30, and HVO-0 samples, respectively; (g) $i/v^{1/2}$ vs. $v^{1/2}$ relationship, and (h) capacitive contribution of MnHVO-30 at different scan rates calculated for the reduction peak at 0.5 V vs. Zn|Zn²⁺. (Reprinted (adapted) with permission from (ACS Appl. Mater. Interfaces 2020, 12, 43, 48542–48552). Copyright (2020) American Chemical Society).

517.3 and 516.1 eV, which signify the coexistence of V⁵⁺ and V⁴⁺.⁴⁵ The mixed vanadium valences may augment the electrochemical performance of the material when employed as the cathode in ARZMB.⁴⁶ Both V⁴⁺ and V⁵⁺ states are detected in HVO-30 (Figure 4.5e) as well; however, the ratio of [V⁵⁺]/[V⁴⁺] in HVO-30 (ca. 7.8) is slightly high compared to that of MnHVO-30 (ca. 4.2). It is reported that the insertion of Mn²⁺ ions into the lattice of HVO creates more low valance states of V (such as V⁴⁺) and more oxygen vacancies in the doped sample.^{25,47,48} This phenomenon is also observed for other vanadium oxide cathodes followed by the introduction of different ionic species, including Mn²⁺ and K⁺.^{35,49,50} Meanwhile, in HVO-0 (Figure 4.5f), the vanadium signal shows only the presence of the V⁵⁺ state. Therefore, the V⁴⁺ created in MnHVO-30 and HVO-30 can influence the V-O bond strength, which is reflected in the FTIR spectra of the respective samples, as discussed in the previous section

(Figure 4.4e). These observations imply that the SDS surfactant has an impact on directing the electronic structure of HVO.

The effect of the anionic SDS surfactant on the nature of porosity and the surface area of the samples has been validated by BET surface area analyses. The specific surface area (Figure 4.6a) of HVO-30 is $16 \text{ m}^2 \text{ g}^{-1}$, a value substantially higher than that of HVO-0 ($3 \text{ m}^2 \text{ g}^{-1}$). A drastic difference is observed in the pore size distribution profiles as well. Figure 4.6b displays that the size of pores in HVO-0 is in the range of 6-13 nm, whereas HVO-30 contains a wide range of pore size distributions within 6-50 nm. This clearly indicates the role of the surfactant as the soft template for creating a porous structure.

4.3.2 Electrochemical characterization

The electrochemical performance of all of the samples is first characterized through the CV analyses within the potential range of 0.2-1.6 V vs. Zn|Zn²⁺. The CV plots of the Zn||MnHVO-30 cell (Figure 4.7a) at various scan rates (0.1, 0.3, 0.5, and 1.0 mV s⁻¹) display two pairs of oxidation and reduction peaks. The redox peaks located at 0.72/0.48 V and 1.12/0.89 V vs. Zn|Zn²⁺ associate with the V⁴⁺/V³⁺ and V⁵⁺/V⁴⁺ redox couples, respectively.⁵¹ The CV profiles at various scan rates recorded for the Zn||HVO-30 and Zn||HVO-0 cells are given in Figure 4.7c and e, respectively. As observed from the CV profiles, the nearly overlapping position of the redox peaks suggests that all the three cathodes undergo faradaic reactions during the charge/discharge process of the respective ARZMB cells. However, the current response traced by the CV curves for the Zn||HVO-0 cell (Figure 4.7e) is inferior compared to both the Zn||MnHVO-30 (Figure 4.7a) and Zn||HVO-30 (Figure 4.7c) cells.

The kinetics of the Zn²⁺ insertion/extraction process is analyzed from the peak current (*i*) vs. scan rate (*v*) relationship ($i = av^b$, where, *a*, and *b* are adjustable parameters) for the oxidation and reduction peaks, and the data are summarized in the form of Log *i* vs. Log *v* plot corresponding to Zn||MnHVO-30 (Figure 4.7b), Zn||HVO-30 (Figure 4.7d), and Zn||HVO-0 (Figure 4.7f).⁵² The slope of the plot represents parameter *b*, which indicates the capacitive contribution in the electrochemical reaction. Typically, the *b* value approaching 1.0 suggests that the charge storage utilizing surface-controlled or capacitive mechanism is dominant, whereas *b* close to 0.5 indicates the dominance of the diffusion-controlled mechanism.^{53,54} The calculated *b* values for the peaks 1, 2, 3 and 4 (Figure 4.7b) in Zn||MnHVO-30 cell are 0.91, 0.97, 0.96, and 0.92, respectively. This suggests that the faradaic reactions at the peak regions are mainly influenced by the surface controlled process within the scan rate ranging from 1.0 to 0.1 mV s⁻¹.^{17,19} The *b* values calculated for the Zn||HVO-30, and Zn||HVO-0 cells are also

Table 4.1. The capacity, voltage window, and cycling stability of the MnHVO-30 cathode are compared with some of the reported high performance of vanadium oxide-based cathode for ARZMBs.

Material	Voltage window	Electrolyte	Capacity	Cycling stability	Ref.
V ₅ O ₁₂ ·6H ₂ O	0.2-1.6 V	3M Zn(CF ₃ SO ₃) ₂	354.8 mAh g ⁻¹ @ 0.5 A g ⁻¹	94% retention over 1000 cycles	19
Mn _{0.15} V ₂ O ₅ ·nH ₂ O	0.2-1.7 V	1M Zn(ClO ₄) ₂ in propylene carbonate	367mAh g ⁻¹ @ 0.1 A g ⁻¹	100% retention over 8000 cycles	21
MnVO	0.2-1.6	3M Zn(CF ₃ SO ₃) ₂	415 mAh g ⁻¹ @ 0.05 A g ⁻¹	92% retention over 2000 cycles	25
V ₂ O ₅ ·2.2 H ₂ O	0.3-1.6 V	3M Zn(CF ₃ SO ₃) ₂	450 mAh g ⁻¹ @ 0.1 A g ⁻¹	72% retention over 3000 cycles	56
(NH ₄) ₂ -V ₁₀ O ₂₅ ·8H ₂ O	0.7-1.7 V	3M Zn(CF ₃ SO ₃) ₂	228.8 mAh g ⁻¹ @ 0.1 A g ⁻¹	94.2% retention over 1000 cycles	57
H ₁₁ Al ₂ V ₆ O _{23.2}	0.4-1.4V	2M ZnSO ₄	305.4 mAh g ⁻¹ @ 1 A g ⁻¹	94% retention over 900 cycles	58
Ca _{0.24} V ₂ O ₅ ·0.83H ₂ O	0.6-1.6	1M ZnSO ₄	340 mAh g ⁻¹ @ 0.2 C	96% retention over 3000 cycles	59
Na _{0.33} V ₂ O ₅	0.2-1.6	3M Zn(CF ₃ SO ₃) ₂	367.1 mAh g ⁻¹ @ 0.1 A g ⁻¹	93% retention over 1000 cycles	60
(Na _{0.33} ,Mn _{0.65})V ₈ O ₂₀ ·0.32H ₂ O	0.3-1.25	3M Zn(CF ₃ SO ₃) ₂	150 mAh g ⁻¹ @ 4 A g ⁻¹	99% retention over 1000 cycles	49
CaV ₃ O ₇	0.2-1.6 V	1M ZnSO ₄	471 mAh g ⁻¹ @ 0.83 A g ⁻¹	82% retention over 400 cycles	62
VOH/PANI	0.4-1.6 V	3M Zn(TfO) ₂ + 6M LiTFSI	346 mAh g ⁻¹ @ 0.3 A g ⁻¹	91% retention over 800 cycle	63
V ₂ O _x @V ₂ CT _x	0.2-1.6 V	1M ZnSO ₄	224 mAh g ⁻¹ @ 0.1 A g ⁻¹	81.6% retention over 200 cycle	64
MgV ₂ O ₄	0.2-1.4 V	2M Zn(TFSI) ₂	272 mAh g ⁻¹ @ 0.2 A g ⁻¹	~80% retention over 500 cycle	65
MnHVO-30	0.2-1.6	1M Zn(CF ₃ SO ₃) ₂	341 mAh g ⁻¹ @ 0.1 A g ⁻¹	82% retention over 1200 cycles	This work

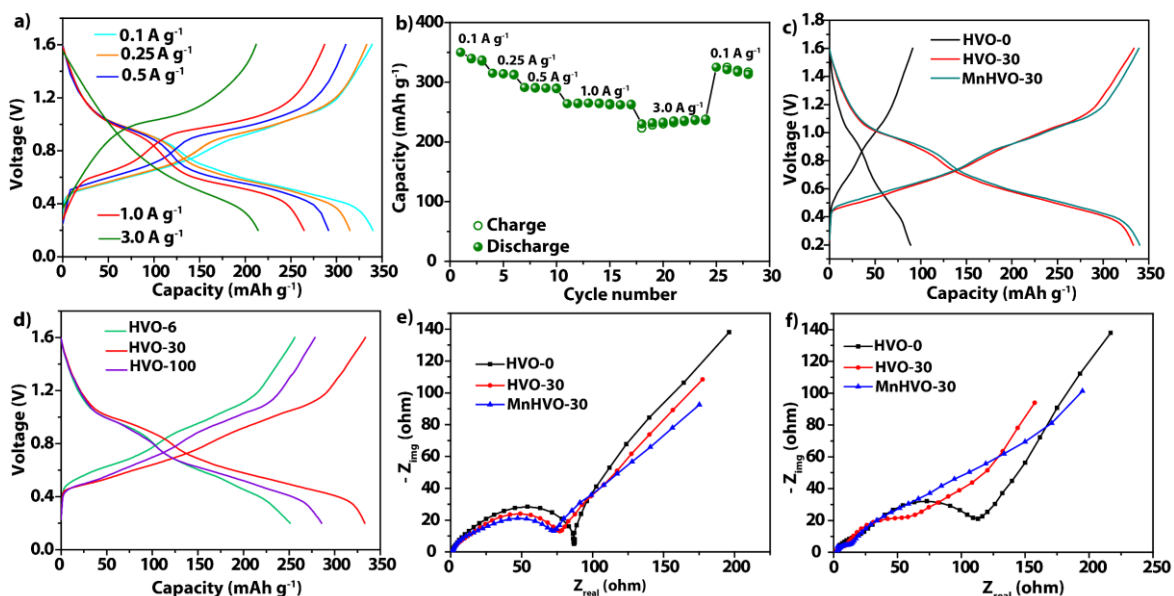


Figure 4.8. (a) GCD profiles recorded at various current rates; (b) rate capability plot for the Zn||MnHVO-30 cell; (c) GCD profiles for the Zn||HVO-0, Zn||HVO-30, and Zn||MnHVO-30 cells at 0.1 A g^{-1} ; (d) GCD plots for the Zn||HVO-6, Zn||HVO-30 and Zn||HVO-100 cells at 0.1 A g^{-1} ; Nyquist plots corresponding to the Zn||MnHVO-30, Zn||HVO-30, and Zn||HVO-0 cells recorded at $0.20 \text{ V vs. Zn|Zn}^{2+}$ (e) after the first discharge and (f) after electrochemical cycling. (Reprinted (adapted) with permission from ACS Appl. Mater. Interfaces 2020, 12, 43, 48542–48552. Copyright (2020) American Chemical Society).

close to 1.0, and the related $\text{Log } i \text{ vs. Log } v$ plots are given in **Figure 4.7d** and **f**. The contributions of the diffusion-controlled and surface-controlled reactions in the total current response obtained in the CV scans in Zn||MnHVO-30 cell are calculated from the following equation:

$$i = k_1 v + k_2 v^{1/2} \dots \quad (\text{Equation 4.1})$$

where, k_1 and k_2 are the constant parameters.⁵⁵ At scan rates of 1.0, 0.5, 0.3, and 0.1 mV s^{-1} , the contributions in the current from the capacitive process are calculated as 87.2, 82.7, 78.7, and 68.1%, respectively (**Figure 4.7g** and **h**) showing that capacitive contribution slightly decreases at slower scan rate.

The GCD curves for the Zn||MnHVO-30 cell (**Figure 4.8a**) display slopes at two different potential regions that are consistent with the CV data (**Figure 4.7a**). At the current rate of 0.1 A g^{-1} , the cell shows a discharge capacity of 341 mAh g^{-1} , a value comparable or superior to many of the previously reported vanadium oxide-based cathodes (**Table 4.1**).^{19,21,25,56-65} Later, the rate performance of the Zn||MnHVO-30 is investigated at various

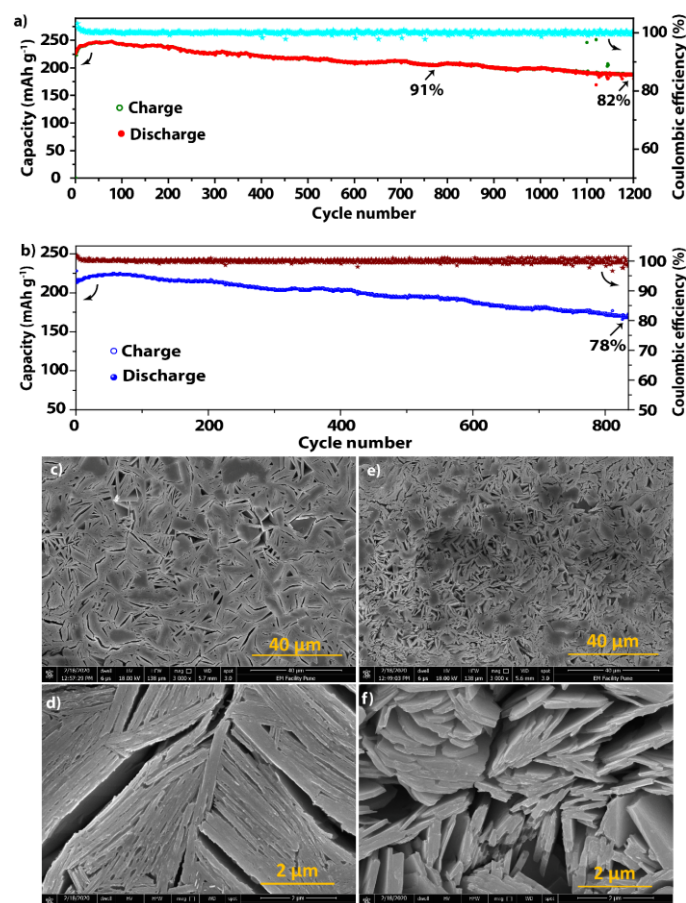


Figure 4.9. Cycling stability data recorded at the current rate of 3.0 A g^{-1} for (a) $\text{Zn}||\text{MnHVO-30}$ and (b) $\text{Zn}||\text{HVO-30}$ cells; FESEM images of the post-stability cathodes recovered from the (c)-(d) the $\text{Zn}||\text{MnHVO-30}$ and (e)-(f) the $\text{Zn}||\text{HVO-30}$ cells. (Reprinted (adapted) with permission from *ACS Appl. Mater. Interfaces* 2020, 12, 43, 48542–48552. Copyright (2020) American Chemical Society).

current rates, and discharge capacities of 314, 291, 265, and 208 mAh g^{-1} are obtained at 0.25, 0.5, 1.0, and 3.0 A g^{-1} , respectively (**Figure 4.8a and b**). The observed rate performance ($\sim 60\%$ retention of capacity when the current varies from 0.1 to 3.0 A g^{-1}) is attributed to the predominantly surface controlled charge storage mechanism of the MnHVO-30 cathode, as discussed in the previous section. The layered structure of MnHVO-30 with large interlayer spacing facilitates the mobility of the electrolyte ions. It enhances the access of the ions to the redox-active centres even at the higher current rate. When the current rate is suddenly changed to 0.1 A g^{-1} , the cell could restore 320 mAh g^{-1} capacity implying the robustness of the MnHVO-30 cathode. Moreover, at all the current rates, the GCD plots show $\sim 98\%$ Coulombic efficiency resulted from the excellent reversibility of the redox reactions associated with the Zn^{2+} insertion/extraction process.

The specific capacities of the Zn||HVO-0 and Zn||HVO-30 cells at 0.1 A g⁻¹ current rate are also measured, and the data are compared in **Figure 4.8c**. The highest capacity obtained from Zn||HVO-30 is 333 mAh g⁻¹, which is slightly lower than that of the Zn||MnHVO-30 cell. The overlapping GCD plots indicate that the doped Mn in the MnHVO-30 sample does not take part in any separate electrochemical process within the mentioned potential range. On the contrary, the GCD profile of Zn||HVO-0 cell exhibits significantly less capacity (87 mAh g⁻¹) compared to the Zn||MnHVO-30, and Zn||HVO-30 cells. The effect of SDS concentration toward the electrochemical performance of the HVO samples is also studied. **Figure 4.8d** explains that the optimum concentration of SDS is 30 mM delivering the maximum reversible capacity among all of the other concentrations.

To investigate the resistance of the ARZMB cells under study, the impedance spectra are recorded after 1st complete discharge (at 0.2 V vs. Zn|Zn²⁺, **Figure 4.8e**) at the current rate of 0.25 A g⁻¹. The charge-transfer resistance (R_{ct}) for the Zn||MnHVO-30 cell (72 Ω) is slightly lower compared to the Zn||HVO-30 (76 Ω) cell; however, after the electrochemical cycling (**Figure 4.8f**), the resistance values are almost equal, justifying the comparable charge storage capacity of these two cells. In contrast, the Zn||HVO-0 cell shows a higher R_{ct} value after the 1st discharge (87 Ω) as well as after the electrochemical cycling (112 Ω). This is due to the absence of the V⁴⁺ state in HVO-0 in contrast to the mixed oxidation states of vanadium (V⁵⁺ and V⁴⁺) in the samples prepared with the SDS surfactant. Nevertheless, the low surface area and lack of desired porosity in the HVO-0 sample (**Figure 4.2f** and **Figure 4.6a**) impede the transport of the electrolyte ions to the interior of the electrode in the Zn||HVO-0 cell, which also contributes to the high resistance of the cell. Therefore, the above discussion underlines the importance of the SDS surfactant during the low-temperature synthesis of HVO for tuning the electronic property as well as the surface area of the material.

Along with the high capacity, the stability of the electrode material during repeated charge/discharge cycling is another important parameter. Therefore, the long-term GCD experiment at the current rate of 3.0 A g⁻¹ was carried out for the Zn||HVO-30 and Zn||MnHVO-30 cells. In **Figure 4.9a**, the Zn||MnHVO-30 cell exhibits 95% retention of the initial capacity (227 mAh g⁻¹) with the Coulombic efficiency close to 100% over 500 charge/discharge cycles. After 1200 cycles, the cell could retain 187 mAh g⁻¹ (82% retention) capacity, demonstrating excellent electrochemical stability. At the same time, the Zn||HVO-30 cell (**Figure 4.9b**) delivers 217 mAh g⁻¹ initial capacity, and with progressive cycling, the cell experiences faster

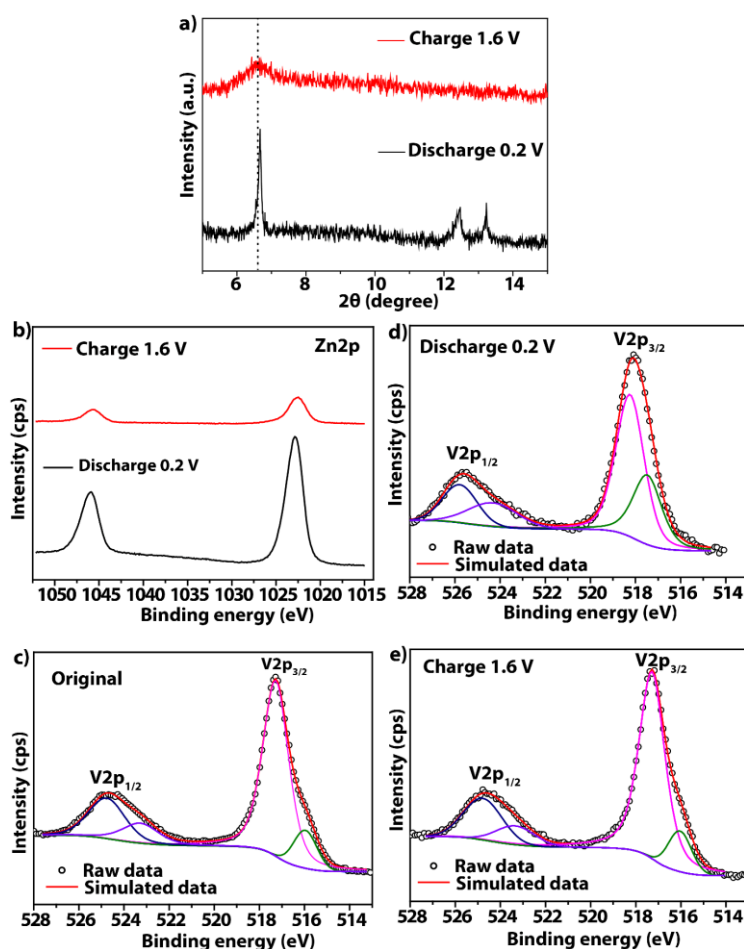


Figure 4.10. (a) XRD data of the MnHVO-30 electrode recovered from the fully charged (1.6 V) and discharged (0.2 V) Zn||MnHVO-30 cells; (b) Zn2p XPS spectra of the MnHVO-30 cathode recovered from the discharged (0.20 V) and charged (1.6 V) Zn||MnHVO-30 cells; V2p XPS spectra of the (c) original MnHVO-30 electrode, (d) and (e) MnHVO-30 electrode after recovering from the discharged (0.20 V) and charged (1.6 V) Zn||MnHVO-30 cells, respectively. (Reprinted (adapted) with permission from *ACS Appl. Mater. Interfaces* 2020, 12, 43, 48542–48552. Copyright (2020) American Chemical Society).

capacity fading compared to the Zn||MnHVO-30 counterpart. As a result, after 830 stability cycles, the specific capacity drops to 169 mAh g^{-1} , which is only 77% of the initial capacity.

It must be noted that both cells are fabricated with the Nafion membrane separator. Nafion, as a cation-selective ionomer membrane, has already been reported to be effective in suppressing the growth of dendritic Zn deposits over the metallic Zn anode during the long-term cycling, as observed in the case with several previous works on ARZMBs.^{26,66,67} Hence, the observed difference in cycling performance is likely to have originated from the cathode side. The superior cycling performance of MnHVO-30 is credited to the unique crystal

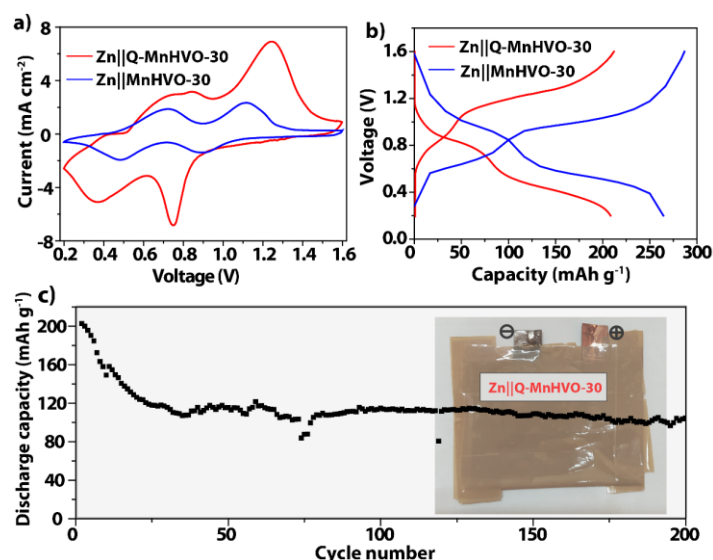


Figure 4.11. (a) CV profiles recorded at a scan rate of 1.0 mV s^{-1} , and (b) GCD profiles of the Q-Zn||MnHVO-30 (at 1.3 A g^{-1}) and Zn||MnHVO-30 (at 1.0 A g^{-1}) cells; (c) cycling stability data of the Q-Zn||MnHVO-30 cell recorded at 1.3 A g^{-1} current rate. (Reprinted (adapted) with permission from *ACS Appl. Mater. Interfaces* 2020, 12, 43, 48542–48552. Copyright (2020) American Chemical Society).

structure of the sample with expanded interlayer spacing that ensued from the preinserted Mn^{2+} ions and interlayer water molecules. Besides, a greater V^{4+} content in MnHVO-30 as explained from the XPS study is likely to augment the electrochemical activity. Therefore, all of these factors facilitate the reversible insertion of Zn^{2+} ions into MnHVO-30, ensuring better structural stability of MnHVO-30 compared to HVO-30 during prolonged cycling. This is also reflected in the morphology of the post-cycling MnHVO-30 and HVO-30 cathodes recovered from the respective electrochemical cells after the stability test. The cathode surface of the Zn||MnHVO-30 cells looks homogeneous (**Figure 4.9c**), and the compact microstructure shows intimate contact among the particles (**Figure 4.9d**), which is favourable for better transport of the charge carrier species throughout the electrode. On the other hand, the HVO-30 cathode possesses a nonuniform surface (**Figure 4.9e**); and the lack of inter-particle contact is visible in **Figure 4.9f**. Therefore, the difference in the morphological change also rationalizes the superior cyclability of the MnHVO-30 cathode.

For an in-depth understanding of the reversibility of the electrode reactions occurring in the Zn||MnHVO-30 cell, the cathode is characterized after recovering from the fully discharged (0.2 V) and charged (1.6 V) cells. The XRD data of the electrodes are compared in **Figure 4.10a**. At the discharged state of the cell, a small shift is observed for the (001) plane to a higher 2θ value (6.7°) compared to the pristine MnHVO-30 sample (6.6° , **Figure 4.4b**).

Table 4.2. The capacity and cycling stability of the Q-Zn||MnHVO-30 cell are compared with some of the previously reported quasi-solid-state ARZMBs. (Reprinted (adapted) with permission from ACS Appl. Mater. Interfaces 2020, 12, 43, 48542–48552. Copyright (2020) American Chemical Society).

Material	Electrolyte	Capacity	Cycling stability	Ref.
NH ₄ V ₃ O ₈ .1.9 H ₂ O	Gelatin/ZnSO ₄	115 mAh g ⁻¹ @ 1 A g ⁻¹	95% retention after 200 cycles	69
V ₂ O ₅ . 2.2 H ₂ O	Gelatin/Zn(CF ₃ SO ₃) ₂	183 mAh g ⁻¹ @1 A g ⁻¹	85% retention after 300 cycles	56
V ₅ O ₁₂ .6H ₂ O	Gelatin/Zn(CF ₃ SO ₃) ₂	300 mAh g ⁻¹ @ 0.1 A g ⁻¹	96% retention after 50 cycles	19
LiMn ₂ O ₄	Gelatin/Li ₂ SO ₄ /ZnSO ₄	110.2 mAh g ⁻¹ @ 25 mA g ⁻¹	90% retention after 100 cycles	70
PANI	PVA/ Zn(CF ₃ SO ₃) ₂	101 mAh g ⁻¹ @ 0.5 A g ⁻¹	~100% retention for 200 cycles	10
MnHVO-30	PVA/ Zn(CF ₃ SO ₃) ₂	200 mAh g ⁻¹ @ 1.3 A g ⁻¹	52% retention over 200 cycles	This work

This is due to the interlayer contraction resulting from the electrostatic interaction between the host material and the inserted Zn²⁺ ions during the discharge process.⁶⁸ Subsequently, at the fully charged state, the Zn²⁺ ions escape from the cathode, and the (001) diffraction peak reappears at the 2θ value similar to that of the pristine sample. The electrodes are subjected to XPS analysis (**Figure 4.10b-e**) after careful washing with water. As displayed in **Figure 4.10b**, the intensity of the Zn2p XPS spectra in the cathode collected from the discharged cell is considerably higher than that in the charged cell. The reduced intensity of the Zn2p XPS spectra corresponding to the charged electrode indicates that most of the inserted Zn²⁺ ions leave the cathode followed by complete charging.⁵⁸ Considering the V2p XPS spectra, the peak in the recovered cathode after being fully discharged (**Figure 4.10d**) is deconvoluted into V⁵⁺ (2p_{3/2}: 518.2 eV) and V⁴⁺ (2p_{3/2}: 517.5 eV) signals. Interestingly, the intensity of the V⁴⁺ signal increases significantly compared to the original electrode (**Figure 4.10c**) which is in accord with the reduction of V⁵⁺ upon discharge. After complete charging to 1.6 V (**Figure 4.10e**), the intensity of V⁴⁺ decreases, and consequently, the ratio of V2p_{3/2}⁵⁺ and V2p_{3/2}⁴⁺ peak area is

found to be retrieved as in the pristine MnHVO-30 sample.⁵⁷ This indeed supports the reversibility of the associated electrochemical reactions occurring in the Zn||MnHVO-30 cell.

Lastly, the advantage of the adopted synthesis protocol is demonstrated by scaling up the process and fabricating a home-made pouch cell with a $3.3 \times 1.6 \text{ cm}^2$ area and 3.6 mg cm^{-2} loading of the active material. A PVA/Zn(CF₃SO₃)₂ gel electrolyte is employed for fabricating the home-made pouch cell. The CV data of the as-fabricated quasi solid-state Zn||MnHVO-30 pouch cell (Q-Zn||MnHVO-30) is compared with that of the Zn||MnHVO-30 coin cell with liquid electrolyte in **Figure 4.11a**. Owing to the higher loading of the active material, the CV profile of the Q-Zn||MnHVO-30 cell traces a higher current response (in mA cm^{-2}) than the latter with 1 mg cm^{-2} loading. The well-resolved redox peaks are clearly visible in the CV profile displaying a similar insertion/extraction mechanism of the Zn²⁺ ions in the Q-Zn||MnHVO-30 cell. Q-Zn||MnHVO-30 delivered 200 mAh g^{-1} discharge capacity at 1.3 A g^{-1} current rate (**Figure 4.11b**), which is comparable to the performance obtained with the $1 \text{ M Zn(CF}_3\text{SO}_3)_2$ liquid electrolyte counterpart tested in coin cell configuration. The durability of the Q-Zn||MnHVO-30 cell is tested at the same current rate (**Figure 4.11c**). During the cycling, the specific capacity of the cell gradually decreases in the initial cycles and stabilizes at 116 mAh g^{-1} after 50 cycles. Later, the Q-Zn||MnHVO-30 cell delivers almost the same capacity over 200 cycles. The lifespan of the Q-Zn||MnHVO-30 cell is relatively short compared to that of the Zn||MnHVO-30 cell with $1 \text{ M Zn(CF}_3\text{SO}_3)_2$ liquid electrolyte in the coin cell configuration. This is due to the gradual evaporation of water from the aqueous gel electrolyte in the home-made quasi-solid-state cell due to the imperfect packaging and sealing. The performance of the Q-Zn||MnHVO-30 cell can be improved by standardizing the method for cell packaging, which requires further studies. Moreover, the quasi-solid-state cell shows comparable performance in terms of capacity and cycling stability to that of the previously reported cells (*e.g.*, Zn||V₅O₁₂.6H₂O, Zn||NH₄V₃O₈.1.9 H₂O, Zn||PANI, *etc.*) as shown in **Table 4.2**.^{10,19,56,69,70}

4.4 Conclusions

In conclusion, we have developed a surfactant-assisted facile and scalable low-temperature synthesis method for preparing Mn-doped hydrated vanadium oxide (MnHVO-30). The as-synthesized material possesses porous morphology, which offers easy diffusion of the electrolyte ions during the faradaic reactions. In addition, the mixed valance states of vanadium in MnHVO-30 created by the anionic surfactant enhance the electrochemical activity of the material. As a result, MnHVO-30 serves as an excellent host for the reversible

insertion/extraction of the Zn^{2+} ions, delivering 341 mAh g^{-1} capacity at 0.1 A g^{-1} . Moreover, the expanded interlayer spacing resulting from the introduction of Mn^{2+} ions significantly improves the cycling performance of the MnHVO-30 cathode (82% capacity retention of the initial capacity over 1200 cycles) than the sample prepared without the doping. We have also tested the performance of the MnHVO-30 cathode in a quasi-solid-state cell with a loading of 3.6 mg cm^{-2} and $3.3 \times 1.6 \text{ cm}^2$ area. The Q-Zn||MnHVO-30 cell shows $\sim 200 \text{ mAh g}^{-1}$ initial capacity and retains more than 100 mAh g^{-1} capacity for 200 cycles. The current study demonstrates a simple synthesis of efficient electrode material following green chemistry principles for a less expensive and safe aqueous ARZMB with high capacity and durability.

4.5 References

- (1) Fang, G.; Zhou, J.; Pan, A.; Liang, S. Recent Advances in Aqueous Zinc-Ion Batteries. *ACS Energy Letters* **2018**, *3*, 2480-2501.
- (2) Demir-Cakan, R.; Palacin, M. R.; Croguennec, L. Rechargeable Aqueous Electrolyte Batteries: from Univalent to Multivalent Cation Chemistry. *Journal of Materials Chemistry A* **2019**, *7*, 20519-20539.
- (3) Shin, J.; Lee, J.; Park, Y.; Choi, J. W. Aqueous Zinc Ion Batteries: Focus on Zinc Metal Anodes. *Chemical Science* **2020**, *11*, 2028-2044.
- (4) Ming, J.; Guo, J.; Xia, C.; Wang, W.; Alshareef, H. N. Zinc-Ion Batteries: Materials, Mechanisms, and Applications. *Materials Science and Engineering: R: Reports* **2019**, *135*, 58-84.
- (5) Xu, C.; Li, B.; Du, H.; Kang, F. Energetic Zinc Ion Chemistry: the Rechargeable Zinc Ion Battery. *Angewandte Chemie International Edition* **2012**, *51*, 933-935.
- (6) Ding, J.; Du, Z.; Gu, L.; Li, B.; Wang, L.; Wang, S.; Gong, Y.; Yang, S. Ultrafast Zn^{2+} Intercalation and Deintercalation in Vanadium Dioxide. *Advanced Materials* **2018**, *30*, 1800762.
- (7) Lee, B.; Lee, H. R.; Kim, H.; Chung, K. Y.; Cho, B. W.; Oh, S. H. Elucidating the Intercalation Mechanism of Zinc Ions into $\alpha\text{-MnO}_2$ for Rechargeable Zinc Batteries. *Chemical communications* **2015**, *51*, 9265-9268.
- (8) Zhang, L.; Chen, L.; Zhou, X.; Liu, Z. Morphology-Dependent Electrochemical Performance of Zinc Hexacyanoferrate Cathode for Zinc-ion Battery. *Scientific reports* **2015**, *5*, 1-11.

- (9) Zhang, L.; Chen, L.; Zhou, X.; Liu, Z. Towards High-Voltage Aqueous Metal-Ion Batteries Beyond 1.5 V: the Zinc/Zinc hexacyanoferrate System. *Advanced Energy Materials* **2015**, *5*, 1400930.
- (10) Wan, F.; Zhang, L.; Wang, X.; Bi, S.; Niu, Z.; Chen, J. An Aqueous Rechargeable Zinc-Organic Battery with Hybrid Mechanism. *Advanced Functional Materials* **2018**, *28*, 1804975.
- (11) Park, M. J.; Yaghoobnejad Asl, H.; Manthiram, A. Multivalent-Ion versus Proton Insertion into Battery Electrodes. *ACS Energy Letters* **2020**, *5*, 2367-2375.
- (12) Pan, H.; Shao, Y.; Yan, P.; Cheng, Y.; Han, K. S.; Nie, Z.; Wang, C.; Yang, J.; Li, X.; Bhattacharya, P. Reversible Aqueous Zinc/Manganese Oxide Energy Storage from Conversion Reactions. *Nature Energy* **2016**, *1*, 1-7.
- (13) Wan, F.; Niu, Z. Design Strategies for Vanadium-based Aqueous Zinc-Ion Batteries. *Angewandte Chemie International Edition* **2019**, *58*, 16358-16367.
- (14) Zhang, N.; Dong, Y.; Jia, M.; Bian, X.; Wang, Y.; Qiu, M.; Xu, J.; Liu, Y.; Jiao, L.; Cheng, F. Rechargeable Aqueous Zn–V₂O₅ Battery with High Energy Density and Long Cycle Life. *ACS Energy Letters* **2018**, *3*, 1366-1372.
- (15) Han, J.; Wang, K.; Liu, W.; Li, C.; Sun, X.; Zhang, X.; An, Y.; Yi, S.; Ma, Y. Rational Design of Nano-Architecture Composite Hydrogel Electrode towards High Performance Zn-Ion Hybrid Cell. *Nanoscale* **2018**, *10*, 13083-13091.
- (16) Wang, X.; Chen, L.; Lu, F.; Liu, J.; Chen, X.; Shao, G. Boosting Aqueous Zn²⁺ Storage in 1, 4, 5, 8-Naphthalenetetracarboxylic Dianhydride through Nitrogen Substitution. *ChemElectroChem* **2019**, *6*, 3644-3647.
- (17) Wei, Q.; Liu, J.; Feng, W.; Sheng, J.; Tian, X.; He, L.; An, Q.; Mai, L. Hydrated Vanadium Pentoxide with Superior Sodium Storage Capacity. *Journal of Materials Chemistry A* **2015**, *3*, 8070-8075.
- (18) Yan, M.; He, P.; Chen, Y.; Wang, S.; Wei, Q.; Zhao, K.; Xu, X.; An, Q.; Shuang, Y.; Shao, Y. Water-Lubricated Intercalation in V₂O₅·nH₂O for High-Capacity and High-Rate Aqueous Rechargeable Zinc Batteries. *Advanced materials* **2018**, *30*, 1703725.
- (19) Zhang, N.; Jia, M.; Dong, Y.; Wang, Y.; Xu, J.; Liu, Y.; Jiao, L.; Cheng, F. Hydrated Layered Vanadium Oxide as a Highly Reversible Cathode for Rechargeable Aqueous Zinc Batteries. *Advanced Functional Materials* **2019**, *29*, 1807331.
- (20) Zhu, K.; Wu, T.; Huang, K. A High Capacity Bilayer Cathode for Aqueous Zn-Ion Batteries. *ACS nano* **2019**, *13*, 14447-14458.

- (21) Geng, H.; Cheng, M.; Wang, B.; Yang, Y.; Zhang, Y.; Li, C. C. Electronic Structure Regulation of Layered Vanadium Oxide via Interlayer Doping Strategy toward Superior High-Rate and Low-Temperature Zinc-Ion Batteries. *Advanced Functional Materials* **2019**, 1907684.
- (22) Ming, F.; Liang, H.; Lei, Y.; Kandambeth, S.; Eddaoudi, M.; Alshareef, H. N. Layered $Mg_xV_2O_5 \cdot nH_2O$ as Cathode Material for High-Performance Aqueous Zinc Ion Batteries. *ACS Energy Letters* **2018**, 3, 2602-2609.
- (23) Pang, Q.; He, W.; Zhao, H.; Yu, X.; Wei, Y.; Tian, Y.; Xing, M.; Fu, Y.; Luo, X. Hierarchical Aluminum Vanadate Microspheres with Structural Water: High-Performance Cathode Materials for Aqueous Rechargeable Zinc Batteries. *ChemPlusChem* **2020**, 85, 1-8.
- (24) Li, Q.; Wei, T.; Ma, K.; Yang, G.; Wang, C. Boosting the Cyclic Stability of Aqueous Zinc-Ion Battery based on Al-doped $V_{10}O_{24} \cdot 12H_2O$ Cathode Materials. *ACS Appl. Mater. Interfaces* **2019**, 11, 20888-20894.
- (25) Liu, C.; Neale, Z.; Zheng, J.; Jia, X.; Huang, J.; Yan, M.; Tian, M.; Wang, M.; Yang, J.; Cao, G. Expanded Hydrated Vanadate for High-Performance Aqueous Zinc-Ion Batteries. *Energy & Environmental Science* **2019**, 12, 2273-2285.
- (26) Ghosh, M.; Vijayakumar, V.; Kurungot, S. Dendrite Growth Suppression by Zn^{2+} -Integrated Nafion Ionomer Membranes: Beyond Porous Separators toward Aqueous Zn/V_2O_5 Batteries with Extended Cycle Life. *Energy Technology* **2019**, 7, 1900442.
- (27) Wang, D.; Ma, Z.; Dai, S.; Liu, J.; Nie, Z.; Engelhard, M. H.; Huo, Q.; Wang, C.; Kou, R. Low-Temperature Synthesis of Tunable Mesoporous Crystalline Transition Metal Oxides and Applications as Au Catalyst Supports. *The Journal of Physical Chemistry C* **2008**, 112, 13499-13509.
- (28) Alonso, B.; Livage, J. Synthesis of Vanadium Oxide Gels from Peroxovanadic Acid Solutions: a 51V NMR Study. *Journal of Solid State Chemistry* **1999**, 148, 16-19.
- (29) Fontenot, C. J.; Wiench, J. W.; Pruski, M.; Schrader, G. L. Vanadia Gel Synthesis via Peroxovanadate Precursors. 1. In situ Laser Raman and 51V NMR Characterization of the Gelation Process. *The Journal of Physical Chemistry B* **2000**, 104, 11622-11631.
- (30) Kaur, G.; Mitra, A.; Yadav, K. Pulsed Laser Deposited Al-Doped ZnO Thin Films for Optical Applications. *Progress in Natural Science: Materials International* **2015**, 25, 12-21.
- (31) Perera, S. D.; Archer, R. B.; Damin, C. A.; Mendoza-Cruz, R.; Rhodes, C. P. Controlling Interlayer Interactions in Vanadium Pentoxide-Poly (ethylene oxide)

- Nanocomposites for Enhanced Magnesium-Ion Charge Transport and Storage. *Journal of Power Sources* **2017**, *343*, 580-591.
- (32) Dong, S.; Shin, W.; Jiang, H.; Wu, X.; Li, Z.; Holoubek, J.; Stickle, W. F.; Key, B.; Liu, C.; Lu, J. Ultra-Fast NH_4^+ Storage: Strong H Bonding between NH_4^+ and Bi-Layered V_2O_5 . *Chem* **2019**, *5*, 1537-1551.
- (33) Durupthy, O.; Steunou, N.; Coradin, T.; Maquet, J.; Bonhomme, C.; Livage, J. Influence of pH and Ionic Strength on Vanadium (V) Oxides Formation. From $\text{V}_2\text{O}_5 \cdot n\text{H}_2\text{O}$ Gels to Crystalline $\text{NaV}_3\text{O}_8 \cdot 1.5\text{H}_2\text{O}$. *Journal of Materials Chemistry* **2005**, *15*, 1090-1098.
- (34) Torardi, C.; Miao, C.; Lewittes, M.; Li, Z. High Lithium Capacity $\text{M}_x\text{V}_2\text{O}_5\text{A}_y \cdot n\text{H}_2\text{O}$ for Rechargeable Batteries. *Journal of Solid State Chemistry* **2002**, *163*, 93-99.
- (35) Tian, M.; Liu, C.; Zheng, J.; Jia, X.; Jahrman, E. P.; Seidler, G. T.; Long, D.; Atif, M.; Alsalhi, M.; Cao, G. Structural Engineering of Hydrated Vanadium Oxide Cathode by K^+ Incorporation for High-Capacity and Long-Cycling Aqueous Zinc Ion Batteries. *Energy Storage Materials* **2020**.
- (36) Ma, R.; Bando, Y.; Sasaki, T. Directly Rolling Nanosheets into Nanotubes. *The Journal of Physical Chemistry B* **2004**, *108*, 2115-2119.
- (37) Zarate, R.; Fuentes, S.; Cabrera, A.; Fuenzalida, V. Structural Characterization of Single Crystals of Sodium Titanate Nanowires Prepared by Hydrothermal Process. *Journal of Crystal Growth* **2008**, *310*, 3630-3637.
- (38) Etman, A. S.; Asfaw, H. D.; Yuan, N.; Li, J.; Zhou, Z.; Peng, F.; Persson, I.; Zou, X.; Gustafsson, T.; Edström, K. A One-Step Water based Strategy for Synthesizing Hydrated Vanadium Pentoxide Nanosheets from $\text{VO}_2(\text{B})$ as Free-Standing Electrodes for Lithium Battery Applications. *Journal of Materials Chemistry A* **2016**, *4*, 17988-18001.
- (39) Lee, J.; Badie, S.; Srimuk, P.; Ridder, A.; Shim, H.; Choudhury, S.; Nah, Y.-C.; Presser, V. Electrodeposition of Hydrated Vanadium Pentoxide on Nanoporous Carbon Cloth for Hybrid Energy Storage. *Sustainable Energy & Fuels* **2018**, *2*, 577-588.
- (40) Manikandan, R.; Raj, C. J.; Rajesh, M.; Kim, B. C.; Park, S.; Yu, K. H. Vanadium Pentoxide with H_2O , K^+ , and Na^+ Spacer between Layered Nanostructures for High-Performance Symmetric Electrochemical Capacitors. *Advanced Materials Interfaces* **2018**, *5*, 1800041.

- (41) McNulty, D.; Buckley, D. N.; O'Dwyer, C. Optimizing the Structure and Yield of Vanadium Oxide Nanotubes by Periodic 2D Layer Scrolling. *RSC advances* **2016**, *6*, 40932-40944.
- (42) Hu, C.-C.; Huang, C.-M.; Chang, K.-H. Anodic Deposition of Porous Vanadium Oxide Network with High Power Characteristics for Pseudocapacitors. *Journal of Power Sources* **2008**, *185*, 1594-1597.
- (43) Kundu, S.; Satpati, B.; Mukherjee, M.; Kar, T.; Pradhan, S. K. Hydrothermal Synthesis of Polyaniline Intercalated Vanadium Oxide Xerogel Hybrid Nanocomposites: Effective Control of Morphology and Structural Characterization. *New Journal of Chemistry* **2017**, *41*, 3634-3645.
- (44) Zeng, H.; Liu, D.; Zhang, Y.; See, K. A.; Jun, Y.-S.; Wu, G.; Gerbec, J. A.; Ji, X.; Stucky, G. D. Nanostructured Mn-Doped V₂O₅ Cathode Material Fabricated From Layered Vanadium Jarosite. *Chemistry of Materials* **2015**, *27*, 7331-7336.
- (45) Silversmit, G.; Depla, D.; Poelman, H.; Marin, G. B.; De Gryse, R. Determination of the V2p XPS Binding Energies for Different Vanadium Oxidation States (V⁵⁺ to V⁰⁺). *Journal of Electron Spectroscopy and Related Phenomena* **2004**, *135*, 167-175.
- (46) Raju, V.; Rains, J.; Gates, C.; Luo, W.; Wang, X.; Stickle, W. F.; Stucky, G. D.; Ji, X. Superior Cathode of Sodium-Ion Batteries: Orthorhombic V₂O₅ Nanoparticles Generated in Nanoporous Carbon by Ambient Hydrolysis Deposition. *Nano letters* **2014**, *14*, 4119-4124.
- (47) Deng, X.; Xu, Y.; An, Q.; Xiong, F.; Tan, S.; Wu, L.; Mai, L. Manganese Ion Pre-Intercalated Hydrated Vanadium Oxide as a High-Performance Cathode for Magnesium Ion Batteries. *Journal of Materials Chemistry A* **2019**, *7*, 10644-10650.
- (48) Yu, D.; Zhang, S.; Liu, D.; Zhou, X.; Xie, S.; Zhang, Q.; Liu, Y.; Cao, G. Effect of Manganese Doping on Li-Ion Intercalation Properties of V₂O₅ Films. *Journal of Materials chemistry* **2010**, *20*, 10841-10846.
- (49) Du, M.; Liu, C.; Zhang, F.; Dong, W.; Zhang, X.; Sang, Y.; Wang, J. J.; Guo, Y. G.; Liu, H.; Wang, S. Tunable Layered (Na, Mn) V₈O₂₀·nH₂O Cathode Material for High-Performance Aqueous Zinc Ion Batteries. *Advanced Science*, 2000083.
- (50) Peng, C.; Xiao, F.; Yang, J.; Li, Z.; Lei, G.; Xiao, Q.; Ding, Y.; Hu, Z. Carbon-Encapsulated Mn-Doped V₂O₅ Nanorods with Long Span Life for High-Power Rechargeable Lithium Batteries. *Electrochimica Acta* **2016**, *192*, 216-226.
- (51) Sambandam, B.; Soundharajan, V.; Kim, S.; Alfaruqi, M. H.; Jo, J.; Kim, S.; Mathew, V.; Sun, Y.-k.; Kim, J. Aqueous Rechargeable Zn-Ion batteries: An Imperishable and

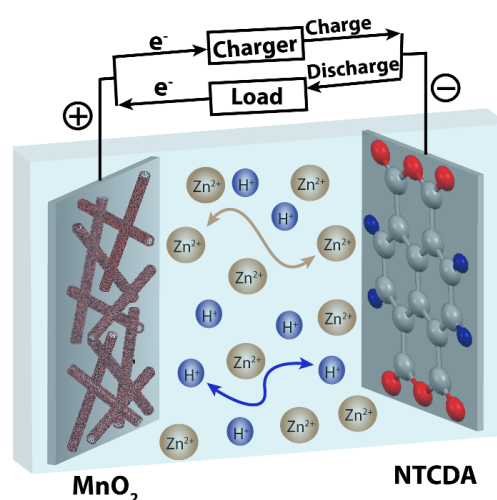
- High-Energy $\text{Zn}_2\text{V}_2\text{O}_7$ Nanowire Cathode Through Intercalation Regulation. *Journal of Materials Chemistry A* **2018**, *6*, 3850-3856.
- (52) Dong, X.; Chen, L.; Liu, J.; Haller, S.; Wang, Y.; Xia, Y. Environmentally-Friendly Aqueous Li (or Na)-Ion Battery with Fast Electrode Kinetics and Super-Long Life. *Science advances* **2016**, *2*, e1501038.
- (53) Simon, P.; Gogotsi, Y.; Dunn, B. Where Do Batteries End and Supercapacitors Begin? *Science* **2014**, *343*, 1210-1211.
- (54) Augustyn, V.; Come, J.; Lowe, M. A.; Kim, J. W.; Taberna, P.-L.; Tolbert, S. H.; Abruña, H. D.; Simon, P.; Dunn, B. High-Rate Electrochemical Energy Storage Through Li^+ Intercalation Pseudocapacitance. *Nature materials* **2013**, *12*, 518-522.
- (55) Wang, J.; Polleux, J.; Lim, J.; Dunn, B. Pseudocapacitive Contributions to Electrochemical Energy Storage in TiO_2 (anatase) Nanoparticles. *The Journal of Physical Chemistry C* **2007**, *111*, 14925-14931.
- (56) Zhao, J.; Ren, H.; Liang, Q.; Yuan, D.; Xi, S.; Wu, C.; Manalastas Jr, W.; Ma, J.; Fang, W.; Zheng, Y. High-Performance Flexible Quasi-Solid-State Zinc-Ion Batteries with Layer-Expanded Vanadium Oxide Cathode and Zinc/Stainless Steel Mesh Composite Anode. *Nano Energy* **2019**, *62*, 94-102.
- (57) Wei, T.; Li, Q.; Yang, G.; Wang, C. Highly Reversible and Long-Life Cycling Aqueous Zinc-Ion Battery Based on Ultrathin $(\text{NH}_4)_2\text{V}_{10}\text{O}_{25}\cdot 8\text{H}_2\text{O}$ Nanobelts. *Journal of Materials Chemistry A* **2018**, *6*, 20402-20410.
- (58) Zhang, W.; Liang, S.; Fang, G.; Yang, Y.; Zhou, J. Ultra-High Mass-Loading Cathode for Aqueous Zinc-Ion Battery Based on Graphene-Wrapped Aluminum Vanadate Nanobelts. *Nano-Micro Letters* **2019**, *11*, 69.
- (59) Xia, C.; Guo, J.; Li, P.; Zhang, X.; Alshareef, H. N. Highly Stable Aqueous Zinc-Ion Storage Using a Layered Calcium Vanadium Oxide Bronze Cathode. *Angewandte Chemie International Edition* **2018**, *57*, 3943-3948.
- (60) He, P.; Zhang, G.; Liao, X.; Yan, M.; Xu, X.; An, Q.; Liu, J.; Mai, L. Sodium Ion Stabilized Vanadium Oxide Nanowire Cathode for High-Performance Zinc-Ion Batteries. *Advanced Energy Materials* **2018**, *8*, 1702463.
- (61) Liu, W.; Dong, L.; Jiang, B.; Huang, Y.; Wang, X.; Xu, C.; Kang, Z.; Mou, J.; Kang, F. Layered Vanadium Oxides with Proton and Zinc Ion Insertion for Zinc Ion Batteries. *Electrochimica Acta* **2019**, *320*, 134565.

- (62) Liang, X.; Hao, J.; Tan, B.; Lu, X.; Li, W. Binder-Free CaV_3O_7 Nanobelts with Rich Oxygen Defects as High Energy Cathode for Aqueous Zn-Ion Battery. *Journal of Power Sources* **2020**, *472*, 228507.
- (63) Wang, M.; Zhang, J.; Zhang, L.; Li, J.; Wang, W.; Yang, Z.; Zhang, L.; Wang, Y.; Chen, J.; Huang, Y. Graphene-Like Vanadium Oxygen Hydrate (VOH) Nanosheets Intercalated and Exfoliated by Polyaniline (PANI) for Aqueous Zinc-Ion Batteries (ZIBs). *ACS applied materials & interfaces* **2020**, *12*, 31564-31574.
- (64) Venkatkarthick, R.; Rodthongkum, N.; Zhang, X.; Wang, S.; Pattananuwat, P.; Zhao, Y.; Liu, R.; Qin, J. Vanadium-Based Oxide on Two-Dimensional Vanadium Carbide MXene ($\text{V}_2\text{O}_x @ \text{V}_2\text{CT}_x$) as Cathode for Rechargeable Aqueous Zinc-Ion Batteries. *ACS Applied Energy Materials* **2020**, *3*, 4677-4689.
- (65) Tang, W.; Lan, B.; Tang, C.; An, Q.; Chen, L.; Zhang, W.; Zuo, C.; Dong, S.; Luo, P. Urchin-Like Spinel MgV_2O_4 as a Cathode Material for Aqueous Zinc-Ion Batteries. *ACS Sustainable Chemistry & Engineering* **2020**, *8*, 3681-3688.
- (66) Ghosh, M.; Vijayakumar, V.; Anothumakkool, B.; Kurungot, S. Nafion Ionomer-Based Single Component Electrolytes for Aqueous Zn/MnO₂ Batteries with Long Cycle Life. *ACS Sustainable Chemistry & Engineering* **2020**, *8*, 5040-5049.
- (67) Lee, B.-S.; Cui, S.; Xing, X.; Liu, H.; Yue, X.; Petrova, V.; Lim, H.-D.; Chen, R.; Liu, P. Dendrite Suppression Membranes for Rechargeable Zinc Batteries. *ACS applied materials & interfaces* **2018**, *10*, 38928-38935.
- (68) Soundharrajan, V.; Sambandam, B.; Kim, S.; Alfaruqi, M. H.; Putro, D. Y.; Jo, J.; Kim, S.; Mathew, V.; Sun, Y.-K.; Kim, J. $\text{Na}_2\text{V}_6\text{O}_{16} \cdot 3\text{H}_2\text{O}$ Barnesite Nanorod: An Open Door to Display a Stable and High Energy for Aqueous Rechargeable Zn-Ion Batteries as Cathodes. *Nano Letters* **2018**, *18*, 2402-2410.
- (69) Lai, J.; Tang, H.; Zhu, X.; Wang, Y. A Hydrated $\text{NH}_4\text{V}_3\text{O}_8$ Nanobelt Electrode for Superior Aqueous and Quasi-Solid-State Zinc Ion Batteries. *Journal of Materials Chemistry A* **2019**, *7*, 23140-23148.
- (70) Han, Q.; Chi, X.; Zhang, S.; Liu, Y.; Zhou, B.; Yang, J.; Liu, Y. Durable, Flexible Self-Standing Hydrogel Electrolytes Enabling High-Safety Rechargeable Solid-State Zinc Metal Batteries. *Journal of Materials Chemistry A* **2018**, *6*, 23046-23054.

Chapter 5

Naphthalene Dianhydride Organic Anode for ‘Rocking-Chair’ Zinc-Proton Hybrid Ion Battery

Rechargeable batteries consisting of a Zn metal anode and a suitable cathode coupled with a Zn^{2+} -conducting electrolyte are recently emerging as promising energy storage devices for stationary applications. However, the formation of high surface area Zn (HSAZ) architectures on the metallic Zn anode deteriorates their performance during prolonged cycling. In this work, we demonstrate the application of 1,4,5,8-naphthalenetetracarboxylic dianhydride (NTCDA), an organic compound, as a replacement for the Zn-metal anode enabling the design of a ‘rocking-chair’ *zinc-proton hybrid ion* battery. The NTCDA electrode material displays a multi-plateau redox behavior delivering a specific discharge capacity value of 143 mAh g^{-1} in the potential window of 1.4 V to 0.30 V vs. $\text{Zn}|\text{Zn}^{2+}$. The detailed electrochemical characterization of NTCDA in various electrolytes (an aqueous solution of 1M $\text{Zn}(\text{CF}_3\text{SO}_3)_2$, an aqueous solution of 0.01M H_2SO_4 , and an organic electrolyte of 0.5 M $\text{Zn}(\text{CF}_3\text{SO}_3)_2/\text{Acetonitrile}$) reveals that the redox processes leading to charge storage involve the contribution from both H^+ and Zn^{2+} . The performance of NTCDA as an anode is further demonstrated by pairing it with MnO_2 cathode, and the resulting $\text{NTCDA}||\text{MnO}_2$ full-cell (*zinc-proton hybrid ion battery*) delivers a specific discharge capacity of $41 \text{ mAh g}_{\text{total}}^{-1}$ (normalized with the total mass-loading of both anode and cathode active materials) with an average operating voltage of 0.80 V.



NTCDA||MnO₂ zinc-proton hybrid ion battery

Contents in this chapter is published in the article: DOI: 10.1039/D0DT04404K. (Reprinted (adapted) with permission from Dalton Trans., 2021, 50, 4237-4243. Copyright (2021) Royal Society of Chemistry.)

5.1 Introduction

Recently, the post-lithium battery technology employing Zn electrochemistry is receiving significant attention among battery enthusiasts. Compared to the lithium-ion batteries (LIBs), the features such as relatively better safety and easy device fabricability by employing cost-effective aqueous electrolytes and electrode materials leverage the prospects of the Zn batteries.¹ A conventional aqueous rechargeable Zn-metal battery (ARZMB) cell consists of a metallic Zn anode, an insertion/conversion-type cathode, and a separator soaked in Zn^{2+} ion conducting liquid electrolyte (pH of 4-6).² However, the major difficulties associated with these ARZMBs are the possible growth of High Surface Area Zinc (HSAZ; also known as dendrite) deposits and hydrogen evolution reaction (HER) at the metallic-anode during the charging steps.³ These drawbacks result in low Coulombic efficiency and cycling stability of ARZMBs.

The aforementioned challenges have been tackled by adopting various strategies that can tune the electrode|electrolyte interface between the Zn-metal and liquid electrolyte in ARZMBs. These attempts include the use of different electrolytes (*e.g.*, $\text{Zn}(\text{CF}_3\text{SO}_3)_2$, $\text{Zn}(\text{TFSI})_2$, *etc.*), utilization of cation-selective ionomer separators (*e.g.*, Nafion and polyacrylonitrile membranes) instead of neutral porous separators (*e.g.*, glass fiber), and surface modification of Zn with carbon, TiO_2 , CaCO_3 , *etc.*⁴⁻⁸ Another logical approach to overcome the problems associated with a Zn metal anode is its replacement with an electrode material that can facilitate reversible insertion/extraction of Zn^{2+} ions so that the transition from ARZMB to the aqueous rechargeable Zn-ion batteries (ARZIBs) can be enabled. Such insertion anode materials are popular with the other post-lithium batteries (Na-ion, Mg-ion, and K-ion batteries); the chemistry is rarely explored in the context of ARZIBs.

The key features desirable for efficient anode material for ARZIBs are the high reversibility and stability toward Zn^{2+} -insertion/extraction at relatively low potentials *vs.* $\text{Zn}|\text{Zn}^{2+}$ delivering high specific capacity. Cheng *et al.* reported the first example of a Zn^{2+} -intercalating anode that utilizes chevrel phase Mo_6S_8 nanocubes.⁹ Kaveevivitchai *et al.* demonstrated the performance of an open-tunnel oxide of $\text{Zn}_x\text{Mo}_{2.5+y}\text{VO}_{9+z}$ that can be used as an insertion anode in both aqueous and nonaqueous electrolytes delivering a high specific capacity of 220 mAh g^{-1} .¹⁰ Li *et al.* demonstrated pre-sodiated TiS_2 as an insertion anode in aqueous ARZIB.¹¹ Despite these few attempts, the research on ‘rocking chair’ ARZIBs, especially with organic materials as anodes, is minimal, and therefore, exploring potential electrode materials is important.

Organic compounds have received tremendous interest as the anode materials in LIB and Na-ion battery applications. Compared to the most commonly used inorganic materials, the organic molecular solids facilitate the reversible uptake/release of the charged species by undergoing molecular reorientation and accompanied redox reactions.¹² In this aspect, developing Zn²⁺-insertion anodes based on organic molecules could be an attractive choice. Here, we investigate the electrochemical performance of 1,4,5,8-naphthalenetetracarboxylic dianhydride (NTCDA) as a reversible Zn²⁺ host in an aqueous electrolyte. During the electrochemical investigation, H⁺ was also found to be contributing to the charge-storage behavior of NTCDA. Finally, to demonstrate the suitability of NTCDA as the insertion anode, a prototype ARZIB full-cell was also fabricated by pairing the NTCDA anode against MnO₂ cathode (NTCDA||MnO₂). The term '*zinc-proton hybrid ion battery*' was coined to address the fabricated ARZIB to emphasize the role of H⁺ and Zn²⁺ in the charge storage mechanism. The cell displayed a specific capacity of 41 mAh g⁻¹_{total}, considering the active material loading in both the positive and negative electrodes. The zinc-proton hybrid ion battery cell also displayed a good average voltage of ~0.80 V, close to several other ARZIBs based on the other cathodes such as V₂O₅, VS₂, and PDA/CNT.¹³⁻¹⁵ To the best of our knowledge, this is the first report on an organic anhydride molecule that can act as an anode capable of storing Zn²⁺ ions, which is used for fabricating aqueous rechargeable ARZIB/zinc-proton hybrid ion batteries.

5.2 Experimental Section

5.2.1 Materials

1,4,5,8-naphthalenetetracarboxylic dianhydride (NTCDA) was purchased from TCI Chemicals and used without further purification. Zinc trifluoromethanesulfonate (Zn(CF₃SO₃)₂/ZnOTF) was procured from Sigma-Aldrich. Nafion 212 and Grafoil sheets were supplied by Du Pont, USA, and Global Nanotech, respectively. The solvent acetonitrile (ACN) used for the electrolyte preparation was purchased from Thomas Baker.

5.2.2 Fabrication of electrodes

For preparing the electrode, at first, 4 mg of NTCDA and 1 mg of the conducting additive (carbon nanofiber, CNF) (80:20 weight ratio) were dispersed in 250 µl of water-isopropanol (2:1) mixture and 10 µl of 5 wt. % Nafion solution (DuPont). A required amount of the dispersion was spread over 1.0 cm² area of Grafoil, and the coated electrodes were dried at 60°C. The loading of the electrodes was maintained as 1 mg cm⁻². The MnO₂ electrode with a mass-loading of 1 mg cm⁻² was prepared by electrodeposition of MnO₂ over the Toray carbon fiber paper following our previous report¹⁶

5.2.3 Fabrication of electrochemical cell

All the electrochemical cells were fabricated in CR2032 coin cell assembly. The Zn||NTCDA half-cells were assembled using a piece of Zn foil (area 1.0 cm²) and NTCDA-coated Grafoil (1.0 mg cm⁻²) as the negative and positive electrodes, respectively. A Nafion 212 membrane soaked in an aqueous solution of 1M ZnOTF electrolyte (1M ZnOTF/Aq.) was used as the separator. This cell was marked as Zn||NTCDA-(N), where ‘N’ stands for the nearly-neutral electrolyte (pH ≈ 4) used for the cell fabrication. For comparison, the NTCDA electrode was also tested in 0.01M H₂SO₄ (pH ≈ 1.7) and 0.5M ZnOTF/ACN electrolytes, and the coin cells are labeled as Zn||NTCDA-(A) and Zn||NTCDA-(O), respectively; here, the letters ‘A’ and ‘O’ stand for acidic and organic electrolytes, respectively. The electrochemical performance of MnO₂ was also tested in a similar way using MnO₂ (1.0 mg cm⁻²) as the positive electrode and Zn foil as the negative electrode separated by the Nafion membrane pre-soaked with the 1M ZnOTF/Aq. electrolyte. The corresponding electrochemical cell was marked as Zn||MnO₂-(N).

The three-electrode characterization of NTCDA electrode in 0.01M H₂SO₄ and 0.1M ZnOTF/Aq. were carried out using NTCDA coated Grafoil as the working electrode, Pt mesh as the counter electrode, and Hg/Hg₂SO₄ as the reference electrode. Similarly, the electrodeposited MnO₂ electrode was also tested in 0.005M H₂SO₄ (pH ≈ 2) and 0.1 M ZnOTF/Aq. electrolyte in the three-electrode cell assembly. Here, a low concentration of the H₂SO₄ electrolyte was taken to ensure minimum dissolution of the MnO₂ in the acid solution. For the fabrication of the ARZIB full-cell, the loadings of the NTCDA anode and MnO₂ cathode were calculated from the following equation:

$$M_{\text{cathode}}/M_{\text{anode}} = Q_{\text{anode}}/Q_{\text{cathode}} \quad (\text{Equation 5.1})$$

where, ‘M’ and ‘Q’ represent the mass-loading and the specific capacity of the electrode materials, respectively.¹⁷ Here, the specific capacity values of the respective electrodes are measured at 0.1 A g⁻¹ current rate from the half-cell study (Zn||NTCDA-(N) and Zn||MnO₂-(N) cells) with the electrode material mass-loading of 1 mg cm⁻².

$$M_{\text{MnO}_2}/M_{\text{NTCDA}} = 143 \text{ mAh g}^{-1}/281 \text{ mAh g}^{-1} = 1/1.9 \quad (\text{Equation 5.2})$$

Comparing the capacity of the electrode materials, the ratio of NTCDA:MnO₂ was taken as *ca.* 2:1 (**Equation 5.2**). Before assembling the full-cell, the MnO₂ electrode was activated by electrochemical cycling for two discharge cycles at a current rate of 0.5 A g⁻¹ in a two-electrode cell configuration, taking MnO₂ as the positive and Zn as the negative electrode in aqueous 1M

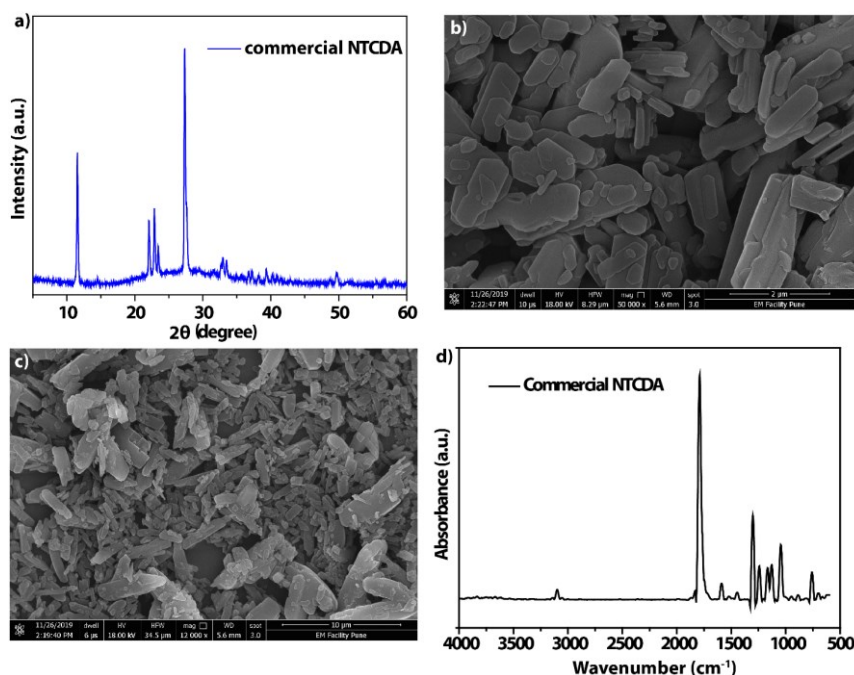


Figure 5.1. (a) XRD data, (b)-(c) FESEM images, and (d) FTIR data of the commercial NTCDA. (Reprinted (adapted) with permission from *Dalton Trans.*, 2021, 50, 4237-4243. Copyright (2021) Royal Society of Chemistry.).

ZnOTF/Aq. electrolyte. After that, the MnO_2 electrode was recovered carefully and paired with the NTCDA electrode for assembling the NTCDA|| MnO_2 full-cell using the 1M ZnOTF/Aq. electrolyte. For calculating the specific capacity of the full-cell, the total capacity was normalized with respect to the cumulative mass-loading of the NTCDA anode (2 mg cm^{-2}) and MnO_2 cathode (1 mg cm^{-2}).

5.2.4 Electrochemical measurements

All the electrochemical measurements were recorded with Biologic VMP3 instrument. The cyclic voltammetry (CV) analysis of the Zn||NTCDA-(N) half-cell was carried out at the scan rates of 0.1, 0.3, 0.5, and 1 mV s^{-1} . Galvanostatic charge-discharge (GCD) data were collected at 0.10, 0.25, 0.50, 1.0, and 2.0 A g^{-1} current rates. The current rates and capacity values in the half-cell study are reported considering the mass-loading of the working electrode alone. The NTCDA|| MnO_2 full-cell was also characterized with CV (at 5 mV s^{-1}) and GCD (0.17, 0.33, 0.67, and $1.0 \text{ A g}_{\text{total}}^{-1}$, the current rates are normalized with respect to the total mass-loading of both electrodes). The GCD data of the Zn|| MnO_2 -(N) half-cell were recorded at various current rates (0.1, 0.25, 0.5, and 1 A g^{-1}) using the Neware battery tester instrument.

5.2.5 Material characterization

Field emission scanning electron microscope (FESEM) Nova Nano SEM 450 and scan-

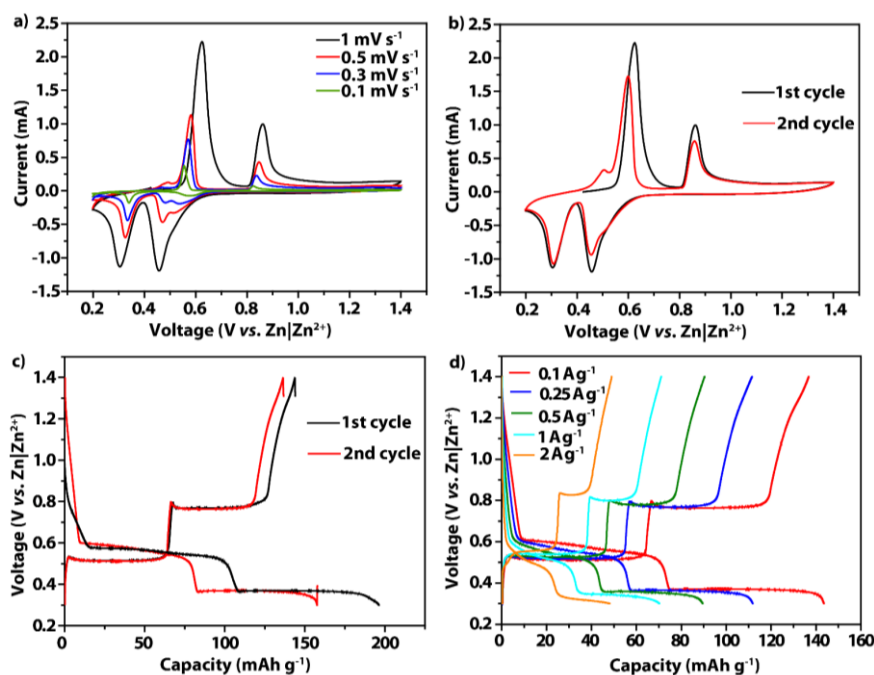


Figure 5.2. (a) CV profiles recorded at various scan rates, (b) CV profiles recorded at the scan rate of 1.0 mV s^{-1} , (c) GCD profiles recorded at the current rate of 0.1 A g^{-1} , and (d) GCD profiles recorded at various current rates for the $\text{Zn}||\text{NTCDA-(N)}$ cell. (Reprinted (adapted) with permission from *Dalton Trans.*, 2021, 50, 4237-4243. Copyright (2021) Royal Society of Chemistry).

ning electron microscope (SEM) Quanta 200-3D FEI instruments were used for investigating the morphology of the samples. The elemental composition was investigated through energy dispersive X-ray spectroscopy (EDAX) analysis. EDAX elemental mapping was carried out with an ESEM-Quanta 200-3D instrument. X-ray diffraction (XRD) analysis was recorded with Rigaku, MicroMax-007HF with high-intensity Microfocus rotating anode X-ray generator ($\text{Cu K}\alpha$ ($\alpha = 1.54 \text{ \AA}$)). XPS data are collected with Thermo Scientific K-Alpha+ instrument. Fourier transform infrared (FTIR) analysis was performed with a Bruker Tensor 27 FTIR instrument.

5.3 Result and discussion

The commercial NTCDA molecule possesses monoclinic crystal structure and belongs to $\text{P2}_1/\text{c}$ space group ($a = 7.880 \text{ \AA}$, $b = 5.322 \text{ \AA}$, $c = 12.601 \text{ \AA}$, $\alpha = 90^\circ$, $\beta = 107.257^\circ$, $\gamma = 90^\circ$). The XRD pattern (**Figure 5.1a**) of the commercial NTCDA indicates the crystalline nature of the sample. The FESEM images (**Figure 5.1b** and **c**) of the material show irregular rod-like morphology. FTIR data of the commercial NTCDA (**Figure 5.1d**) displays a strong peak at

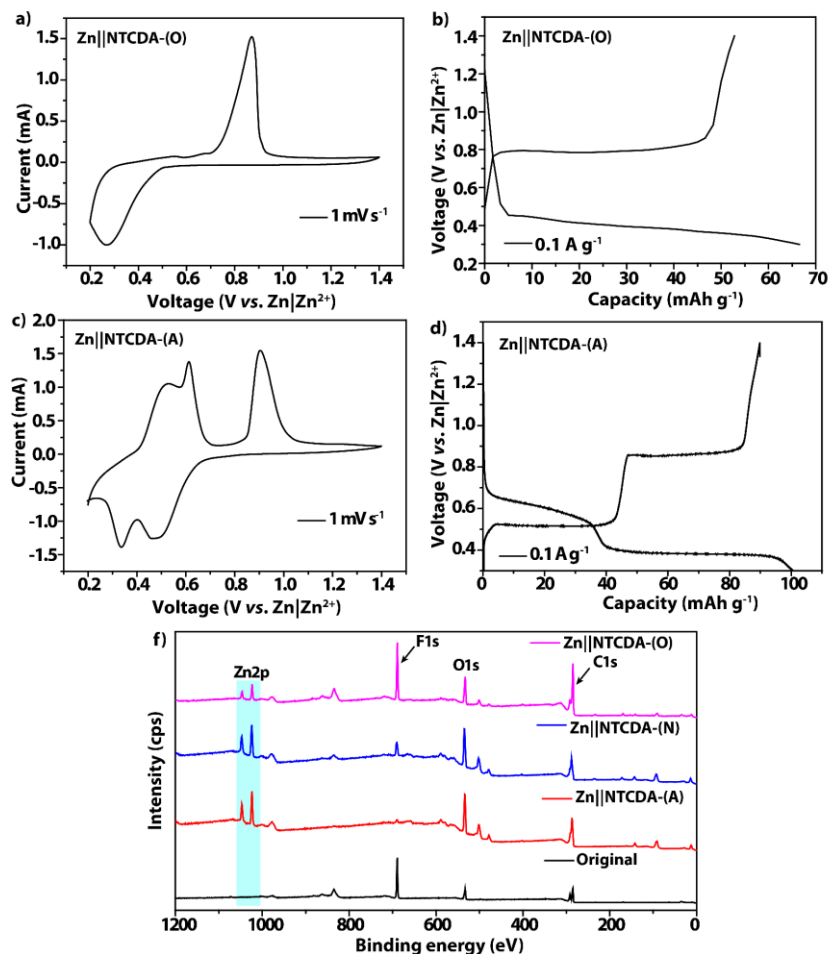


Figure 5.3. (a) CV and (b) GCD profiles for the Zn||NTCDA-(O) cell; (c) CV and (d) GCD profiles for the Zn||NTCDA-(A) cell; (f) XPS survey spectra of the NTCDA electrodes at the original state and after recovering from the Zn||NTCDA-(N), Zn||NTCDA-(A), and Zn||NTCDA-(O) cells at the discharged state. (Reprinted (adapted) with permission from Dalton Trans., 2021, 50, 4237-4243. Copyright (2021) Royal Society of Chemistry).

1790 cm⁻¹ corresponding to the C=O bond vibration of the anhydride moiety. At first, the electrochemical performance of NTCDA is evaluated in 1M ZnOTF/Aq. electrolyte in the Zn||NTCDA-(N) half-cell. As shown in **Figure 5.2a**, the CV profiles of the cell at different scan rates exhibit two pairs of reversible redox peaks. At a scan rate of 1 mV s⁻¹, the cathodic peaks appear at 0.45 and 0.31 V vs. Zn|Zn²⁺ and the anodic peaks at 0.59 and 0.85 V vs. Zn|Zn²⁺. By comparing the first and second CV cycles at the same scan rate (1 mV s⁻¹), a slight drop in current response is observed (**Figure 5.2b**), showing irreversible capacity loss during the cycling.

The charge/discharge capacity of NTCDA is obtained from the GCD experiment. **Figure 5.2c** represents the GCD plots recorded at the current rate of 0.1 A g⁻¹, showing the

initial capacity. The charge and discharge plateaus in the GCD curves (**Figure 5.2c** and **d**) are consistent with the redox peaks present in the CV profile (**Figure 5.2a**), suggesting multi-step redox reactions. As shown in **Figure 5.2c**, in the first discharge, NTCDA delivers a high discharge capacity of 197 mAh g⁻¹. However, a slight drop in the capacity is observed in the subsequent cycles resulting in the discharge capacities of 157 and 143 mAh g⁻¹ in the 2nd and 3rd discharge, respectively. The capacity loss observed during the initial cycles could be caused by the slight irreversibility in the discharging and charging processes due to the trapping of ions into the NTCDA matrix, which cannot travel back to the electrolyte during the reverse scan. The GCD plots at different current rates (**Figure 5.2d**) display that NTCDA could deliver specific discharge capacities of 112, 89, 70, and 47 mAh g⁻¹ at 0.25, 0.50, 1.0, and 2.0 A g⁻¹, respectively.

The multi-plateau characteristic of the Zn||NTCDA-(N) cell could be originated from the insertion of both the H⁺ and Zn²⁺ ions in the NTCDA host assisted by the redox active C=O groups present in it. It is known that the Zn²⁺-based aqueous electrolyte inevitably contains protons (H⁺) that could take part in the electrochemical processes.¹⁸ To prove and understand the possible contribution from water and proton toward the charge/discharge capacity of NTCDA, the electrochemical characterization of NTCDA is investigated in 0.01M H₂SO₄ (Zn||NTCDA-(A)) and 0.5M ZnOTF/ACN (Zn||NTCDA-(O)) electrolytes. In aprotic organic electrolyte (0.5M ZnOTF/ACN), the NTCDA electrode shows only one pair of oxidation and reduction peaks (**Figure 5.3a**), delivering a specific discharge capacity of 66 mAh g⁻¹ (**Figure 5.3b**). The reduction peak of NTCDA (onset potential of 0.47 V vs. Zn|Zn²⁺) in an aprotic electrolyte (**Figure 5.3a**) appears close to the low-voltage reduction peak (onset potential of 0.40 V vs. Zn|Zn²⁺) in 1M ZnOTF/Aq. (**Figure 5.2a**). This resemblance suggests that the coordination of Zn²⁺ with the reduced C=O groups takes place at a lower potential region (vs. Zn|Zn²⁺) in a Zn²⁺ conducting electrolyte.^{19, 20}

However, the CV feature of NTCDA in H₂SO₄ electrolyte (**Figure 5.3c**) shows two distinct reduction peaks (onset potential of 0.40 V and 0.65 V vs. Zn|Zn²⁺). These two peaks indicate the plausible interaction of the C=O groups with H⁺ and Zn²⁺ in the successive steps (**Figure 5.3d**). In the acidic electrolyte, during the 1st discharge of Zn||NTCDA-(A) cell, the metallic Zn anode may dissolve in the electrolyte as Zn²⁺. Therefore, the dissolved Zn²⁺ ions in the electrolyte can diffuse into NTCDA and interact with the C=O groups during electrochemical cycling. To confirm the presence of Zn²⁺, the NTCDA electrode was collected at the discharged state of the Zn||NTCDA-(A) cell and characterized by XPS analysis. As shown in the survey spectra (**Figure 5.3e**), the NTCDA electrode in 0.01M H₂SO₄ electrolyte

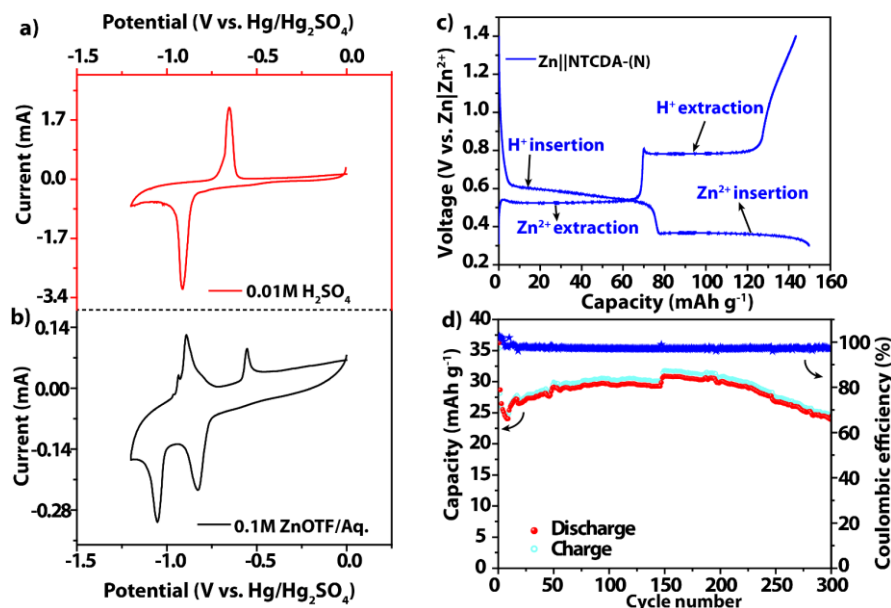


Figure 5.4. CV profiles recorded for the NTCDA electrode characterized in the three-electrode cell with respect to Hg/Hg₂SO₄ reference electrode in (a) 0.01M H₂SO₄ and (b) 0.1M ZnOTF/Aq. electrolytes; (c) GCD plots for the Zn||NTCDA-(N) cell (at 0.1 A g⁻¹ current rate) showing the potential region for predominant Zn²⁺ and/or H⁺ coordination with NTCDA ; (d) cycling stability data measured at a current rate of 2 A g⁻¹ for the Zn||NTCDA-(N) cell. (Reprinted (adapted) with permission from Dalton Trans., 2021, 50, 4237-4243. Copyright (2021) Royal Society of Chemistry).

displays an intense Zn2p XPS peak similar to the other two electrodes in the ZnOTF/ACN and ZnOTF/Aq. electrolytes in the discharged state. Hence, the XPS data supports the Zn corrosion in the H₂SO₄ electrolyte, which justifies the involvement of both H⁺ and Zn²⁺ charge carriers in the Faradaic reactions leading to the origin of the two reduction peaks as appeared in the CV profile of the Zn||NTCDA-(A) cell.

To further confirm the H⁺ association with NTCDA, the CV analysis was carried out in a standard three-electrode cell in 0.01M H₂SO₄ electrolyte taking Pt mesh as the counter electrode and Hg/Hg₂SO₄ as the reference electrode. As displayed in **Figure 5.4a**, the NTCDA exhibits a single reduction peak at an onset potential of -0.84 V vs. Hg/Hg₂SO₄. It must be noted that the aforementioned three-electrode cell does not contain Zn, and H⁺ is the only positive charge carrier present in the electrolyte. Hence, the obtained redox peaks in the CV profile (**Figure 5.4a**) associate H⁺ uptake by the C=O groups of NTCDA. Interestingly, when the electrolyte is switched to 0.1M ZnOTF/Aq. (**Figure 5.4b**), the reduction peak at higher voltage (onset potential -0.75 V vs. Hg/Hg₂SO₄) is retained followed by the appearance of an

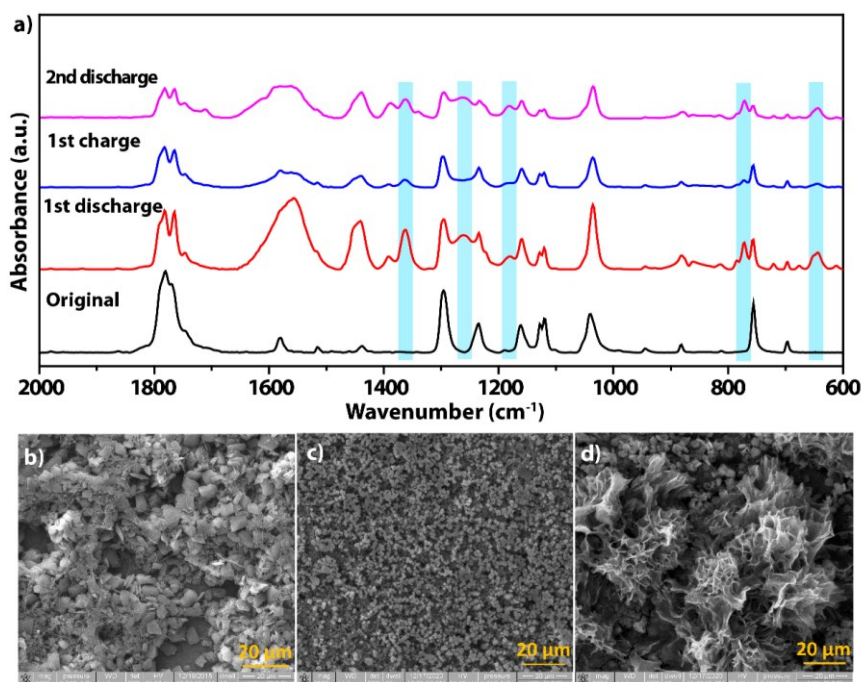


Figure 5.5. (a) FTIR data of the NTCDA electrodes obtained at the original state and after recovering from the Zn||NTCDA-(N) cells at the discharged and charged states; SEM image of the NTCDA electrodes obtained at (b) original state, recovered from the Zn||NTCDA-(N) cell at (c) discharged and (d) charged states. (Reprinted (adapted) with permission from Dalton Trans., 2021, 50, 4237-4243. Copyright (2021) Royal Society of Chemistry).

additional peak at a lower voltage (onset potential -1.0 V vs. Hg/Hg₂SO₄). Based on the aforementioned observations, the reduction process of NTCDA in ZnOTF/Aq. electrolyte is divided into two steps: the first step at a higher voltage region mainly involves H⁺ coordination, whereas Zn²⁺ coordination is predominant in the second step (**Figure 5.4c**). Therefore, the above discussion clearly points out that both the Zn²⁺ and H⁺ storage have significant contribution to the total capacity obtained for NTCDA electrode in the ZnOTF/Aq. electrolyte.

The long-term cycling stability of the Zn||NTCDA-(N) cell is recorded at 2 A g⁻¹ current rate. As given in **Figure 5.4d**, the cell shows a performance drop in the initial cycles reaching a discharge capacity of 24 mAh g⁻¹. In the following cycles, the capacity of the cell is found to increase gradually, delivering 30 mAh g⁻¹ capacity after 150 cycles. The observed increment in the capacity could be due to the electrochemical activation of NTCDA with cycling. Moreover, the cell could be cycled over 300 charge/discharge cycles with good capacity retention. The gradual capacity loss of NTCDA could be due to the hydrolysis of the anhydride groups in aqueous electrolyte (pH ≈ 4).²¹

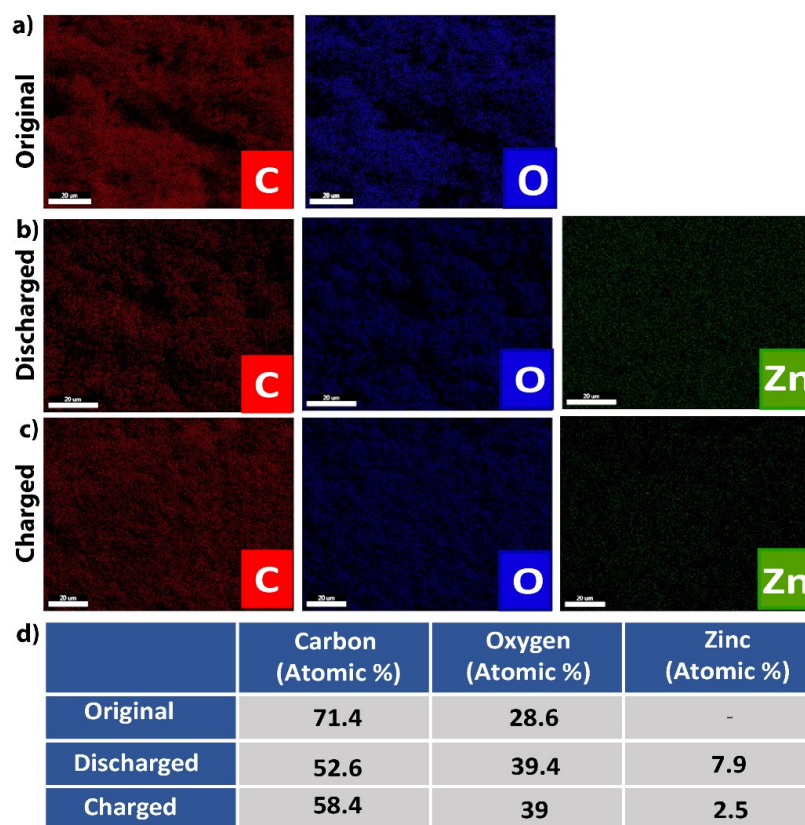


Figure 5.6. Elemental mapping of the NTCDA electrodes at the (a) original state, and after recovering from the Zn||NTCDA-(N) half-cells at the (b) discharged (0.30 V vs. Zn|Zn²⁺) and (c) charged (1.4 V vs. Zn|Zn²⁺) states; (d) atomic percentage of the elements obtained from the EDAX analysis of the NTCDA electrodes recovered from the Zn||NTCDA-(N) half-cells. (Reprinted (adapted) with permission from Dalton Trans., 2021, 50, 4237-4243. Copyright (2021) Royal Society of Chemistry).

To understand the charge storage mechanism of NTCDA, we have recovered the electrodes from the Zn||NTCDA-(N) cell at the completely discharged (to 0.30 V vs. Zn|Zn²⁺) and charged (to 1.4 V vs. Zn|Zn²⁺) states. After recovering from the respective cells, the electrodes were carefully washed with water to remove the ZnOTF electrolyte salt from the electrode surface. The FTIR data (**Figure 5.5a**) of the original electrode and the recovered electrodes from the discharged and charged cells are compared. In the pristine electrode, the strong peak at 1780 cm⁻¹ corresponds to the anhydride functional group present in the NTCDA molecule.²² Upon the first discharge, we have not observed any significant change in the anhydride peak. However, a new peak at 1362 cm⁻¹ has been appeared, which is attributed to the formation of enolate (C-O⁻) from the carbonyl group (C=O) of the anhydride functionalities.^{21, 23} Additionally, few other peaks at 1260, 1182, 772, and 647 cm⁻¹ are found to evolve after the discharge. These additional peaks indicate the structural changes that

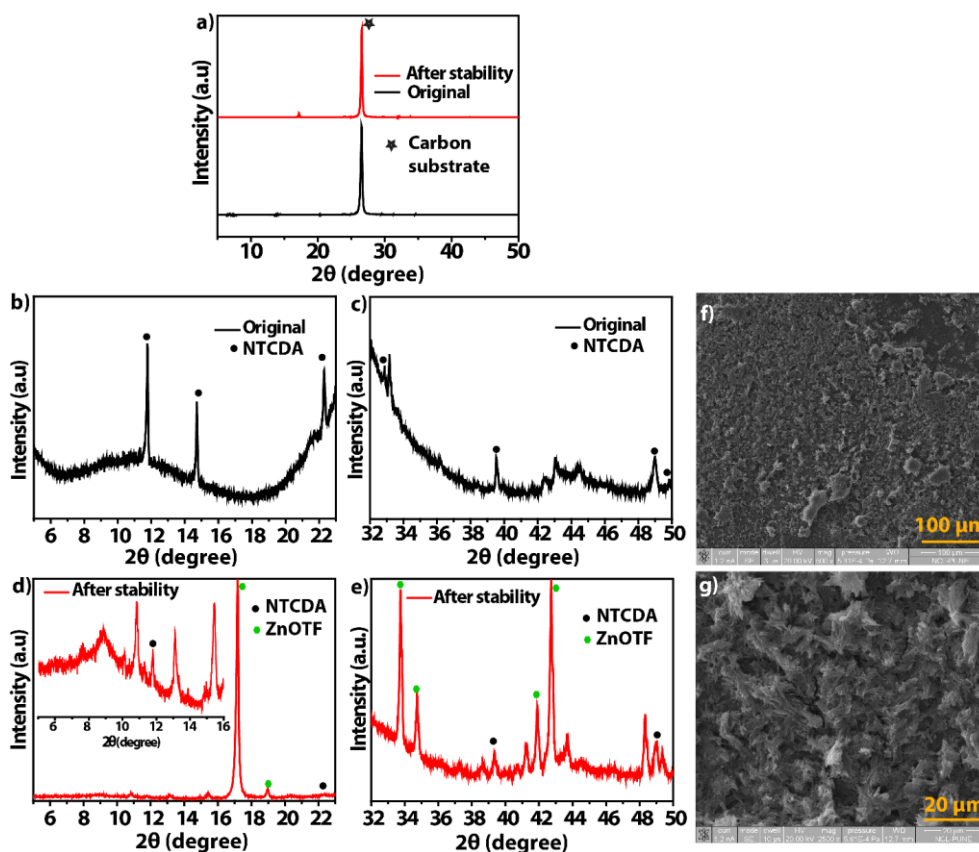


Figure 5.7. (a) XRD profiles of the NTCDA cathode recorded at the original state and after recovering from the post-cycled Zn||NTCDA-(N) half-cell; (b)-(c) and (d)-(e) show the zoomed view of the XRD data of the original electrode and the post stability electrode, respectively; (f)-(g) SEM images of the NTCDA electrode recovered from the Zn||NTCDA-(N) half-cell after the cycling stability test (the electrodes were washed with water and dried before the analysis). (Reprinted (adapted) with permission from Dalton Trans., 2021, 50, 4237-4243. Copyright (2021) Royal Society of Chemistry).

occurred due to the interaction of NTCDA with the H^+/Zn^{2+} ions. Moreover, the intensity of the peaks mentioned above diminishes on complete charging, which confirms the reversibility of the electrochemical reactions occurring at the electrode.

Later, the NTCDA electrodes (original and recovered electrodes from the charged and discharged cells) were subjected to SEM imaging and elemental mapping analysis. A significant change in the electrode morphology is also observed upon H^+/Zn^{2+} -insertion and extraction. The original electrode (**Figure 5.5b**) consists of micrometer size block-like particles along with the carbon nanofiber strands, which are used as the conducting additives for improving the electronic conductivity. Upon full discharge (**Figure 5.5c**), the particle morphology converts to small granules. Interestingly, after the complete charging (**Figure**

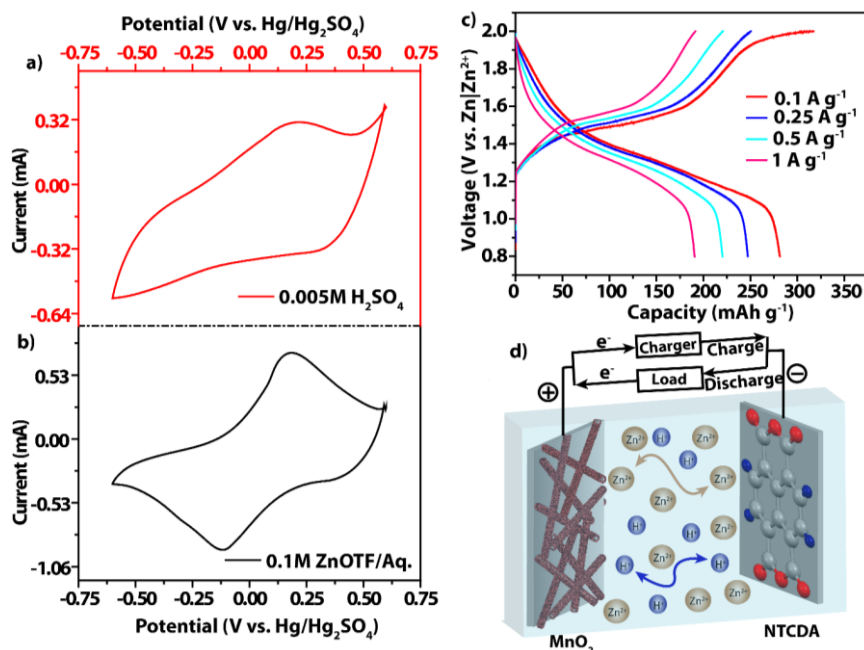


Figure 5.8. CV profiles for the MnO₂ electrode characterized in the three-electrode cell with respect to the Hg/Hg₂SO₄ reference electrode in (a) 0.005M H₂SO₄ and (b) 0.1M ZnOTF/Aq. electrolyte; (c) GCD profiles of the Zn||MnO₂(N) half-cell recorded at different current rates; (d) schematic presentation of the NTCDA||MnO₂ full-cell. (Reprinted (adapted) with permission from Dalton Trans., 2021, 50, 4237-4243. Copyright (2021) Royal Society of Chemistry).

5.5d), the morphology of the electrode does not return to the original state. Instead, a non-uniform morphology is observed in the charged state containing aggregated nanosheets along with irregularly shaped particles. The remarkable morphology evolution of NTCDA at the discharged and charged states associates with the phase transition, which is evident from the sharp redox peak in the CV profile as well as the well-defined plateaus in the GCD curves of the Zn||NTCDA-(N) cell. A similar morphological change is also reported with the other organic electrode materials (such as p-chloranil) for ARZMBs.¹² However, further studies are required to understand the underlying mechanism for the observed structural changes in the NTCDA electrode. The elemental mapping profiles are summarized in **Figure 5.6a-c**, which display the presence of C, O, and Zn in both the discharged and charged electrodes; however, the Zn content is found to be significantly higher in the former. The elemental compositions of the original and cycled electrodes obtained from the EDAX analysis (**Figure 5.6d**) also show higher content of Zn in the discharged electrode compared to that of the charged electrode. The presence of Zn in the charged electrode could be resulted from the irreversibly consumed Zn²⁺

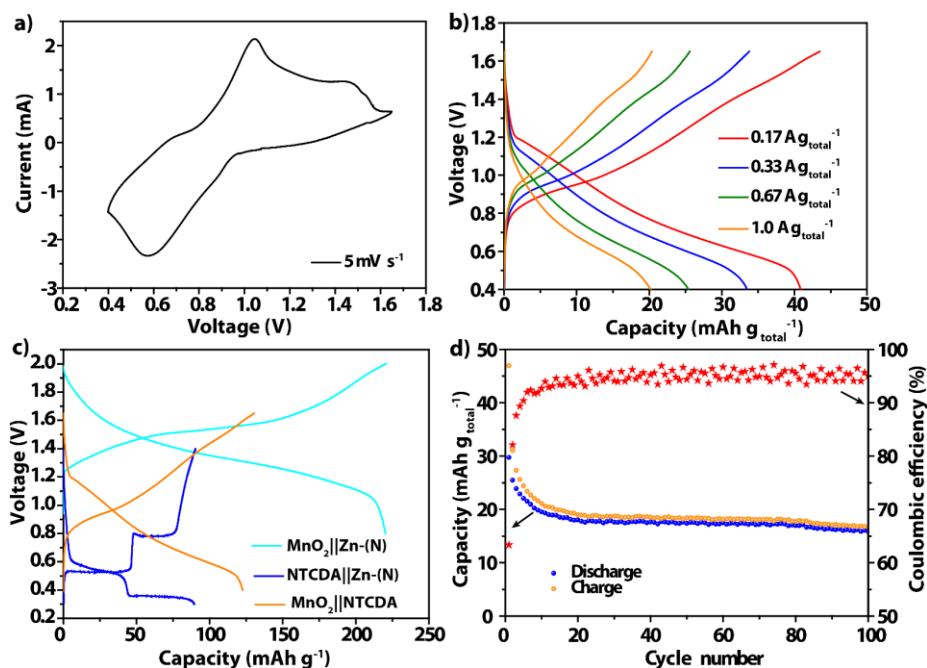


Figure 5.9. (a) CV profile, (b) GCD profiles recorded at various current rates of the NTCDA||MnO₂ full-cell; (c) charge/discharge capacities of the Zn||MnO₂||-(N), Zn||NTCDA-(N), and NTCDA||MnO₂ cells recorded at the current rate of 0.50 A g⁻¹ (here, the capacity values and current rate are normalized with respect to the mass-loading of the electrode material in the positive electrode); (d) cycling stability data recorded at the current rate of 0.33 A g_{total}⁻¹ for the NTCDA||MnO₂ full-cell. (Reprinted (adapted) with permission from Dalton Trans., 2021, 50, 4237-4243. Copyright (2021) Royal Society of Chemistry).

by the NTCDA electrode, which results in capacity loss during the first charging cycle (**Figure 5.2b** and **c**).

The structural and morphological changes occurring in the NTCDA electrode after the cycling stability test are studied. From the XRD profiles of the original and cycled electrodes (**Figure 5.7a-e**), it is observed that some peaks match with that of the original electrode, as indicated in **Figure 5.7d** and **e**. Besides, the XRD data of the cycled electrode contains several new peaks with good intensity, which could be related to the structural changes associated with the electrode material and the residual electrolyte salt trapped in the electrode. The morphological evolution of the NTCDA electrode after the cycling is further evident from the SEM images given in **Figure 5.7f** and **g**. Compared to the original NTCDA electrode possessing irregular block-like morphology (**Figure 5.5b**), the cycled electrode is observed to exhibit aggregated nanosheet-like morphology, which resembles that of the charged electrode (**Figure 5.5d**).

Table 5.1. The electrochemical performance parameters of NTCDA in the Zn||NTCDA half-cell and NTCDA||MnO₂ full-cell configurations are compared with the performance of some of the previously reported anode materials for ARZIBs. (Reprinted (adapted) with permission from Dalton Trans., 2021, 50, 4237-4243. Copyright (2021) Royal Society of Chemistry).

Cathode Anode	Performance in half-cell			Performance in full-cell			Ref.
	Capacity (current rate)	Voltage	Cycling stability	Capacity	Voltage	Cycling stability	
PB PTCDI/rGO	141 mAh g ⁻¹ (0.5 A g ⁻¹)	0.38 V	95% (1200 cycles)	48 mAh g _{total} ⁻¹	0.95 V	75% (150 cycles)	27
ZnMn ₂ O ₄ Na _{0.14} TiS ₂	120 mAh g ⁻¹ (0.1 A g ⁻¹)	0.30 V	77% (5000 cycles)	38 mAh g _{total} ⁻¹	0.95 V	74% (100 cycles)	11
PB Zn ₂ Mo ₆ S ₈	~60 mAh g ⁻¹ (0.128 A g ⁻¹)	0.35 V	-	62 mAh g _{total} ⁻¹	1.40 V	-	28
MnO ₂ PI-COF	92 mAh g ⁻¹ (0.7 A g ⁻¹)	-	85% (4000 cycles)	60 mAh g _{total} ⁻¹	~0.90- 0.80 V	82.5% (2000 cycles)	29
PB Ferrocene/C	106 mAh g ⁻¹ (1C)	-	70% (2000 cycles)	30 mAh g _{total} ⁻¹	0.90 V	58% (1000 cycles)	30
MnO ₂ NTCDA	143 mAh g ⁻¹ (0.1 A g ⁻¹)	0.46 V	~75% (300 cycles)	41 mAh g _{total} ⁻¹	0.80 V	~60% (100 cycles)	This work

The performance of NTCDA as the insertion anode in full-cell is investigated by pairing it with the electrodeposited MnO₂ cathode. We have chosen MnO₂ as the cathode because of its high average voltage and adequate capacity. The MnO₂ electrode was characterized in the three-electrode cell assembly using 0.005M H₂SO₄ (**Figure 5.8a**) and 0.1M ZnOTF/Aq. (**Figure 5.8b**) electrolytes. The broad redox peaks in the cathodic and anodic CV scans suggest the redox-assisted H⁺ storage/release in the MnO₂ electrode in the 0.005M H₂SO₄ electrolyte. On the other hand, the CV data taken in 0.1M ZnOTF/Aq. electrolyte shows more distinct oxidation and reduction peaks associated with the insertion/extraction of Zn²⁺ and H⁺ ions. Moreover, several earlier reports on the MnO₂ cathode have also confirmed that the charge storage behavior in the Zn²⁺-conducting aqueous electrolytes involves co-insertion of the Zn²⁺ and H⁺ ions.²⁴⁻²⁶ The specific discharge capacity of the Zn||MnO₂-(N) half-cell is obtained from the GCD analysis, and the related plots are given in **Figure 5.8c**.

Later the NTCDA||MnO₂ full-cell was assembled, and the cell is schematically presented in **Figure 5.8d**. The NTCDA||MnO₂ ARZIB full-cell facilitated by the Zn²⁺ and H⁺ insertion at both anode and cathode (as discussed in the previous sections) can be called a Zn²⁺/H⁺ hybrid battery (or zinc-proton hybrid ion battery). The CV profile of the

NTCDA||MnO₂ full-cell is shown in **Figure 5.9a**, which displays the reversible redox processes occurring in the cell during the cathodic and anodic scan. The GCD profiles recorded at various current rates are given in **Figure 5.9b**. The full-cell delivers 41, 33, 25, and 20 mAh g_{total}⁻¹ discharge capacity values at 0.17, 0.33, 0.67, and 1.0 A g_{total}⁻¹ current rates. The term ‘total’ in the units of capacity and current rates represents the cumulative mass-loading in both the positive and negative electrodes. The maximum energy density obtained for the full-cell is 32 Wh kg_{total}⁻¹. For a better understanding of the average voltage of the full-cell, the GCD profiles of NTCDA||MnO₂, Zn||MnO₂-(N), and Zn||NTCDA-(N) cells are summarized in **Figure 5.9c**. As shown in the figure, the MnO₂ and NTCDA electrodes display an average voltage of 1.35 V and 0.46 V vs. Zn|Zn²⁺, respectively. When NTCDA is paired with the MnO₂ cathode, the resulting full-cell shows an average voltage of 0.80 V (**Figure 5.9c**). The cycling stability of the full-cell is investigated at 0.33 A g_{total}⁻¹ current rate. **Figure 5.9d** shows that NTCDA||MnO₂ cell exhibits capacity fading in the first few cycles reaching a capacity of 22 mAh g_{total}⁻¹ at the 5th cycle. In the following cycles, the drop in capacity value is found to be reduced, resulting in 15 mAh g_{total}⁻¹ capacity retention over 100 cycles. Moreover, the overall performance of the full-cell is also comparable to some of the previously reported ARZIB full-cells (**Table 5.1**).^{11, 27-30} Therefore, the replacement of metallic Zn with NTCDA anode shows a new direction toward developing aqueous rechargeable batteries based on Zn-ion chemistry.

5.4 Conclusions

In conclusion, this work demonstrates that NTCDA exhibits adequate capacity (143 mAh g⁻¹) and cycling stability in aqueous 1M ZnOTF/Aq. electrolyte. The electrochemical characterizations reveal that both Zn²⁺ and H⁺ present in aqueous electrolytes contribute to the charge storage performance of NTCDA. The suitable low-voltage plateau (vs. Zn|Zn²⁺) of NTCDA allows its use as the anode material in combination with the MnO₂ cathode for assembling a *zinc-proton hybrid ion battery* full-cell (NTCDA||MnO₂). The prototype full-cell delivers 41 mAh g_{total}⁻¹ initial capacity with an average voltage of 0.80 V higher than that of Zn||NTCDA-(N) half-cell. Ultimately, in contrast to the previously reported inorganic materials, this work provides new insights to design insertion anodes based on the environment-friendly organic molecule for aqueous ‘rocking chair’ ARZIBs.

5.5 References

- (1) Li, C.; Zhang, X.; He, W.; Xu, G.; Sun, R. Cathode materials for rechargeable zinc-ion batteries: From synthesis to mechanism and applications. *Journal of Power Sources* **2020**, *449*, 227596.

- (2) Han, Q.; Chi, X.; Liu, Y.; Wang, L.; Du, Y.; Ren, Y.; Liu, Y. An inorganic salt reinforced Zn²⁺-conducting solid-state electrolyte for ultra-stable Zn metal batteries. *Journal of Materials Chemistry A* **2019**, *7*, 22287-22295.
- (3) Shin, J.; Lee, J.; Park, Y.; Choi, J. W. Aqueous zinc ion batteries: focus on zinc metal anodes. *Chemical Science* **2020**, *11*, 2028-2044.
- (4) Zhang, N.; Cheng, F.; Liu, Y.; Zhao, Q.; Lei, K.; Chen, C.; Liu, X.; Chen, J. Cation-deficient spinel ZnMn₂O₄ cathode in Zn (CF₃SO₃)₂ electrolyte for rechargeable aqueous Zn-ion battery. *Journal of the American Chemical Society* **2016**, *138*, 12894-12901.
- (5) Zhao, K.; Wang, C.; Yu, Y.; Yan, M.; Wei, Q.; He, P.; Dong, Y.; Zhang, Z.; Wang, X.; Mai, L. Ultrathin surface coating enables stabilized zinc metal anode. *Advanced Materials Interfaces* **2018**, *5*, 1800848.
- (6) Li, W.; Wang, K.; Zhou, M.; Zhan, H.; Cheng, S.; Jiang, K. Advanced low-cost, high-voltage, long-life aqueous hybrid sodium/zinc batteries enabled by a dendrite-free zinc anode and concentrated electrolyte. *ACS applied materials & interfaces* **2018**, *10*, 22059-22066.
- (7) Lee, B.-S.; Cui, S.; Xing, X.; Liu, H.; Yue, X.; Petrova, V.; Lim, H.-D.; Chen, R.; Liu, P. Dendrite suppression membranes for rechargeable zinc batteries. *ACS applied materials & interfaces* **2018**, *10*, 38928-38935.
- (8) Liu, X.; Yang, F.; Xu, W.; Zeng, Y.; He, J.; Lu, X. Zeolitic Imidazolate Frameworks as Zn²⁺ Modulation Layers to Enable Dendrite-Free Zn Anodes. *Advanced Science* **2020**, *7*, 2002173.
- (9) Cheng, Y.; Luo, L.; Zhong, L.; Chen, J.; Li, B.; Wang, W.; Mao, S. X.; Wang, C.; Sprenkle, V. L.; Li, G. Highly reversible zinc-ion intercalation into chevrel phase Mo₆S₈ nanocubes and applications for advanced zinc-ion batteries. *ACS applied materials & interfaces* **2016**, *8*, 13673-13677.
- (10) Kaveevivitchai, W.; Manthiram, A. High-capacity zinc-ion storage in an open-tunnel oxide for aqueous and nonaqueous Zn-ion batteries. *Journal of Materials Chemistry A* **2016**, *4*, 18737-18741.
- (11) Li, W.; Wang, K.; Cheng, S.; Jiang, K. An Ultrastable Presodiated Titanium Disulfide Anode for Aqueous “Rocking-Chair” Zinc Ion Battery. *Advanced Energy Materials* **2019**, *9*, 1900993.
- (12) Kundu, D.; Oberholzer, P.; Glaros, C.; Bouzid, A.; Tervoort, E.; Pasquarello, A.; Niederberger, M. Organic cathode for aqueous Zn-ion batteries: taming a unique phase

- evolution toward stable electrochemical cycling. *Chemistry of materials* **2018**, *30*, 3874-3881.
- (13) Wan, F.; Niu, Z. Design Strategies for Vanadium-based Aqueous Zinc-Ion Batteries. *Angewandte Chemie International Edition* **2019**, *58*, 16358-16367.
- (14) Yue, X.; Liu, H.; Liu, P. Polymer grafted on carbon nanotubes as a flexible cathode for aqueous zinc ion batteries. *Chemical Communications* **2019**, *55*, 1647-1650.
- (15) He, P.; Yan, M.; Zhang, G.; Sun, R.; Chen, L.; An, Q.; Mai, L. Layered VS₂ nanosheet-based aqueous Zn ion battery cathode. *Advanced Energy Materials* **2017**, *7*, 1601920.
- (16) Ghosh, M.; Vijayakumar, V.; Anothumakkool, B.; Kurungot, S. Nafion Ionomer-Based Single Component Electrolytes for Aqueous Zn/MnO₂ Batteries with Long Cycle Life. *ACS Sustainable Chemistry & Engineering* **2020**, *8*, 5040-5049.
- (17) Kasnatscheew, J.; Placke, T.; Streipert, B.; Rothermel, S.; Wagner, R.; Meister, P.; Laskovic, I. C.; Winter, M. A tutorial into practical capacity and mass balancing of lithium ion batteries. *Journal of The Electrochemical Society* **2017**, *164*, A2479.
- (18) Tie, Z.; Liu, L.; Deng, S.; Zhao, D.; Niu, Z. Proton Insertion Chemistry of a Zinc–Organic Battery. *Angewandte Chemie International Edition* **2020**, *59*, 4920-4924.
- (19) Zhang, H.; Fang, Y.; Yang, F.; Liu, X.; Lu, X. Aromatic organic molecular crystal with enhanced π – π stacking interaction for ultrafast Zn-ion storage. *Energy & Environmental Science* **2020**, *13*, 2515-2523.
- (20) Na, M.; Oh, Y.; Byon, H. R. Effects of Zn²⁺ and H⁺ Association with Naphthalene Diimide Electrodes for Aqueous Zn-Ion Batteries. *Chemistry of Materials* **2020**, *32*, 6990-6997.
- (21) Rodríguez-Pérez, I. A.; Yuan, Y.; Bommier, C.; Wang, X.; Ma, L.; Leonard, D. P.; Lerner, M. M.; Carter, R. G.; Wu, T.; Greaney, P. A. Mg-ion battery electrode: an organic solid's herringbone structure squeezed upon Mg-ion insertion. *Journal of the American Chemical Society* **2017**, *139*, 13031-13037.
- (22) Burtman, V.; Zelichonok, A.; Pakoulev, A. V. Molecular photovoltaics in nanoscale dimension. *International journal of molecular sciences* **2011**, *12*, 173-225.
- (23) Wu, J.; Xu, W.; Lin, Y.; Shi, X.; Yang, F.; Lu, X. Tuning electronic structure endows 1, 4-naphthoquinones with significantly boosted Zn-ion storage capability and output voltage. *Journal of Power Sources* **2021**, *483*, 229114.
- (24) Sun, W.; Wang, F.; Hou, S.; Yang, C.; Fan, X.; Ma, Z.; Gao, T.; Han, F.; Hu, R.; Zhu, M. Zn/MnO₂ battery chemistry with H⁺ and Zn²⁺ coinsertion. *Journal of the American Chemical Society* **2017**, *139*, 9775-9778.

- (25) Park, M. J.; Yaghoobnejad Asl, H.; Manthiram, A. Multivalent-Ion versus Proton Insertion into Battery Electrodes. *ACS Energy Letters* **2020**, *5*, 2367-2375.
- (26) Zhao, Q.; Huang, X.; Zhou, M.; Ju, Z.; Sun, X.; Sun, Y.; Huang, Z.; Li, H.; Ma, T. Proton Insertion Promoted a Polyfurfural/MnO₂ Nanocomposite Cathode for a Rechargeable Aqueous Zn–MnO₂ Battery. *ACS Applied Materials & Interfaces* **2020**, *12*, 36072-36081.
- (27) Liu, N.; Wu, X.; Zhang, Y.; Yin, Y.; Sun, C.; Mao, Y.; Fan, L.; Zhang, N. Building High Rate Capability and Ultrastable Dendrite-Free Organic Anode for Rechargeable Aqueous Zinc Batteries. *Advanced Science* **2020**, *7*, 2000146.
- (28) Chae, M. S.; Hong, S.-T. Prototype System of Rocking-Chair Zn-Ion Battery Adopting Zinc Chevrel Phase Anode and Rhombohedral Zinc Hexacyanoferrate Cathode. *Batteries* **2019**, *5*, 3.
- (29) Yu, M.; Chandrasekhar, N.; Raghupathy, R. K. M.; Ly, K. H.; Zhang, H.; Dmitrieva, E.; Liang, C.; Lu, X.; Kühne, T. D.; Mirhosseini, H. A High-Rate Two-Dimensional Polyarylimide Covalent Organic Framework Anode for Aqueous Zn-Ion Energy Storage Devices. *Journal of the American Chemical Society* **2020**.
- (30) Wu, X.; Xu, Y.; Zhang, C.; Leonard, D. P.; Markir, A.; Lu, J.; Ji, X. Reverse dual-ion battery via a ZnCl₂ water-in-salt electrolyte. *Journal of the American Chemical Society* **2019**, *141*, 6338-6344.

1) DETAILS OF THE PUBLICATIONS EMANATING FROM THE THESIS WORK

List of publication(s) in SCI Journal(s) (published & accepted) emanating from the thesis work, with complete bibliographic details

1. Dendrite Growth Suppression by Zn²⁺-Integrated Nafion Ionomer Membranes: Beyond Porous Separators toward Aqueous Zn/V₂O₅ Batteries with Extended Cycle Life, **M Ghosh**, V Vijayakumar, S Kurungot, Energy Technology, 2019, 7, 1900442.
2. Nafion Ionomer-Based Single Component Electrolytes for Aqueous Zn/MnO₂ Batteries with Long Cycle Life, **M Ghosh**, V Vijayakumar, B Anothumakkool, S Kurungot, ACS Sustainable Chem. Eng. 2020, 8, 13, 5040–5049.
3. Scalable synthesis of manganese-doped hydrated vanadium oxide as a cathode material for aqueous zinc-metal batteries, **M Ghosh**, S Dilwale, V Vijayakumar, S Kurungot, ACS Appl. Mater. Interfaces 2020, 12, 43, 48542–48552.
4. Naphthalene dianhydride organic anode for a ‘rocking-chair’ zinc–proton hybrid ion battery, **M Ghosh**, V Vijayakumar, M Kurian, S Dilwale, S Kurungot, Dalton Trans., 2021, 50, 4237- 4243.

2) DETAILS OF OTHER PUBLICATIONS NOT RELATED TO THESIS WORK

Research articles

1. Rationally designed standing V₂O₅ electrode for high voltage non-aqueous all-solid-state symmetric (2.0 V) and asymmetric (2.8 V) supercapacitors, **M Ghosh**, V Vijayakumar, R Soni, S Kurungot, Nanoscale, 2018, 10, 8741-8751.
2. One-Pot Synthesis of Exfoliated Ti₃C₂T_x MXene via a Mild Etching Process as an Electrode Material for Asymmetric Supercapacitor, **M Ghosh**, S Szunerits, S Kurungot, R Boukherroub, Manuscript under preparation.
3. Zinc Ion Interactions in a Two-Dimensional Covalent Organic Framework based Aqueous Zinc Ion Battery, A Khayum M, **M Ghosh**, V Vijayakumar, A Halder, M Nurhuda, S Kumar, M Addicoat, S Kurungot, Rahul Banerjee, Chem. Sci., 2019,10, 8889-8894.
4. An In Situ Cross-Linked Nonaqueous Polymer Electrolyte for Zinc-Metal Polymer Batteries and Hybrid Supercapacitors, V Vijayakumar, **M Ghosh**, M Kurian, A Torris, S Dilwale, M V. Badiger, M Winter, J R Nair, S Kurungot, , Small, 2020, 16, 2002528.
5. A water-in-acid gel polymer electrolyte realized through phosphoric acid enriched polyelectrolyte matrix towards solid-state supercapacitors, V Vijayakumar, **M Ghosh**,

- A Torris A. T., Nikhil M.K., S Nair, M V. Badiger, S Kurungot, ACS Sustainable Chem. Eng. 2018, 6, 10, 12630–12640.
- Interlayer hydrogen- bonded covalent organic frameworks for high performance supercapacitors, A Halder, **M Ghosh**, A Khayum M, S Bera, M Addicoat, H S Sasmal, S Karak, S Kurungot, R Banerjee, J. Am. Chem. Soc., 2018, 140 (35), 10941–10945.
 - Weak Intermolecular Interactions in Covalent Organic Framework-Carbon Nanofiber based Crystalline, Yet Flexible Devices, A Khayum M, V Vijayakumar, A Halder, **M Ghosh**, M Addicoat, U P Bansode, S Kurungot, R Banerjee, ACS Appl. Mater. Interfaces, 2019, DOI: 10.1021/acsami.9b08625.
 - Biomass-derived activated carbon material from native European deciduous trees as an inexpensive and sustainable energy material for supercapacitor application, A Jain, **M Ghosh**, M Krajewski, S Kurungot, M Michalska, Journal of Energy Storage 34 (2021) 102178.
 - High-Voltage Non-Aqueous Hybrid Supercapacitor Based on N2200 Polymer Supported Over Multiwalled Carbon Nanotube, B A Wavhal, **M Ghosh**, S Sharma, S Kurungot, A Syamakumari, Nanoscale, 2021, 13, 12314-12326.

Patents filed

- A Metal-Ion Battery having Ionomer Membrane Separator and Free-Standing Electrode, **M Ghosh**, V Vijayakumar, S Kurungot, (International Application No. PCT/IN2020/050109).
- Sulfonated Polyvinyl Alcohol Ionomer Membrane for Aqueous Rechargeable Zinc Metal Battery, V Vijayakumar, M Kurian, A Torris, **M Ghosh**, M V. Badiger, S Kurungot. (Patent under process)

Chapters in books

- Electrolytes for Microsupercapacitors, V Vijayakumar, **M Ghosh**, R Soni, B Anothumakkool, S Kurungot, M Winter, JR Nair, (under editorial revision, *Elsevier Publications*).
- 2D Nanomaterials as Polymer Composite Electrolytes for Lithium-Based batteries, V Vijayakumar, **M Ghosh**, PK Samantaray, S Kurungot, M Winter, JR Nair, (in press, inorganic materials books series published by the RSC).

3) LIST OF PAPERS WITH ABSTRACT PRESENTED (ORAL/POSTER) AT NATIONAL/INTERNATIONAL CONFERENCES/SEMINARS WITH COMPLETE DETAILS

1. Oral presentation entitled **Aqueous Zinc-Ion Battery: Prospects and Challenges** in CSIR Inter Institutional Student Conference on “Sustainable Chemistry for Health, Environment and Materials (SuCHEM YUVA July 2019) at ICT, Hyderabad, India.

Abstract

Development of electrochemical energy storage (EES) devices is one of the most crucial part toward the wide-scale applications the carbon-free renewable energy resources. As of the current scenario, Lithium-ion batteries (LIBs) are considered the most matured EES technology. However, it is widely accepted that the use of organic electrolytes in state-of-the-art LIBs incites several challenges pertaining to safety. This has intensified the research toward the development of aqueous batteries based on earth-abundant multivalent metals. In this arena, aqueous rechargeable zinc-ion batteries (ZIBs) are of greater importance. However, the commercialization of ZIBs is constrained due to low energy density and the limited life span of the cell. Here, a novel strategy is adopted to improve the overall performance of ZIBs by replacing the conventional porous separator with cation-selective ionomer membrane. A variety of transition metal oxides are used as the cathode materials for fabricating the lab-scale ZIB unit-cell comprising ionomer membrane separator. The ionomer membrane separator prevents the poisoning of the anode by undesirable diffusion of discharge side-products from the cathode and mitigates the tendency to form ion-concentration gradient near to the metallic anode surface.

2. Presented a poster entitled **V₂O₅ Based All-Solid-State Asymmetric Supercapacitor: A Highly Efficient Energy Storage Device Bridging Conventional Batteries and Capacitors** in CEAMCR-2018 (International Conference on Electrochemistry in Advanced Materials, Corrosion, and Radiopharmaceuticals) conference jointly organized by the Indian Society for Electro Analytical Chemistry and Bhabha Atomic Research Centre.

Abstract

The low energy density of conventional supercapacitors is a significant existing issue for their wide range of applications. Simultaneous improvement of specific capacitance of the electrode material and voltage window of the device are appeared to be equally

essential to get a high-energy supercapacitor. In this aspect, the integration of pseudocapacitive materials and non-aqueous electrolytes can be a beneficial solution. However, this strategy often fails to cater to the advantages envisaged by non-aqueous electrolytes due to the drastically low pseudocapacitance of the active materials in non-aqueous electrolytes. This study reports a novel high-performance non-aqueous all-solid-state asymmetric supercapacitor based on V_2O_5 as active material with non-aqueous gel electrolyte. A hierarchically porous V_2O_5 electrode is prepared to gain an improved electrode-electrolyte interface and increase the number of redox-active sites for enhanced pseudocapacitance. Homogeneous distribution of nanostructured V_2O_5 and its good contact with the conductive support give rise to a good electronic conductivity throughout the electrode. As an outcome, the prototype solid-state device delivers a high energy density at a substantially high power density. Such a superior performance of our device can demonstrate the importance of the use of non-aqueous electrolytes with pseudocapacitive materials to bridge between high-energy Lithium-ion batteries and high-power conventional supercapacitors.

3. Oral presentation entitled **Cation Selective Separator: A Viable Tool to Improve the Cycling Stability of Aqueous Rechargeable Zinc-Metal Batteries** in ElecNano9 (9th meeting of Electrochemistry in Nanoscience) virtual conference organized by Sorbonne Université and the sub-Division of Electrochemistry of the French Chemical Society in 2020.

Abstract

Aqueous rechargeable batteries are emerging as a safe and promising electrochemical energy storage technologies suitable for large-scale stationary applications. Aqueous zinc-metal batteries (ZMBs), comprising metallic zinc anode and an insertion-type cathode, have received unprecedented research interest in the past few years owing to the high volumetric capacity, low reduction potential, and good compatibility of zinc with water-based electrolytes. However, the zinc anode is prone to form high surface area zinc (HSAZ) or dendrite-like zinc deposits during the electrochemical cycling causing severe capacity decay. To address this issue, we have demonstrated the effectiveness of ionomer separator based on sulfonated tetrafluoroethylene copolymer (Nafion) in ZMBs. It is observed that the Nafion membrane combined with Zn^{2+} -ion-conducting aqueous electrolytes (aqueous solution of $ZnSO_4$ or $Zn(CF_3SO_3)_2$) offers stable plating/stripping of zinc in $Zn|Zn$ symmetric cell with lower overpotential compared to that observed with traditional porous separators (viz. glass fibre paper

and polypropylene separator). This is credited to the cation-selective nature of the Nafion, which provides a high Zn^{2+} -ion transference number and maintains uniform ion flux near to the electrode surface. Interestingly, the superior performance of the Nafion membrane is found to be retained when it is employed as the separator in $V_2O_5||Zn$ and $MnO_2||Zn$ cells. The detailed characterization of the post-stability electrodes recovered from the ZMB cell reveals that Nafion separator effectively suppresses the growth of zinc dendrites or HSAZ by facilitating the uniform and smooth deposition of zinc on the anode surface, leading to an improved capacity retention of ZMBs over 1000 stability cycles. Besides, the Nafion membrane blocks the diffusion of discharge products from the cathode to the anode side, which prevents the poisoning of the zinc surface. Therefore, the use of Nafion separator could also eliminate the requirement of electrolyte additives which is otherwise necessary for mitigating the dissolution of cathode material in porous separator-based ZMBs. Ultimately, this work shows a new way toward improving the longevity of rechargeable ZMBs.

4) AWARDS & RECOGNITIONS

1. Recipient of Raman-Charpak Fellowship 2019 implemented by Indo French Centre for Promotion of Advanced Research (IFCPAR/ CEFIPRA).
2. Best Poster Award at National Chemical Laboratory, Pune on Science day 2019.
3. Recipient of Prof. Joshi-Dr. Sivaram Award for Best Research Paper with Highest Impact Factor for the year 2020.
4. CSIR-UGC NET and Junior Research Fellowship (JRF) with an all India rank of 31 (June, 2015)
5. National INSPIRE scholarship for higher education (2009-2013).

5) A COPY OF ALL SCI PUBLICATION(S), EMANATING FROM THE THESIS ARE ATTACHED AT THE END OF THE THESIS.

Erratum

Dendrite Growth Suppression by Zn²⁺-Integrated Nafion Ionomer Membranes: Beyond Porous Separators toward Aqueous Zn/V₂O₅ Batteries with Extended Cycle Life

Meena Ghosh, Vidyanand Vijayakumar, and Sreekumar Kurungot*

The dendritic/irregular growth of zinc deposits in the anode surface is often considered as a major intricacy limiting the lifespan of aqueous zinc-ion batteries. The effect of separators on the evolution of the surface morphology of the anode/cathode is never thoroughly studied. Herein, for the first time, the efficacy of the Zn²⁺-integrated Nafion ionomer membrane is demonstrated as a separator to effectively suppress the growth of irregular zinc deposits in the metallic anode of an aqueous Zn/V₂O₅ battery. The Zn²⁺-ions coordinated with the SO₃⁻ moieties in Nafion result in a high transference number of the Zn²⁺ cation, all the while facilitating a high ionic conductivity. The Zn²⁺-integrated Nafion membrane enables the Zn/V₂O₅ cell to deliver a high specific capacity of 510 mAh g⁻¹ at a current of 0.25 A g⁻¹, which is close to the theoretical capacity of anhydrous V₂O₅ (589 mAh g⁻¹). Moreover, the same cell exhibits an excellent cycling stability of 88% retention of the initial capacity even after 1800 charge–discharge cycles, superior to that of the Zn/V₂O₅ cells comprising conventional porous separators.

1. Introduction

The widespread utilization of renewable energy sources and their intermittent nature demands the concomitant development of cost-effective and high performing energy storage devices.^[1,2] The conventional alkali metal ion batteries (AMIBs) are considered as the benchmark energy storage aid due to their wide range of applications extending from micro-electronics to electric vehicles. However, their high cost and the use of inflammable organic electrolytes raise several concerns pertaining to the safety as well as environmental benignity.^[3,4] These drawbacks propel the research toward the development of low-cost rechargeable aqueous-ion batteries.^[5–7] Although aqueous electrolyte prototypes are available for AMIBs,^[8] the high reactive alkali metals

cannot generate a stable interface with an aqueous electrolyte, damaging the prospects of realizing futuristic metal battery designs.^[9–11] Therefore, aqueous battery chemistry beyond alkali metal ions is evolving as an important area in the energy storage research.^[12,13]

Recently, Xu et al. reported a rechargeable zinc-ion battery (ZIB) prototype using metallic zinc (Zn), MnO₂, and aqueous ZnSO₄ as the anode, cathode, and electrolyte, respectively.^[14] Compared with the previously known Zn/MnO₂ nonrechargeable aqueous batteries based on corrosive alkaline electrolytes, discussions regarding the aforementioned system have dominated research in recent years. This has opened up new challenges as well as opportunities in the realization of more efficient aqueous ZIBs (AZIBs) with a variety of other cathode materials.^[15–21] Although other chemistries based on Al/Al³⁺ and


Mg/Mg²⁺ have been proposed,^[22–24] the Zn/Zn²⁺ systems are considered to be the leading candidate due to the high theoretical capacity (820 mAh g⁻¹), low redox potential (–0.76 V vs standard hydrogen electrode [SHE]), natural abundance, and low cost of Zn metal.^[25–28]

Despite the availability of efficient cathode materials, the AZIBs often suffer from severe performance deterioration during prolonged cycling. The inferior life-span of AZIBs originates due to the dendritic growth of Zn deposits in the metallic anode during cycling.^[29,30] The use of electrodeposited Zn on foreign substrates instead of a commercial Zn foil is found to be an effective way to suppress the formation of the Zn dendrite.^[31] Pretreatment of the Zn surface with carbon-based materials is also found to minimize the dendrite growth.^[30,32] However, such complicated procedures preclude the use of these strategies beyond the laboratory scale. Therefore, exploring practical strategies to impede the formation of Zn dendrites is indeed important despite the challenges involved. In this context, the separators may also have a decisive role in the structural evolution of the anode surface. Unfortunately, no study has been carried out to decipher the influence of different separators in the cycling stability of AZIBs.

Here, for the first time, we demonstrate the fabrication of an aqueous Zn/V₂O₅ battery combining zinc-metal, cation-selective Zn²⁺-integrated Nafion ionomer membrane, and

M. Ghosh, V. Vijayakumar, Dr. S. Kurungot
Physical and Materials Chemistry Division
CSIR-National Chemical Laboratory
Pune 411008, Maharashtra, India
E-mail: k.sreekumar@ncl.res.in

M. Ghosh, V. Vijayakumar, Dr. S. Kurungot
Academy of Scientific and Innovative Research (AcSIR)
Sector 19, Kaila Nehru Nagar, Ghaziabad, Uttar Pradesh 201002, India

 The ORCID identification number(s) for the author(s) of this article can be found under <https://doi.org/10.1002/ente.201900442>.

DOI: 10.1002/ente.201900442

electrodeposited V_2O_5 as anode, separator, and cathode, respectively. The Nafion ionomer membrane separator is found to effectively suppress the formation of Zn dendrites compared with the conventional porous separator (glass fiber, filter paper, and polypropylene)-based AZIBs. The nonporous cation selective Nafion membrane offers preferential transport of Zn^{2+} , which in turn helps to maintain uniform ion flux close to the anode surface. This is reflected in the augmented lifespan of the Nafion-based Zn/ V_2O_5 cell; all-the-while, the electrochemically synthesized cathode (nanostructured V_2O_5 over a prefunctionalized carbon fiber paper) helps in achieving a high capacity. A discharge capacity of 510 mAh g^{-1} is delivered by the Zn^{2+} -integrated Nafion-based Zn/ V_2O_5 cell, which, to the best of our knowledge, is the highest ever reported and is close to the theoretical Zn^{2+} storage capacity of anhydrous V_2O_5 (589 mAh g^{-1}).^[33] Apart from the high discharge capacity, the system is found to retain 88% of the initial capacity even after prolonged cycling for 1800 cycles at a current rate of 10 A g^{-1} . This study reveals the drawbacks of the porous separators and proposes a viable way to suppress the dendrite growth in AZIBs.

2. Results and Discussion

2.1. Physical Characterization

A self-standing, binder-free electrode (V-CP) was prepared by electrodepositing V_2O_5 over a prefunctionalized carbon fiber paper (fCP) (experimental details are given in the Experimental Section). The synthesis scheme of the V-CP electrode and fabrication of the Zn/ V_2O_5 cell using Nafion and a porous separator are schematically shown in Figure 1a. The field emission scanning electron microscopy (FESEM) images of the V-CP specimen in Figure 1b,c confirm the growth of a V_2O_5 nanostructure on fCP. An interlayer spacing of 0.9 nm in the V-CP sample is evidenced from the transmission electron microscopy (TEM) image (Figure 1d), which can facilitate the co-insertion/extraction of Zn^{2+} and H^+ during the electrochemical cycling of the cell.^[34,35] In the X-ray photoelectron spectroscopy (XPS) data (Figure 1e), the peaks located at 517.3 and 525.2 eV for the $V 2p_{3/2}$ and $V 2p_{1/2}$ doublets correspond to the +5 oxidation state of vanadium. The presence of the +4 oxidation state is also detected

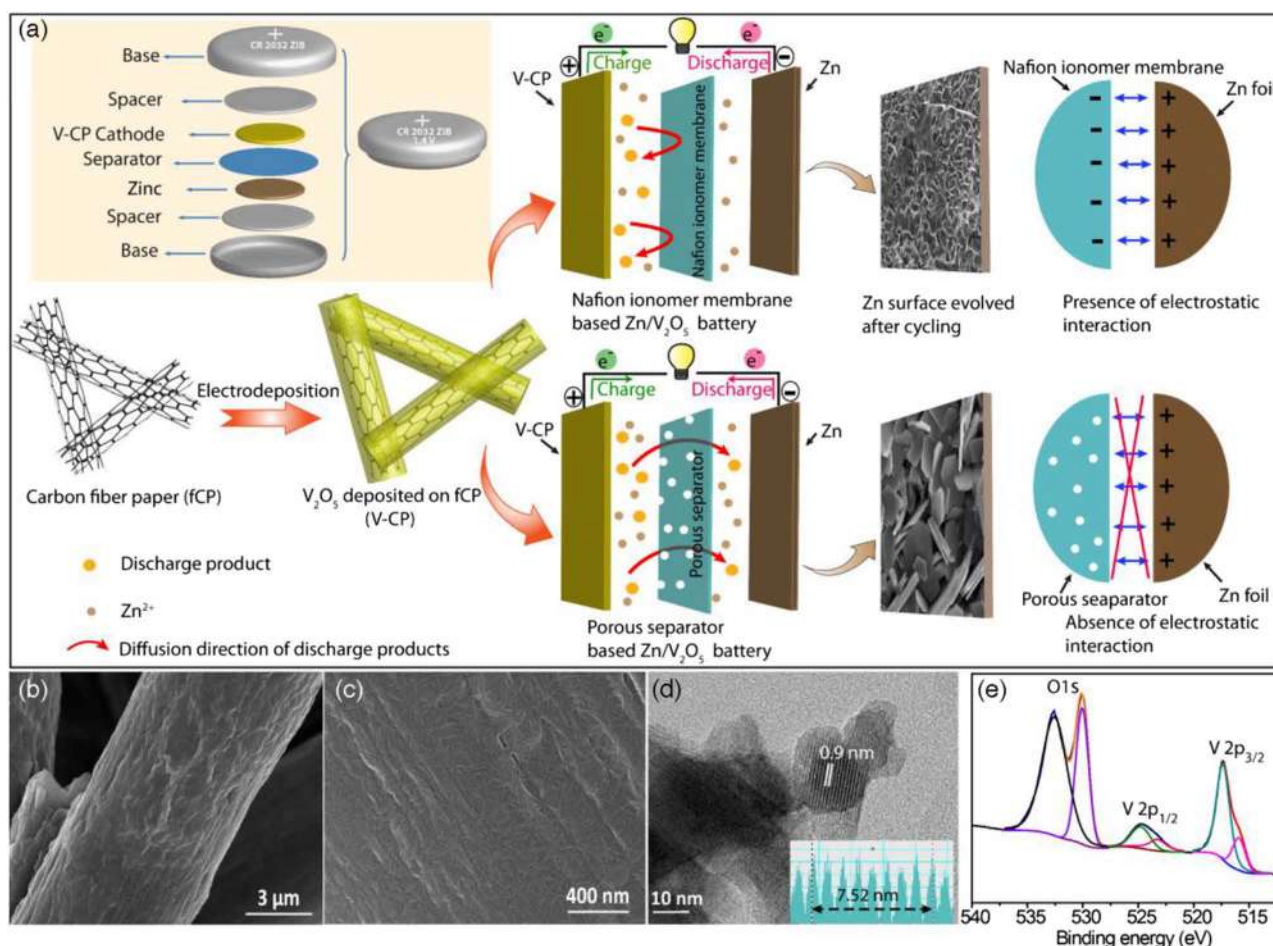


Figure 1. a) Schematic representation of the different Zn/ V_2O_5 cell configurations containing Zn^{2+} -integrated Nafion ionomer and conventional porous membrane separator. b) Low and c) high magnification FESEM images of the V-CP sample. d) The TEM image of the V_2O_5 particle taken from the V-CP specimen. e) Deconvoluted XPS spectra of vanadium and oxygen in the V-CP specimen.

from the peaks that appear at a binding energy of 515.9 and 523.8 eV.^[36,37] The O1s peak indicates the presence of oxygen in V-CP. The peaks located at 530.0 and 532.6 eV are attributed to the oxygen atom coordinated with vanadium (O—V) and carbon (O—C) in the V-CP specimen, respectively.^[38] Further characterizations of the V-CP sample are given in the Supporting Information (SI) (Figure S1a–c, Supporting Information). The morphology of various separator membranes (Nafion, glass fiber, Celgard, and filter paper) is given in Figure S2a–d, Supporting Information.

2.2. Electrochemical Analysis

2.2.1. Selection of the Separator

The integration of Zn^{2+} in the Nafion membrane is confirmed from the Fourier transform infrared (FTIR) spectra (Figure S3a, b, Supporting Information). The data with relevant explanations are given in SI (Section S3, Supporting Information).^[39,40] A schematic representation of the Zn^{2+} -integrated Nafion is given in Figure S3c, Supporting Information. In **Figure 2a**, the ionic conductivity (at 30 °C) of the Zn^{2+} -integrated Nafion ionomer membrane (3M-Nafion) is presented with that of the conventional porous separators (3M-Glass fiber, 3M-Filter paper, and 3M-Celgard), which were soaked in a 3 M $ZnSO_4$ solution prior to use. The conductivity value (2.6 mS cm^{-1}) is higher than its 3M-Celgard and 3M-Filter paper counterparts. The interaction of SO_3^- moieties in Nafion with Zn^{2+} ions can enhance the dissociation of $ZnSO_4$, which facilitates the transport of Zn^{2+} . This is reflected in the lower equivalent series resistance (ESR) value in the Nyquist plot when 3M-Nafion (Figure S4a–d, Supporting Information) is used. The slightly higher ionic conductivity (2.8 mS cm^{-1}) in 3M-Glass fiber may be due to

its better wettability and intrinsic porous nature (Figure S2b, Supporting Information). The activation energy toward ion conduction is calculated from slope of the $\ln \sigma$ versus $1/T$ plot (Figure 2b).^[41] The lowest activation energy (0.069 eV) is obtained with the 3M-Nafion membrane (Figure 2b) and that with other porous membranes are given in Table S1, Supporting Information.

The effect of various membrane separators and the concentration of $ZnSO_4$ electrolyte (0, 1, 2, and 3 M) in the plating/stripping behavior of Zn is analyzed by cyclic voltammetry (CV) experiments at a scan rate of 5 mV s^{-1} using pristine carbon paper (pCP) as a working electrode and Zn foil as counter and reference electrodes (CP-XM-Y cell, where, “X” and “Y” stands for the concentration of the electrolyte and type of separator, respectively. Details of the cell fabrication method are given in the Experimental Section). The overpotential measured for the Zn plating/stripping in the CP-3M-Nafion (Figure 2c) cell is only 75 mV (at 5 mV s^{-1}), which is lower compared with CP-1M-Nafion (115 mV) and CP-2M-Nafion (99 mV) (the data corresponding to the effect of $ZnSO_4$ concentration in plating/stripping behavior are given in Figure S5, Supporting Information). The increase in the plating/stripping current in the CV with an increase in $ZnSO_4$ concentration (Figure S5, Supporting Information) can be a result of the reduced solvation effect due to the lesser number of water molecules surrounding Zn^{2+} .^[42] Zn plating on the pCP is confirmed by the FESEM analysis of pCP after the potential cycling, and the corresponding data are given in Figure S6a, b, Supporting Information.

Compared with CP-3M-Nafion, all the porous separator-based CP-3M-Y cells display higher overpotentials for Zn plating/stripping (Figure 2d–f). The values obtained for CP-3M-Glass fiber, CP-3M-Filter paper, and CP-3M-Celgards are 84, 92, and 263 mV, respectively. The higher ionic conductivity

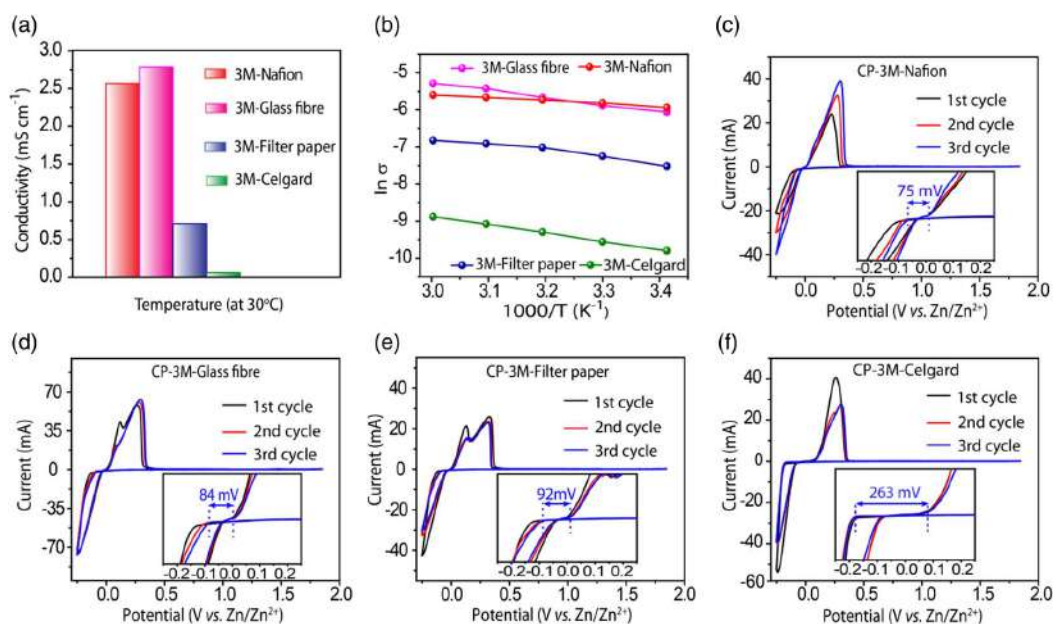


Figure 2. a) Ionic conductivity of 3M-Nafion and other porous 3M-Y membranes at 30 °C temperature. b) $\ln \sigma$ versus $1/T$ plots for 3M-Nafion and 3M-Y membranes. CV profiles corresponding to the plating/stripping behavior of Zn in c) CP-3M-Nafion, d) CP-3M-Glass fiber, e) CP-3M-Filter paper, and f) CP-3M-Celgard cells at 5 mV s^{-1} scan rate.

(Figure 2a), low activation energy (Figure 2b), and low R_{ct} value (Figure S7, Supporting Information) along with the better interface formed by the Nafion ionomer membrane with the respective electrodes (Zn and pCP) (explained in Section 2.3) are the reasons for the better plating/stripping behavior of Zn in case of the 3M-Nafion separator (Figure 2c).

Several literatures highlight that the charge storage in AZIBs can be due to the intercalation of Zn^{2+} or H^+ or by the co-intercalation of both Zn^{2+} and H^+ .^[34,43] The existence of H^+ in the electrolyte of the AZIBs is expected due to the low pH of the $ZnSO_4$ aqueous solution (Figure S8, Supporting Information). Therefore, it is indeed important to understand the effect of H^+ ions alone in the charge storage mechanism of AZIB. Here, we have fabricated the CP-0M-Nafion cell using the $ZnSO_4$ -free Nafion ionomer membrane (0M-Nafion). As observed in Figure S9a, Supporting Information, there is no significant positive current response during the oxidation of Zn in the first cycle of the CV. However, as we move from the first to the third cycle, the current corresponding to Zn oxidation is found to increase gradually. This can directly indicate the occurrence of some sort of Zn plating/stripping even in the absence of $ZnSO_4$ in the system. The acidic nature of the activated Nafion ionomer in the 0M-Nafion membrane causes the dissolution of the Zn electrode, which eventually takes part in the plating/stripping reaction on the working electrode.

Interestingly, Figure S9b, Supporting Information, shows that, after several cycles, the CV profile of the CP-0M-Nafion cell (15th cycle) appears similar to that of the CP-3M-Nafion cell (3rd cycle). However, the low current (at 15th cycle) and higher overpotential (149 mV) in the CV plot indicate the inferior kinetics of the Zn plating/stripping in the CP-0M-Nafion cell.

In addition to the above observation, an oxidation peak is observed beyond 1.5 V in the first CV cycle (Figure S9a, Supporting Information) related to the water decomposition. However, this peak diminishes with the evolution of the oxidation peak corresponding to Zn. This confirms that the presence of Zn^{2+} in the electrolyte not only provides better reversibility but also increases the anodic stability of the electrolyte. These observations prove the importance of Zn^{2+} integration in the Nafion membrane.

The Zn plating/stripping behavior in the presence of the 3M-Nafion ionomer membrane and other porous 3M-Y membranes are further evaluated in the Zn/Zn symmetric cell (Zn-XM-Y, where, “X” stands for the concentration of the electrolyte and “Y” represents the type of separator used). Figure 3a–d shows the voltage versus time profiles during galvanostatic cycling at a constant current of 0.1 mA cm^{-2} . As evident from the enlarged part (Figure 3a–d) at various cycles, the Zn-3M-Nafion cell (Figure 3a) displays a significant decrease in the overpotential (71 mV at 30th cycle) upon potential cycling. On the contrary, the gradual enhancement in the voltage separation between charging and discharging in case of the porous separator-based Zn-3M-Y cells (at 30th cycle, the corresponding overpotential of Zn-3M-Glass fiber, Zn-3M-Filter paper, and Zn-3M-Celgard are 90, 83.3, and 284 mV, respectively, Figure 3b–d) further indicates the superiority of the 3M-Nafion ionomer membrane separator. The inferior plating/stripping behavior of the Zn-0M-Nafion cell is shown in Figure S10, Supporting Information (Section S10, Supporting Information).

The transference number of Zn^{2+} ($t_{Zn^{2+}}$) in the 3M-Nafion membrane and other porous separators (3M-Glass fibre, 3M-Filter paper, and 3M-Celgard) are calculated from Equation (1) proposed by Abhraham et al.^[44,45]

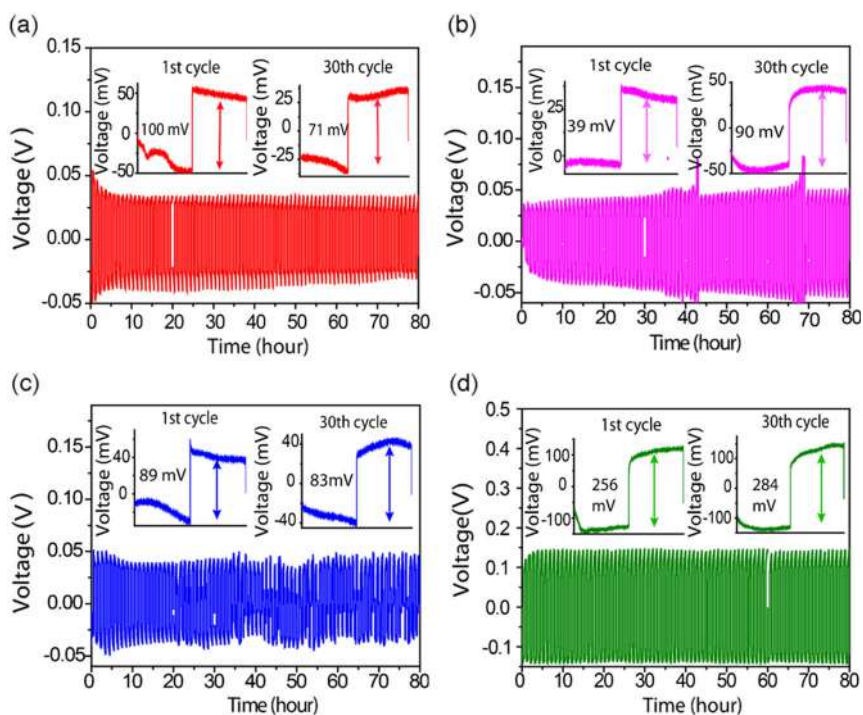


Figure 3. Galvanostatic cycling of the Zn/Zn symmetric cell at a current rate of 0.1 mA cm^{-2} in the presence of a) 3M-Nafion, b) 3M-Glass fiber, c) 3M-Filter paper, and d) 3M-Celgard membrane separators.

$$t_{\text{Zn}^{2+}} = \frac{I_{\text{SS}} R_{\Omega, \text{SS}} (\Delta V - I_0 R_{\text{ct}, 0})}{I_0 R_{\Omega, 0} (\Delta V - I_{\text{SS}} R_{\text{ct}, \text{SS}}} \quad (1)$$

Here, V is the DC polarization voltage, I_0 and I_{SS} are the initial and steady-state current responses during the DC polarization, R_{Ω} and R_{ct} stand for the ESR and charge transfer resistance obtained from the Nyquist plot, respectively.^[44,45] The calculated $t_{\text{Zn}^{2+}}$ for the Zn^{2+} -integrated Nafion ionomer membrane is 0.52, which is higher than the same obtained for the other porous separators ($t_{\text{Zn}^{2+}}$ obtained for porous separators is close to 0.31). The higher $t_{\text{Zn}^{2+}}$ in 3M-Nafion (transport number corresponding to the porous separators are listed in Table S2, Supporting Information and corresponding plots are given in Figure S11, Supporting Information) indicates the preferential role of Zn^{2+} transport in maintaining the ionic current. The coordinated Zn^{2+} with the SO_3^- moieties in the Nafion helps in selective migration of the cation in the direction of the electric field resulting in a higher $t_{\text{Zn}^{2+}}$ value.^[46] On the other hand, in the case of the porous separators, the low $t_{\text{Zn}^{2+}}$ indicates a lesser extent of contribution toward the ionic conductivity by the cation due to the lack of negatively charged moieties as in the case of Nafion. The high transference number of Zn^{2+} in Nafion can reduce the concentration polarization near to the anode surface, preventing the nonuniform deposition of Zn metal making them a potential candidate to be used in AZIBs.

2.2.2. Electrochemical Characterization of Zn/V₂O₅ Cells

The electrochemical performance of the V-CP electrode was evaluated in the CR2032 coin cell using a Zn foil as an anode, desired membrane as a separator, and 3 M ZnSO_4 as an electrolyte (V-3M-Y, where “Y” represents the type of membrane used). **Figure 4a** shows the current response in the CV corresponding to the V-3M-Nafion cell at different scan rates ranging from 0.1 to

1.0 mV s^{-1} . The overlapping CV plots (Figure S12a, Supporting Information) indicate a stable performance of the V-3M-Nafion cell during subsequent scans. The appearance of multiple anodic and cathodic peaks can be attributed to the multistep reversible intercalation of Zn^{2+} into the V-CP cathode. The plot of $\log(i)$ versus $\log(\nu)$ in Figure 4b shows the current dependence on the scan rate, and the charge storage behavior is investigated using the following equation

$$i = a \nu^b \quad (2)$$

where i is the current, ν is the scan rate and a and b represent adjustable parameters.^[47] The b -values corresponding to the peaks O1, O2, R1, and R2 are obtained as 0.94, 0.71, 0.89, and 0.80, respectively. The b -values that are significantly higher than 0.5 indicate that the corresponding redox reactions in the V-CP cathode are surface controlled and capacitive in nature (Figure 4c).^[48,49] This pseudocapacitive behavior indicates the accelerated intercalation/deintercalation kinetics of Zn^{2+} , which is highly desirable for enhancing the power output of the device.^[48]

The V-3M-Nafion cell is characterized by galvanostatic charge-discharge (GCD) experiment at current rates of 0.25–10 A g^{-1} . A high average discharge capacity of 510 mAh g^{-1} is obtained at a current of 0.25 A g^{-1} (Figure 4d,e, and Figure S12b, Supporting Information). In Table S3, Supporting Information, the capacity values reported for various ZIB systems are summarized. To the best of our knowledge, the capacity value obtained for the V-3M-Nafion cell is the highest ever reported for a AZIB so far.^[15–19,27,32–34,42,43,49–58] In addition, the V-3M-Nafion cell shows an average capacity of 330 mAh g^{-1} when it is discharged at a very high current rate of 10 A g^{-1} , which corresponds to 65% retention of the capacity obtained at 0.25 A g^{-1} .

The high rate capability as well as high discharge capacity can be attributed to the rational design of the binder-free V-CP

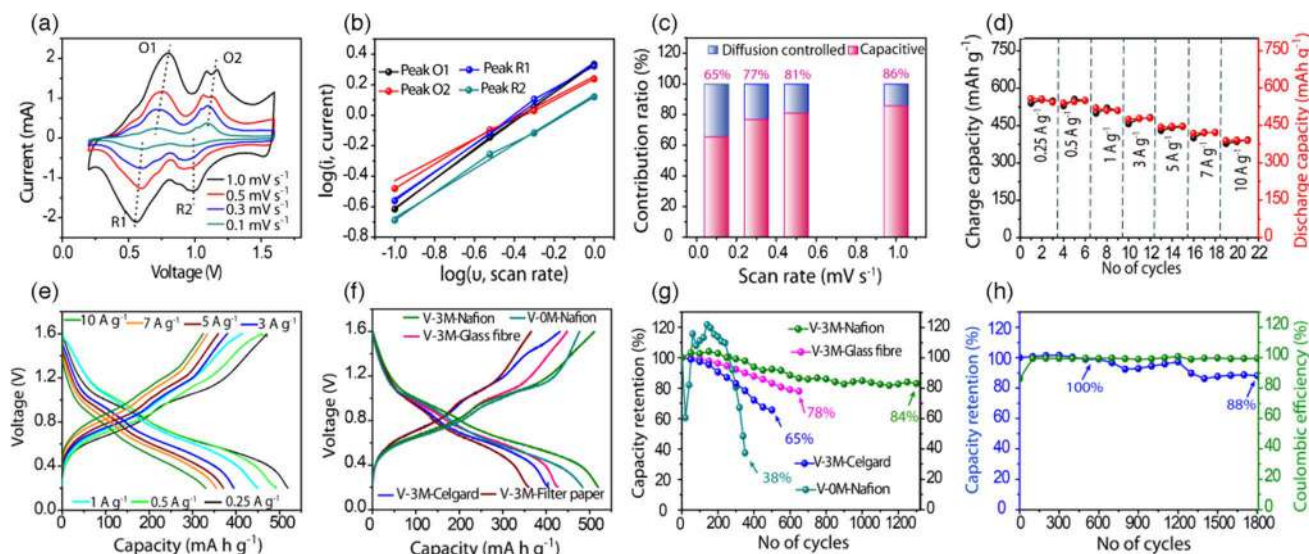


Figure 4. a) The CV plots scanned from 0.1 to 1.0 mV s^{-1} . b) $\log i$ versus $\log \nu$ plots. c) Contribution ratio of capacitive and diffusion-limited capacities at various scan rates (at 0.56 V, peak R1). d) Rate capability plot. e) Charge–discharge capacities at various currents of the V-3M-Nafion cell. f) CD profiles of V-3M-Nafion and V-3M-Y cells at 0.25 A g^{-1} current density. g) Cycling stability comparison of the V-3M-Nafion cell with other V-3M-Y cells at 5 A g^{-1} current density and h) cycling stability and coulombic efficiency of V-3M-Nafion cell at current density of 10 A g^{-1} .

cathode. The conventional methods for cathode fabrication involve the use of insulating polymer binder and multistep coating of chemically synthesized V_2O_5 over various metallic current collectors. This results in the evolution of a high contact resistance between the current collector and active material, which may restrict achieving a high capacity. However, in this work, the thin deposition of V_2O_5 integrated with the carbon skeleton (Figure 1b,c) in the V-CP cathode provides an interconnected pathway that facilitates the transport of electrons throughout the electrode. Therefore, the contact resistance is reduced with the added advantage of increased number of accessible redox active sites that promotes the Zn^{2+} uptake capacity, thereby contributing to the high capacity of the cell. The better charge transport is evident from the low charge transfer resistance (R_{ct}) value of 110Ω (Figure S12c, Supporting Information) for the V-3M-Nafion cell compared with other literature reports adopting the conventional coating methods.^[49,59] The reversible Zn^{2+} insertion is further investigated by the XPS analysis, and the corresponding data with a relevant explanation is given in SI (Section S13, Figure S13a–c, Supporting Information).

For comparison, Zn/V_2O_5 cells are fabricated with a 0M-Nafion membrane and conventional porous separators as well. The discharge capacity of the V-3M-Nafion cell is compared with that of the other membrane counterparts (Figure 4f), and further electrochemical characterizations of these cells are given in SI (Figure S14–S17, Supporting Information). Figure 4f shows that the discharge capacity (at 0.25 A g^{-1}) obtained for the V-0M-Nafion (484 mAh g^{-1}), V-3M-Glass fiber (430 mAh g^{-1}), V-3M-Celgard (400 mAh g^{-1}), and V-3M-Filter paper (360 mAh g^{-1}) cells are significantly lower compared with that of the V-3M-Nafion cell. This can be due to the better Zn^{2+} transport property of the Nafion ionomer membrane as discussed in the previous sections (Figure 2 and 3). Explanations for the observed performance of the V-0M-Nafion cell are given in Section S14, Supporting Information.

Apart from the high discharge capacity, the V-3M-Nafion cell exhibits an outstanding cycling stability at 5 A g^{-1} (Figure 4g and Figure S18, Supporting Information) and 10 A g^{-1} (Figure 4h)

with a retention of 84% of the initial capacity after 1300 cycles and 88% of initial capacity after 1800 cycles, respectively. It is worth mentioning that a high coulombic efficiency of 99% is maintained throughout the cycling stability experiment. The concomitant delivery of long cycle life and high discharge capacity is rarely found in AZIB literature (Table S3, Supporting Information), which highlights the importance of the V-3M-Nafion cell in a futuristic perspective.

Figure 4g also compares the cycling stability of the V-3M-Nafion cell with other membranes. From Figure 4g, the V-3M-Glass fiber and V-3M-Celgard show only 78% retention of the initial capacity after 650 cycles and 65% retention of the initial capacity after 500 cycles, respectively. The V-3M-filter paper cell is found to be failed after few cycles (Figure S17b, Supporting Information). This shows the superiority of the cation-selective Nafion ionomer membrane for realizing high-performance AZIB. The cycling stability performance of the V-0M-Nafion cell is also included in Figure 4g. From the data, it is evident that irrespective of a sharp increase in the capacity during the initial few cycles, a sudden drop is observed in the region of 200 cycles. After 250 cycles, only 38% of the initial capacity is retained. This further supports the claim that the integration of Zn^{2+} into the Nafion membrane is inevitable to improve the cycling stability of the AZIB. The underlying reasons pertaining to the difference in stability in the presence of different membranes are further deciphered through the postmortem analyses of the anode and cathode. The results are explained in the following sections.

2.3. Postmortem Analysis of Anode

The post-stability FESEM images of Zn anode corresponding to the V-3M-Nafion cell are shown in Figure 5a–d. Figure 5a indicates that the Zn anode in the V-3M-Nafion cell after 500 stability cycles manifests a surface more or less similar to that of the pristine Zn foil (Figure S19a and b, Supporting Information), although with a few regions of random/irregular morphology. At a higher magnification (Figure 5b), this morphology is found

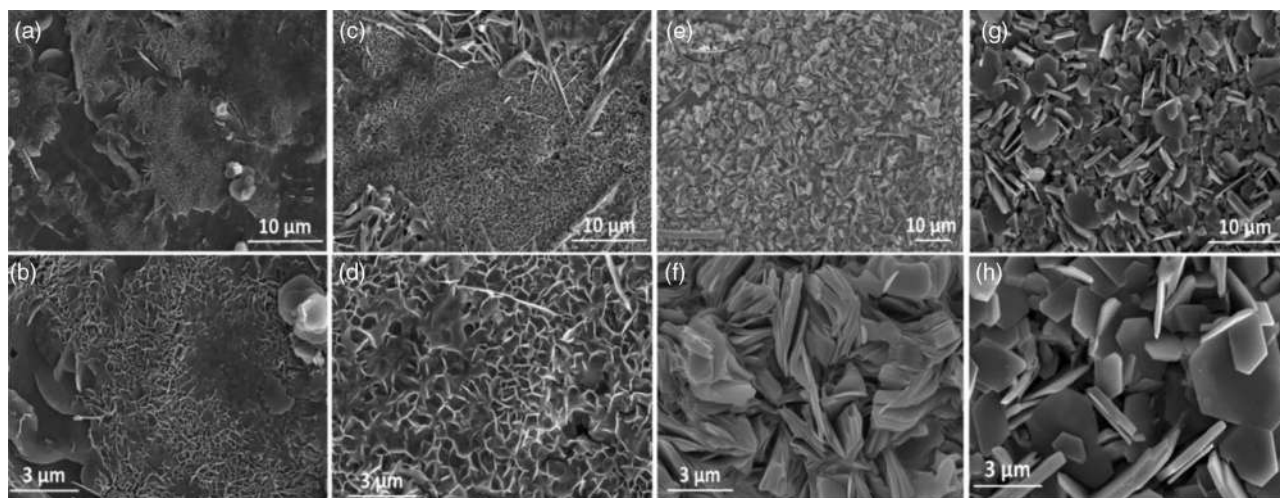


Figure 5. Morphology of the Zn anode after cycling: a,b) 500 cycles of V-3M-Nafion cell; c,d) 1300 cycles of the V-3M-Nafion cell; e,f) 650 cycles of V-3M-Glass fiber; and g,h) 500 cycles of V-3M-Celgard cell.

to possess a nanowall-like growth pattern, which is confirmed to be composed of Zn deposits from the X-ray diffraction (XRD) data given in SI (Figure S20, Supporting Information). The Zn nanowalls can be considered embedded in the nearly flat surface of the pristine Zn (Figure S19b, Supporting Information). After 1300 cycles, the density of the nanowalls is found to have extended (Figure 5c), covering the Zn surface more evenly. The 2D, thin, uniform, and interconnected nanowall pattern (Figure 5d and Figure S21, Supporting Information) favors the homogeneous distribution of the electric field in the anode even after long cycling. This inhibits the nonuniform polarization of the electrode as well as the further growth of the irregular bulk Zn deposits. Moreover, the higher intensity of the (002) plane of the fully discharged Zn (after 1300 cycles) in the V-3M-Nafion cell (Figure S20, Supporting Information) strongly suggests that the dendritic growth in the respective anode is less likely.^[31]

The suppressed bulk/dendritic deposition of Zn in the V-3M-Nafion cell can be due to the combined contribution from the inherent single ion conducting property and the presence of the anionic $-\text{SO}_3^-$ group in the Nafion ionomer. The electrostatic interaction between electron-rich SO_3^- groups in the Nafion ionomer, and the positively charged Zn can provide a strong interfacial interaction that suppresses the dendritic growth during prolonged cycling and facilitates the uniform deposition of Zn.^[60,61] This interfacial interaction assists in maintaining an efficient contact between the Zn anode and the Nafion ionomer membrane. This is schematically shown in Figure 1a. The dendrite suppressing nature of single-ion conducting electrolytes is already proved in the literature.^[62,63]

The anode morphology corresponding to the other separators (Figure 5e–h and Figure S22, Supporting Information) is also explored. The Zn deposits in the anode coupled with the glass fiber membrane is found to be composed of highly dense 3D-scales of Zn with sharp edges and irregular morphology (Figure 5e,f). On the other hand, the Celgard separator leads to the 3D hexagonal growth of micrometer-sized bulk Zn deposits (Figure 5g,h). The sharp edges of these protruding Zn deposits (Figure 5f,h) can damage the porous separators. Such kind of bulk deposits can be due to the absence of any electrostatic interaction between anode and porous separators.

The morphology of the Zn anode corresponding to the V-0M-Nafion cell is given in Figure S22a and b, Supporting Information. Unlike the porous separator-based cells, the Zn deposits in V-0M-Nafion is composed of several micrometer-sized sheets. Despite its inferior stability, the absence of bulk deposits in V-0M-Nafion is an indirect proof toward the role electrostatic interaction in suppressing the dendritic growth as already claimed in the V-3M-Nafion cell (represented in Figure 1a). The morphology of the Zn deposits during cycling is in accordance with the excellent plating/stripping behavior (Figure 2c and 3a) as well as cycling stability obtained in the presence of the 3M-Nafion membrane as discussed in the previous sections (Figure 4g).

The energy-dispersive X-ray spectroscopy (EDAX) analysis of the post-stability Zn anodes of the respective cells is also performed, and the data are summarized in Figure S23a–c, Supporting Information. The vanadium content in case of the V-3M-Nafion cell is lower compared with the other porous

separator-based cells. This is a direct indication of the minimized diffusion of the negatively charged discharge products toward the anode during the cycling due to the intrinsic cation-selective ion-conducting nature of the Nafion ionomer. On the contrary, porous separators (Figure S2b–d, Supporting Information) offer a facile pathway for the discharge products (Figure 1a), which may poison the anode surface and in turn decrease the cycle life of the cells. The digital images of the cathode, anode, and separator of all the cells under investigation followed by cycling stability analyses are given in Figure S24a–e, Supporting Information.

2.4. Postmortem Analysis of Cathode

The FESEM images corresponding to the morphology of the V-CP cathode of the V-3M-Nafion cell after the stability test are shown in Figure 6a,b. It possesses a thin and uniform coating of exfoliated nanosheets over the porous carbon paper. This is different from the dense and agglomerated morphology of the V-CP cathode in other separator-based cells (Figure S25a–f, Supporting Information). From the XRD analysis (Figure 6c), it is apparent that the appearance of a new peak at a 2θ value of 12.3° is consistent in all the V-CP cathodes, which corresponds to the formation of a $\text{Zn}_x\text{V}_2\text{O}_5$ phase.^[52] It can be also noted that the XRD plots of all cathodes are more or less similar. This draws the conclusion that the plausible limiting factor for the cyclic stability of ZIB is the morphological evolution of both anode and cathode during cycling.

2.5. Ragone Plot and Real-Life Demonstration

The Ragone plot representing the energy and power density of the V-3M-Nafion cell is shown in Figure 7a. At the different

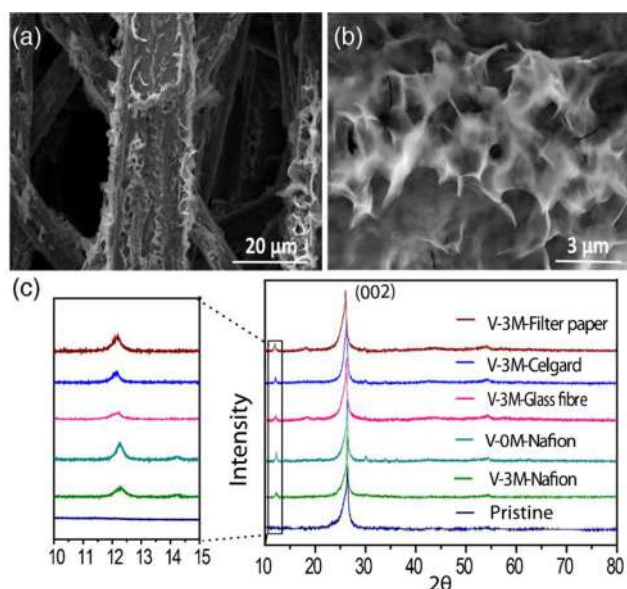


Figure 6. a) Lower and b) higher magnification FESEM images of the V-CP cathode of the V-3M-Nafion cell after the stability test. c) XRD plots of the V-CP cathodes of the various separator-based cells followed by the stability test.

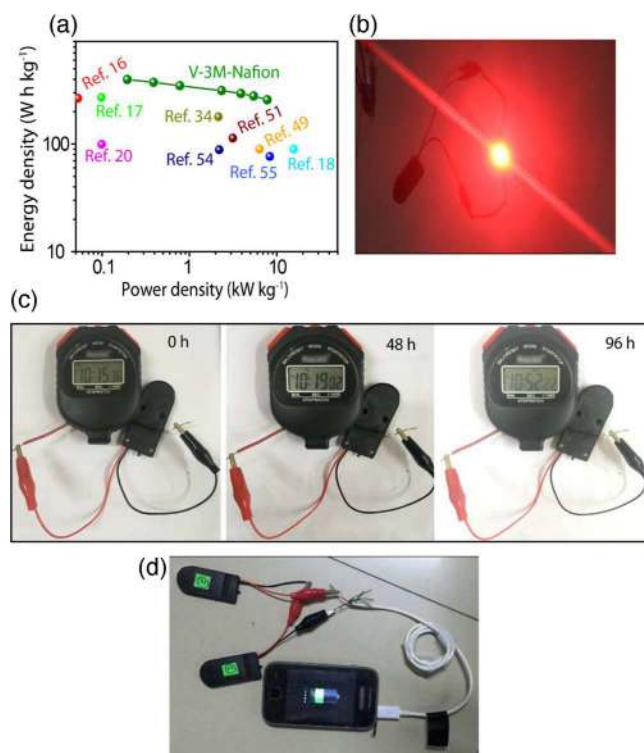


Figure 7. a) Ragone plot (energy density vs power density) corresponding to the V-3M-Nafion cell. b–d) Real-life demonstration of the Zn/V₂O₅ battery (b) by lighting a red LED bulb, c) by powering a 1.5 V stopwatch, and d) by powering a smart phone.

power densities of 195 and 7800 W kg⁻¹, the device delivers high energy densities of 398 and 257 Wh kg⁻¹, respectively (energy density of the cell is evaluated, considering the loading of V₂O₅ on cathode, and the corresponding calculations are given in SI, Section S1 and S20, Supporting Information). This is far higher than extant AZIBs, which use conventional separators.^[15,42,49–51,53–56,58] The combination of high energy and power density of the V-3M-Nafion cell can narrow the gap between the supercapacitors and batteries. The application of AZIBs in various real-life situations is also demonstrated. Figure 7b shows two cells connected in series being used for powering a red light-emitting diode (LED) bulb with a nominal voltage of 1.8 V. The setup is used for powering a digital clock continuously for 96 h (Figure 7c). Figure 7d shows powering of a smart phone by using four Zn/V₂O₅ cells connected in series. All the associated videos are compiled and included in Supporting Information.

3. Conclusions

In this work, we have demonstrated the advantage of using a Zn²⁺-integrated Nafion ionomer membrane over conventional porous separators (glass fiber, filter paper, polypropylene, etc.) to realize high-performance ZIBs. The use of a Nafion ionomer membrane stabilizes the anode in a Zn/V₂O₅ cell (V-3M-Nafion) by suppressing the growth of bulk/dendritic Zn deposits during

cycling. The unique thin and nanowall-like morphology of the Zn surface is found to promote the cycling stability of the cell compared with the micrometer-sized sharp-edged deposit obtained with porous separators. The cathode morphology is also found to have the favorable thin Zn_xV₂O₅ phase in case of Zn²⁺-integrated Nafion separator. The high Zn²⁺ transference number and low activation energy offered by the 3M-Nafion ionomer membrane reduce the overpotential of Zn plating/stripping, which is an added advantage compared with other separators. The high discharge capacity of 510 mAh g⁻¹ at a current density of 0.25 A g⁻¹ obtained for the V-3M-Nafion cell is the highest ever reported for a ZIB, which is facilitated by the rationally designed V₂O₅ cathode. The Nafion-based cell is found to retain a capacity of 84% even after 1300 continuous charge–discharge cycles at 5 A g⁻¹ current density. Therefore, it can be concluded that the strategy of using the Zn²⁺-integrated Nafion ionomer membrane separator has several advantages, which are essential for the high capacity as well as long cycling life of AZIBs.

4. Experimental Section

Materials: Vanadium sulfate oxide hydrate (VOSO₄·xH₂O) was procured from Alfa-Aesar. Lithium perchlorate (LiClO₄) was purchased from Sigma-Aldrich. Zinc sulfate (ZnSO₄·7H₂O) was purchased from HiMedia Laboratories Pvt. Limited. Toray carbon paper, Glass fiber paper (grade GF/F), Celgard separator (polypropylene membrane), and Whatman filter paper (Quartz microfiber filters-QMA) were supplied by Global Nanotech. Nafion 212 was purchased from Du Pont, USA.

Fabrication of the Cathode: The free-standing cathode was prepared by a method previously reported by our group.^[64] A piece of pristine carbon fiber paper (pCP) was electrochemically functionalized (fCP) in an aqueous electrolyte (by applying a bias voltage of 10 V in 0.1 M Na₂SO₄ electrolyte) followed by the chronopotentiometric electrodeposition of V₂O₅. A constant current of 3 mA cm⁻² was applied for 177 s to obtain a loading of 1 mg of V₂O₅ in 1 cm² area of fCP. The obtained electrode was subjected to annealing at 250 °C for 2 h and marked as V-CP.

Pretreatment of the Nafion Ionomer Membranes: Prior to use, the Nafion ionomer membrane (Nafion 212) was treated sequentially at 80 °C for 30 min in 1) 4 wt% H₂O₂; 2) DI water; 3) 0.8 M H₂SO₄; and 4) DI water, respectively, with the numbers representing the order of treatment.^[50] The coupons of the as-obtained activated Nafion ionomer membrane (thickness 60 μm) were dipped in the desired electrolyte (aqueous ZnSO₄) with a salt concentration of 0, 1, 2 and 3 M, for 3 days. The respective membranes are marked as XM-Nafion, where “X” stands for the concentration of the electrolyte solution used.

Modification of the Conventional Porous Membranes: To study the effect of conventional porous separators on the performance of the AZIB, three different porous membranes (Celgard, Whatman filter paper, and glass fiber with a thickness of 40, 175, and 270 μm, respectively) were used. All the porous membranes were also soaked in 3 M ZnSO₄ prior to the use and the corresponding membranes termed as 3M-Y, where “Y” represents the type of the membrane used.

Assembly of Zn/V₂O₅ Cells: All the Zn/V₂O₅ cells were assembled in the CR2032 coin cell in a traditional fashion, where a zinc foil (area 1 cm²), a freshly prepared V-CP electrode (area 1 cm²), and desired Nafion membrane presoaked in an aqueous ZnSO₄ electrolyte (XM-Nafion) were used as an anode, cathode, and separator, respectively. Here, the terms anode and cathode are used for the negative and positive electrodes, respectively, considering the discharge state of the cell. For the purpose of comparison, several other Zn/V₂O₅ cells were also assembled in a similar fashion (CR2032 coin cell) using conventional porous separators. In accordance with the various separators used, the respective cells are designated as V-XM-Y. Here also “X” stand for the concentration of the ZnSO₄ electrolyte and “Y” for the type of the membrane used.

Material Characterization: Morphology investigations of V-CP samples were carried out with field emission scanning electron microscope (FESEM) Nova Nano SEM 450 and FEI-Quanta 450-FEG instrument. The morphologies of the various separators were obtained with ESEM-Quanta 200-3D instrument. Energy dispersive X-ray spectroscopy (EDAX) analysis and energy dispersive X-ray spectroscopy (EDS) elemental mapping were performed with ESEM-Quanta 200-3D instrument. Transmission electron microscopy (TEM) imaging was carried out using Tecnai T-20 instrument at an accelerating voltage of 200 kV. Thermogravimetric analysis (TGA) was performed using an SDT Q600 DSC-TGA instrument with a temperature ramp of $10\text{ }^{\circ}\text{C min}^{-1}$ in a nitrogen atmosphere. Fourier transform infrared (FTIR) analysis of the sample was carried out with a Bruker Tensor27 FTIR instrument. A Thermo K-alpha+ X-ray spectrometer was used for the X-ray photoelectron spectroscopy (XPS) analysis. X-ray diffraction (XRD) analysis was carried out using Rigaku, MicroMax-007HF with high-intensity Microfocus rotating anode X-ray generator (Cu K α [$\alpha = 1.54\text{ \AA}$]).

Electrochemical Characterization: The electrochemical analyses were carried out in BioLogic VMP3 Potentio-Galvanostat instrument. Electrochemical impedance spectroscopy (EIS) analysis was used to determine the ionic conductivity of Zn²⁺ in various membranes. The frequency for the EIS analysis was varied from 1 MHz to 1 Hz against an open-circuit potential with a sinus amplitude of 10 mV ($V_{\text{rms}} = 7.07\text{ mV}$). The conductivity cells were fabricated in the CR2032 coin cell by keeping the desired membranes in between two stainless steel plates with 1 mm thickness. The conductivity measurements were carried out between 20 to 60 °C at every 10 °C interval. The temperature was controlled by using the Espec environmental test chamber.

To study the effect of Nafion ionomer-based membranes in the plating/stripping behavior of Zn, electrochemical cells were fabricated by using pCP (1 cm² area) as a working electrode, a piece of Zn foil (1 cm² area) as a counter and reference electrodes, and the desired Nafion membrane as a separator in the CR2032 coin cell. For the comparison purposes, the same kind of cells was prepared with other porous membranes as well. The cells are designated as CP-XM-Y, where X and Y carry the same information as mentioned in the previous section. These Zn/CP cells were characterized by cyclic voltammetry (CV) analysis. The reversibility of Zn plating/stripping in the presence of various separator membranes were also studied in the Zn/Zn symmetric cell with two Zn foils separated by desired Nafion ionomer membranes or other porous separator membranes. The cells are designated as Zn-XM-Y, where X and Y carry the same information as mentioned in the previous section. These cells were characterized by galvanostatic cycling at a current rate of 0.1 mA cm⁻² for 30 min in each half-cycle. For evaluating the transference number of Zn²⁺ in the presence of various separators, the chronoamperometry experiments were carried out at 25 mV potential in the Zn/Zn symmetric cell. The resistance values before and after the DC polarization were obtained from the EIS analyses.

To check the performance of the Zn/V₂O₅ cells, CV (at scan rates of 1.0, 0.5, 0.3, and 0.1 mV s⁻¹) and galvanostatic charge/discharge (GCD) (at constant current rates of 0.25, 0.5, 1, 3, 5, 7, and 10 A g⁻¹) analyses were carried out in the voltage window of 1.6–0.2 V. The cycling stability tests were performed by the GCD experiment at current rates of 5 and 10 A g⁻¹.

Supporting Information

Supporting Information is available from the Wiley Online Library or from the author.

Acknowledgements

M.G. and V.V. contributed equally to this work. M.G. and V.V. acknowledge CSIR and UGC, respectively, for the research fellowship. K.S. acknowledges CSIR, New Delhi, for project funding (TLP003526).

Conflict of Interest

The authors declare no conflict of interest.

Keywords

aqueous zinc-ion batteries, dendrite suppression, long cycling stability, Nafion ionomer membranes, separator

Received: April 16, 2019

Revised: April 26, 2019

Published online:

- [1] B. Dunn, H. Kamath, J.-M. Tarascon, *Science* **2011**, *334*, 928.
- [2] Z. Yang, J. Zhang, M. C. W. Kintner-Meyer, X. Lu, D. Choi, J. P. Lemmon, J. Liu, *Chem. Rev.* **2011**, *111*, 3577.
- [3] H. Kim, J. Hong, K.-Y. Park, H. Kim, S.-W. Kim, K. Kang, *Chem. Rev.* **2014**, *114*, 11788.
- [4] G. Wang, L. Fu, N. Zhao, L. Yang, Y. Wu, H. Wu, *Angew. Chem., Int. Ed.* **2007**, *46*, 295.
- [5] J.-Y. Luo, Y.-Y. Xia, *Adv. Funct. Mater.* **2007**, *17*, 3877.
- [6] Y. Wang, J. Yi, Y. Xia, *Adv. Energy Mater.* **2012**, *2*, 830.
- [7] W. Li, J. R. Dahn, D. S. Wainwright, *Science* **1994**, *264*, 1115.
- [8] Z. Chang, C. Li, Y. Wang, B. Chen, L. Fu, Y. Zhu, L. Zhang, Y. Wu, W. Huang, *Sci. Rep.* **2016**, *6*, 28421.
- [9] L. Suo, O. Borodin, T. Gao, M. Olguin, J. Ho, X. Fan, C. Luo, C. Wang, K. Xu, *Science* **2015**, *350*, 938.
- [10] R.-S. Kühnel, D. Reber, C. Battaglia, *ACS Energy Lett.* **2017**, *2*, 2005.
- [11] L. Suo, O. Borodin, Y. Wang, X. Rong, W. Sun, X. Fan, S. Xu, M. A. Schroeder, A. V. Cresce, F. Wang, C. Yang, Y.-S. Hu, K. Xu, C. Wang, *Adv. Energy Mater.* **2017**, *7*, 1701189.
- [12] X. Wang, F. Wang, L. Wang, M. Li, Y. Wang, B. Chen, Y. Zhu, L. Fu, L. Zha, L. Zhang, Y. Wu, W. Huang, *Adv. Mater.* **2016**, *28*, 4904.
- [13] X. Wang, M. Li, Y. Wang, B. Chen, Y. Zhu, Y. Wu, *J. Mater. Chem. A* **2015**, *3*, 8280.
- [14] C. Xu, B. Li, H. Du, F. Kang, *Angew. Chem., Int. Ed.* **2012**, *51*, 933.
- [15] P. Hu, M. Yan, T. Zhu, X. Wang, X. Wei, J. Li, L. Zhou, Z. Li, L. Chen, L. Mai, *ACS Appl. Mater. Interfaces* **2017**, *9*, 42717.
- [16] C. Xia, J. Guo, P. Li, X. Zhang, H. N. Alshareef, *Angew. Chem., Int. Ed.* **2018**, *57*, 3943.
- [17] T. Wei, Q. Li, G. Yang, C. Wang, *J. Mater. Chem. A* **2018**, *6*, 8006.
- [18] V. Soundharajan, B. Sambandam, S. Kim, M. H. Alfaruqi, D. Y. Putro, J. Jo, S. Kim, V. Mathew, Y.-K. Sun, J. Kim, *Nano Lett.* **2018**, *18*, 2402.
- [19] P. He, M. Yan, G. Zhang, R. Sun, L. Chen, Q. An, L. Mai, *Adv. Energy Mater.* **2017**, *7*, 1601920.
- [20] L. Zhang, L. Chen, X. Zhou, Z. Liu, *Adv. Energy Mater.* **2015**, *5*, 1400930.
- [21] R. Trócoli, F. La Mantia, *ChemSusChem* **2015**, *8*, 481.
- [22] A. Holland, R. D. Mckerracher, A. Cruden, R. G. A. Wills, *J. Appl. Electrochem.* **2018**, *48*, 243.
- [23] H. Zhang, K. Ye, K. Zhu, R. Cang, J. Yan, K. Cheng, G. Wang, D. Cao, *Chem.: Eur. J.* **2017**, *23*, 17118.
- [24] F. Wang, X. Fan, T. Gao, W. Sun, Z. Ma, C. Yang, F. Han, K. Xu, C. Wang, *ACS Central Sci.* **2017**, *3*, 1121.
- [25] F. Wang, O. Borodin, T. Gao, X. Fan, W. Sun, F. Han, A. Faraone, J. A. Dura, K. Xu, C. Wang, *Nat. Mater.* **2018**, *17*, 543.
- [26] J. Lee, J. B. Ju, W. I. Cho, B. W. Cho, S. H. Oh, *Electrochim. Acta* **2013**, *112*, 138.
- [27] D. Kundu, B. D. Adams, V. Duffort, S. H. Vajargah, L. F. Nazar, *Nat. Energy* **2016**, *1*, 16119.

- [28] B. Häupler, C. Rössel, A. M. Schwenke, J. Winsberg, D. Schmidt, A. Wild, U. S. Schubert, *NPG Asia Mater.* **2016**, *8*, e283.
- [29] Y. Song, J. Hu, J. Tang, W. Gu, L. He, X. Ji, *ACS Appl. Mater. Interfaces* **2016**, *8*, 32031.
- [30] W. Li, K. Wang, M. Zhou, H. Zhan, S. Cheng, K. Jiang, *ACS Appl. Mater. Interfaces* **2018**, *10*, 22059.
- [31] K. E. K. Sun, T. K. A. Hoang, T. N. L. Doan, Y. Yu, X. Zhu, Y. Tian, P. Chen, *ACS Appl. Mater. Interfaces* **2017**, *9*, 9681.
- [32] W. Li, K. Wang, S. Cheng, K. Jiang, *Energy Storage Mater.* **2018**, *15*, 14.
- [33] N. Zhang, Y. Dong, M. Jia, X. Bian, Y. Wang, M. Qiu, J. Xu, Y. Liu, L. Jiao, F. Cheng, *ACS Energy Lett.* **2018**, *3*, 1366.
- [34] F. Wan, L. Zhang, X. Dai, X. Wang, Z. Niu, J. Chen, *Nat. Commun.* **2018**, *9*, 1656.
- [35] V. S. Reddy Channu, R. Holze, I.-H. Yeo, S.-I. Mho, R. R. Kalluru, *Appl. Phys. A* **2011**, *104*, 707.
- [36] X. Wang, W. Jia, L. Wang, Y. Huang, Y. Guo, Y. Sun, D. Jia, W. Pang, Z. Guo, X. Tang, *J. Mater. Chem. A* **2016**, *4*, 13907.
- [37] Y.-Z. Zheng, H. Ding, E. Uchaker, X. Tao, J.-F. Chen, Q. Zhang, G. Cao, *J. Mater. Chem. A* **2015**, *3*, 1979.
- [38] A. Venkatesan, N. R. Krishna Chandar, A. Kandasamy, M. Karl Chinnu, K. N. Marimuthu, R. Mohan Kumar, R. Jayavel, *RSC Adv.* **2015**, *5*, 21778.
- [39] X. Yu, J. Joseph, A. Manthiram, *J. Mater. Chem. A* **2015**, *3*, 15683.
- [40] I. Bauer, S. Thieme, J. Brückner, H. Althues, S. Kaskel, *J. Power Sources* **2014**, *251*, 417.
- [41] V. Vijayakumar, M. Ghosh, A. T. Arun Torris, M. K. Nikhil Chandran, S. B. Nair, M. V. Badiger, S. Kurungot, *ACS Sustainable Chem. Eng.* **2018**, *6*, 12630.
- [42] N. Zhang, F. Cheng, Y. Liu, Q. Zhao, K. Lei, C. Chen, X. Liu, J. Chen, *J. Am. Chem. Soc.* **2016**, *138*, 12894.
- [43] W. Sun, F. Wang, S. Hou, C. Yang, X. Fan, Z. Ma, T. Gao, F. Han, R. Hu, M. Zhu, C. Wang, *J. Am. Chem. Soc.* **2017**, *139*, 9775.
- [44] K. M. Abraham, Z. Jiang, B. Carroll, *Chem. Mater.* **1997**, *9*, 1978.
- [45] L. Porcarelli, P. S. Vlasov, D. O. Ponkratov, E. I. Lozinskaya, D. Y. Antonov, J. R. Nair, C. Gerbaldi, D. Mecerreyes, A. S. Shaplov, *Eur. Polym. J.* **2018**, *107*, 218.
- [46] Z. Cai, Y. Liu, S. Liu, L. Li, Y. Zhang, *Energy Environ. Sci.* **2012**, *5*, 5690.
- [47] H.-S. Kim, J. B. Cook, H. Lin, S. Ko Jesse, H. Tolbert Sarah, V. Ozolins, B. Dunn, *Nat. Mater.* **2016**, *16*, 454.
- [48] J. Wang, J. Polleux, J. Lim, B. Dunn, *J. Phys. Chem. C* **2007**, *111*, 14925.
- [49] M. Yan, P. He, Y. Chen, S. Wang, Q. Wei, K. Zhao, X. Xu, Q. An, Y. Shuang, Y. Shao, K. T. Mueller, L. Mai, J. Liu, J. Yang, *Adv. Mater.* **2018**, *30*, 1703725.
- [50] Q. Zhao, W. Huang, Z. Luo, L. Liu, Y. Lu, Y. Li, L. Li, J. Hu, H. Ma, J. Chen, *Sci. Adv.* **2018**, *4*, eaao1761.
- [51] B. Sambandam, V. Soundharrajan, S. Kim, M. H. Alfaruqi, J. Jo, S. Kim, V. Mathew, Y.-K. Sun, J. Kim, *J. Mater. Chem. A* **2018**, *6*, 3850.
- [52] J. Zhou, L. Shan, Z. Wu, X. Guo, G. Fang, S. Liang, *Chem. Commun.* **2018**, *54*, 4457.
- [53] J. Ding, Z. Du, L. Gu, B. Li, L. Wang, S. Wang, Y. Gong, S. Yang, *Adv. Mater.* **2018**, *30*, 1800762.
- [54] Q. Pang, C. Sun, Y. Yu, K. Zhao, Z. Zhang, P. M. Voyles, G. Chen, Y. Wei, X. Wang, *Adv. Energy Mater.* **2018**, *8*, 1800144.
- [55] C. Shen, X. Li, N. Li, K. Xie, J.-G. Wang, X. Liu, B. Wei, *ACS Appl. Mater. Interfaces* **2018**, *10*, 25446.
- [56] C. Xia, J. Guo, Y. Lei, H. Liang, C. Zhao, H. N. Alshareef, *Adv. Mater.* **2018**, *30*, 1705580.
- [57] S. Islam, M. H. Alfaruqi, V. Mathew, J. Song, S. Kim, S. Kim, J. Jo, J. P. Baboo, D. T. Pham, D. Y. Putro, Y.-K. Sun, J. Kim, *J. Mater. Chem. A* **2017**, *5*, 23299.
- [58] P. He, G. Zhang, X. Liao, M. Yan, X. Xu, Q. An, J. Liu, L. Mai, *Adv. Energy Mater.* **2018**, *8*, 1702463.
- [59] X. Wu, Y. Xiang, Q. Peng, X. Wu, Y. Li, F. Tang, R. Song, Z. Liu, Z. He, X. Wu, *J. Mater. Chem. A* **2017**, *5*, 17990.
- [60] W.-K. Shin, A. G. Kannan, D.-W. Kim, *ACS Appl. Mater. Interfaces* **2015**, *7*, 23700.
- [61] J. Gao, C. Sun, L. Xu, J. Chen, C. Wang, D. Guo, H. Chen, *J. Power Sources* **2018**, *382*, 179.
- [62] Y. Lu, M. Tikekar, R. Mohanty, K. Hendrickson, L. Ma, L. A. Archer, *Adv. Energy Mater.* **2015**, *5*, 1402073.
- [63] W. Zhang, Z. Tu, J. Qian, S. Choudhury, L. A. Archer, Y. Lu, *Small* **2018**, *14*, 1703001.
- [64] M. Ghosh, V. Vijayakumar, R. Soni, S. Kurungot, *Nanoscale* **2018**, *10*, 8741.

Nafion Ionomer-Based Single Component Electrolytes for Aqueous Zn/MnO₂ Batteries with Long Cycle Life

Meena Ghosh, Vidyanand Vijayakumar, Bihag Anothumakkool, and Sreekumar Kurungot*

Cite This: *ACS Sustainable Chem. Eng.* 2020, 8, 5040–5049

Read Online

ACCESS |



Metrics & More



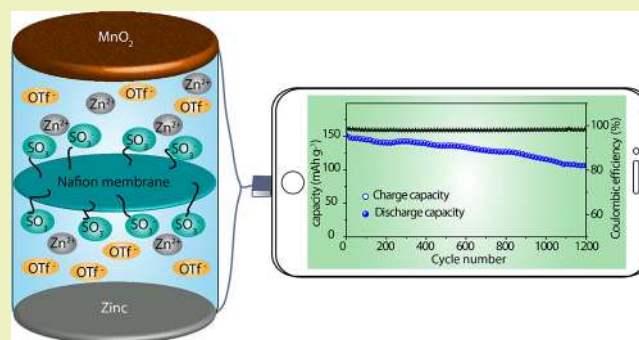
Article Recommendations



Supporting Information

ABSTRACT: Recently, aqueous rechargeable Zn/MnO₂ batteries are emerging as promising energy storage aids owing to their improved safety, low cost of fabrication, and high energy density. However, the rapid decay of capacity during extended charge–discharge cycles hinders the prospect of this technology beyond lab-scale. In the conventional Zn/MnO₂ cell, additives such as Mn²⁺ have been used to tackle the stability issue. Here, we demonstrate that cycling performance of the Zn/MnO₂ cell can be improved substantially by using Nafion ionomer as the separator in combination with zinc-ion conducting electrolytes. The Nafion ionomer-based Zn/MnO₂ cells do not require any Mn²⁺ additive in the electrolyte and hence termed as “single component” electrolytes. The postmortem study of the post-cycled electrodes reveals that the structural evolution of both the anode and cathode in various electrolytes (1 M Zn(CF₃SO₃)₂, 1 M ZnSO₄·7H₂O, and 3 M ZnSO₄·7H₂O) during prolonged cycling significantly influences the cycle life of the respective cells. Optimizing the Nafion ionomer membrane with a suitable electrolyte could render the desired combination of high capacity and high cycle life for a Zn/MnO₂ cell.

KEYWORDS: aqueous Zn-ion batteries, electrodeposition, single component electrolyte, Nafion ionomer separator, cycling stability, dendrite suppression, MnO₂



INTRODUCTION

State-of-the-art lithium-ion batteries (LIBs) use a graphite anode in combination with flammable organic electrolytes inciting several safety concerns.^{1,2} Although the prospect of aqueous electrolyte- and solid-state electrolyte-based LIBs is heavily researched,^{3,4} their commercial potential is debated due to the poor interfaces and stability issues. In this scenario, post-lithium rechargeable battery chemistries are receiving significant attention. Among them, aqueous rechargeable zinc-metal batteries (ZMBs) conceiving the reversible shuttling of zinc ion (Zn²⁺) between a metallic zinc anode and an intercalation cathode are of particular interest.^{5,6} Zinc is naturally abundant and possesses a low reduction potential of -0.78 V versus standard hydrogen electrode.⁷ It is expected that the use of a high-capacity zinc anode (820 mAh g^{-1}) in combination with a suitable high-voltage cathode could make the ZMBs reach up to 190 Wh Kg^{-1} ; however, due to poor cathode performance, values are around $80\text{--}90 \text{ Wh kg}^{-1}$.⁸

MnO₂ is considered as one of the promising cathode materials for the reversible insertion of Zn²⁺ ions.^{9,10} The MnO₂ cathode exhibits a high average potential (~ 1.4 V) along with a high capacity ($>200 \text{ mAh g}^{-1}$), which enhances the possible energy output of ZMBs.¹¹ However, despite the abovementioned advantages, the further development of rechargeable Zn/MnO₂ batteries is still constrained due to

severe capacity fading during cycling. As per the current understanding, this shortcoming originates from the dissolution of Mn²⁺ into the electrolyte.¹² In this aspect, Mn(II) salts such as MnSO₄ and Mn(CF₃SO₃)₂ are employed as additives in the Zn-ion conducting electrolytes and are proved to improve the cycle life of the Zn/MnO₂ battery.¹³ The presence of a Mn(II) salt in the electrolyte maintains an equilibrium concentration of Mn²⁺ at the electrode/electrolyte interface, suppressing the dissolution of the electrode material.^{14,15} Also, the Mn(II) salt could be electrodeposited on the cathode during electrochemical cycling of the cell, leading to higher loading of the active material.^{16,17} This lead to the over-estimation of the cell performance, which is often not taken into account. Despite the know-how regarding the Mn²⁺ dissolution leading to capacity fading in the Zn/MnO₂ battery, the other factors contributing to the same still remain ambiguous. Therefore, an alternate strategy to improve the

Received: November 14, 2019

Revised: February 8, 2020

Published: February 23, 2020

cycle life of the Zn/MnO₂ battery without a pre-added Mn(II) salt is desirable.

Few recent reports have demonstrated that accumulation of an irreversible byproduct (such as ZnMn₃O₇·2H₂O or woodruffite structure) on the cathode impedes the reversibility of the Zn²⁺ shuttling, deteriorating the overall performance of the battery.^{18–20} Besides, ZMBs suffer from low cycle life owing to the dendrite-like structural evolution on the surface of the metallic zinc-anode.^{21–23} In addition to this, recently Zhao et al. have shown the poisoning of the anode by means of diffused discharge byproducts from the cathode to be detrimental to the cycling stability in ZMBs.²⁴ Therefore, in the case of the Zn/MnO₂ battery, the poisoning of the zinc surface by Mn(II) deposition could possibly be another factor contributing toward the observed performance degradation. In fact, reports on a manganese-based LIB cathode have proved that dissolved Mn²⁺ diffuses, migrates, and eventually gets deposited on the anode, leading to poisoning of the solid electrolyte interphase (SEI) layer on the anode.²⁵ The aforementioned intricacies can be mitigated by using a cation selective ionomer membrane such as Nafion as the separator. Recently, our group has explored this strategy with two different cathodes, viz., V₂O₅ and covalent organic framework (COF).^{26,27}

Here, we investigate the electrochemical performance of lab-scale Zn/MnO₂ unit cells with Nafion ionomer membrane as the separator in combination with zinc-ion conducting liquid electrolytes. Unlike the plethora of available reports on ZMBs, no additional Mn(II) salt is added into the electrolytes, and hence they are called “single component” electrolytes. Specific attention is dedicated to the Nafion membrane-based Zn/MnO₂ cells comprising Zn(CF₃SO₃)₂ or ZnSO₄ in the electrolytes, which offer a more favorable electrode/electrolyte interface and wide electrochemical stability window compared to other salts such as ZnCl₂, Zn(OOCCH₃)₂, and Zn(NO₃)₂. In 1 M Zn(CF₃SO₃)₂, the Nafion-based Zn/MnO₂ cell exhibits a high capacity of 350 mAh g⁻¹ at 100 A g⁻¹ and excellent cycling stability (89% of the initial capacity is retained after 500 cycles at 3 A g⁻¹ current rate) compared to all the other electrolytes. On the other hand, in 1 M ZnSO₄·7H₂O, the Zn/MnO₂ cell delivers a high initial capacity; however, the capacity drops drastically to 110 mAh g⁻¹ after 500 cycles. Such capacity fading is found to be reduced in a concentrated electrolyte (3 M ZnSO₄·7H₂O). Most importantly, the current study emphasizes that, irrespective of the type of the liquid electrolyte used, all the Nafion-based Zn/MnO₂ cells outperform the porous separator (glass fiber paper and polypropylene)-based counterparts. This highlights the utility of the Nafion-based single component electrolyte to eliminate the necessity of Mn(II) additives in the electrolyte in the Zn/MnO₂ cells. Additionally, through detailed structural analyses of the post-cycling electrodes, we have also elucidated the underlying factors contributing to the improved performance of Nafion-based Zn/MnO₂ cells as a function of different electrolytes.

■ EXPERIMENTAL SECTION

Materials. Manganese acetate (Mn(OOCCH₃)₂), ammonium acetate (NH₄OOCCH₃), zinc trifluoromethanesulfonate (Zn(CF₃SO₃)₂), zinc nitrate hexahydrate (Zn(NO₃)₂·6H₂O), zinc chloride (ZnCl₂), and zinc sulfate heptahydrate (ZnSO₄·7H₂O) were procured from Sigma Aldrich. Zinc acetate (Zn(OOCCH₃)₂) was purchased from Rankem Chemicals. Toray carbon fiber paper was

supplied by Global Nanotech. Nafion membrane (212) was procured from DuPont, USA. Glass fiber (Grade GF/F) and polypropylene-based Celgard were supplied by Global Nanotech.

Fabrication of the Cathode. The precursor solution was prepared by dissolving 432 mg of Mn(OOCCH₃)₂ (0.1 M) and 193 mg of (NH₄OOCCH₃) (0.1 M) in 25 mL of deionized water. Electrochemical deposition of MnO₂ was carried out in a three-electrode setup using pristine Toray carbon paper (CP; 1 cm² area) as the working electrode, platinum mesh as the counter electrode, and platinum wire as the quasi-reference electrode in a Biologic VMP3 potentiostat instrument. A constant current of 4 mA cm⁻² was applied for different time intervals of 560, 1663, and 2772 s to obtain MnO₂ loading values of 1, 3, and 5 mg, respectively. Followed by the electrodeposition, all the electrodes were rinsed thoroughly with water and dried at 60 °C. The as-prepared electrodes are marked as MnCP-X, where “X” stands for the loading of MnO₂ on CP.

Material Characterization. Morphology of the MnCP-X samples was investigated with field emission scanning electron microscopy (FESEM; Nova Nano SEM 450). Energy-dispersive X-ray spectroscopy (EDAX) analysis and EDAX elemental mapping were performed with an ESEM-Quanta 200-3D instrument. A Tecnai T-20 instrument at an accelerating voltage of 200 kV was used for transmission electron microscopy (TEM) imaging. Fourier transform infrared (FTIR) analysis was carried out with a Bruker Tensor27 FTIR instrument. X-ray photoelectron spectroscopy (XPS) analysis was performed using a Thermo K-alpha+ X-ray spectrometer. A Rigaku MicroMax-007HF with high-intensity Microfocus rotating anode X-ray generator (Cu Kα (α = 1.54 Å)) was used for X-ray diffraction (XRD) analysis.

Electrochemical Characterization. A BioLogic VMP3 Potentiostat-Galvanostat instrument was used for all the electrochemical analyses. All the electrochemical cells were fabricated in a CR2032 coin cell configuration using Nafion membrane as the separator. Prior to use, the Nafion membranes were pre-treated by following the previously reported method.²⁶ In this work, aqueous solutions of 1 M Zn(CF₃SO₃)₂, 1 M ZnSO₄·7H₂O, 1 M ZnCl₂, 1 M Zn(NO₃)₂·6H₂O, 1 M Zn(OOCCH₃)₂, or 3 M ZnSO₄·7H₂O were used as the electrolytes. The electrolytes in combination with Nafion membrane are represented as Naf-T-1, Naf-S-1, Naf-C-1, Naf-N-1, Naf-A-1, and Naf-S-3, respectively, where “Naf” stands for Nafion, the letter followed by “Naf” indicates the type of conducting salt (T = Zn(CF₃SO₃)₂, S = Zn(SO₄)₂, C = ZnCl₂, N = Zn(NO₃)₂, and A = Zn(OOCCH₃)₂) and the digits “1” and “3” represent the concentration of the electrolytes. Cyclic voltammetry (CV) analyses were carried out in a Zn|Y|Zn cell configuration using CP and metallic zinc as the working and reference electrodes, respectively. Here, the letter “Y” is used as a general representation for the aforementioned electrolyte-soaked Nafion membranes (e.g., Naf-T-1, Naf-S-1, etc.). Similarly, the galvanostatic Zn plating/stripping experiments were carried out at a current rate of 0.1 mA cm⁻² (30 min Zn plating and 30 min Zn stripping) in a Zn|Y|Zn symmetric cell configuration.

Ionic conductivity values of the electrolytes were determined by the electrochemical impedance spectroscopy (EIS) technique. The frequency for the EIS analysis was varied from 1 MHz to 1 Hz against an open-circuit potential with a sinus amplitude of 10 mV (V_{rms} = 7.07 mV). The conductivity cells were fabricated in CR2032 coin cell by keeping the desired electrolyte-soaked Nafion membrane in between two stainless steel plates with 1 mm thickness. The conductivity measurements were carried out between 20 to 60 °C at every 10 °C interval. The temperature was controlled by using an Espec environmental test chamber. The transference number of Zn²⁺ ion (t_{Zn²⁺}) in the electrolyte-infused Nafion membranes was also analyzed in the Zn|Y|Zn symmetric cell configuration, and t_{Zn²⁺} values were calculated from the following equation (eq 1) proposed by Abraham et al.^{28,29}

$$t_{\text{Zn}^{2+}} = \frac{I_{\text{SS}}R_{\Omega,\text{SS}}(\Delta V - I_0R_{\text{ct},0})}{I_0R_{\Omega,0}(\Delta V - I_{\text{SS}}R_{\text{ct,SS}})} \quad (1)$$

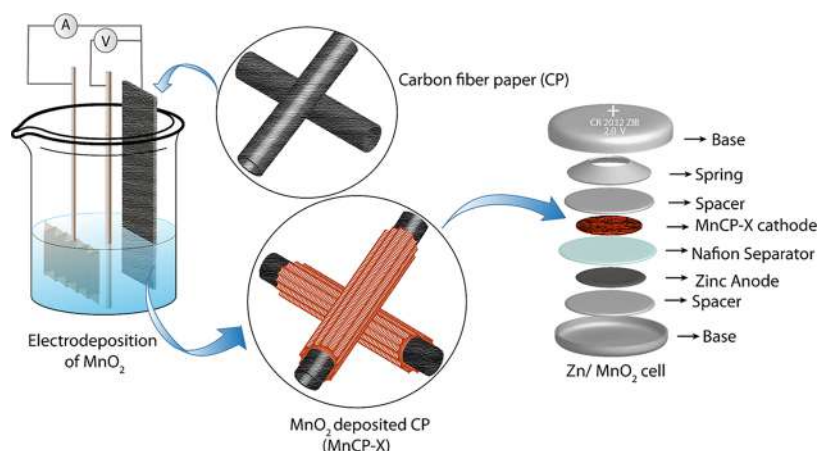


Figure 1. Schematic presentation of the fabrication of the MnCP-X electrode.

where V stands for the DC polarization voltage, I_0 and I_{SS} are the initial and steady-state current response during the polarization, respectively, and R_{Ω} and R_{ct} are the equivalent series resistance (ESR) and charge transfer resistance obtained from the impedance data at the initial and steady state, respectively.

The electrochemical performance of MnCP-X cathodes was studied in the CR2032 coin cell (Zn|Y|MnCP-X), where “X” and “Y” indicate the amount of MnO_2 loading on CP and the type of the electrolyte used. The CV (at scan rates of 1.0, 0.5, 0.3, and 0.1 mV s^{-1}) and galvanostatic charge–discharge (GCD) (at constant current rates of 100, 250, 500, 1000, and 3000 mA g^{-1}) techniques were employed to characterize the Zn/ MnO_2 unit cells within the voltage window of 0.80 V–2.0 V versus Zn/Zn^{2+} . The cycling stability tests were performed by the GCD experiment at a current rate of 3000 mA g^{-1} . The gravimetric capacities are calculated from the GCD plots considering the loading of the active material (MnO_2) in the cathode. The overall resistance of the Zn|Y|MnCP-X cells was monitored by impedance analyses within the 1 MHz to 50 mHz frequency range with a sinus amplitude of 10 mV ($V_{\text{rms}} = 7.07$ mV). The spectra were recorded during the 1st and 100th discharge cycles at a potential of 1.25 V versus Zn/Zn^{2+} . For comparison purpose, Zn/ MnO_2 cells are also fabricated with glass fiber paper (GFP) and polypropylene (CEL) as the separator using 1 M $\text{Zn}(\text{CF}_3\text{SO}_3)_2$, 1 M $\text{ZnSO}_4 \cdot 7\text{H}_2\text{O}$, and 3 M $\text{ZnSO}_4 \cdot 7\text{H}_2\text{O}$ electrolytes. The cells with GFP are represented as Zn|GFP-T-1|MnCP-X, Zn|GFP-S-1|MnCP-X, and Zn|GFP-S-3|MnCP-X, respectively. The polypropylene-based cells are marked as Zn|CEL-T-1|MnCP-X, Zn|CEL-S-1|MnCP-X, and Zn|CEL-S-3|MnCP-X, respectively.

RESULTS AND DISCUSSION

Physical Characterizations. The fabrication of the MnO_2 electrode (MnCP-X) is schematically presented in Figure 1. The FESEM image of CP (Figure S1) shows the network of the intertwined carbon fibers possessing a smooth surface. Followed by the electrodeposition, in the MnCP-1 sample, the surface of the fibers is observed to be uniformly covered with vertically aligned MnO_2 nanosheets (Figure 2a and Figure S2a,b). The nanosheets are interconnected with each other to form a uniform porous network over the carbon fibers. In order to understand the effect of deposition time on the MnO_2 morphology, the electrodeposition was carried out for 1163 and 2772 s to obtain a loading of 3 mg (MnCP-3) and 5 mg (MnCP-5), respectively. Figure S2c–f exhibits the formation of dense MnO_2 nanosheets in MnCP-3 and MnCP-5. The TEM image of MnCP-1 (Figure 2b) also reveals the growth of thin and interconnected MnO_2 nanosheets. The uniform distribution of manganese (Mn) and oxygen (O) over the carbon (C) fibers is confirmed by elemental mapping analysis

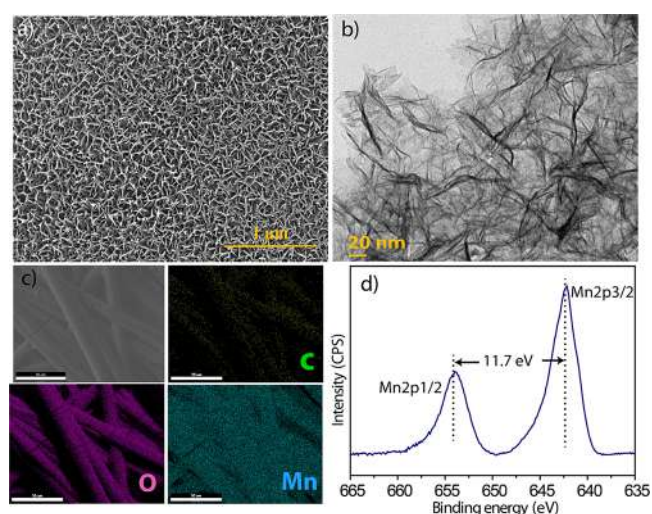


Figure 2. (a) FESEM image, (b) TEM image, (c) elemental mapping of carbon, oxygen, and manganese, and (d) Mn 2p XPS of the MnCP-1 sample.

of MnCP-1 (Figure 2c). In the XRD data of the MnCP-1 sample (Figure S2g), the absence of prominent characteristic peaks for MnO_2 may be due to the amorphous nature of the sample. The formation of the MnO_2 phase is supported through XPS analysis (Figure 2d and Figure S2h,i). In Figure 2d, the appearance of two peaks at binding energies of 642.4 and 654.0 eV correspond to the Mn 2p_{3/2} and Mn 2p_{1/2} doublet of the +4 oxidation state of Mn, respectively. The spacing of 11.7 eV between the doublets validates the +4 oxidation state of Mn.³⁰ The O 1s spectra at the binding energy of 529.0 eV correspond to the Mn–O–Mn coordination in the MnO_2 lattice (Figure S2i).³¹ Moreover, the atomic percentage of the elements in MnCP-1 confirms the presence of Mn and O with a stoichiometric ratio of 1:2.

Selection of Electrolytes. The reversibility of the Zn plating/stripping process in different electrolytes and the electrochemical stability of the respective electrolytes are primarily investigated by CV analyses at a scan rate of 5 mV s^{-1} . In Figure 3a, the pair of the redox peaks corresponds to the plating and stripping of Zn in the Zn|Naf-S-1|CP and Zn|Naf-T-1|CP cells. Apart from these two peaks, no significant current response is observed in the anodic region up to a potential of 2.1 V versus Zn/Zn^{2+} . The wide potential window

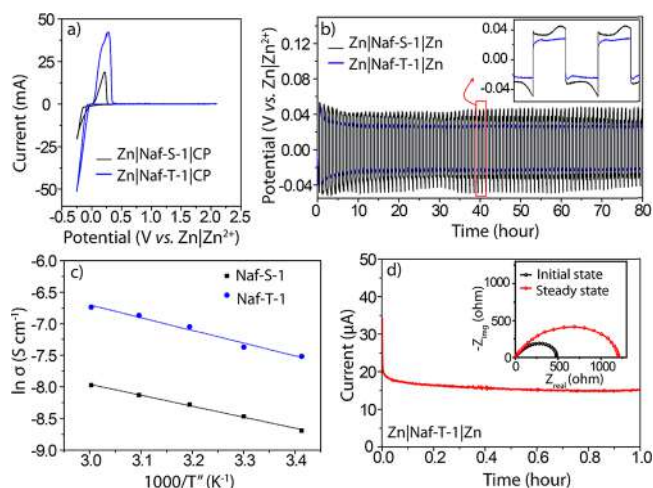


Figure 3. (a) CV plots of Zn|Naf-T-1|CP and Zn|Naf-S-1|CP cells at a scan rate of 5 mV s^{-1} . (b) Voltage versus time profiles of the Zn|Naf-T-1|Zn and Zn|Naf-S-1|Zn cells. (c) Arrhenius plot representing the linear relationship between ionic conductivity (σ) and temperature (T) for Naf-T-1 and Naf-S-1 electrolytes. (d) Chronoamperometry data of the Zn|Naf-T-1|Zn cell at a bias potential of 25 mV, where the corresponding impedance plots are given in the inset.

suggests the compatibility of the aforementioned electrolytes to be employed with a high voltage cathode such as MnO_2 . However, the difference between the onset potential for the plating and stripping processes is more in the case of the Zn|Naf-S-1|CP cell. This indicates the lower overpotential and better reversibility of Zn plating/stripping in 1 M $\text{Zn}(\text{CF}_3\text{SO}_3)_2$.

The reversibility of Zn plating/stripping is further confirmed from the long-time plating/stripping behavior in Zn|Naf-S-1|Zn and Zn|Naf-T-1|Zn symmetric cell configurations (Figure 3b). In both the cells, a gradual drop in the voltage polarization during the initial cycles indicates the formation of a stable electrode/electrolyte interface. As given in the enlarged image (Figure 3b), the plating/stripping overpotential obtained for the Zn|Naf-T-1|Zn cell is lower (52 mV) than that of the Zn|Naf-S-1|Zn cell (94 mV). Nevertheless, compared to the flat voltage profile in 1 M $\text{Zn}(\text{CF}_3\text{SO}_3)_2$, both plating and stripping processes in 1 M $\text{ZnSO}_4 \cdot 7\text{H}_2\text{O}$ experience small voltage shoot up, which is a characteristic of porous and non-uniform electrode surface evolved during repeated cycling.³² However, in our previous report, a favorable plating and stripping process with a lower overpotential value of 71 mV in a concentrated ZnSO_4 electrolyte (3 M $\text{ZnSO}_4 \cdot 7\text{H}_2\text{O}$) has already been proved.²⁶ The superior electrochemical behavior of the Zn|Naf-T-1|Zn cell can be ascribed to the bulky CF_3SO_3^- counterpart present in the $\text{Zn}(\text{CF}_3\text{SO}_3)_2$ electrolyte.³³ The large size of the anion reduces the number of solvating water molecules surrounding the Zn^{2+} ions, which facilitates the mobility of the Zn^{2+} ions under the applied potential. This could lead to uniform plating of zinc during the electrochemical cycling.³⁴

The Zn plating/stripping processes are also studied in three other Zn^{2+} -ion conducting electrolytes (1 M $\text{Zn}(\text{NO}_3)_2 \cdot 6\text{H}_2\text{O}$, 1 M $\text{Zn}(\text{OOCCH}_3)_2$, and 1 M ZnCl_2). The associated data are displayed in Figure S3a–f. Among them, only the Zn|Naf-C-1|Zn cell could sustain stable plating/stripping for 80 h with an overpotential of 80 mV (Figure S3a). However, in the CV plot of the Zn|Naf-C-1|CP cell (Figure S3d), the steep increase in

the current at 1.2 V versus Zn/Zn^{2+} originates from the low electrochemical stability of the ZnCl_2 electrolyte.³⁵ On the other hand, the cycling data of the Zn|Naf-N-1|Zn and Zn|Naf-A-1|Zn cells (Figure S3b,c) shows a gradual increase in voltage polarization with respect to time. The appearance of spikes in the plating and stripping half indicates the internal short circuits by means of the inferior electrode/electrolyte interface.³⁶ Such interfacial instability leads to cell failure just after 30 h of operation. Nevertheless, the reversible peaks for the Zn plating/stripping process are not observed in the CV profile of the Zn|Naf-N-1|CP cell (Figure S2e) due to corrosion of zinc in the presence of the strong oxidizing NO_3^- ions in the electrolyte.³⁷

Considering the wide electrochemical stability, low plating/stripping overpotential, and long cyclic stability obtained in 1 M $\text{Zn}(\text{CF}_3\text{SO}_3)_2$ and 1 M $\text{ZnSO}_4 \cdot 7\text{H}_2\text{O}$ electrolytes, we have opted for these two electrolytes for subsequent studies. The interaction of Zn^{2+} with Nafion membrane is confirmed through FTIR analyses, and the data are given in Figure S4a (Supporting Information). Later, the temperature-dependent ionic conductivities of Naf-T-1 and Naf-S-1 membranes were measured, and the corresponding data are summarized in the form of Arrhenius plot in Figure 3c.^{38,39} The related EIS plots are also given in Figure S4b,c. At 40 °C, Naf-T-1 and Naf-S-1 membranes offer more or less similar ionic conductivity (0.87 and 0.25 mS cm^{-1} , respectively) and activation energy (0.17 and 0.15 eV, respectively) (Table S1). In order to check the cationic contribution toward the total ionic transport, the Zn^{2+} -transference numbers ($t_{\text{Zn}^{2+}}$) are evaluated for Zn|Naf-T-1|Zn and Zn|Naf-S-1|Zn cells. The $t_{\text{Zn}^{2+}}$ values obtained for 1 M $\text{Zn}(\text{CF}_3\text{SO}_3)_2$ - and 1 M $\text{ZnSO}_4 \cdot 7\text{H}_2\text{O}$ -based membranes are 0.54 and 0.51, respectively. The $t_{\text{Zn}^{2+}}$ values higher than 0.50 are credited to the cation selective Nafion ionomer membrane as the separator in both the cells.⁴⁰

Electrochemical Analysis of the Zn/ MnO_2 Cell in 1 M $\text{Zn}(\text{CF}_3\text{SO}_3)_2$. The Zn^{2+} storage property of the MnCP-1 electrode in the 1 M $\text{Zn}(\text{CF}_3\text{SO}_3)_2$ electrolyte (Zn|Naf-T-1|MnCP-1 cell) is primarily investigated by CV analysis within a voltage range of 0.80–2.0 V versus Zn/Zn^{2+} . In Figure 4a, the CV plots at different scan rates exhibit a pair of redox peaks at

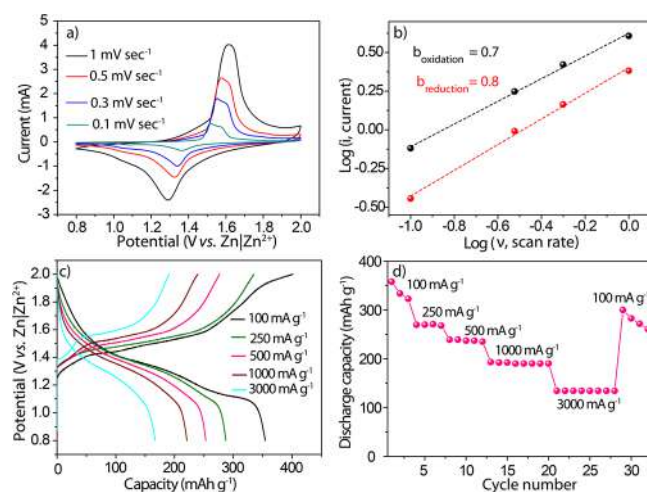


Figure 4. (a) CV plots of the Zn|Naf-T-1|MnCP-1 cell at various scan rates. (b) $\text{Log}(i)$ versus $\text{Log}(v)$ plots of oxidation and reduction peaks as shown in (a). (c) Charge–discharge capacity. (d) Rate performance of the Zn|Naf-T-1|MnCP-1 cell.

potentials of 1.3 V/1.6 V versus Zn/Zn^{2+} , implying the reversible intercalation of Zn^{2+} into the MnO_2 lattice. The charge storage mechanism is investigated by analyzing the dependence of the peak current (i) on the scan rate (ν) using the following equation:

$$i = a\nu^b \quad (2)$$

where a and b are the adjustable parameters.⁴¹ In particular, $b = 0.5$ and $b = 1.0$ signify the contribution from the diffusion-controlled and surface-controlled faradaic processes, respectively.^{42,43} b values for the anodic and cathodic peaks of $\text{Zn}/\text{Naf-T-1}|\text{MnCP-1}$ cells are obtained from the $\text{Log}(i)$ versus $\text{Log}(\nu)$ relationship (Figure 4b). A b value higher than 0.5 (0.73 for the oxidation peak and 0.82 for the reduction peak) indicates that the Zn^{2+} storage in the MnCP-1 cathode is hybrid with dominant contribution from the surface-controlled process.⁴⁴

The $\text{Zn}/\text{Naf-T-1}|\text{MnCP-1}$ cell could maintain the open-circuit voltage (1.5 V vs Zn/Zn^{2+}) for more than 24 h, indicating negligible self-discharge (Figure S5a). The charge storage capacity of the MnCP-1 sample in the 1 M $\text{Zn}(\text{CF}_3\text{SO}_3)_2$ electrolyte is analyzed by the GCD method. At a current rate of 100 mA g^{-1} , the cell achieves high discharge capacities of 300 and 350 mAh g^{-1} in the 1st and 2nd cycles, respectively (Figure S5b).

To assess the rate capability of the $\text{Zn}/\text{Naf-T-1}|\text{MnCP-1}$ cell, the capacities at various current rates are recorded. The cell delivers average discharge capacities of 350, 300, 250, 225, and 175 mAh g^{-1} at current rates of 100, 250, 500, 1000, and 3000 mA g^{-1} , respectively (Figure 4c,d). The obtained capacity values indicate a good rate capability of the cell with 50% retention of the capacity when the current rate is varied from 100 to 3000 mA g^{-1} . Notably, when the current rate is abruptly decreased to 100 mA g^{-1} , the cell could recover a discharge capacity of 290 mAh g^{-1} (Figure 4d). A slight decrease in capacity at 100 mA g^{-1} during the following cycles can be due to the degradation of the cathode at a very low current rate. Moreover, the symmetric appearance of the charge–discharge profiles at all the current rates (Figure 4c) suggests the reversible Zn^{2+} insertion/de-insertion process occurring in the MnCP-1 cathode.

The remarkable capacity and rate performance of the $\text{Zn}/\text{Naf-T-1}|\text{MnCP-1}$ cell can be credited to the unique architecture of the MnCP-1 cathode. The vertically aligned MnO_2 nanosheets (Figure 2a) over the carbon fibers can expose more number of redox sites and facilitate the access of the electrolyte to the interior of the electrode. This extended electrode/electrolyte interfacial contact reduces the diffusion path for the electrolyte ions.⁴⁵ Besides, the carbon fiber backbone of the MnCP-1 cathode ensures the easy transport of electrons even when the electrochemical reactions are performed at higher current rates. The synergic effect of the aforementioned factors maximizes the number of accessible active sites for accommodating the Zn^{2+} ions in the MnCP-1 cathode.

The discharge capacities of the other MnCP-X electrodes are also measured as a function the MnO_2 loading (Figure S5c). At a current rate of 100 mA g^{-1} , the MnCP-3 and MnCP-5 samples exhibit discharge capacities of 292 and 216 mAh g^{-1} , respectively. The drop in the discharge capacity with higher loading is obvious as observed in the other charge storage devices based on semiconducting MnO_2 .^{46,47} Due to the thick coating of MnO_2 in MnCP-3 and MnCP-5 , the electrolyte ions

can access only a fraction of the active material, which could further take part in the associated redox reactions. Still, considering the high loading, the specific capacity of MnCP-5 is appreciable in comparison to the other MnO_2 -based ZMB cathodes reported previously.^{48–50}

Electrochemical Analysis of the Zn/MnO_2 Cell in 1 M $\text{ZnSO}_4 \cdot 7\text{H}_2\text{O}$. The electrochemical performance of MnCP-1 is further explored in the 1 M $\text{ZnSO}_4 \cdot 7\text{H}_2\text{O}$ electrolyte ($\text{Zn}/\text{Naf-S-1}|\text{MnCP-1}$ cell). The CV profiles (Figure S6a) of the $\text{Zn}/\text{Naf-S-1}|\text{MnCP-1}$ cell display two distinct pairs of reversible redox peaks, which could be related to the insertion/de-insertion of H^+ (1.5 V/1.39 V) and Zn^{2+} (1.59 V/1.24 V) ions into the MnO_2 lattice. The charge storage mechanism of the $\text{Zn}/\text{Naf-S-1}|\text{MnCP-1}$ cell is also analyzed from the current versus scan rate relationship (eq 2; Figure S6b). Similar to the $\text{Zn}/\text{Naf-T-1}|\text{MnCP-1}$ cell, the b values for the oxidation and reduction peaks are in the range of 0.70–0.80, signifying dominant contribution of the surface-controlled redox reactions.

The charge–discharge capacity and rate performance of the $\text{Zn}/\text{Naf-S-1}|\text{MnCP-1}$ cell are given in Figure S6c,d, respectively. At current a rate of 100 mA g^{-1} , the cell achieves a discharge capacity of 420 mAh g^{-1} (Figure S6c), a value that is superior to that of the $\text{Zn}/\text{Naf-T-1}|\text{MnCP-1}$ cell (Figure S4d). However, at a current rate of 3000 mA g^{-1} , the same cell could retain only 120 mAh g^{-1} discharge capacity (30% of the obtained capacity at 100 mA g^{-1} ; Figure S6d). Unlike the 1 M $\text{Zn}(\text{CF}_3\text{SO}_3)_2$, the 1st discharge profile of the $\text{Zn}/\text{Naf-S-1}|\text{MnCP-1}$ cell appears with a sharp voltage plateau, while two sloping voltage curves are observed in the subsequent cycles (Figure S6c). According to the recent reports, the single discharge platform in the 1st cycle associates with the phase transformation in the MnO_2 cathode followed by $\text{H}^+/\text{Zn}^{2+}$ insertion.^{51,52}

Cycling Stability of Zn/MnO_2 Cells. The cycling stability of $\text{Zn}/\text{Naf-T-1}|\text{MnCP-1}$ and $\text{Zn}/\text{Naf-S-1}|\text{MnCP-1}$ cells was investigated at a current rate of 3000 mA g^{-1} (Figure 5a). The $\text{Zn}/\text{Naf-T-1}|\text{MnCP-1}$ cell exhibits a discharge capacity of 151 mAh g^{-1} and retains 89% of the initial capacity after 500 cycles. With continuous cycling, the same cell could still deliver a capacity of 114 mAh g^{-1} (75% retention) and 105 mAh g^{-1} capacity (69% retention) over 1000 and 1200 stability cycles, respectively. To the best of our knowledge, the $\text{Zn}/\text{Naf-T-1}|\text{MnCP-1}$ cell surpasses the cycling performance of all the previously reported single component electrolyte-based Zn/MnO_2 cells (see Table S3).^{48,53–55} It can be also noted that the obtained discharge capacity and cyclability of the $\text{Zn}/\text{Naf-T-1}|\text{MnCP-1}$ cell are superior to many of the reported $\text{Mn}(\text{II})$ additive-based Zn/MnO_2 cells as shown in Table S2.^{50,56–59} At the same time, the discharge capacity obtained for the $\text{Zn}/\text{Naf-S-1}|\text{MnCP-1}$ cell is 185 mAh g^{-1} . Despite the high initial capacity, in the subsequent cycle, the performance drops to 110 mAh g^{-1} within 500 cycles (with a retention of 61%) and 80 mAh g^{-1} after 1200 cycles (43% retention of initial capacity).

Later, the cycling stability of the Zn/MnO_2 cell was performed in the 3 M $\text{ZnSO}_4 \cdot 7\text{H}_2\text{O}$ electrolyte. Note that the preparation of the $\text{Zn}(\text{CF}_3\text{SO}_3)_2$ electrolyte with the same concentration (3 M) is difficult due to low water solubility of the $\text{Zn}(\text{CF}_3\text{SO}_3)_2$ salt. Also, considering the high cost, the use of the concentrated electrolyte with $\text{Zn}(\text{CF}_3\text{SO}_3)_2$ (~18 times more costly than the ZnSO_4 salt) is not economically viable. The CV and GCD plots of the $\text{Zn}/\text{Naf-S-3}|\text{MnCP-1}$ cell are presented in Figure S7a,b featuring similar charge storage

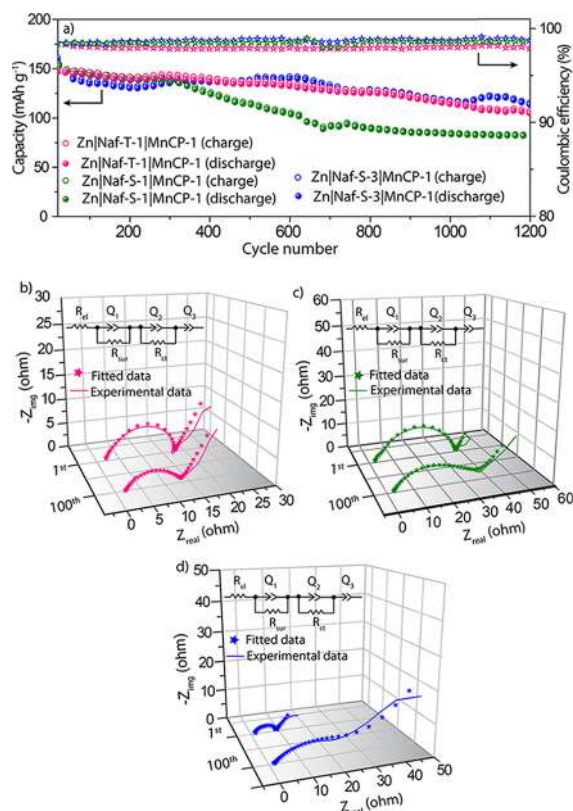


Figure 5. (a) Comparison of the cycling stability. (b–d) Impedance plots of the (b) Zn|Naf-T-1|MnCP-1 cell, (c) Zn|Naf-S-1|MnCP-1 cell, and (d) Zn|Naf-S-3|MnCP-1 cells at a discharge voltage of 1.25 V versus Zn|Zn²⁺ during the 1st and 100th discharge cycles.

properties as in 1 M ZnSO₄. Interestingly, the Zn/MnO₂ cell with a concentrated electrolyte exhibits substantial improvement in capacity retention at the current rate of 3000 mA g⁻¹. To be more specific, the initial discharge capacity obtained for the Zn|Naf-S-3|MnCP-1 cell is 205 mAh g⁻¹ and gradually stabilizes to 150 mAh g⁻¹ within 30 charge–discharge cycles (Figure S8). In the following cycles, the capacity drop is reduced, resulting in 112 mAh g⁻¹ capacity after 1200 charge–discharge cycles (55% retention of its initial capacity and 75% retention of the capacity obtained at the 30th cycle). Despite the initial drop, the overall capacity retention of the Zn|Naf-S-3|MnCP-1 cell is superior compared to that of its 1 M ZnSO₄·7H₂O counterpart (Figure 5a).

The improved cycle life of the Zn|Naf-T-1|MnCP-1 and Zn|Naf-S-3|MnCP-1 cells is attributed to the influence of the Nafion ionomer separator. In contrast to the conventionally used porous separators, Nafion membrane offers improved interfacial stability to the anode and cathode of the respective cells, which can potentially improve the capacity retention with cycle. Additionally, the ionomer separator arrests the diffusion of the undesired discharge side products from the cathode and mitigates the surface poisoning on the anode. In order to validate this, we have performed the stability experiment of Zn/MnO₂ cells using two types of porous separators, GFP and CEL (Figures S9–S11). A bar diagram representing the initial discharge capacities of all the cells with different separators and electrolytes is given in Figure S9. The initial capacities of the Zn/MnO₂ cells with various separators are more or less comparable. However, compared to the Nafion cells, all the porous separators exhibit dramatic deterioration in terms of

capacity retention. Over 250 stability cycles, the Zn|GFP-S-1|MnCP-1 cell retains only 46% of its initial capacity, whereas the Zn|GFP-T-1|MnCP-1 and Zn|GFP-S-3|MnCP-1 cells display 58 and 56% capacity retention, respectively (Figure S10a–c). Nevertheless, capacity retention values in the CEL cells are found to be even lower, and all the cells failed after few initial cycles due to the internal short circuit. Zn|CEL-T-1|MnCP-1, Zn|CEL-S-1|MnCP-1, and Zn|CEL-S-3|MnCP-1 cells delivers 80, 76, and 42% of their initial capacity after 70, 12, and 100 charge–discharge cycles, respectively (Figure S11a–c). Moreover, the above discussion points out the critical role of the ionomer membrane in maintaining the performance of the Zn/MnO₂ cell in the Mn(II) additive-free electrolyte.

Impedance Analyses of the Zn/MnO₂ Cells with Cycle. EIS analyses are carried out to understand the influence of various electrolytes to the cycle life of the Zn/MnO₂ cells. Impedance spectra are recorded at 1.25 V versus Zn|Zn²⁺ in the 1st and 100th discharge cycles (Figure 5b–d). A simple equivalent circuit (Figure 5b–d, inset) is used to fit the impedance spectra, and the obtained resistance values are tabulated in Table 1. The equivalent circuit consists of the

Table 1. Electrolyte Resistance, Surface Resistance, and Charge Transfer Resistance of the Zn/MnO₂ Cells during the 1st and 100th Discharge Cycles

Zn/MnO ₂ cell	cycle	R _{el} (Ω)	R _{sur} (Ω)	R _{ct} (Ω)
Zn Naf-T-1 MnCP-1	1st	1.9	4.1	11.7
Zn Naf-T-1 MnCP-1	100th	1.8	0.5	11.5
Zn Naf-S-1 MnCP-1	1st	2.1	2.4	33.1
Zn Naf-S-1 MnCP-1	100th	2.0	20.0	14.7
Zn Naf-S-3 MnCP-1	1st	1.2	2.6	4.9
Zn Naf-S-3 MnCP-1	100th	1.3	4.4	15.9

three main components denoted as the bulk resistance (R_{el}), surface resistance (R_{sur}), and charge transfer resistance (R_{ct}). R_{el} is the equivalent series resistance (ESR) of the cell, which is mainly contributed from the ohmic resistance of the electrolyte and cell components. R_{sur} and R_{ct} represent the nature of the SEI layer and resistance to the charge transfer reactions occurring at the electrode/electrolyte interface, respectively.^{60,61} The overall resistance of the cells (R_{el} + R_{sur} + R_{ct}) is represented as R_t.

As given in Table 1, in the 1st discharge, the R_t values of Zn|Naf-T-1|MnCP-1 (17.7 Ω) and Zn|Naf-S-3|MnCP-1 (8.7 Ω) cells are much lower than that of the Zn|Naf-S-1|MnCP-1 cell (37.6 Ω). Followed by cycling, the R_{sur} of the Zn|Naf-S-1|MnCP-1 cell is increased to 20.0 Ω, a value much higher than those of Zn|Naf-T-1|MnCP-1 (0.5 Ω) and Zn|Naf-S-3|MnCP-1 (4.4 Ω). The higher R_{sur} value indicates the inferior SEI layer resulting from the low Zn/electrolyte interface stability in 1 M ZnSO₄·7H₂O, causing faster degradation of the cell performance (Figure 5a and Figure S8). The slightly high R_{sur} of the Zn|Naf-S-3|MnCP-1 cell could be responsible for the initial capacity drop in the Zn|Naf-S-3|MnCP-1 cell (Figure S8); however, the percentage increase in the R_{sur} from the 1st to 100th cycles is less than that of 1 M ZnSO₄·7H₂O. Hence, the R_{sur} and R_t values suggest that 1 M Zn(CF₃SO₃)₂ and 3 M ZnSO₄·7H₂O electrolytes offer much better interfacial compatibility with the zinc anode contributing to the stability of the Nafion-based Zn/MnO₂ cells. These results further agree with the plating/stripping overpotential of zinc in the Zn|Zn configuration in the respective electrolytes (Figure 3b).

The impedance analysis for the Zn/MnO₂ cells is extended to the GFP and CEL separators. As the Zn(CF₃SO₃)₂ electrolyte provides better cycling stability in all the cases, the impedance data with porous separators are taken in 1 M Zn(CF₃SO₃)₂, and the related EIS data are compared in Figure S12a,b and Table S2. The R_t of the Zn|GFP-T-1|MnCP-1 cell (16.9 Ω) in the 1st cycle is close to that of the Zn|Naf-T-1|MnCP-1 cell (Table 1). However, at the 100th cycle, the R_{sur} of the GFP cell is increased to 10.5 Ω, suggesting the formation of the inferior SEI layer that hampers the transport of Zn²⁺ ions at the zinc/electrolyte interface. On the other hand, the Nyquist plot of the Zn|CEL-T-1|MnCP-1 cell shows an exceptionally high resistance ($R_t = 129 \Omega$) in the 1st cycle. This could be due to the low electrolyte retention capacity of the polypropylene separator. Nevertheless, we could not compare the change in impedance after cycling of Zn|CEL-T-1|MnCP-1 due to failure of the cell within 80 cycles.

Physical Characterization of Post-stability Electrodes.

We have investigated the composition of the post-stability cathodes of the Nafion-based Zn/MnO₂ cells using XRD analyses. The XRD data presented in Figure 6a are taken

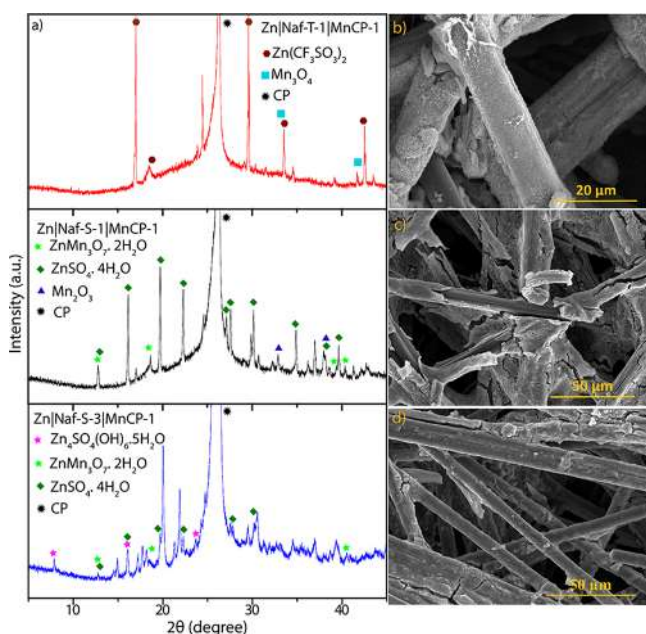


Figure 6. (a) XRD profiles of the cycled cathodes. (b–d) FESEM images of (b) the Zn|Naf-T-1|MnCP-1 cathode, (c) the Zn|Naf-S-1|MnCP-1 cathode, and (d) the Zn|Naf-S-3|MnCP-1 cathode after the cycling stability test.

without any prior washing of the recovered cathodes under consideration. Compared to the pristine MnCP-1 sample (Figure S2g), the XRD data of the cycled cathodes exhibit several intense peaks, apparently formed due to associated structural changes occurred during prolonged cycling of the cells.

In the case of Zn|Naf-T-1|MnCP-1, the XRD peaks are found to match with that of the Zn(CF₃SO₃)₂ salt and Mn₃O₄ (JCPDS 01-075-0765) phase. On the other hand, in the case of Zn|Naf-S-1|MnCP-1, along with the characteristic peaks of the ZnSO₄ salt (JCPDS 00-031-0818; Figure S13), the new peaks found at 12.7, 18.6, 39.4, and 40.3° could be indexed to the woodruffite phase (ZnMn₃O₇·2H₂O; JCPDS 00-047-1825). Few peaks corresponding to the Mn₂O₃ (JCPDS 00-041-1442)

phase are also detected in the XRD data.¹⁵ The formation of the woodruffite phase is also evidenced in the XRD profile retrieved from the cathode of the Zn|Naf-S-3|MnCP-1 cell (Figure 6a). In addition to this, few new peaks at 7.9, 16.0, and 24.3° could be assigned to the Zn₄SO₄(OH)₆·5H₂O layered double hydroxide (LDH).⁶² Recently, Kundu et al. proposed that the LDH formed on the cathode surface plays a favorable role in maintaining the stable capacity of Zn/MnO₂ cells, which could be responsible for better cycling stability of the Zn|Naf-S-3|MnCP-1 cell.⁶³ It is interesting to note that peaks related to the woodruffite phase are absent in the Zn|Naf-T-1|MnCP-1 cell. This indicates the influence of electrolytes in directing the structural changes in the cathode of Zn/MnO₂ cells.

The XRD data associated with the post-stability cathodes followed by washing (with water) are also collected and compared with the pristine MnCP-1 sample (Figure S14). Interestingly, in the case of ZnSO₄ and Zn(CF₃SO₃)₂ salt-based cells, the XRD profiles overlap with each other. This in turn indicates that the structural changes mostly took place at the surface of the electrode material, whereas the bulk remains more or less similar to the pristine electrode, except for three new peaks observed at 18.5, 30.5, and 39.1°. Despite the aforementioned similarity, the difference in electrochemical performance indicates that the side reactions occurring at the electrode surface are rather important in line with determining the stability of Zn/MnO₂ cells. Additionally, the XRD data of the cycled anodes (Figure S15a) appears similar to that of the pristine zinc foil, indicating the dominant reaction of plating and stripping of zinc (Zn/Zn²⁺).⁵⁶

Apart from the change in electrode composition, morphological changes on the electrode surface are also an important factor influencing the cycling stability of electrochemical cells. In the following sections, we have discussed the change in morphology of both the cathode (Figure 6b–d) and anode (Figure 7a–f) of the post-stability cells through FESEM

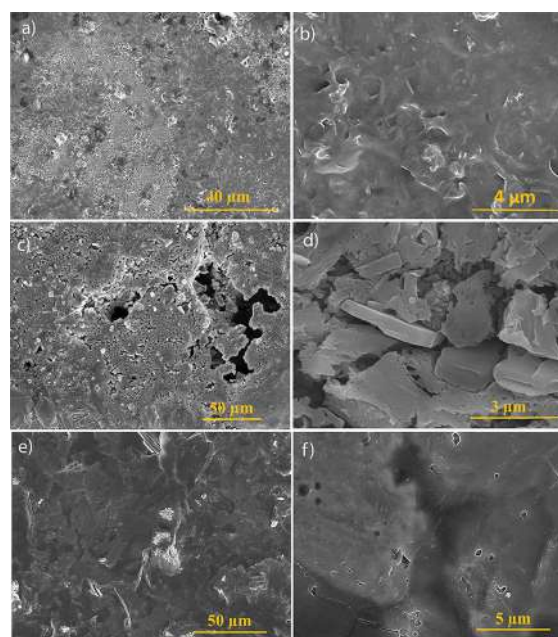


Figure 7. (a–f) FESEM images of the (a, b) Zn|Naf-T-1|MnCP-1 anode, (c, d) Zn|Naf-S-1|MnCP-1 anode, and (e, f) Zn|Naf-S-3|MnCP-1 anode after the cycling stability test.

analyses. The FESEM images are taken after washing the respective electrodes to avoid any interference from the precipitated electrolyte salt or other side-reaction products present on the surface.

As seen in Figure 6b, no obvious structural change is observed in the Zn|Naf-T-1|MnCP-1 cathode, and the contact between the electrode material and carbon fibers remains unaffected during the cycling. On the contrary, the FESEM image of the Zn|Naf-S-1|MnCP-1 cathode (Figure 6c) reveals a significant number of cracks and fractures causing detachment of the active material from the carbon fiber skeleton. The disconnection between the active material and conductive support hinders the Zn^{2+} uptake in the cathode of the Zn|Naf-S-1|MnCP-1 cell, which could deteriorate the battery life (Figure 5a). The cathode morphology in the concentrated ZnSO_4 electrolyte (Zn|Naf-S-3|MnCP-1 cathode) looks (Figure 6d) more or less similar to that of the Zn|Naf-T-1|MnCP-1 cell. This suggests the superiority of $\text{Zn}(\text{CF}_3\text{SO}_3)_2$ and concentrated ZnSO_4 electrolytes over the low-concentrated ZnSO_4 counterpart.

Later, the morphology of the post-cycled zinc anode of the all three cells is also compared. As shown in Figure 7a,b, the surface of the Zn|Naf-T-1|MnCP-1 anode looks smooth and dense, which is similar to the pristine Zn foil (Figure S15b). The absence of any obvious protrusion indicates the uniform plating of zinc during cycling in 1 M $\text{Zn}(\text{CF}_3\text{SO}_3)_2$, whereas the Zn|Naf-S-1|MnCP-1 anode consists of a significant number of protruded Zn deposits (Figure 7c,d) and microscale cracks, which are responsible for the origin of the porous zinc surface with large holes (Figure 7c). The evolution of such non-uniform surface and numerous grain boundaries impedes the reversible electrochemical reactions occurring at the zinc/electrolyte interface.

Despite the presence of the Nafion ionomer separator, the undesired morphology (Figure 7d) of the zinc anode in the Zn|Naf-S-1|MnCP-1 cell is responsible for the higher voltage polarization during the Zn plating/stripping process (Figure 3b). Also, a low concentration of the electrolyte induces the Zn^{2+} -ion concentration gradient near to the anode surface, resulting in localized deposition of zinc. This effect is believed to be mitigated in the concentrated electrolyte,⁶⁴ which is indeed confirmed from the smooth and dendrite-free surface of the Zn|Naf-S-3|MnCP-1 anode (Figure 7e,f). Therefore, it is reasonable to say that the difference in electrode morphology evolved during prolong cycling is the critical reason for the different cycle life of the Nafion-based Zn/MnO₂ cells under study.

For comparison, post-cycling morphology of the zinc-metal surface coupled with GFP and CEL separators are also characterized by FESEM analyses. The uneven and rough surface of zinc is clearly evident in Figures S16a–f and S17a–f. It is worth mentioning that, in the case of the porous separators, such a morphology evolved just after few initial charge–discharge cycles. While the zinc anode coupled with the Naf-T-1 or Naf-S-3 electrolyte maintains an almost flat surface, the flake-like deposits with sharp edges are observed with the CEL-T-1 and CEL-S-3 electrolytes. At the same time, the granular and flaky morphology on the zinc surface of the GFP-based cells is also evident. This indicates that the favorable surface structure evolution on the anode surface as in the case of Nafion promotes the improved cycle life and reduced cell resistance compared to the GFP and CEL separator-based Zn/MnO₂ cells.

CONCLUSIONS

In conclusion, this study shows the remarkable performance of Zn/MnO₂ cells in single component electrolytes or, in other words, Mn(II) salt-free electrolyte by utilizing the Nafion ionomer separator. The improved stability of the Nafion-based cells originates from the suppression of the zinc dendrite growth compared to the traditional GFP or CEL separators. Also, compared to 1 M $\text{ZnSO}_4 \cdot 7\text{H}_2\text{O}$, 1 M $\text{Zn}(\text{CF}_3\text{SO}_3)_2$ and 3 M $\text{ZnSO}_4 \cdot 7\text{H}_2\text{O}$ offer the evolution of dendrite-free anode morphology and at the same time preserving the structural integrity of the cathode. This in turn helps in achieving longer cycle life of the Zn/MnO₂ cell with 75% retention of capacity over 1000 cycles. Unlike the existing ZMB reports emphasizing the importance of Mn(II) salts in Zn/MnO₂ cells, this work directs an alternate way to realize the long cycle life of Zn/MnO₂ cells in the absence of any electrolyte additive. The results provide significant evidence that an ionomer membrane along with an appropriate zinc-ion conducting electrolyte is effective in maintaining the desired structural evolution of the electrodes and preventing the capacity loss of the Zn/MnO₂ cell.

ASSOCIATED CONTENT

Supporting Information

The Supporting Information is available free of charge at <https://pubs.acs.org/doi/10.1021/acssuschemeng.9b06798>.

Material characterization, FESEM images, FTIR study, XPS spectra, XRD plot, electrochemical characterization, and supporting table (PDF)

AUTHOR INFORMATION

Corresponding Author

Sreekumar Kurungot – Physical and Materials Chemistry Division, CSIR-National Chemical Laboratory, Pune 411008, Maharashtra, India; orcid.org/0000-0001-5446-7923; Email: k.sreekumar@ncl.res.in

Authors

Meena Ghosh – Physical and Materials Chemistry Division, CSIR-National Chemical Laboratory, Pune 411008, Maharashtra, India; Academy of Scientific and Innovative Research, Ghaziabad, Uttar Pradesh 201002, India

Vidyanand Vijayakumar – Physical and Materials Chemistry Division, CSIR-National Chemical Laboratory, Pune 411008, Maharashtra, India; Academy of Scientific and Innovative Research, Ghaziabad, Uttar Pradesh 201002, India

Bihag Anothumakkool – TNO-Holst Centre, Dutch National Institute for Applied Scientific Research, S656 AE Eindhoven, The Netherlands

Complete contact information is available at: <https://pubs.acs.org/doi/10.1021/acssuschemeng.9b06798>

Author Contributions

All authors have given approval to the final version of the manuscript.

Notes

The authors declare no competing financial interest.

ACKNOWLEDGMENTS

M.G. and V.V. acknowledge CSIR, New Delhi and UGC, New Delhi, respectively, for the research fellowship. K.S. acknowl-

edges CSIR, New Delhi, for project funding (TLP003526). Authors thank Mr. Shibin T for discussion on the theoretical XRD patterns.

REFERENCES

- (1) Balakrishnan, P. G.; Ramesh, R.; Prem Kumar, T. Safety mechanisms in lithium-ion batteries. *J. Power Sources* **2006**, *155*, 401–414.
- (2) Yang, C.; Chen, J.; Qing, T.; Fan, X.; Sun, W.; von Cresce, A.; Ding, M. S.; Borodin, O.; Vatamanu, J.; Schroeder, M. A.; Eidson, N.; Wang, C.; Xu, K. 4.0 V Aqueous Li-Ion Batteries. *Joule* **2017**, *1*, 122–132.
- (3) Suo, L.; Borodin, O.; Gao, T.; Olguin, M.; Ho, J.; Fan, X.; Luo, C.; Wang, C.; Xu, K. “Water-in-salt” electrolyte enables high-voltage aqueous lithium-ion chemistries. *Science* **2015**, *350*, 938–943.
- (4) Suo, L.; Borodin, O.; Wang, Y.; Rong, X.; Sun, W.; Fan, X.; Xu, S.; Schroeder, M. A.; Cresce, A. V.; Wang, F.; Yang, C.; Hu, Y.-S.; Xu, K.; Wang, C. “Water-in-Salt” Electrolyte Makes Aqueous Sodium-Ion Battery Safe, Green, and Long-Lasting. *Adv. Energy Mater.* **2017**, *7*, 1701189.
- (5) Selvakumaran, D.; Pan, A.; Liang, S.; Cao, G. A review on recent developments and challenges of cathode materials for rechargeable aqueous Zn-ion batteries. *J. Mater. Chem. A* **2019**, *7*, 18209–18236.
- (6) Chen, S.; Zhang, Y.; Geng, H.; Yang, Y.; Rui, X.; Li, C. C. Zinc ions pillared vanadate cathodes by chemical pre-intercalation towards long cycling life and low-temperature zinc ion batteries. *J. Power Sources* **2019**, *441*, 227192.
- (7) Hu, P.; Zhu, T.; Wang, X.; Wei, X.; Yan, M.; Li, J.; Luo, W.; Yang, W.; Zhang, W.; Zhou, L.; Zhou, Z.; Mai, L. Highly Durable $\text{Na}_2\text{V}_6\text{O}_{16} \cdot 1.63\text{H}_2\text{O}$ Nanowire Cathode for Aqueous Zinc-Ion Battery. *Nano Lett.* **2018**, *18*, 1758–1763.
- (8) Ming, J.; Guo, J.; Xia, C.; Wang, W.; Alshareef, H. N. Zinc-ion batteries: Materials, mechanisms, and applications. *Mater. Sci. Eng., R* **2019**, *135*, 58–84.
- (9) Xu, C.; Li, B.; Du, H.; Kang, F. Energetic Zinc Ion Chemistry: The Rechargeable Zinc Ion Battery. *Angew. Chem., Int. Ed.* **2012**, *51*, 933–935.
- (10) Zeng, Y.; Zhang, X.; Meng, Y.; Yu, M.; Yi, J.; Wu, Y.; Lu, X.; Tong, Y. Achieving Ultrahigh Energy Density and Long Durability in a Flexible Rechargeable Quasi-Solid-State Zn– MnO_2 Battery. *Adv. Mater.* **2017**, *29*, 1700274.
- (11) Fang, G.; Zhou, J.; Pan, A.; Liang, S. Recent Advances in Aqueous Zinc-Ion Batteries. *ACS Energy Lett.* **2018**, *3*, 2480–2501.
- (12) Pan, H.; Shao, Y.; Yan, P.; Cheng, Y.; Han, K. S.; Nie, Z.; Wang, C.; Yang, J.; Li, X.; Bhattacharya, P.; Mueller, K. T.; Liu, J. Reversible aqueous zinc/manganese oxide energy storage from conversion reactions. *Nat. Energy* **2016**, *1*, 16039.
- (13) Zhang, N.; Cheng, F.; Liu, J.; Wang, L.; Long, X.; Liu, X.; Li, F.; Chen, J. Rechargeable aqueous zinc-manganese dioxide batteries with high energy and power densities. *Nat. Commun.* **2017**, *8*, 405.
- (14) Wu, B.; Zhang, G.; Yan, M.; Xiong, T.; He, P.; He, L.; Xu, X.; Mai, L. Graphene Scroll-Coated $\alpha\text{-MnO}_2$ Nanowires as High-Performance Cathode Materials for Aqueous Zn-Ion Battery. *Small* **2018**, *14*, 1703850.
- (15) Huang, Y.; Mou, J.; Liu, W.; Wang, X.; Dong, L.; Kang, F.; Xu, C. Novel Insights into Energy Storage Mechanism of Aqueous Rechargeable Zn/ MnO_2 Batteries with Participation of Mn^{2+} . *Nano-Micro Lett.* **2019**, *11*, 49.
- (16) Li, H.; Ma, L.; Han, C.; Wang, Z.; Liu, Z.; Tang, Z.; Zhi, C. Advanced rechargeable zinc-based batteries: Recent progress and future perspectives. *Nano Energy* **2019**, *62*, 550–587.
- (17) Qiu, N.; Chen, H.; Yang, Z.; Sun, S.; Wang, Y. Synthesis of manganese-based complex as cathode material for aqueous rechargeable batteries. *RSC Adv.* **2018**, *8*, 15703–15708.
- (18) Li, Y.; Wang, S.; Salvador, J. R.; Wu, J.; Liu, B.; Yang, W.; Yang, J.; Zhang, W.; Liu, J.; Yang, J. Reaction Mechanisms for Long-Life Rechargeable Zn/ MnO_2 Batteries. *Chem. Mater.* **2019**, *31*, 2036–2047.
- (19) Poyraz, A. S.; Laughlin, J.; Zec, Z. Improving the cycle life of cryptomelane type manganese dioxides in aqueous rechargeable zinc ion batteries: The effect of electrolyte concentration. *Electrochim. Acta* **2019**, *305*, 423–432.
- (20) Zhao, S.; Han, B.; Zhang, D.; Huang, Q.; Xiao, L.; Chen, L.; Ivey, D. G.; Deng, Y.; Wei, W. Unravelling the reaction chemistry and degradation mechanism in aqueous Zn/ MnO_2 rechargeable batteries. *J. Mater. Chem. A* **2018**, *6*, 5733–5739.
- (21) Kang, L.; Cui, M.; Jiang, F.; Gao, Y.; Luo, H.; Liu, J.; Liang, W.; Zhi, C. Nanoporous CaCO_3 Coatings Enabled Uniform Zn Stripping/Plating for Long-Life Zinc Rechargeable Aqueous Batteries. *Adv. Energy Mater.* **2018**, *8*, 1801090.
- (22) Wang, L.-P.; Li, N.-W.; Wang, T.-S.; Yin, Y.-X.; Guo, Y.-G.; Wang, C.-R. Conductive graphite fiber as a stable host for zinc metal anodes. *Electrochim. Acta* **2017**, *244*, 172–177.
- (23) Zeng, Y.; Zhang, X.; Qin, R.; Liu, X.; Fang, P.; Zheng, D.; Tong, Y.; Lu, X. Dendrite-Free Zinc Deposition Induced by Multifunctional CNT Frameworks for Stable Flexible Zn-Ion Batteries. *Adv. Mater.* **2019**, *31*, 1903675.
- (24) Zhao, Q.; Huang, W.; Luo, Z.; Liu, L.; Lu, Y.; Li, Y.; Li, L.; Hu, J.; Ma, H.; Chen, J. High-capacity aqueous zinc batteries using sustainable quinone electrodes. *Sci. Adv.* **2018**, *4*, No. eaao1761.
- (25) Zhan, C.; Lu, J.; Jeremy Kropf, A.; Wu, T.; Jansen, A. N.; Sun, Y.-K.; Qiu, X.; Amine, K. Mn(II) deposition on anodes and its effects on capacity fade in spinel lithium manganate–carbon systems. *Nat. Commun.* **2013**, *4*, 2437.
- (26) Ghosh, M.; Vijayakumar, V.; Kurungot, S. Dendrite Growth Suppression by Zn^{2+} -Integrated Nafion Ionomer Membranes: Beyond Porous Separators toward Aqueous Zn/ V_2O_5 Batteries with Extended Cycle Life. *Energy Technol.* **2019**, *7*, 1900442.
- (27) Khayum M, A.; Ghosh, M.; Vijayakumar, V.; Halder, A.; Nurhuda, M.; Kumar, S.; Addicoat, M. A.; Kurungot, S.; Banerjee, R. Zinc Ion Interactions in a Two-Dimensional Covalent Organic Framework based Aqueous Zinc Ion Battery. *Chem. Sci.* **2019**, *10*, 8889–8894.
- (28) Abraham, K. M.; Jiang, Z.; Carroll, B. Highly Conductive PEO-like Polymer Electrolytes. *Chem. Mater.* **1997**, *9*, 1978–1988.
- (29) Vijayakumar, V.; Diddens, D.; Heuer, A.; Kurungot, S.; Winter, M.; Nair, J. R. Dioxolanone-Anchored Poly(allyl ether)-Based Cross-Linked Dual-Salt Polymer Electrolytes for High-Voltage Lithium Metal Batteries. *ACS Appl. Mater. Interfaces* **2019**, *12*, 567–579.
- (30) Li, Z.; Wang, J.; Liu, X.; Liu, S.; Ou, J.; Yang, S. Electrostatic layer-by-layer self-assembly multilayer films based on graphene and manganese dioxide sheets as novel electrode materials for supercapacitors. *J. Mater. Chem.* **2011**, *21*, 3397–3403.
- (31) Toupin, M.; Brousse, T.; Bélanger, D. Charge Storage Mechanism of MnO_2 Electrode Used in Aqueous Electrochemical Capacitor. *Chem. Mater.* **2004**, *16*, 3184–3190.
- (32) Li, N.-W.; Yin, Y.-X.; Li, J.-Y.; Zhang, C.-H.; Guo, Y.-G. Passivation of Lithium Metal Anode via Hybrid Ionic Liquid Electrolyte toward Stable Li Plating/Stripping. *Adv. Sci.* **2017**, *4*, 1600400.
- (33) Song, M.; Tan, H.; Chao, D.; Fan, H. J. Recent Advances in Zn-Ion Batteries. *Adv. Funct. Mater.* **2018**, *28*, 1802564.
- (34) Shah, D. B.; Olson, K. R.; Karny, A.; Mecham, S. J.; DeSimone, J. M.; Balsara, N. P. Effect of anion size on conductivity and transference number of perfluoroether electrolytes with lithium salts. *J. Electrochem. Soc.* **2017**, *164*, A3511–A3517.
- (35) Zhang, L.; Rodríguez-Pérez, I. A.; Jiang, H.; Zhang, C.; Leonard, D. P.; Guo, Q.; Wang, W.; Han, S.; Wang, L.; Ji, X. ZnCl_2 “Water-in-Salt” Electrolyte Transforms the Performance of Vanadium Oxide as a Zn Battery Cathode. *Adv. Funct. Mater.* **2019**, *29*, 1902653.
- (36) Bieker, G.; Winter, M.; Bieker, P. Electrochemical in situ investigations of SEI and dendrite formation on the lithium metal anode. *Phys. Chem. Chem. Phys.* **2015**, *17*, 8670–8679.
- (37) Hoang, T. K. A.; Doan, T. N. L.; Sun, K. E. K.; Chen, P. Corrosion chemistry and protection of zinc & zinc alloys by polymer-containing materials for potential use in rechargeable aqueous batteries. *RSC Adv.* **2015**, *5*, 41677–41691.

- (38) Vijayakumar, V.; Ghosh, M.; Arun Torris, A. T.; Nikhil Chandran, M. K.; Nair, S. B.; Badiger, M. V.; Kurungot, S. Water-in-Acid Gel Polymer Electrolyte Realized through a Phosphoric Acid-Enriched Polyelectrolyte Matrix toward Solid-State Supercapacitors. *ACS Sustainable Chem. Eng.* **2018**, *6*, 12630–12640.
- (39) Aziz, S. B.; Woo, T. J.; Kadir, M. F. Z.; Ahmed, H. M. A conceptual review on polymer electrolytes and ion transport models. *J. Sci.: Adv. Mater. Devices* **2018**, *3*, 1–17.
- (40) Lu, Y.; Tikekar, M.; Mohanty, R.; Hendrickson, K.; Ma, L.; Archer, L. A. Stable Cycling of Lithium Metal Batteries Using High Transference Number Electrolytes. *Adv. Energy Mater.* **2015**, *5*, 1402073.
- (41) Wang, J.; Polleux, J.; Lim, J.; Dunn, B. Pseudocapacitive Contributions to Electrochemical Energy Storage in TiO₂ (Anatase) Nanoparticles. *J. Phys. Chem. C* **2007**, *111*, 14925–14931.
- (42) Lindström, H.; Södergren, S.; Solbrand, A.; Rensmo, H.; Hjelm, J.; Hagfeldt, A.; Lindquist, S.-E. Li⁺ Ion Insertion in TiO₂ (Anatase). 2. Voltammetry on Nanoporous Films. *J. Phys. Chem. B* **1997**, *101*, 7717–7722.
- (43) Geng, H.; Cheng, M.; Wang, B.; Yang, Y.; Zhang, Y.; Li, C. C. Electronic Structure Regulation of Layered Vanadium Oxide via Interlayer Doping Strategy toward Superior High-Rate and Low-Temperature Zinc-Ion Batteries. *Adv. Funct. Mater.* **2019**, *30*, 1907684.
- (44) Yu, P.; Li, C.; Guo, X. Sodium Storage and Pseudocapacitive Charge in Textured Li₄Ti₅O₁₂ Thin Films. *J. Phys. Chem. C* **2014**, *118*, 10616–10624.
- (45) Anothumakkool, B.; Kurungot, S. Electrochemically grown nanoporous MnO₂ nanowalls on a porous carbon substrate with enhanced capacitance through faster ionic and electrical mobility. *Chem. Commun.* **2014**, *50*, 7188–7190.
- (46) Huang, M.; Li, F.; Dong, F.; Zhang, Y. X.; Zhang, L. L. MnO₂-based nanostructures for high-performance supercapacitors. *J. Mater. Chem. A* **2015**, *3*, 21380–21423.
- (47) Wang, J.-G.; Yang, Y.; Huang, Z.-H.; Kang, F. Coaxial carbon nanofibers/MnO₂ nanocomposites as freestanding electrodes for high-performance electrochemical capacitors. *Electrochim. Acta* **2011**, *56*, 9240–9247.
- (48) Zhang, N.; Cheng, F.; Liu, Y.; Zhao, Q.; Lei, K.; Chen, C.; Liu, X.; Chen, J. Cation-Deficient Spinel ZnMn₂O₄ Cathode in Zn-(CF₃SO₃)₂ Electrolyte for Rechargeable Aqueous Zn-Ion Battery. *J. Am. Chem. Soc.* **2016**, *138*, 12894–12901.
- (49) Guo, X.; Li, J.; Jin, X.; Han, Y.; Lin, Y.; Lei, Z.; Wang, S.; Qin, L.; Jiao, S.; Cao, R. A Hollow-Structured Manganese Oxide Cathode for Stable Zn-MnO₂ Batteries. *Nanomaterials* **2018**, *8*, 301.
- (50) Wu, X.; Xiang, Y.; Peng, Q.; Wu, X.; Li, Y.; Tang, F.; Song, R.; Liu, Z.; He, Z.; Wu, X. Green-low-cost rechargeable aqueous zinc-ion batteries using hollow porous spinel ZnMn₂O₄ as the cathode material. *J. Mater. Chem. A* **2017**, *5*, 17990–17997.
- (51) Lee, B.; Lee, H. R.; Kim, H.; Chung, K. Y.; Cho, B. W.; Oh, S. H. Elucidating the intercalation mechanism of zinc ions into α -MnO₂ for rechargeable zinc batteries. *Chem. Commun.* **2015**, *51*, 9265–9268.
- (52) Alfaruqi, M. H.; Mathew, V.; Gim, J.; Kim, S.; Song, J.; Baboo, J. P.; Choi, S. H.; Kim, J. Electrochemically Induced Structural Transformation in a γ -MnO₂ Cathode of a High Capacity Zinc-Ion Battery System. *Chem. Mater.* **2015**, *27*, 3609–3620.
- (53) Alfaruqi, M. H.; Islam, S.; Putro, D. Y.; Mathew, V.; Kim, S.; Jo, J.; Kim, S.; Sun, Y.-K.; Kim, K.; Kim, J. Structural transformation and electrochemical study of layered MnO₂ in rechargeable aqueous zinc-ion battery. *Electrochim. Acta* **2018**, *276*, 1–11.
- (54) Alfaruqi, M. H.; Gim, J.; Kim, S.; Song, J.; Pham, D. T.; Jo, J.; Xiu, Z.; Mathew, V.; Kim, J. A layered δ -MnO₂ nanoflake cathode with high zinc-storage capacities for eco-friendly battery applications. *Electrochem. Commun.* **2015**, *60*, 121–125.
- (55) Stoševski, I.; Bonakdarpour, A.; Cuadra, F.; Wilkinson, D. P. Highly crystalline ramsdellite as a cathode material for near-neutral aqueous MnO₂/Zn batteries. *Chem. Commun.* **2019**, *55*, 2082–2085.
- (56) Wang, L.; Cao, X.; Xu, L.; Chen, J.; Zheng, J. Transformed Akhtenskite MnO₂ from Mn₃O₄ as Cathode for a Rechargeable Aqueous Zinc Ion Battery. *ACS Sustainable Chem. Eng.* **2018**, *6*, 16055–16063.
- (57) Islam, S.; Alfaruqi, M. H.; Mathew, V.; Song, J.; Kim, S.; Kim, S.; Jo, J.; Baboo, J. P.; Pham, D. T.; Putro, D. Y.; Sun, Y.-K.; Kim, J. Facile synthesis and the exploration of the zinc storage mechanism of β -MnO₂ nanorods with exposed (101) planes as a novel cathode material for high performance eco-friendly zinc-ion batteries. *J. Mater. Chem. A* **2017**, *5*, 23299–23309.
- (58) Dong, W.; Shi, J.-L.; Wang, T.-S.; Yin, Y.-X.; Wang, C.-R.; Guo, Y.-G. 3D zinc@carbon fiber composite framework anode for aqueous Zn–MnO₂ batteries. *RSC Adv.* **2018**, *8*, 19157–19163.
- (59) Huang, Y.; Liu, J.; Huang, Q.; Zheng, Z.; Hiralal, P.; Zheng, F.; Ozgit, D.; Su, S.; Chen, S.; Tan, P.-H.; Zhang, S.; Zhou, H. Flexible high energy density zinc-ion batteries enabled by binder-free MnO₂/reduced graphene oxide electrode. *npj Flexible Electron.* **2018**, *2*, 21.
- (60) Gao, X.-W.; Deng, Y.-F.; Wexler, D.; Chen, G.-H.; Chou, S.-L.; Liu, H.-K.; Shi, Z.-C.; Wang, J.-Z. Improving the electrochemical performance of the LiNi_{0.5}Mn_{1.5}O₄ spinel by polypyrrole coating as a cathode material for the lithium-ion battery. *J. Mater. Chem. A* **2015**, *3*, 404–411.
- (61) Liu, F.; Chen, Z.; Fang, G.; Wang, Z.; Cai, Y.; Tang, B.; Zhou, J.; Liang, S. V₂O₅ Nanospheres with mixed vanadium valences as high electrochemically active aqueous zinc-ion battery cathode. *Nano-Micro Letters* **2019**, *11*, 25.
- (62) Jin, Y.; Zou, L.; Liu, L.; Engelhard, M. H.; Patel, R. L.; Nie, Z.; Han, K. S.; Shao, Y.; Wang, C.; Zhu, J.; Pan, H.; Liu, J. Joint Charge Storage for High-Rate Aqueous Zinc–Manganese Dioxide Batteries. *Adv. Mater.* **2019**, *31*, 1900567.
- (63) Oberholzer, P.; Tervoort, E.; Bouzid, A.; Pasquarello, A.; Kundu, D. Oxide versus Nonoxide Cathode Materials for Aqueous Zn Batteries: An Insight into the Charge Storage Mechanism and Consequences Thereof. *ACS Appl. Mater. Interfaces* **2019**, *11*, 674–682.
- (64) Jeong, S.-K.; Seo, H.-Y.; Kim, D.-H.; Han, H.-K.; Kim, J.-G.; Lee, Y. B.; Iriyama, Y.; Abe, T.; Ogumi, Z. Suppression of dendritic lithium formation by using concentrated electrolyte solutions. *Electrochem. Commun.* **2008**, *10*, 635–638.

Scalable Synthesis of Manganese-Doped Hydrated Vanadium Oxide as a Cathode Material for Aqueous Zinc-Metal Battery

Meena Ghosh, Swati Dilwale, Vidyanand Vijayakumar, and Sreekumar Kurungot*

Cite This: *ACS Appl. Mater. Interfaces* 2020, 12, 48542–48552

Read Online

ACCESS |



Metrics & More



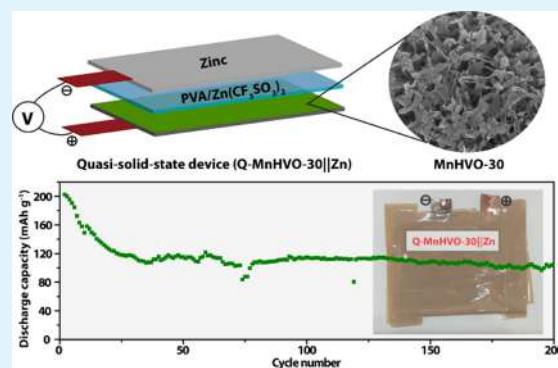
Article Recommendations



Supporting Information

ABSTRACT: Rechargeable aqueous zinc-metal batteries (ZMBs) are considered as potential energy storage devices for stationary applications. Despite the significant developments in recent years, the performance of ZMBs is still limited due to the lack of advanced cathode materials delivering high capacity and long cycle life. In this work, we report a low-temperature and scalable synthesis method following a surfactant-assisted route for preparing manganese-doped hydrated vanadium oxide (MnHVO-30) and its application as the cathode material for ZMB. The as-prepared material possesses a porous architecture and expanded interlayer spacing. Therefore, the MnHVO-30 cathode offers fast and reversible insertion of Zn^{2+} ions during the charge/discharge process and delivers 341 mAh g^{-1} capacity at 0.1 A g^{-1} . Moreover, the MnHVO-30||Zn cell retains 82% of its initial capacity over 1200 stability cycles, which is higher compared to that of the undoped system. Besides, a quasi-solid-state home-made pouch cell with an area of $3.3 \times 1.6 \text{ cm}^2$ and 3.6 mg cm^{-2} loading is assembled, achieving 115 mAh g^{-1} capacity over 100 stability cycles. Therefore, this work provides an easy and attractive way for preparing efficient cathode materials for aqueous ZMBs.

KEYWORDS: post-lithium battery, hydrated vanadium pentoxide, anionic surfactant, Nafion ionomer membrane, quasi-solid-state battery



INTRODUCTION

In recent years, multivalent ion-based aqueous batteries (such as Zn^{2+} , Mg^{2+} , and Al^{3+}) are receiving immense research interest because of their high capacity, easy fabrication, and inherent safety.^{1,2} Rechargeable zinc-metal batteries (ZMBs) comprising metallic zinc as the anode and a Zn^{2+} -ion insertion cathode in mild aqueous zinc-ion conducting electrolytes are at the forefront of next-generation aqueous batteries. Considering the high theoretical capacity of metallic zinc (820 mAh g^{-1}), ZMBs have the potential to surpass the energy density of graphite anode (theoretical capacity of $\approx 380 \text{ mAh g}^{-1}$)-based commercial lithium-ion batteries.^{3–5} However, like the other electrochemical devices, the advancement of ZMBs requires the development of a suitable electrolyte, electrode materials, separator, and cell-fabrication techniques. Although significant efforts have already been made toward this direction, unfortunately, the overall performance of ZMBs in terms of capacity, cell voltage, and cycle life is still inadequate to meet the commercial need.

To date, several inorganic and organic compounds have been demonstrated as efficient hosts for the Zn^{2+} ion, *viz.*, vanadium oxide, manganese oxide, Prussian blue analogs, conducting polymers, and so on.^{6–10} The performance of ZMBs constructed with different cathodes depends on the nature of the redox center, the number of electron transfer during the faradic reactions, reaction kinetics, and the

associated reaction mechanism involving the participation of Zn^{2+} and/or H^+ ions.¹¹ For instance, the average discharge-voltage plateau for manganese oxide often appears at $1.25 \text{ V vs Zn/Zn}^{2+}$ with a specific capacity of $200\text{--}300 \text{ mAh g}^{-1}$.⁴ Despite the high capacity and average voltage, manganese oxide experiences low capacity retention due to the dissolution of active material and irreversible phase transition during battery cycling.¹² Zn^{2+} insertion in the Prussian blue analog occurs at an even higher voltage ($\sim 1.5 \text{ V vs Zn/Zn}^{2+}$); however, the maximum discharge capacity obtained with this material is only around 65 mAh g^{-1} .⁹ Furthermore, the cathode materials based on vanadium oxides exhibit an average voltage at $0.80 \text{ V vs Zn/Zn}^{2+}$.¹³ However, the high specific capacity offered by the multiple oxidation states of vanadium (+5, +4, and +3) as well as the excellent structural stability for >1000 charge/discharge cycles makes them attractive cathodes for ZMBs.¹⁴ Similarly, polyaniline and organic molecules are also found to deliver good capacity. Still, they often suffer from a low voltage plateau and inferior cycle life.^{15,16} In short, designing of a ZMB

Received: July 22, 2020

Accepted: October 8, 2020

Published: October 20, 2020



cathode with high capacity, cell voltage, and long lifespan is still challenging.

Hydrated vanadium oxides (HVOs), which are layered-type compounds, have been recently employed as cathode materials in ZMBs. The HVO structure consists of water molecules intercalated between the two-dimensional V_2O_5 layers with large interlayer spacing ranging from 8.8 to 13.8 Å.¹⁷ These water molecules reduce the electrostatic interaction between the bivalent Zn^{2+} and the host lattice, ensuring the resilience of the electrode material against the back and forth movement of Zn^{2+} ions across the layered framework. In a recent report, Yan et al. have demonstrated that the intercalated water molecules in the $V_2O_5 \cdot nH_2O$ lattice lubricate the insertion of the Zn^{2+} ion, showing excellent electrochemical stability.¹⁸ Various strategies have been developed to reinforce the electrochemical performance of HVOs. These include designing nanostructured HVOs, tuning the interlayer spacing, and integrating with carbon materials. Zhang et al. have reported electrodeposition of $V_5O_{12} \cdot 6H_2O$ with 1.18 nm interlayer spacing, delivering a Zn^{2+} -storage capacity of 354.8 mAh g^{-1} .¹⁹ The preinsertion of foreign cations (*viz.*, Mn^{2+} , Co^{2+} , Na^+ , Ca^{2+} , Al^{3+} , *etc.*) into the HVO lattice could tune the interlayer spacing, resulting in better stability of the host framework.^{20–23} It is observed that the Al-doped $V_{10}O_{24} \cdot 12H_2O$ cathode could retain 98% of the initial capacity of over 3000 cycles, which is significantly higher than that of the undoped $V_{10}O_{24} \cdot 12H_2O$ (68% retention).²⁴ Cao et al. have reported remarkable improvement in the cycling stability of the HVO cathode by chemically inserting Mn^{2+} ions into the HVO lattice.²⁵ However, the complex and multistep synthesis methods involving hydrothermal treatment, high-temperature annealing, *etc.* make them unsuited for large-scale production. Therefore, the development of the facile and green synthesis of nanostructured HVOs is indeed important.

Herein, we report a low-temperature one-pot synthesis of HVO by an evaporation-assisted method from an aqueous solution of V_2O_5 in the presence of anionic dodecyl sulfate as a surfactant. The synthesis method is facile and scalable, producing a high yield of HVO. The lab-scale ZMB cell fabricated with the HVO cathode delivers a specific capacity of 330 mAh g^{-1} with excellent rate performance. To improve the cycling stability of the HVO sample, we introduced Mn doping into the HVO lattice during the synthesis step. The final Mn-doped HVO shows a homogeneous distribution of Mn, and no separate manganese oxide phase was detected. Moreover, compared to the undoped sample (78% retention of the initial capacity after 800 cycles), the Mn-doped HVO sample shows a profound improvement in capacity retention (91% of the initial capacity over 800 cycles). The physical analyses of both the doped and undoped HVO samples justify the observed change in the electrochemical performance. Finally, we have demonstrated the scalability of the synthesis strategy by fabricating a large electrode with 3.3×1.6 cm² area and 3.6 mg cm⁻² loading, and the electrochemical performance was demonstrated in a home-made pouch cell.

EXPERIMENTAL SECTION

Materials. Vanadium pentoxide (V_2O_5), manganese chloride tetrahydrate ($MnCl_2 \cdot 4H_2O$), zinc trifluoromethanesulfonate ($Zn(CF_3SO_3)_2$), sodium dodecyl sulfate (SDS), and poly(vinylalcohol) (PVA, molecular weight 85 000) were procured from Sigma-Aldrich. The Nafion (212) membrane separator was supplied by DuPont. Grafoil roll was supplied by Global Nanotech.

Synthesis of Hydrated Vanadium Oxide. In a typical process, at first, 150 mg of the SDS surfactant was dissolved in 15 mL of deionized water followed by the addition of 180 mg of commercial bulk V_2O_5 powder. Later, 2.5 mL of 30% H_2O_2 was added into the solution for the complete dissolution of V_2O_5 . The solution was stirred for 1 h at room temperature. Finally, the solution (solution A) was transferred into a Petri dish and kept at 40–45 °C for 3 days for complete evaporation of the water. The obtained green-colored powder material was washed with a copious amount of water to remove the SDS surfactant, and this was finally dried at 60 °C. The sample was labeled as HVO-30, where the number “30” represents the concentration of SDS (in mM) in the reaction mixture. Also, different amounts of SDS (30 and 500 mg) were added while preparing the reaction mixture, and the corresponding samples were marked as HVO-6 and HVO-100, respectively. The numbers 6 and 100 also represent the concentration of SDS in the precursor solution. For comparison purposes, the HVO sample without the SDS surfactant (HVO-0) was prepared, and the sample was dark-orange in color.

Synthesis of Mn-doped Hydrated Vanadium Oxide. First, 100 mg of $MnCl_2 \cdot 4H_2O$ salt was added into solution A (as mentioned in the previous section) and was stirred for another 15 min. (solution B). Solution B was transferred into a Petri dish, the temperature of which was maintained at 40–45 °C for 3 days, leading to complete evaporation of the water. The final sample was obtained after washing with water and drying at 60 °C. This sample was marked as MnHVO-30. The average yields for all of the HVO samples were 80–85% of the total weight of the solid-state commercial bulk V_2O_5 precursor used in the synthesis.

Preparation of Electrolyte. The electrolyte used in this study is an aqueous solution of 1 M $Zn(CF_3SO_3)_2$ salt. A piece of preactivated Nafion membrane²⁶ was soaked in this liquid electrolyte for 2 days, and the electrolyte-impregnated Nafion membrane was employed as a separator. For the fabrication of a scaled-up cell, PVA/ $Zn(CF_3SO_3)_2$ gel electrolyte was prepared by dissolving 0.7 g of PVA in 4 mL of water at 110 °C. In the next step, 1 g of $Zn(CF_3SO_3)_2$ salt was dissolved into the transparent PVA solution.

Fabrication of ZMB Cells. The electrochemical cells were fabricated in a CR2032 coin cell in an open atmosphere. To prepare the cathode, the HVO-0, HVO-30, or MnHVO-30 sample, conducting carbon, and poly(vinylidene fluoride) (PVDF) binder were taken with a weight ratio of 80:15:5, and the mixture was blended in *N*-methylpyrrolidone (NMP) for 5 h. The uniform slurry was coated on a Grafoil sheet to obtain 1 mg cm⁻² loading. Finally, the electrode was dried overnight at 70 °C. CR2032 coin cells were fabricated with metallic zinc anode, a liquid electrolyte-soaked Nafion membrane separator, the Grafoil loaded with the desired material as the cathode, and 1 M $Zn(CF_3SO_3)_2$ liquid electrolyte. The coin cells were marked as HVO-0||Zn, HVO-30||Zn, and MnHVO-30||Zn. In a similar way, the electrochemical cells were fabricated for analyzing the performance of HVOs prepared with different amounts of SDS, and the cells were marked as HVO-6||Zn and HVO-100||Zn.

For fabricating the scaled-up prototype home-made pouch cell, a thick slurry was prepared by mixing the MnHVO-30 sample, conducting carbon, and PVDF binder in an 80:15:5 weight ratio in NMP. The slurry was probe-sonicated for 15 min and coated over a Grafoil sheet with the help of a bar coater, and the MnHVO-30-coated Grafoil sheet was dried at 80 °C for 12 h. The coated Grafoil sheet was cut into a 3.3×1.6 cm² area, and the required amount of the PVA/ $Zn(CF_3SO_3)_2$ gel electrolyte was spread over the electrode. A thin layer of the gel electrolyte was also coated over a piece of zinc foil with the same area. Two small-sized copper tapes were attached to the respective electrodes, which serve as the anode and cathode current collectors. Later, the electrodes were sandwiched together by keeping the Nafion separator for preventing contact between the electrodes. The cell was correctly sealed with adhesive tape to minimize the electrolyte evaporation. This quasi-solid-state pouch cell was labeled as Q-MnHVO-30||Zn.

Material Characterization. A Rigaku, MicroMax-007HF, with a high-intensity microfocus rotating anode X-ray generator ($Cu K\alpha$ ($\alpha = 1.54$ Å)) was used for X-ray diffraction (XRD) analysis. The

morphology of HVO-0, HVO-30, and MnHVO-30 samples was analyzed with a field emission scanning electron microscope (FESEM) Nova Nano SEM 450. Elemental mapping was performed with energy dispersive X-ray analysis system attached to an ESEM-Quanta 200-3D instrument. The transmission electron microscopy (TEM) imaging, and energy-dispersive X-ray spectroscopy (EDAX) was recorded with a Tecnai T-20 instrument at an accelerating voltage of 200 kV. A Bruker Tensor27 FTIR instrument was used to perform Fourier transform infrared (FTIR) analysis. X-ray photoelectron spectroscopy (XPS) analysis was performed using a Thermo K-Alpha + X-ray spectrometer. Thermogravimetric analysis (TGA) was performed with an SDT Q600 DSC-TGA instrument under an air atmosphere with a temperature ramp of 10 °C per min. Brunauer–Emmett–Teller (BET) analysis was carried out in a Quantachrome Quadrasorb instrument for studying the N₂ adsorption/desorption properties and pore size distribution patterns of the samples.

Electrochemical Measurements. The electrochemical performance of the cathode samples HVO-0, HVO-30, and MnHVO-30 was studied in a CR2032 coin cell. The cells were characterized by cyclic voltammetry (CV) (at scan rates of 1.0, 0.5, 0.3, and 0.1 mV s⁻¹) and galvanostatic charge–discharge (GCD) (at constant current rates of 0.1, 0.25, 0.5, 1.0, and 3.0 A g⁻¹) techniques within the voltage window of 0.2–1.6 V vs Zn/Zn²⁺, using BioLogic VMP3 and Neware battery tester (SV, 10 mA), respectively. The capacity of the cells was calculated from eq S1 given in the Supporting Information (SI). The cycling stability tests were performed by a GCD experiment at the current rate of 3.0 A g⁻¹. The impedance analyses were carried out (using BioLogic VMP3) in the frequency range of 1 MHz to 100 mHz with a sinus amplitude of 10 mV ($V_{\text{rms}} = 7.07$ mV). The Q-MnHVO-30||Zn cell was tested by CV at the scan rate of 1.0 mV s⁻¹ and the GCD technique at a 1.3 A g⁻¹ current rate with BioLogic VMP3 instrument. For the *ex situ* characterization of the MnHVO-30||Zn cell, the cathodes were recovered from the cells after the first complete discharge to 0.2 V and complete charge to 1.6 V, respectively, at 0.1 A g⁻¹ current rate.

RESULTS AND DISCUSSION

Physical Characterization. The synthesis of the MnHVO-30 sample is schematically presented in Figure 1. The desired material is obtained from an aqueous solution of

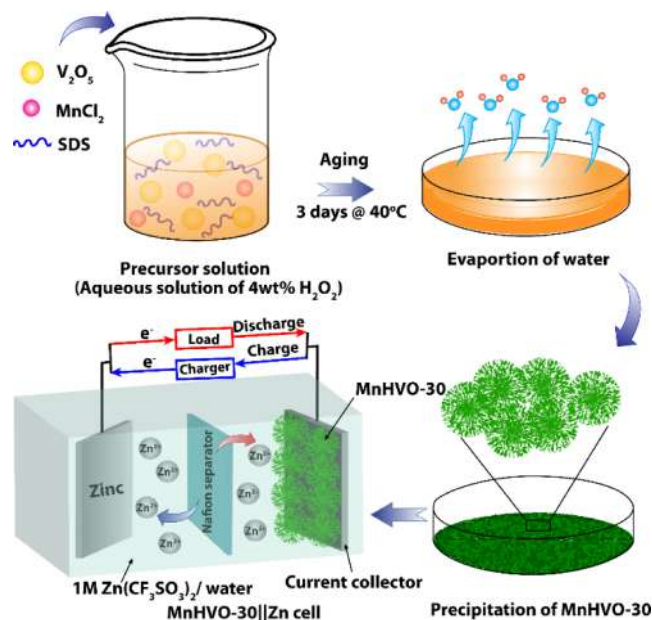


Figure 1. Schematic representation for the synthesis and application of the MnHVO-30 sample. For simplicity, the anionic counterpart of the electrolyte is not shown in the figure.

the commercial V₂O₅ and MnCl₂ additive in the presence of the SDS surfactant and 4 wt % H₂O₂. The adopted synthesis protocol is cost-effective and eco-friendly, and the process does not require any additional high-temperature treatment. Here, we have selected an anionic surfactant so that it can strongly interact with the cationic species generated in the reaction mixture to form a surfactant–metal cation composite.²⁷

The processes occurring during the evolution of the aforementioned reaction mixture can be briefly explained as follows. In the diluted solution of H₂O₂, the bulk V₂O₅ powder undergoes a vigorous reaction forming O₂ gas and the diperoxo anion [VO(O₂)₂(OH)₂]⁻, which later decomposes into the monoperoxo cation [VO(O₂)(OH)₂]₃⁺.²⁸ These complexes further react to form [VO₂]⁺ ions in the solution, liberating O₂ bubbles;²⁹ the change in solution color from yellow to dark-orange indicates the formation of different intermediates during the reaction. The associated chemical reactions (eq S2–S5) are given in the Supporting Information (SI). In the presence of SDS with 30 mM concentration (\gg critical micelle concentration (CMC) of SDS), the surfactant molecules are likely to form micellar structures, which could serve as soft templates. The [VO₂]⁺ ions can get absorbed over these micelles through the electrostatic interaction with SO₃⁻ moieties of SDS. During aging, [VO₂]⁺ ions start to nucleate and undergo the crystallization process to form V₂O₅·*n*H₂O. During crystal growth, the preadded Mn²⁺ species in the reaction mixture could intercalate between the layers of V₂O₅·*n*H₂O, resulting in the doping of Mn into the HVO lattice.

As given in Figure 2a,b, the MnHVO-30 sample exhibits a porous 3D architecture consisting of randomly assembled nanoflake structures. The elemental mapping profile validates the uniform dispersion of V, Mn, and O in the MnHVO-30 sample, proving the Mn doping (Figure 2c–e). For comparison, we have prepared a control sample without introducing Mn doping (HVO-30). The HVO-30 sample also possesses (Figure S1a,b) self-assembled microstructures similar to that of the Mn-doped material. This implies that the addition of Mn²⁺ salt in the precursor reaction mixture does not induce significant morphological change except for the doping of Mn. Contrarily, the sample prepared in the absence of the SDS surfactant (HVO-0) agglomerated and showed a less porous (Figure S1c,d) morphology. Hence, it is evident that the SDS surfactant present in the solution acts as a pore-creating as well as a structure-directing agent during the synthesis.

The morphology of MnHVO-30 is further characterized by TEM analyses. Figure 2f shows the aggregation of nanoflakes in a randomly orientated manner. Figure 2g reveals that the nanoflakes possess an average interlayer spacing of ~0.8 nm, possibly resulting from the insertion of water molecules and Mn²⁺ ions into the interlayer space of the lattice structure. In fact, such a high interlayer spacing could favor the fast and reversible diffusion of Zn²⁺ ions when employed as the cathode material in ZMBs. The TEM image of HVO-30 also points out a layered structure with an interlayer spacing of ~0.8 nm (Figure S1e). It may be noted that the interlayer spacing in both samples is obtained after averaging the measurements from different sections of the TEM sample. The SAED patterns of MnHVO-30 (Figure 2h inset) and HVO-30 (Figure S1e inset) show the polycrystalline nature of the samples.³⁰ The EDAX data of MnHVO-30 (Figure 2h) displays the presence of O, V, and Mn in the sample. The

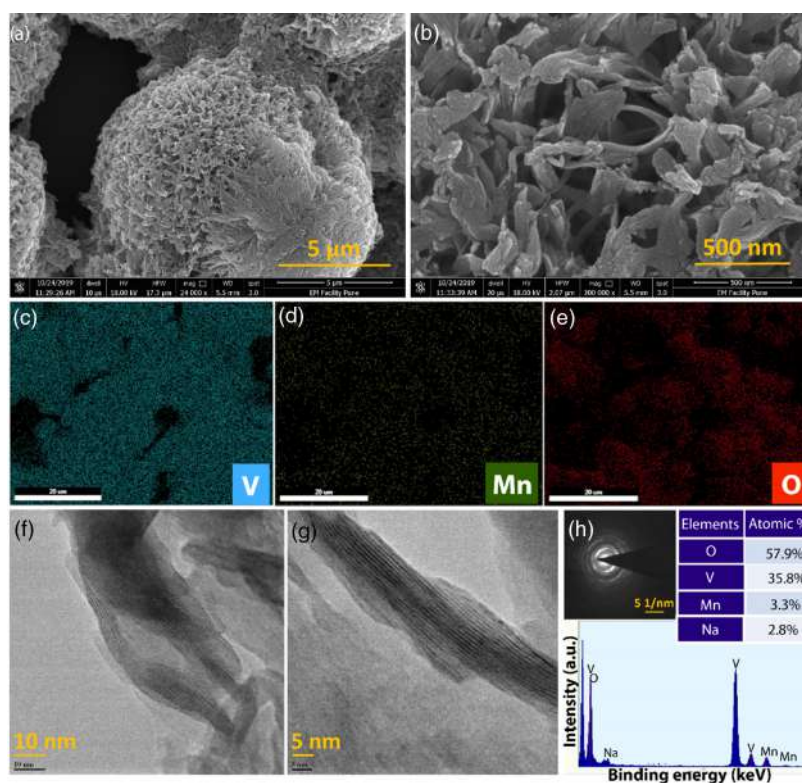


Figure 2. (a, b) FESEM images of MnHVO-30; elemental mapping of (c) V, (d) Mn, and (e) O in MnHVO-30. (f), and (g) TEM images and (h) EDAX data of the MnHVO-30 sample. Selected area electron diffraction (SAED) pattern of the sample is shown in the inset of (h).

sample also contains a small amount of Na coming from the cationic counterpart of the SDS surfactant.

Later, the crystal structure of the samples was studied by XRD analyses. The XRD patterns of all of the samples (Figure 3a) appear different from that of the commercial bulk V_2O_5 ($C-V_2O_5$, Figure S2a), indicating the changes that occurred in the original crystal structure of $C-V_2O_5$ after the reaction with H_2O_2 . The XRD data of the HVO-0 sample matches with the diffraction pattern of $V_2O_5 \cdot nH_2O$ (JCPDS 40-1296, Figure S2b), as reported earlier.^{31,32} The strong peak at the 2θ value of 7.2° is assigned to the (001) plane of $V_2O_5 \cdot nH_2O$. The additional peaks at 22.9 , 30.8 , and 38.7° correspond to (003), (004), and (005) planes of $V_2O_5 \cdot nH_2O$, which indicate the layered structure of HVO-0, showing a preferred orientation along the (00l) planes. In addition to the above (00l) planes, the small peak appearing at 2θ of 25.4° relates to the in-plane (*hkl*) reflection of HVO, as mentioned in the previous reports.³¹

The XRD patterns of HVO-30 and MnHVO-30 exhibit a strong peak at $2\theta < 10^\circ$ related to the (001) plane of $V_2O_5 \cdot nH_2O$, suggesting that the layered crystal structure is preserved. The increased intensity of the (*hkl*) reflection compared to HVO-0 is due to the reduced stacking of the vanadium oxide layers.³³ Moreover, the XRD patterns of HVO-30 and MnHVO-30 match with the previously reported cation inserted (*viz.*, Na^+ , Mn^{2+} , Ni^{2+} , K^+ , *etc.*) $V_2O_5 \cdot nH_2O$.^{25,34,35} Besides, no significant diffraction peaks corresponding to the crystalline phase of manganese oxide are observed in MnHVO-30. Interestingly, the strongest peak at $2\theta < 10^\circ$ for MnHVO-30 relates to an expanded interlayer spacing of 13.3 \AA , a value higher than 11.2 \AA calculated for HVO-30. The observed shift indicates the incorporation of Mn^{2+} ions into the interlayer space of MnHVO-30.^{22,25} However, the interplanar spacing

calculated from the XRD data is slightly higher than the values obtained from the corresponding TEM data. This could be due to the shrinkage of the interlayer spacing during the TEM experiment as a consequence of the evaporation of the interlayer water molecules under the intense electron beam in a vacuum.^{36,37}

The presence of water molecules in the samples is also supported through TGA analysis. In Figure S3, the TGA profiles of all three samples show a rapid weight loss before 100°C due to the removal of loosely bound water molecules. After that, the gradual removal of crystalline water molecules is observed in the temperature range of $100\text{--}200^\circ\text{C}$.^{38,39} These water molecules residing in the interlayer space of HVO could act as “lubricant” and facilitate the electrochemical insertion/extraction of divalent Zn^{2+} ions.¹⁸

In the Raman spectra of HVO-0 (Figure 3b), the peak at 155 cm^{-1} is related to the vibration of the V–O–V chain in the layered $V_2O_5 \cdot nH_2O$.^{31,35} A similar lattice vibrational mode in HVO-30 and MnHVO-30 is observed at 143 cm^{-1} .⁴⁰ Besides, other peaks located at 282 , 404 , 698 , and 993 cm^{-1} match with that of the different vibrational modes of the cation inserted $V_2O_5 \cdot nH_2O$. The FTIR data of all of the samples are compared in Figure 3c; the peak located in the range of $997\text{--}1006 \text{ cm}^{-1}$ originates from the characteristic V=O stretching vibration in the samples.⁴¹ Figure 3d shows a red shift of V=O stretching in the cases of HVO-30 and MnHVO-30 (997 cm^{-1}) compared to that of HVO-0 (1006 cm^{-1}). This observed shift signifies a weakening of the V=O bond in the former due to the reduction of a small amount of the V^{5+} to the V^{4+} state.²⁵

The oxidation states of the elements in the respective HVO samples are analyzed by XPS (Figures 3e,f, and S4). From the XPS elemental analysis of MnHVO-30, the contents of V and

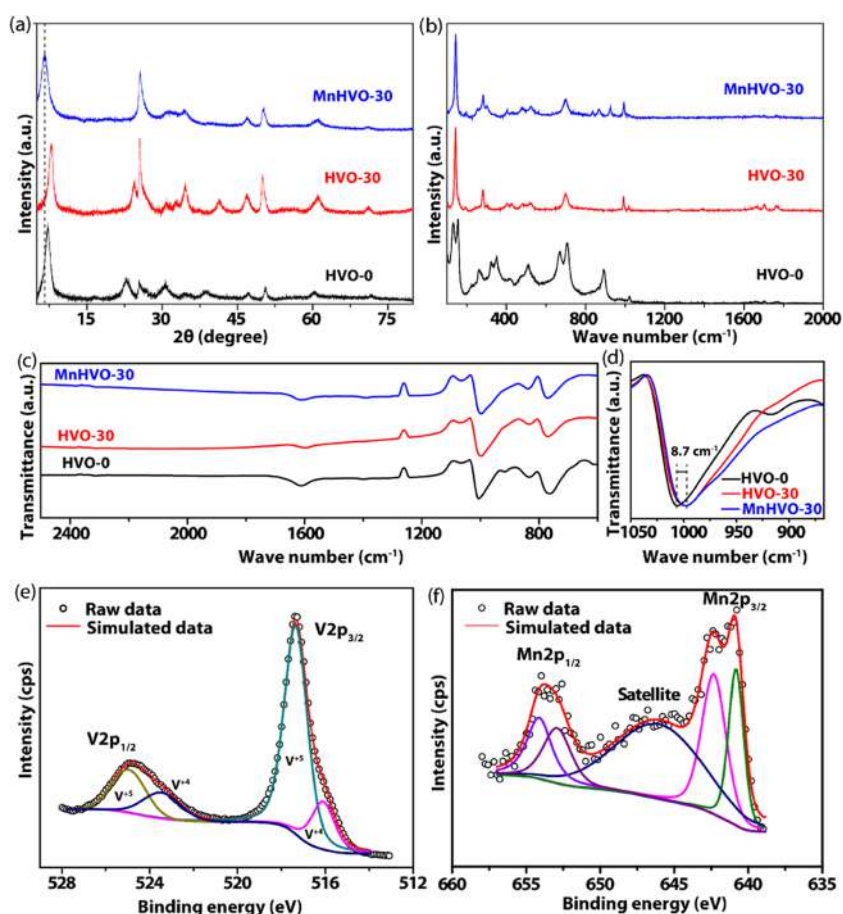


Figure 3. (a) XRD patterns, (b) Raman spectra, (c) and (d) FTIR spectra, (e) V 2p XPS spectra, and (f) Mn 2p XPS spectra of the MnHVO-30 sample.

Mn are obtained as 32.5 and 1.3%, respectively (Figure S4a), suggesting the low doping level of Mn. In O 1s XPS data of MnHVO-30 (Figure S4b), HVO-30 (Figure S4d), and HVO-0 (Figure S4f), the characteristic strong peak at the binding energy of 530 eV corresponds to the surface O atom coordinated with V.⁴² The other peaks at the higher binding energy values (531.2 and 532.9 eV) with low intensity come from the hydroxyl group bonded with the V atom and surface-absorbed water molecules, respectively.^{40,43} Figure 3e,f displays the deconvoluted XPS spectra of V and Mn, respectively, present in MnHVO-30. The characteristic signal of Mn 2p_{3/2} at 640.9 and 642.6 eV implies that the preinserted Mn ions are present in both the divalent and the higher valent oxidation states. The ionic radius of Mn⁴⁺ is similar to that of V⁵⁺, and Mn²⁺ possesses a higher radius; therefore, the latter accounts for the observed structural changes in MnHVO-30 upon Mn doping.⁴⁴ The intense V 2p_{3/2} spectra (Figure 3e) are deconvoluted into two peaks at 517.3 and 516.1 eV, which signify the coexistence of V⁵⁺ and V⁴⁺.⁴⁵ The mixed vanadium valences may augment the electrochemical performance of the material when employed as the cathode in ZMB.⁴⁶ Both V⁴⁺ and V⁵⁺ states are detected in HVO-30 (Figure S4c) as well; however, the ratio of [V⁵⁺]/[V⁴⁺] in HVO-30 (*ca.* 7.8) is slightly high compared to that of MnHVO-30 (*ca.* 4.2). It is reported that the insertion of Mn²⁺ ions into the lattice of HVO creates more low valence states of V (such as V⁴⁺) and more oxygen vacancies in the doped sample.^{25,47,48} This phenomenon is also observed for other vanadium oxide

cathodes followed by the introduction of different ionic species, including Mn²⁺ and K⁺.^{35,49,50} Meanwhile, in HVO-0 (Figure S4e), the vanadium signal shows only the presence of the V⁵⁺ state. Therefore, the V⁴⁺ created in MnHVO-30 and HVO-30 can influence the V=O bond strength, which is reflected in the FTIR spectra of the respective samples, as discussed in the previous section (Figure 3d). These observations imply that the SDS surfactant has an impact on directing the electronic structure of HVO.

The effect of the anionic SDS surfactant on the nature of porosity and the surface area of the samples was validated by BET surface area analyses. The specific surface area (Figure S5a) of HVO-30 is 16 m² g⁻¹, a value substantially higher than that of HVO-0 (3 m² g⁻¹). A drastic difference is observed in the pore size distribution profiles as well. Figure S5b displays that the size of pores in HVO-0 is in the range of 6–13 nm, whereas HVO-30 contains a wide range of pore size distributions within 6–50 nm. This clearly indicates the role of the surfactant as the soft template for creating a porous structure.

Electrochemical Characterization. The electrochemical performance of all of the samples is first characterized through CV analyses within the potential range of 0.2–1.6 V *vs* Zn|Zn²⁺. The CV plots of the MnHVO-30|Zn cell (Figure 4a) at various scan rates (0.1, 0.3, 0.5, and 1.0 mV s⁻¹) display two pairs of oxidation and reduction peaks. The redox peaks located at 0.72/0.48 and 1.12/0.89 V *vs* Zn|Zn²⁺ associated with the V⁴⁺/V³⁺ and V⁵⁺/V⁴⁺ redox couples, respectively.⁵¹ In

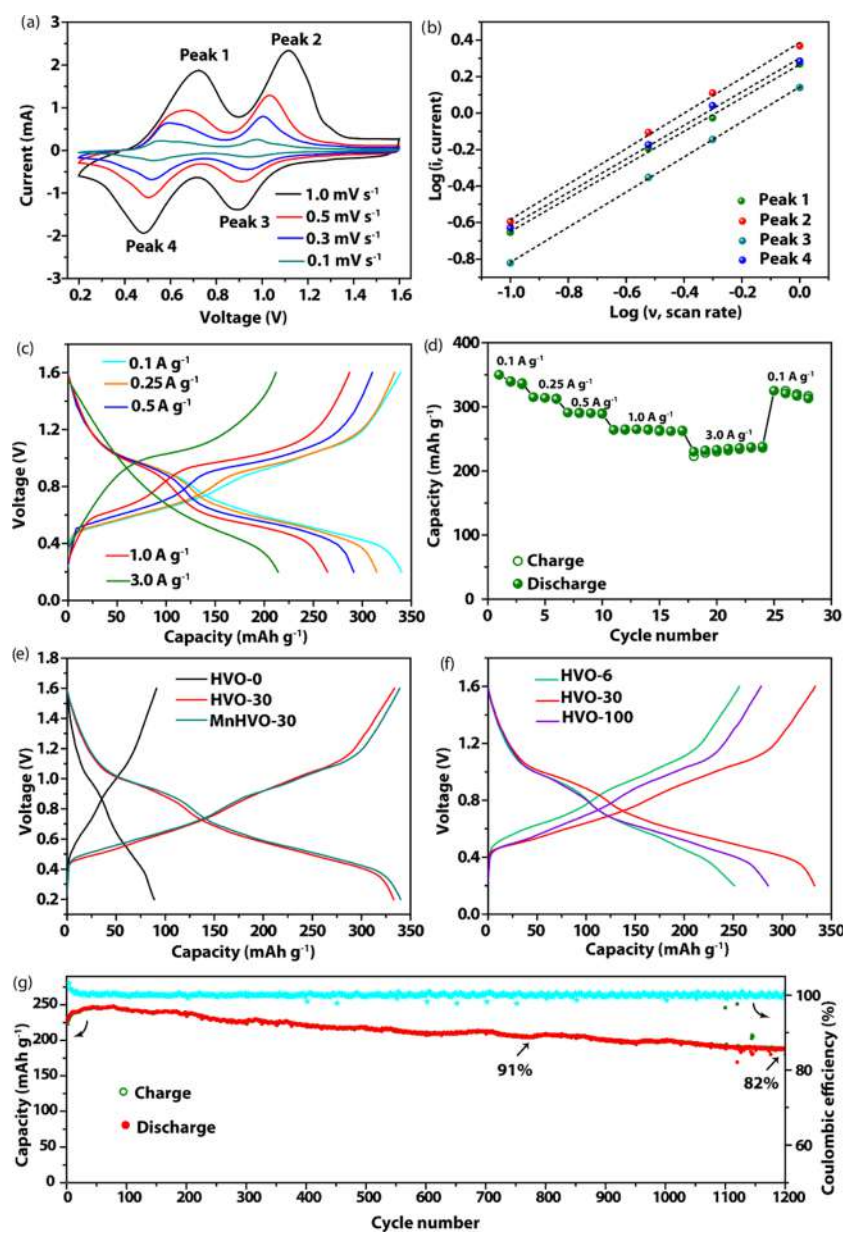


Figure 4. (a) CV profiles recorded at various scan rates; (b) $\log i$ vs $\log \nu$ plots; (c) GCD profiles recorded at various current rates; (d) rate capability plot for the MnHVO-30||Zn cell; (e) GCD profiles for HVO-0||Zn, HVO-30||Zn, and MnHVO-30||Zn cells at 0.1 A g^{-1} ; (f) GCD plots for HVO-6||Zn, HVO-30||Zn, and HVO-100||Zn cells at 0.1 A g^{-1} ; (g) cycling stability data for the MnHVO-30||Zn cell recorded at the current rate of 3.0 A g^{-1} . (All of the electrochemical characterizations presented in Figure 4 were carried out in the coin cell configuration with liquid electrolyte).

Figure S6a, the CV profile of MnHVO-30 recorded at 1.0 mV s^{-1} scan rate is compared with that of the HVO-30 and HVO-0 samples. The nearly overlapping position of the redox peaks suggests that all three cathodes undergo faradic reactions during the charge/discharge process of the respective ZMB cells. The CV profiles at various scan rates recorded for the HVO-0||Zn and HVO-30||Zn cells are given in Figure S6b,c. As seen in the figures, the current response traced by the CV curves for the HVO-0||Zn cell is inferior compared to both the MnHVO-30||Zn and HVO-30||Zn cells.

The kinetics of the Zn^{2+} insertion/extraction process is analyzed from the peak current (i) vs scan rate (ν) relationship ($I = a\nu^b$, where a and b are adjustable parameters) for the oxidation and reduction peaks, and the data are summarized in the form of a $\log i$ vs $\log \nu$ plot (Figures 4b, and S6d,e).⁵² The

slope of the plot represents the parameter b , which indicates the capacitive contribution in the electrochemical reaction. Typically, the b value approaching 1.0 suggests that the charge storage utilizing surface-controlled or capacitive mechanism is dominant, whereas b close to 0.5 indicates the dominance of the diffusion-controlled mechanism.^{53,54} The calculated b values for the peaks 1, 2, 3, and 4 (Figure 4b) in the MnHVO-30||Zn cell are 0.91, 0.97, 0.96, and 0.92, respectively. This suggests that the faradic reactions at the peak regions are mainly influenced by the surface-controlled process within the scan rate ranging from 1.0 to 0.1 mV s^{-1} .^{17,19} The b values calculated for the HVO-30||Zn and HVO-0||Zn cells are also close to 1.0, and the related $\log i$ vs $\log \nu$ plots are given in Figure S6d,e. The contributions of the diffusion-controlled and surface-controlled reactions in the total current response

obtained in the CV scans in the MnHVO-30||Zn cell are calculated from the following equation: $i = k_1\nu + k_2\nu^{1/2}$, where k_1 and k_2 are the constant parameters.⁵⁵ At scan rates of 1.0, 0.5, 0.3, and 0.1 mV s⁻¹, the contributions in the current from the capacitive process are calculated as 87.2, 82.7, 78.7, and 68.1%, respectively (Figure S7a,b), showing that capacitive contribution slightly decreases at a slower scan rate.

The GCD curves for the MnHVO-30||Zn cell (Figure 4c) display slopes at two different potential regions that are consistent with the CV data (Figure 4a). At the current rate of 0.1 A g⁻¹, the cell shows a discharge capacity of 341 mAh g⁻¹, a value comparable or superior to many of the previously reported vanadium oxide-based cathodes (Table S1).^{19,21,25,56–65} Later, the rate performance of MnHVO-30||Zn is investigated at various current rates, and discharge capacities of 314, 291, 265, and 215 mAh g⁻¹ are obtained at 0.25, 0.5, 1.0, and 3.0 A g⁻¹, respectively (Figure 4d). The observed rate performance (~60% retention of capacity when the current varies from 0.1 to 3.0 A g⁻¹) is attributed to the predominantly surface-controlled charge storage mechanism of the MnHVO-30 cathode, as discussed in the previous section. The layered structure of MnHVO-30 with a large interlayer spacing facilitates the mobility of the electrolyte ions. It enhances the access of the ions to the redox-active centers even at higher current rates. When the current rate is suddenly changed to 0.1 A g⁻¹, the cell could restore 320 mAh g⁻¹ capacity, implying the robustness of the MnHVO-30 cathode. Moreover, at all of the current rates, the GCD plots show ~98% Coulombic efficiency resulted from the excellent reversibility of the redox reactions associated with the Zn²⁺ insertion/extraction process.

The specific capacities of the HVO-0||Zn and HVO-30||Zn cells at 0.1 A g⁻¹ current rate are also measured, and the data are compared in Figure 4e. The GCD plots at the different current rates for these two cells are displayed in Figure S8a,b. The highest capacity obtained from HVO-30||Zn is 333 mAh g⁻¹, which is slightly lower than that of the MnHVO-30||Zn cell. The overlapping GCD plots indicate that the doped Mn in the MnHVO-30 sample does not take part in any separate electrochemical process within the mentioned potential range. On the contrary, the GCD profile of the HVO-0||Zn cell exhibits significantly less capacity (87 mAh g⁻¹) compared to the MnHVO-30||Zn and HVO-30||Zn cells. The effect of SDS concentration toward the electrochemical performance of the HVO samples is also studied. Figure 4f explains that the optimum concentration of SDS is 30 mM delivering the maximum reversible capacity among all of the other concentrations.

To investigate the resistance of the ZMB cells under study, the impedance spectra are recorded after the first complete discharge (at 0.2 V vs Zn|Zn²⁺, Figure S9a) at the current rate of 0.25 A g⁻¹. The charge-transfer resistance (R_{ct}) for the MnHVO-30||Zn cell (72 Ω) is slightly lower compared to the HVO-30||Zn (76 Ω) cell; however, after electrochemical cycling (Figure S9b), the resistance values are almost equal, justifying the comparable charge storage capacity of these two cells. In contrast, the HVO-0||Zn cell shows a higher R_{ct} value after the first discharge (87 Ω) as well as after the electrochemical cycling (112 Ω). This is due to the absence of the V⁴⁺ state in HVO-0 in contrast to the mixed oxidation states of vanadium (V⁵⁺ and V⁴⁺) in the samples prepared with the SDS surfactant. Nevertheless, the low surface area and lack of desired porosity in the HVO-0 sample (Figures S1c and

S5a) impede the transport of the electrolyte ions to the interior of the electrode in the HVO-0||Zn cell, which also contributes to the high resistance of the cell. Therefore, the above discussion underlines the importance of the SDS surfactant during the low-temperature synthesis of HVO for tuning the electronic property as well as the surface area of the material.

Along with the high capacity, the stability of the electrode material during repeated charge/discharge cycling is another important parameter. Therefore, the long-term GCD experiment at the current rate of 3.0 A g⁻¹ was carried out for the HVO-30||Zn and MnHVO-30||Zn cells. In Figure 4g, the MnHVO-30||Zn cell exhibits 95% retention of the initial capacity (227 mAh g⁻¹) with the Coulombic efficiency close to 100% over 500 charge/discharge cycles. After 1200 cycles, the cell could retain 187 mAh g⁻¹ (82% retention) capacity, demonstrating excellent electrochemical stability. At the same time, the HVO-30||Zn cell (Figure S10) delivers 217 mAh g⁻¹ initial capacity, and with progressive cycling, the cell experiences faster capacity fading compared to the MnHVO-30||Zn counterpart. As a result, after 830 stability cycles, the specific capacity drops to 169 mAh g⁻¹, which is only 77% of the initial capacity.

It must be noted that both cells are fabricated with the Nafion membrane separator. Nafion, as a cation-selective ionomer membrane, has already been reported to be effective in suppressing the growth of dendritic Zn deposits over the metallic Zn anode during long-term cycling, as observed in the case with several previous works on ZMBs.^{26,66,67} Hence, the observed difference in cycling performance is likely to have originated from the cathode side. The superior cycling performance of MnHVO-30 is credited to the unique crystal structure of the sample with expanded interlayer spacing that ensued from the preinserted Mn²⁺ ions and interlayer water molecules. Besides, a greater V⁴⁺ content in MnHVO-30 as explained from the XPS study is likely to augment the electrochemical activity. Therefore, all of these factors facilitate the reversible insertion of Zn²⁺ ions into MnHVO-30, ensuring better structural stability of MnHVO-30 compared to HVO-30 during prolonged cycling. This is also reflected in the morphology of postcycling MnHVO-30 and HVO-30 cathodes recovered from the respective electrochemical cells after the stability test. The cathode surface of the MnHVO-30||Zn cells looks homogeneous (Figure 5a), and the compact micro-

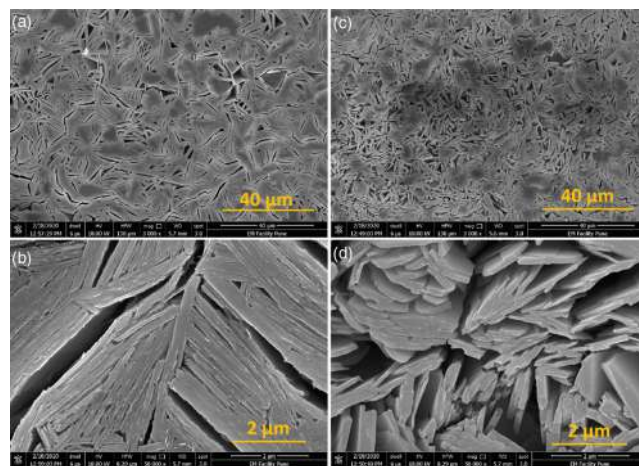


Figure 5. FESEM images of poststability cathodes recovered from (a, b) MnHVO-30||Zn and (c, d) HVO-30||Zn cells.

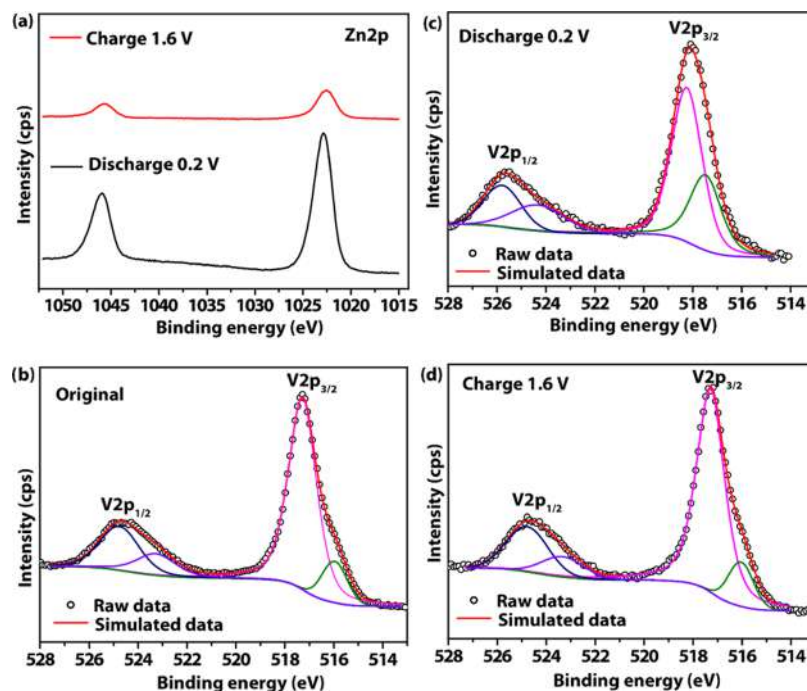


Figure 6. (a) Zn 2p XPS spectra of the MnHVO-30 cathode recovered from the discharged (0.20 V) and charged (1.6 V) MnHVO-30||Zn cells; V 2p XPS spectra of the (b) original MnHVO-30 electrode and (c, d) MnHVO-30 electrode after recovering from the discharged (0.20 V) and charged (1.6 V) MnHVO-30||Zn cells, respectively.

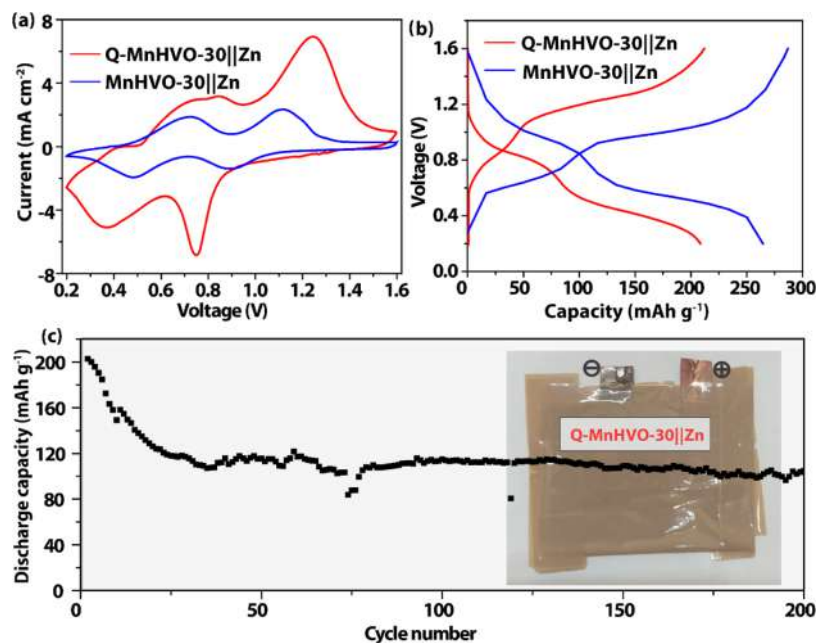


Figure 7. (a) CV profiles recorded at a scan rate of 1.0 mV s^{-1} , and (b) GCD profiles of the Q-MnHVO-30||Zn (at 1.3 A g^{-1}) and MnHVO-30||Zn (at 1.0 A g^{-1}) cells. (c) Cycling stability data of the Q-MnHVO-30||Zn cell recorded at 1.3 A g^{-1} current rate.

structure shows intimate contact among the particles (Figure 5b), which is favorable for better transport of the charge carrier species throughout the electrode. On the other hand, the HVO-30 cathode possesses a nonuniform surface (Figure 5c), and the lack of interparticle contact is visible in Figure 5d. Therefore, the difference in the morphological change also rationalizes the superior cyclability of the MnHVO-30 cathode.

For an in-depth understanding of the reversibility of the electrode reactions occurring in the MnHVO-30||Zn cell, the cathode is characterized after recovering from the fully

discharged (0.2 V) and charged (1.6 V) cells. The XRD data of the electrodes are compared in Figure S11. At the discharged state of the cell, a small shift is observed for the (001) plane to a higher 2θ value (6.7°) compared to the pristine MnHVO-30 sample (6.6° , Figure 3a). This is due to the interlayer contraction resulting from the electrostatic interaction between the host material and the inserted Zn^{2+} ions during the discharge process.⁶⁸ Subsequently, at the fully charged state, the Zn^{2+} ions escape from the cathode, and the (001) diffraction peak reappears at the 2θ value similar to that

of the pristine sample (Figure 3a). The electrodes are subjected to XPS analysis (Figure 6a–d) after careful washing with water. As displayed in Figure 6a, the intensity of the Zn 2p XPS spectra in the cathode collected from the discharged cell is considerably higher than that in the charged cell. The reduced intensity of the Zn 2p XPS spectra corresponding to the charged electrode indicates that most of the inserted Zn^{2+} ions leave the cathode followed by complete charging.⁵⁸ Considering the V 2p XPS spectra, the peak in the recovered cathode after being fully discharged (Figure 6c) is deconvoluted into V^{3+} ($2p_{3/2}$: 518.2 eV) and V^{4+} ($2p_{3/2}$: 517.5 eV) signals. Interestingly, the intensity of the V^{4+} signal increases significantly compared to the original electrode (Figure 6b), which is in accord with the reduction of V^{5+} upon discharge. After complete charging to 1.6 V (Figure 6d), the intensity of V^{4+} decreases, and consequently, the ratio of the V $2p_{3/2}^{5+}$ and V $2p_{3/2}^{4+}$ peak area is found to be retrieved as in the pristine MnHVO-30 sample.⁵⁷ This indeed supports the reversibility of the associated electrochemical reactions occurring in the MnHVO-30||Zn cell.

Lastly, the advantage of the adopted synthesis protocol is demonstrated by scaling up the process and fabricating a home-made pouch cell with $3.3 \times 1.6 \text{ cm}^2$ area and 3.6 mg cm^{-2} loading of the active material. A PVA/Zn(CF_3SO_3)₂ gel electrolyte is employed for fabricating the home-made pouch cell. The CV data of the as-fabricated quasi-solid-state MnHVO-30||Zn pouch cell (Q-MnHVO-30||Zn) is compared with that of the MnHVO-30||Zn coin cell with liquid electrolyte in Figure 7a. Owing to the higher loading of the active material, the CV profile of the Q-MnHVO-30||Zn cell traces a higher current response (in mA cm^{-2}) than the latter with 1 mg cm^{-2} loading. The well-resolved redox peaks are clearly visible in the CV profile displaying a similar insertion/extraction mechanism of the Zn^{2+} ions in the Q-MnHVO-30||Zn cell. Q-MnHVO-30||Zn delivered 200 mAh g^{-1} discharge capacity at 1.3 A g^{-1} current rate (Figure 7b), which is comparable to the performance obtained with the $1 \text{ M Zn}(\text{CF}_3\text{SO}_3)_2$ liquid electrolyte counterpart tested in the coin cell configuration. The durability of the Q-MnHVO-30||Zn cell is tested at the same current rate (Figure 7c). During the cycling, the specific capacity of the cell gradually decreases in the initial cycles and stabilizes at 116 mAh g^{-1} after 50 cycles. Later, the Q-MnHVO-30 cell delivers almost the same capacity over 200 cycles. The lifespan of the Q-MnHVO-30||Zn cell is relatively short compared to that of the MnHVO-30||Zn cell with $1 \text{ M Zn}(\text{CF}_3\text{SO}_3)_2$ liquid electrolyte in the coin cell configuration. This is due to the gradual evaporation of water from the aqueous gel electrolyte in the home-made quasi-solid-state cell due to the imperfect packaging and sealing. The performance of the Q-MnHVO-30||Zn cell can be improved by standardizing the method for cell packaging, which requires further studies. Moreover, the quasi-solid-state cell shows comparable performance in terms of capacity and cycling stability to that of the previously reported cells (e.g., $\text{V}_5\text{O}_{12} \cdot 6\text{H}_2\text{O}||\text{Zn}$, $\text{NH}_4\text{V}_3\text{O}_8 \cdot 1.9 \text{ H}_2\text{O}||\text{Zn}$, PANI||Zn, etc.) as shown in Table S2.^{10,19,56,69,70}

CONCLUSIONS

In conclusion, we have developed a surfactant-assisted facile and scalable low-temperature synthesis method for preparing Mn-doped hydrated vanadium oxide (MnHVO-30). The as-synthesized material possesses a porous morphology, which offers easy diffusion of the electrolyte ions during the faradic

reactions. In addition, the mixed valance states of vanadium in MnHVO-30 created by the anionic surfactant enhance the electrochemical activity of the material. As a result, MnHVO-30 serves as an excellent host for the reversible insertion/extraction of the Zn^{2+} ions, delivering 341 mAh g^{-1} capacity at 0.1 A g^{-1} . Moreover, the expanded interlayer spacing resulting from the introduction of Mn^{2+} ions significantly improves the cycling performance of the MnHVO-30 cathode (82% capacity retention of the initial capacity over 1200 cycles) compared to the sample prepared without the doping. We have also tested the performance of the MnHVO-30 cathode in a quasi-solid-state cell with a loading of 3.6 mg cm^{-2} and $3.3 \times 1.6 \text{ cm}^2$ area. The Q-MnHVO-30||Zn cell shows $\sim 200 \text{ mAh g}^{-1}$ initial capacity and retains more than 100 mAh g^{-1} capacity for 200 cycles. The current study demonstrates a simple synthesis of an efficient electrode material following green chemistry principles for a less expensive and safe aqueous ZMB with high capacity and durability.

ASSOCIATED CONTENT

Supporting Information

The Supporting Information is available free of charge at <https://pubs.acs.org/doi/10.1021/acsami.0c13221>.

Equations and calculations used for the preparation of the electrodes and their electrochemical performance evaluation, FESEM images, TEM images, XRD profile, EDAX data, TGA data, XPS data, BET isotherm and pore size distribution profiles, associated electrochemistry plots, capacity, voltage window, and cycling stability of the MnHVO-30 cathode compared with some of the reported high performance of vanadium oxide-based cathodes for ZMBs, and capacity and cycling stability of the Q-MnHVO-30||Zn cell compared with some of the previously reported quasi-solid-state ZMBs (PDF)

AUTHOR INFORMATION

Corresponding Author

Sreekumar Kurungot – Physical and Materials Chemistry Division, CSIR-National Chemical Laboratory, Pune 411008, Maharashtra, India; orcid.org/0000-0001-5446-7923; Email: k.sreekumar@ncl.res.in

Authors

Meena Ghosh – Physical and Materials Chemistry Division, CSIR-National Chemical Laboratory, Pune 411008, Maharashtra, India; Academy of Scientific and Innovative Research, Ghaziabad 201002, Uttar Pradesh, India

Swati Dilwale – Physical and Materials Chemistry Division, CSIR-National Chemical Laboratory, Pune 411008, Maharashtra, India; Academy of Scientific and Innovative Research, Ghaziabad 201002, Uttar Pradesh, India

Vidyanand Vijayakumar – Physical and Materials Chemistry Division, CSIR-National Chemical Laboratory, Pune 411008, Maharashtra, India; Academy of Scientific and Innovative Research, Ghaziabad 201002, Uttar Pradesh, India

Complete contact information is available at: <https://pubs.acs.org/doi/10.1021/acsami.0c13221>

Notes

The authors declare no competing financial interest.

ACKNOWLEDGMENTS

M.G. acknowledges CSIR, India, for the research fellowship. S.D. and V.V. acknowledge UGC, India, for the research fellowship. S.K. acknowledges the Department of Science and Technology (DST), New Delhi, for the research funding (GAP328726).

REFERENCES

- (1) Fang, G.; Zhou, J.; Pan, A.; Liang, S. Recent Advances in Aqueous Zinc-Ion Batteries. *ACS Energy Lett.* **2018**, *3*, 2480–2501.
- (2) Demir-Cakan, R.; Palacin, M. R.; Croguennec, L. Rechargeable Aqueous Electrolyte Batteries: from Univalent to Multivalent Cation Chemistry. *J. Mater. Chem. A* **2019**, *7*, 20519–20539.
- (3) Shin, J.; Lee, J.; Park, Y.; Choi, J. W. Aqueous Zinc Ion Batteries: Focus on Zinc Metal Anodes. *Chem. Sci.* **2020**, *11*, 2028–2044.
- (4) Ming, J.; Guo, J.; Xia, C.; Wang, W.; Alshareef, H. N. Zinc-Ion Batteries: Materials, Mechanisms, and Applications. *Mater. Sci. Eng., R* **2019**, *135*, 58–84.
- (5) Xu, C.; Li, B.; Du, H.; Kang, F. Energetic Zinc Ion Chemistry: the Rechargeable Zinc Ion Battery. *Angew. Chem., Int. Ed.* **2012**, *51*, 933–935.
- (6) Ding, J.; Du, Z.; Gu, L.; Li, B.; Wang, L.; Wang, S.; Gong, Y.; Yang, S. Ultrafast Zn²⁺ Intercalation and Deintercalation in Vanadium Dioxide. *Adv. Mater.* **2018**, *30*, No. 1800762.
- (7) Lee, B.; Lee, H. R.; Kim, H.; Chung, K. Y.; Cho, B. W.; Oh, S. H. Elucidating the Intercalation Mechanism of Zinc Ions into α -MnO₂ for Rechargeable Zinc Batteries. *Chem. Commun.* **2015**, *51*, 9265–9268.
- (8) Zhang, L.; Chen, L.; Zhou, X.; Liu, Z. Morphology-Dependent Electrochemical Performance of Zinc Hexacyanoferrate Cathode for Zinc-ion Battery. *Sci. Rep.* **2015**, *5*, No. 18263.
- (9) Zhang, L.; Chen, L.; Zhou, X.; Liu, Z. Towards High-Voltage Aqueous Metal-Ion Batteries Beyond 1.5 V: the Zinc/Zinc hexacyanoferrate System. *Adv. Energy Mater.* **2015**, *5*, No. 1400930.
- (10) Wan, F.; Zhang, L.; Wang, X.; Bi, S.; Niu, Z.; Chen, J. An Aqueous Rechargeable Zinc-Organic Battery with Hybrid Mechanism. *Adv. Funct. Mater.* **2018**, *28*, No. 1804975.
- (11) Park, M. J.; Yaghoobnejad Asl, H.; Manthiram, A. Multivalent-Ion versus Proton Insertion into Battery Electrodes. *ACS Energy Lett.* **2020**, *5*, 2367–2375.
- (12) Pan, H.; Shao, Y.; Yan, P.; Cheng, Y.; Han, K. S.; Nie, Z.; Wang, C.; Yang, J.; Li, X.; Bhattacharya, P.; et al. Reversible Aqueous Zinc/Manganese Oxide Energy Storage from Conversion Reactions. *Nat. Energy* **2016**, *1*, No. 16039.
- (13) Wan, F.; Niu, Z. Design Strategies for Vanadium-based Aqueous Zinc-Ion Batteries. *Angew. Chem., Int. Ed.* **2019**, *58*, 16358–16367.
- (14) Zhang, N.; Dong, Y.; Jia, M.; Bian, X.; Wang, Y.; Qiu, M.; Xu, J.; Liu, Y.; Jiao, L.; Cheng, F. Rechargeable Aqueous Zn–V₂O₅ Battery with High Energy Density and Long Cycle Life. *ACS Energy Lett.* **2018**, *3*, 1366–1372.
- (15) Han, J.; Wang, K.; Liu, W.; Li, C.; Sun, X.; Zhang, X.; An, Y.; Yi, S.; Ma, Y. Rational Design of Nano-Architecture Composite Hydrogel Electrode towards High Performance Zn-Ion Hybrid Cell. *Nanoscale* **2018**, *10*, 13083–13091.
- (16) Wang, X.; Chen, L.; Lu, F.; Liu, J.; Chen, X.; Shao, G. Boosting Aqueous Zn²⁺ Storage in 1, 4, 5, 8-Naphthalenetetracarboxylic Dianhydride through Nitrogen Substitution. *ChemElectroChem* **2019**, *6*, 3644–3647.
- (17) Wei, Q.; Liu, J.; Feng, W.; Sheng, J.; Tian, X.; He, L.; An, Q.; Mai, L. Hydrated Vanadium Pentoxide with Superior Sodium Storage Capacity. *J. Mater. Chem. A* **2015**, *3*, 8070–8075.
- (18) Yan, M.; He, P.; Chen, Y.; Wang, S.; Wei, Q.; Zhao, K.; Xu, X.; An, Q.; Shuang, Y.; Shao, Y.; et al. Water-Lubricated Intercalation in V₂O₅·nH₂O for High-Capacity and High-Rate Aqueous Rechargeable Zinc Batteries. *Adv. Mater.* **2018**, *30*, No. 1703725.
- (19) Zhang, N.; Jia, M.; Dong, Y.; Wang, Y.; Xu, J.; Liu, Y.; Jiao, L.; Cheng, F. Hydrated Layered Vanadium Oxide as a Highly Reversible Cathode for Rechargeable Aqueous Zinc Batteries. *Adv. Funct. Mater.* **2019**, *29*, No. 1807331.
- (20) Zhu, K.; Wu, T.; Huang, K. A High Capacity Bilayer Cathode for Aqueous Zn-Ion Batteries. *ACS Nano* **2019**, *13*, 14447–14458.
- (21) Geng, H.; Cheng, M.; Wang, B.; Yang, Y.; Zhang, Y.; Li, C. C. Electronic Structure Regulation of Layered Vanadium Oxide via Interlayer Doping Strategy toward Superior High-Rate and Low-Temperature Zinc-Ion Batteries. *Adv. Funct. Mater.* **2019**, No. 1907684.
- (22) Ming, F.; Liang, H.; Lei, Y.; Kandambeth, S.; Eddaoudi, M.; Alshareef, H. N. Layered Mg_xV₂O₅·nH₂O as Cathode Material for High-Performance Aqueous Zinc Ion Batteries. *ACS Energy Lett.* **2018**, *3*, 2602–2609.
- (23) Pang, Q.; He, W.; Zhao, H.; Yu, X.; Wei, Y.; Tian, Y.; Xing, M.; Fu, Y.; Luo, X. Hierarchical Aluminum Vanadate Microspheres with Structural Water: High-Performance Cathode Materials for Aqueous Rechargeable Zinc Batteries. *ChemPlusChem* **2020**, *85*, 2129–2135.
- (24) Li, Q.; Wei, T.; Ma, K.; Yang, G.; Wang, C. Boosting the Cyclic Stability of Aqueous Zinc-Ion Battery based on Al-doped V₁₀O₂₄·12H₂O Cathode Materials. *ACS Appl. Mater. Interfaces* **2019**, *11*, 20888–20894.
- (25) Liu, C.; Neale, Z.; Zheng, J.; Jia, X.; Huang, J.; Yan, M.; Tian, M.; Wang, M.; Yang, J.; Cao, G. Expanded Hydrated Vanadate for High-Performance Aqueous Zinc-Ion Batteries. *Energy Environ. Sci.* **2019**, *12*, 2273–2285.
- (26) Ghosh, M.; Vijayakumar, V.; Kurungot, S. Dendrite Growth Suppression by Zn²⁺-Integrated Nafion Ionomer Membranes: Beyond Porous Separators toward Aqueous Zn/V₂O₅ Batteries with Extended Cycle Life. *Energy Technol.* **2019**, *7*, No. 1900442.
- (27) Wang, D.; Ma, Z.; Dai, S.; Liu, J.; Nie, Z.; Engelhard, M. H.; Huo, Q.; Wang, C.; Kou, R. Low-Temperature Synthesis of Tunable Mesoporous Crystalline Transition Metal Oxides and Applications as Au Catalyst Supports. *J. Phys. Chem. C* **2008**, *112*, 13499–13509.
- (28) Alonso, B.; Livage, J. Synthesis of Vanadium Oxide Gels from Peroxovanadic Acid Solutions: a 51V NMR Study. *J. Solid State Chem.* **1999**, *148*, 16–19.
- (29) Fontenot, C. J.; Wiench, J. W.; Pruski, M.; Schrader, G. L. Vanadia Gel Synthesis via Peroxovanadate Precursors. 1. In situ Laser Raman and 51V NMR Characterization of the Gelation Process. *J. Phys. Chem. B* **2000**, *104*, 11622–11631.
- (30) Kaur, G.; Mitra, A.; Yadav, K. Pulsed Laser Deposited Al-Doped ZnO Thin Films for Optical Applications. *Prog. Nat. Sci.: Mater. Int.* **2015**, *25*, 12–21.
- (31) Perera, S. D.; Archer, R. B.; Damin, C. A.; Mendoza-Cruz, R.; Rhodes, C. P. Controlling Interlayer Interactions in Vanadium Pentoxide-Poly (ethylene oxide) Nanocomposites for Enhanced Magnesium-Ion Charge Transport and Storage. *J. Power Sources* **2017**, *343*, 580–591.
- (32) Dong, S.; Shin, W.; Jiang, H.; Wu, X.; Li, Z.; Holoubek, J.; Stickle, W. F.; Key, B.; Liu, C.; Lu, J.; et al. Ultra-Fast NH₄⁺ Storage: Strong H Bonding between NH₄⁺ and Bi-Layered V₂O₅. *Chem* **2019**, *5*, 1537–1551.
- (33) Durupthy, O.; Steunou, N.; Coradin, T.; Maquet, J.; Bonhomme, C.; Livage, J. Influence of pH and Ionic Strength on Vanadium (V) Oxides Formation. From V₂O₅·nH₂O Gels to Crystalline NaV₃O₈·1.5H₂O. *J. Mater. Chem.* **2005**, *15*, 1090–1098.
- (34) Torardi, C.; Miao, C.; Lewittes, M.; Li, Z. High Lithium Capacity MxV₂O₅Ay·nH₂O for Rechargeable Batteries. *J. Solid State Chem.* **2002**, *163*, 93–99.
- (35) Tian, M.; Liu, C.; Zheng, J.; Jia, X.; Jahrman, E. P.; Seidler, G. T.; Long, D.; Atif, M.; Alsalhi, M.; Cao, G. Structural Engineering of Hydrated Vanadium Oxide Cathode by K⁺ Incorporation for High-Capacity and Long-Cycling Aqueous Zinc Ion Batteries. *Energy Storage Mater.* **2020**, *29*, 9–16.
- (36) Ma, R.; Bando, Y.; Sasaki, T. Directly Rolling Nanosheets into Nanotubes. *J. Phys. Chem. B* **2004**, *108*, 2115–2119.
- (37) Zárte, R.; Fuentes, S.; Cabrera, A.; Fuenzalida, V. Structural Characterization of Single Crystals of Sodium Titanate Nanowires

Prepared by Hydrothermal Process. *J. Cryst. Growth* **2008**, *310*, 3630–3637.

(38) Etman, A. S.; Asfaw, H. D.; Yuan, N.; Li, J.; Zhou, Z.; Peng, F.; Persson, I.; Zou, X.; Gustafsson, T.; Edström, K.; et al. A One-Step Water based Strategy for Synthesizing Hydrated Vanadium Pentoxide Nanosheets from VO₂ (B) as Free-Standing Electrodes for Lithium Battery Applications. *J. Mater. Chem. A* **2016**, *4*, 17988–18001.

(39) Lee, J.; Badie, S.; Srimuk, P.; Ridder, A.; Shim, H.; Choudhury, S.; Nah, Y.-C.; Presser, V. Electrodeposition of Hydrated Vanadium Pentoxide on Nanoporous Carbon Cloth for Hybrid Energy Storage. *Sustainable Energy Fuels* **2018**, *2*, 577–588.

(40) Manikandan, R.; Raj, C. J.; Rajesh, M.; Kim, B. C.; Park, S.; Yu, K. H. Vanadium Pentoxide with H₂O, K⁺, and Na⁺ Spacer between Layered Nanostructures for High-Performance Symmetric Electrochemical Capacitors. *Adv. Mater. Interfaces* **2018**, *5*, No. 1800041.

(41) McNulty, D.; Buckley, D. N.; O'Dwyer, C. Optimizing the Structure and Yield of Vanadium Oxide Nanotubes by Periodic 2D Layer Scrolling. *RSC Adv.* **2016**, *6*, 40932–40944.

(42) Hu, C.-C.; Huang, C.-M.; Chang, K.-H. Anodic Deposition of Porous Vanadium Oxide Network with High Power Characteristics for Pseudocapacitors. *J. Power Sources* **2008**, *185*, 1594–1597.

(43) Kundu, S.; Satpati, B.; Mukherjee, M.; Kar, T.; Pradhan, S. K. Hydrothermal Synthesis of Polyaniline Intercalated Vanadium Oxide Xerogel Hybrid Nanocomposites: Effective Control of Morphology and Structural Characterization. *New J. Chem.* **2017**, *41*, 3634–3645.

(44) Zeng, H.; Liu, D.; Zhang, Y.; See, K. A.; Jun, Y.-S.; Wu, G.; Gerbec, J. A.; Ji, X.; Stucky, G. D. Nanostructured Mn-Doped V₂O₅ Cathode Material Fabricated From Layered Vanadium Jarosite. *Chem. Mater.* **2015**, *27*, 7331–7336.

(45) Silversmit, G.; Depla, D.; Poelman, H.; Marin, G. B.; De Gryse, R. Determination of the V2p XPS Binding Energies for Different Vanadium Oxidation States (V⁵⁺ to V⁰⁺). *J. Electron Spectrosc. Relat. Phenom.* **2004**, *135*, 167–175.

(46) Raju, V.; Rains, J.; Gates, C.; Luo, W.; Wang, X.; Stickle, W. F.; Stucky, G. D.; Ji, X. Superior Cathode of Sodium-Ion Batteries: Orthorhombic V₂O₅ Nanoparticles Generated in Nanoporous Carbon by Ambient Hydrolysis Deposition. *Nano Lett.* **2014**, *14*, 4119–4124.

(47) Deng, X.; Xu, Y.; An, Q.; Xiong, F.; Tan, S.; Wu, L.; Mai, L. Manganese Ion Pre-Intercalated Hydrated Vanadium Oxide as a High-Performance Cathode for Magnesium Ion Batteries. *J. Mater. Chem. A* **2019**, *7*, 10644–10650.

(48) Yu, D.; Zhang, S.; Liu, D.; Zhou, X.; Xie, S.; Zhang, Q.; Liu, Y.; Cao, G. Effect of Manganese Doping on Li-Ion Intercalation Properties of V₂O₅ Films. *J. Mater. Chem.* **2010**, *20*, 10841–10846.

(49) Du, M.; Liu, C.; Zhang, F.; Dong, W.; Zhang, X.; Sang, Y.; Wang, J. J.; Guo, Y. G.; Liu, H.; Wang, S. Tunable Layered (Na, Mn) V₈O₂₀·nH₂O Cathode Material for High-Performance Aqueous Zinc Ion Batteries. *Adv. Sci.* **2020**, *7*, 2000083. DOI: 10.1002/advs.202000083.

(50) Peng, C.; Xiao, F.; Yang, J.; Li, Z.; Lei, G.; Xiao, Q.; Ding, Y.; Hu, Z. Carbon-Encapsulated Mn-Doped V₂O₅ Nanorods with Long Span Life for High-Power Rechargeable Lithium Batteries. *Electrochim. Acta* **2016**, *192*, 216–226.

(51) Sambandam, B.; Soundharrajan, V.; Kim, S.; Alfaruqi, M. H.; Jo, J.; Kim, S.; Mathew, V.; Sun, Y.-k.; Kim, J. Aqueous Rechargeable Zn-Ion batteries: An Imperishable and High-Energy Zn₂V₂O₇ Nanowire Cathode Through Intercalation Regulation. *J. Mater. Chem. A* **2018**, *6*, 3850–3856.

(52) Dong, X.; Chen, L.; Liu, J.; Haller, S.; Wang, Y.; Xia, Y. Environmentally-Friendly Aqueous Li (or Na)-Ion Battery with Fast Electrode Kinetics and Super-Long Life. *Sci. Adv.* **2016**, *2*, No. e1501038.

(53) Simon, P.; Gogotsi, Y.; Dunn, B. Where Do Batteries End and Supercapacitors Begin? *Science* **2014**, *343*, 1210–1211.

(54) Augustyn, V.; Come, J.; Lowe, M. A.; Kim, J. W.; Taberna, P.-L.; Tolbert, S. H.; Abruña, H. D.; Simon, P.; Dunn, B. High-Rate Electrochemical Energy Storage Through Li⁺ Intercalation Pseudocapacitance. *Nat. Mater.* **2013**, *12*, 518–522.

(55) Wang, J.; Polleux, J.; Lim, J.; Dunn, B. Pseudocapacitive Contributions to Electrochemical Energy Storage in TiO₂ (anatase) Nanoparticles. *J. Phys. Chem. C* **2007**, *111*, 14925–14931.

(56) Zhao, J.; Ren, H.; Liang, Q.; Yuan, D.; Xi, S.; Wu, C.; Manalastas, W., Jr; Ma, J.; Fang, W.; Zheng, Y.; et al. High-Performance Flexible Quasi-Solid-State Zinc-Ion Batteries with Layer-Expanded Vanadium Oxide Cathode and Zinc/Stainless Steel Mesh Composite Anode. *Nano Energy* **2019**, *62*, 94–102.

(57) Wei, T.; Li, Q.; Yang, G.; Wang, C. Highly Reversible and Long-Life Cycling Aqueous Zinc-Ion Battery Based on Ultrathin (NH₄)₂V₁₀O₂₅·8H₂O Nanobelts. *J. Mater. Chem. A* **2018**, *6*, 20402–20410.

(58) Zhang, W.; Liang, S.; Fang, G.; Yang, Y.; Zhou, J. Ultra-High Mass-Loading Cathode for Aqueous Zinc-Ion Battery Based on Graphene-Wrapped Aluminum Vanadate Nanobelts. *Nano-Micro Lett.* **2019**, *11*, No. 69.

(59) Xia, C.; Guo, J.; Li, P.; Zhang, X.; Alshareef, H. N. Highly Stable Aqueous Zinc-Ion Storage Using a Layered Calcium Vanadium Oxide Bronze Cathode. *Angew. Chem., Int. Ed.* **2018**, *57*, 3943–3948.

(60) He, P.; Zhang, G.; Liao, X.; Yan, M.; Xu, X.; An, Q.; Liu, J.; Mai, L. Sodium Ion Stabilized Vanadium Oxide Nanowire Cathode for High-Performance Zinc-Ion Batteries. *Adv. Energy Mater.* **2018**, *8*, No. 1702463.

(61) Liu, W.; Dong, L.; Jiang, B.; Huang, Y.; Wang, X.; Xu, C.; Kang, Z.; Mou, J.; Kang, F. Layered Vanadium Oxides with Proton and Zinc Ion Insertion for Zinc Ion Batteries. *Electrochim. Acta* **2019**, *320*, No. 134565.

(62) Liang, X.; Hao, J.; Tan, B.; Lu, X.; Li, W. Binder-Free CaV₃O₇ Nanobelts with Rich Oxygen Defects as High Energy Cathode for Aqueous Zn-Ion Battery. *J. Power Sources* **2020**, *472*, No. 228507.

(63) Wang, M.; Zhang, J.; Zhang, L.; Li, J.; Wang, W.; Yang, Z.; Zhang, L.; Wang, Y.; Chen, J.; Huang, Y.; et al. Graphene-Like Vanadium Oxygen Hydrate (VOH) Nanosheets Intercalated and Exfoliated by Polyaniline (PANI) for Aqueous Zinc-Ion Batteries (ZIBs). *ACS Appl. Mater. Interfaces* **2020**, *12*, 31564–31574.

(64) Venkatkarthick, R.; Rodthongkum, N.; Zhang, X.; Wang, S.; Pattananuwat, P.; Zhao, Y.; Liu, R.; Qin, J. Vanadium-Based Oxide on Two-Dimensional Vanadium Carbide MXene (V₂O_x@V₂CT_x) as Cathode for Rechargeable Aqueous Zinc-Ion Batteries. *ACS Appl. Energy Mater.* **2020**, *3*, 4677–4689.

(65) Tang, W.; Lan, B.; Tang, C.; An, Q.; Chen, L.; Zhang, W.; Zuo, C.; Dong, S.; Luo, P. Urchin-Like Spinel MgV₂O₄ as a Cathode Material for Aqueous Zinc-Ion Batteries. *ACS Sustainable Chem. Eng.* **2020**, *8*, 3681–3688.

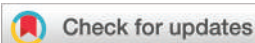
(66) Ghosh, M.; Vijayakumar, V.; Anothumakkool, B.; Kurungot, S. Nafion Ionomer-Based Single Component Electrolytes for Aqueous Zn/MnO₂ Batteries with Long Cycle Life. *ACS Sustainable Chem. Eng.* **2020**, *8*, 5040–5049.

(67) Lee, B.-S.; Cui, S.; Xing, X.; Liu, H.; Yue, X.; Petrova, V.; Lim, H.-D.; Chen, R.; Liu, P. Dendrite Suppression Membranes for Rechargeable Zinc Batteries. *ACS Appl. Mater. Interfaces* **2018**, *10*, 38928–38935.

(68) Soundharrajan, V.; Sambandam, B.; Kim, S.; Alfaruqi, M. H.; Putro, D. Y.; Jo, J.; Kim, S.; Mathew, V.; Sun, Y.-K.; Kim, J. Na₂V₆O₁₆·3H₂O Barnesite Nanorod: An Open Door to Display a Stable and High Energy for Aqueous Rechargeable Zn-Ion Batteries as Cathodes. *Nano Lett.* **2018**, *18*, 2402–2410.

(69) Lai, J.; Tang, H.; Zhu, X.; Wang, Y. A Hydrated NH₄V₃O₈ Nanobelt Electrode for Superior Aqueous and Quasi-Solid-State Zinc Ion Batteries. *J. Mater. Chem. A* **2019**, *7*, 23140–23148.

(70) Han, Q.; Chi, X.; Zhang, S.; Liu, Y.; Zhou, B.; Yang, J.; Liu, Y. Durable, Flexible Self-Standing Hydrogel Electrolytes Enabling High-Safety Rechargeable Solid-State Zinc Metal Batteries. *J. Mater. Chem. A* **2018**, *6*, 23046–23054.

Cite this: *Dalton Trans.*, 2021, **50**, 4237

Naphthalene dianhydride organic anode for a 'rocking-chair' zinc–proton hybrid ion battery†

Meena Ghosh,^{a,b} Vidyannand Vijayakumar,^b Maria Kurian,^a Swati Dilwale^{a,b} and Sreekumar Kurungot^b *^a

Rechargeable batteries consisting of a Zn metal anode and a suitable cathode coupled with a Zn²⁺ ion-conducting electrolyte are recently emerging as promising energy storage devices for stationary applications. However, the formation of high surface area Zn (HSAZ) architectures on the metallic Zn anode deteriorates their performance upon prolonged cycling. In this work, we demonstrate the application of 1,4,5,8-naphthalenetetracarboxylic dianhydride (NTCDA), an organic compound, as a replacement for the Zn–metal anode enabling the design of a 'rocking-chair' zinc–proton hybrid ion battery. The NTCDA electrode material displays a multi-plateau redox behaviour, delivering a specific discharge capacity of 143 mA h g⁻¹ in the potential window of 1.4 V to 0.3 V vs. Zn|Zn²⁺. The detailed electrochemical characterization of NTCDA in various electrolytes (an aqueous solution of 1 M ZnOTF, an aqueous solution of 0.01 M H₂SO₄, and an organic electrolyte of 0.5 M ZnOTF/acetonitrile) reveals that the redox processes leading to charge storage involve a contribution from both H⁺ and Zn²⁺. The performance of NTCDA as an anode is further demonstrated by pairing it with a MnO₂ cathode, and the resulting MnO₂||NTCDA full-cell (zinc–proton hybrid ion battery) delivers a specific discharge capacity of 41 mA h g_{total}⁻¹ (normalized with the total mass-loading of both anode and cathode active materials) with an average operating voltage of 0.80 V.

Received 29th December 2020,
Accepted 18th February 2021

DOI: 10.1039/d0dt04404k

rsc.li/dalton

Introduction

Recently, the post-lithium battery technology employing Zn electrochemistry has been receiving significant attention among battery enthusiasts. Compared to lithium-ion batteries (LIBs), the features such as relatively better safety and easy device fabricability by employing cost-effective aqueous electrolytes and electrode materials leverage the prospects of Zn batteries.¹ A conventional rechargeable Zn metal battery (ZMB) cell consists of a metallic Zn anode, an insertion/conversion-type cathode, and a separator soaked in a Zn ion conducting liquid electrolyte (pH 4–6).² However, the major difficulties associated with these ZMBs are the possible growth of high surface area zinc (HSAZ; also known as dendrite) deposits and hydrogen evolution reaction (HER) at the metallic-anode during the charging steps.³ These drawbacks result in the low coulombic efficiency and cycling stability of ZMBs.

The aforementioned challenges have been tackled by adopting various strategies that can tune the electrode–electrolyte interface between the Zn metal and liquid electrolyte in ZMBs. These attempts include the use of different electrolytes (*e.g.*, Zn(CF₃SO₃)₂, Zn(TFSI)₂, *etc.*), utilization of cation-selective ionomer separators (*e.g.*, Nafion and polyacrylonitrile membranes) instead of neutral porous separators (*e.g.*, glass fiber), and surface modification of Zn with carbon, TiO₂, CaCO₃, *etc.*^{4–8} Another logical approach to overcome the problems associated with a Zn-metal anode is its replacement with an electrode material that can facilitate the reversible insertion/extraction of Zn-ions so that the transition from ZMB to Zn ion batteries (ZIBs) can be enabled. Such insertion anode materials are popular with the other post-lithium batteries (Na-ion, Mg-ion, and K-ion batteries); the chemistry is rarely explored in the context of ZIBs.

The key features desirable for efficient anode material for ZIBs are high reversibility and stability towards Zn²⁺-insertion/extraction at relatively low potentials vs. Zn|Zn²⁺ and delivering high specific capacity. Cheng *et al.* reported the first example of a Zn²⁺-intercalating anode that utilizes chevrel phase Mo₆S₈ nanocubes.⁹ Kaveevivitchai *et al.* demonstrated the performance of an open-tunnel oxide of Zn_xMo_{2.5+y}VO_{9+z} that can be used as an insertion anode in both aqueous and nonaqueous electrolytes delivering a high specific capacity of 220 mA h

^aPhysical and Materials Chemistry Division, CSIR-National Chemical Laboratory, Pune, 411008 Maharashtra, India. E-mail: k.sreekumar@ncl.res

^bAcademy of Scientific and Innovative Research, Sector 19, Kamlia Nehru Nagar, Ghaziabad, Uttar Pradesh 201002, India

† Electronic supplementary information (ESI) available: FESEM image, XRD data, elemental mapping, SEM images, XPS data, supporting electrochemistry data, supporting table. See DOI: 10.1039/d0dt04404k

g^{-1} .¹⁰ Li *et al.* demonstrated pre-sodiated TiS_2 as an insertion anode in aqueous ZIB.¹¹ Despite these few attempts, the research on 'rocking chair' ZIBs, especially with organic materials as anodes, is minimal, and therefore, exploring potential electrode materials is important.

Organic compounds have received tremendous interest as anode materials in LIB and Na-ion battery applications. Compared to the most commonly used inorganic materials, the organic molecular solids facilitate the reversible uptake/release of the charged species by undergoing molecular reorientation and accompanied redox reactions.¹² In this aspect, developing Zn^{2+} -insertion anodes based on organic molecules could be an attractive choice. Here, we investigate the electrochemical performance of 1,4,5,8-naphthalenetetracarboxylic dianhydride (NTCDA) as a reversible Zn^{2+} -host in an aqueous electrolyte. During the electrochemical investigation, H^+ was also found to be contributing to the charge-storage behavior of NTCDA. Finally, to demonstrate the suitability of NTCDA as an insertion anode, a prototype ZIB full-cell was also fabricated by pairing the NTCDA anode against a MnO_2 cathode ($\text{MnO}_2||\text{NTCDA}$). The term 'zinc-proton hybrid ion battery' was coined to address the fabricated ZIB to emphasize the role of H^+ and Zn^{2+} in the charge storage mechanism. The cell displayed a specific capacity of $41 \text{ mA h g}_{\text{total}}^{-1}$, considering the active material loading in both the positive and negative electrodes. The zinc-proton hybrid ion battery cell also displayed a high average voltage of $\sim 0.80 \text{ V}$, close to several other ZIBs based on other cathodes such as V_2O_5 , VS_2 , and PDA/CNT.^{13–15} To the best of our knowledge, this is the first report on an organic anhydride molecule that can act as an anode capable of storing Zn^{2+} ions, which is used for fabricating aqueous rechargeable ZIB/zinc-proton hybrid ion batteries.

Experimental section

Materials

1,4,5,8-Naphthalenetetracarboxylic dianhydride (NTCDA) was purchased from TCI Chemicals and used without further purification. Zinc trifluoromethanesulfonate ($\text{Zn}(\text{CF}_3\text{SO}_3)_2/\text{ZnOTF}$) was procured from Sigma-Aldrich. Nafion 212 and Grafoil sheets were supplied by Du Pont, USA, and Global Nanotech, respectively. The solvent acetonitrile (ACN) used for electrolyte preparation was purchased from Thomas Baker.

Fabrication of electrodes

For preparing the electrodes, first, 4 mg of NTCDA and 1 mg of conducting additive (carbon nanofibre, CNF) (80:20 weight ratio) were dispersed in 250 μl of water-isopropanol (2:1) mixture and 10 μl of 5 wt% Nafion solution (DuPont). A required amount of the dispersion was spread over a 1.0 cm^2 area of Grafoil, and the coated electrodes were dried at $60 \text{ }^\circ\text{C}$. The loading of the electrodes was maintained as 1 mg cm^{-2} . The MnO_2 electrode with a mass-loading of 1 mg cm^{-2} was prepared by the electrodeposition of MnO_2 over a Toray carbon fibre paper following our previous report.¹⁶

Fabrication of electrochemical cells

All of the electrochemical cells were fabricated in a CR2032 coin cell assembly. The NTCDA||Zn half-cells were assembled using a piece of Zn foil (area 1.0 cm^2) and an NTCDA-coated Grafoil (1.0 mg cm^{-2}) as the negative and positive electrodes, respectively. A Nafion 212 membrane soaked in an aqueous solution of 1 M ZnOTF electrolyte (1 M ZnOTF/Aq.) was used as a separator. This cell was marked as NTCDA||Zn-(N), where 'N' stands for the nearly neutral electrolyte ($\text{pH} \approx 4$) used for cell fabrication. For comparison, the NTCDA electrode was also tested in 0.01 M H_2SO_4 ($\text{pH} \approx 1.7$) and 0.5 M ZnOTF/ACN electrolyte, and the coin-cells were labeled as NTCDA||Zn-(A) and NTCDA||Zn-(O), respectively; here, the letters 'A' and 'O' stand for acidic and organic electrolytes, respectively. The electrochemical performance of MnO_2 was also tested in a similar way using MnO_2 (1.0 mg cm^{-2}) as the positive electrode and Zn foil as the negative electrode separated by the Nafion membrane pre-soaked with the 1 M ZnOTF/Aq. electrolyte. The corresponding electrochemical cell was marked as $\text{MnO}_2||\text{Zn}-(\text{N})$.

The three-electrode characterizations of the NTCDA electrode in 0.01 M H_2SO_4 and 0.1 M ZnOTF/Aq. were carried out using NTCDA coated Grafoil as the working electrode, Pt mesh as the counter electrode, and $\text{Hg}/\text{Hg}_2\text{SO}_4$ as the reference electrode. Similarly, the electrodeposited MnO_2 electrode was also tested in 0.005 M H_2SO_4 ($\text{pH} \approx 2$) and 0.1 M ZnOTF/Aq. electrolyte in the three-electrode cell assembly. Here, a low concentration of the H_2SO_4 electrolyte was used to ensure minimum dissolution of MnO_2 in the acid solution.

For the fabrication of a ZIB full-cell, the loading of the NTCDA anode and MnO_2 cathode was calculated from the following equation:

$$M_{\text{cathode}}/M_{\text{anode}} = Q_{\text{anode}}/Q_{\text{cathode}} \dots \quad (1)$$

where 'M' and 'Q' represent the mass-loading and the specific capacity of the electrode materials, respectively.¹⁷ Here, the specific capacity values of the respective electrodes are measured at a current rate of 0.1 A g^{-1} from the half-cell study (NTCDA||Zn-(N) and $\text{MnO}_2||\text{Zn}-(\text{N})$ cells) with an electrode material mass-loading of 1 mg cm^{-2} .

$$M_{\text{MnO}_2}/M_{\text{NTCDA}} = 143 \text{ mA h g}^{-1}/281 \text{ mA h g}^{-1} = 1/1.9 \dots \quad (2)$$

Comparing the capacity of the electrode materials, the ratio of NTCDA: MnO_2 was taken as *ca.* 2:1 (eqn (2)). Before assembling the full-cell, the MnO_2 electrode was activated by electrochemical cycling for two discharge cycles at a current rate of 0.5 A g^{-1} in a two-electrode cell configuration, taking MnO_2 as the positive electrode and Zn as the negative electrode in the aqueous 1 M ZnOTF/Aq. electrolyte. After that, the MnO_2 electrode was recovered carefully and paired with the NTCDA electrode for assembling the $\text{MnO}_2||\text{NTCDA}$ full-cell using the 1 M ZnOTF/Aq. electrolyte. For calculating the specific capacity of the full-cell, the total capacity was normalized with respect to the cumulative mass-loading of the NTCDA anode (2 mg cm^{-2}) and MnO_2 cathode (1 mg cm^{-2}).

Electrochemical measurements

All of the electrochemical measurements were recorded using a Biologic VMP3 instrument. The cyclic voltammetry (CV) analysis of the NTCDA||Zn-(N) half-cell was carried out at scan rates of 0.1, 0.3, 0.5, and 1 mV s^{-1} . The galvanostatic charge-discharge (GCD) data were collected at 0.1, 0.25, 0.5, 1, and 2 A g^{-1} current rates. The current rates and capacity values of the half-cell study are reported considering the mass-loading of the working electrode alone. The NTCDA||MnO₂ full-cell was also characterized with CV (at 5 mV s^{-1}) and GCD (0.17, 0.33, 0.67, and 1.0 $\text{A g}_{\text{total}}^{-1}$); the current rates were normalized with respect to the total mass-loading of both electrodes). The GCD data of the MnO₂||Zn-(N) half-cell was recorded at various current rates (0.1, 0.25, 0.5, and 1 A g^{-1}) using a Neware battery tester instrument.

Material characterization

A Nova Nano SEM 450 field emission scanning electron microscope (FESEM) and a Quanta 200-3D FEI scanning electron microscope (SEM) were used for investigating the morphology of the samples. The elemental composition was investigated through an energy dispersive X-ray spectroscopy (EDAX) analysis. The EDAX elemental mapping was carried out using an ESEM-Quanta 200-3D instrument. X-ray diffraction (XRD) analysis was performed using a Rigaku, MicroMax-007HF with a high-intensity Microfocus rotating anode X-ray generator (Cu K α ($\alpha = 1.54 \text{ \AA}$)). The XPS data were collected using a Thermo Scientific K-Alpha+ instrument. The Fourier transform infrared (FTIR) analysis was performed using a Bruker Tensor 27 FTIR instrument.

Results and discussion

The crystal structure information of the commercial NTCDA is given in Table S1.† The XRD pattern (Fig. S1a†) of the commercial NTCDA indicates the crystalline nature of the sample. The FESEM image (Fig. S1b and c†) of the material shows an irregular rod-like morphology. The FTIR data of commercial NTCDA (Fig. S1d†) display a strong peak at 1790 cm^{-1} corresponding to the C=O bond vibration of the anhydride moiety.

At first, the electrochemical performance of NTCDA is evaluated in 1 M ZnOTF/Aq. electrolyte in the NTCDA||Zn-(N) half-cell. As shown in Fig. 1a, the CV profiles of the cell at different scan rates exhibit two pairs of reversible redox peaks. At a scan rate of 1 mV s^{-1} , the cathodic peaks appear at 0.45 and 0.31 V vs. Zn|Zn²⁺ and the anodic peaks at 0.59 and 0.85 V vs. Zn|Zn²⁺. By comparing the first and second CV cycles at the same scan rate (1 mV s^{-1}), a slight drop in the current response is observed (Fig. S2a†), showing the irreversible capacity loss during the cycling.

The charge/discharge capacity of NTCDA is obtained from the GCD experiment. Fig. S2b† represents the GCD plots recorded at a current rate of 0.1 A g^{-1} , showing the initial capacity. The charge and discharge plateaus in the GCD curves (Fig. S2b† and Fig. 1b) are consistent with the redox peaks present in the CV profile (Fig. 1a), suggesting multi-step redox reactions. As shown in Fig. S2b,† in the first discharge, NTCDA delivers a high discharge capacity of 197 mA h g^{-1} . However, a slight drop in the capacity is observed in the subsequent cycles, resulting in the discharge capacities of 157 and 143 mA h g^{-1} in the 2nd and 3rd discharge, respectively. The capacity loss observed during the initial cycles could be caused by the slight irreversibility in the discharging and charging processes due to the trapping of ions into the NTCDA matrix which cannot travel back to the electrolyte during the reverse scan. The GCD plots at different current rates (Fig. 1b) display that NTCDA could deliver specific discharge capacities of 112, 89, 70, and 47 mA h g^{-1} at 0.25, 0.5, 1, and 2 A g^{-1} , respectively.

The multi-plateau characteristic of the NTCDA||Zn-(N) cell could originate from the insertion of both the H⁺ and Zn²⁺ ions into the NTCDA host assisted by the redox active C=O groups present in it. It is known that the Zn²⁺-based aqueous electrolyte inevitably contains protons (H⁺) that could take part in the electrochemical processes.¹⁸ To prove and understand the possible contribution from water and proton towards the charge/discharge capacity of NTCDA, the electrochemical characterization of NTCDA is investigated in 0.01 M H₂SO₄ (NTCDA||Zn-(A)) and 0.5 M ZnOTF/ACN (NTCDA||Zn-(O)) electrolytes. In aprotic organic electrolytes (0.5 M ZnOTF/ACN), the NTCDA electrode shows only one pair of oxidation and reduction peaks (Fig. S3a†), delivering a specific discharge

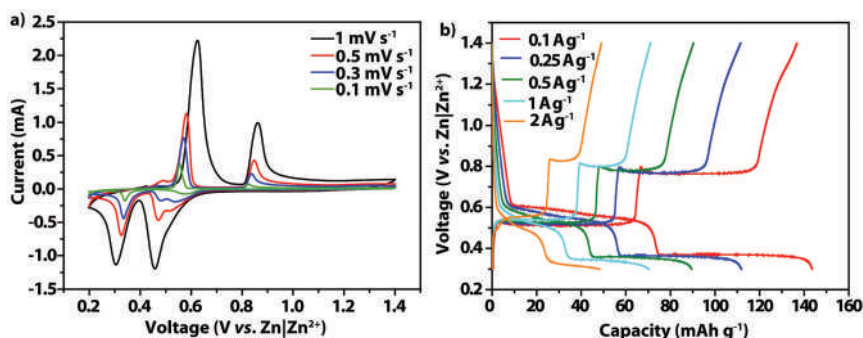


Fig. 1 (a) CV profiles recorded at various scan rates and (b) GCD profiles recorded at various current rates of the NTCDA||Zn-(N) cell.

capacity of 66 mA h g^{-1} (Fig. S3b†). The reduction peak of NTCDA (onset potential of $0.47 \text{ V vs. Zn|Zn}^{2+}$) in an aprotic electrolyte (Fig. S3a†) appears close to the low-voltage reduction peak (an onset potential of $0.40 \text{ V vs. Zn|Zn}^{2+}$) in 1 M ZnOTf/Aq. (Fig. 1a). This resemblance suggests that the coordination of Zn^{2+} with the reduced C=O groups takes place at a lower potential region (*vs. Zn|Zn*²⁺) in a Zn^{2+} conducting electrolyte.^{19,20}

However, the CV feature of NTCDA in H_2SO_4 electrolyte (Fig. S4a†) shows two distinct reduction peaks (onset potentials of 0.40 V and $0.65 \text{ V vs. Zn|Zn}^{2+}$). These two peaks indicate the plausible interaction of the C=O groups with H^+ and Zn^{2+} in the successive steps (Fig. S4b†). In the acidic electrolyte, during the 1st discharge of the NTCDA||Zn-(A) cell, the metallic Zn anode may dissolve in the electrolyte as Zn^{2+} . Therefore, the dissolved Zn^{2+} ions in the electrolyte can diffuse into NTCDA and interact with the C=O groups during electrochemical cycling. To confirm the presence of Zn^{2+} , the NTCDA electrode was collected at the discharged state of the NTCDA||Zn-(A) cell and characterized by XPS analysis. As shown in the survey spectra (Fig. S5†), the NTCDA electrode in $0.01 \text{ M H}_2\text{SO}_4$ electrolyte displays an intense Zn 2p XPS peak similar to the other two electrodes in ZnOTf/ACN and ZnOTf/Aq. electrolytes in the discharged state. Hence, the XPS data support the Zn corrosion in H_2SO_4 electrolyte, which justifies the involvement of both H^+ and Zn^{2+} charge carriers in the faradaic reactions leading to the origin of the two reduction peaks as appeared in the CV profile of the NTCDA||Zn-(A) cell.

To further confirm the H^+ association with NTCDA, a CV analysis was carried out in a standard three-electrode cell in $0.01 \text{ M H}_2\text{SO}_4$ electrolyte using a Pt mesh as the counter electrode and $\text{Hg/Hg}_2\text{SO}_4$ as the reference electrode. As displayed in Fig. 2a, NTCDA exhibits a single reduction peak at an onset

potential of $-0.84 \text{ V vs. Hg/Hg}_2\text{SO}_4$. It must be noted that the aforementioned three-electrode cell does not contain Zn, and H^+ is the only positive charge carrier present in the electrolyte. Hence, the obtained redox peaks in the CV profile (Fig. 2a) indeed originate from the H^+ uptake by the C=O groups of NTCDA. Interestingly, when the electrolyte is switched to 0.1 M ZnOTf/Aq. (Fig. 2b), the reduction peak at a higher voltage (onset potential $-0.75 \text{ V vs. Hg/Hg}_2\text{SO}_4$) is retained followed by the appearance of an additional peak at a lower voltage (onset potential $-1.0 \text{ V vs. Hg/Hg}_2\text{SO}_4$). Based on the aforementioned observations, the reduction process of NTCDA in a ZnOTf/Aq. electrolyte is divided into two steps: the first step at a higher voltage region mainly involves H^+ coordination, whereas Zn^{2+} coordination is predominant in the second step (Fig. 3a). Therefore, the above discussion clearly points out that both the Zn^{2+} and H^+ storage significantly contribute to the total capacity obtained by the NTCDA electrode in the ZnOTf/Aq. electrolyte.

The long-term cycling stability of the NTCDA||Zn-(N) cell is recorded at a 2 A g^{-1} current rate. As shown in Fig. 3b, the cell shows a performance drop in the initial cycles reaching a discharge capacity of 24 mA h g^{-1} . In the following cycles, the capacity of the cell is found to increase gradually, delivering an average capacity of 30 mA h g^{-1} after 150 cycles. The observed increment in the capacity could be due to the electrochemical activation of NTCDA with cycling. Moreover, the same performance is almost maintained for over 300 charge/discharge cycles. The gradual capacity loss of NTCDA could be due to the hydrolysis of anhydride groups in aqueous electrolyte ($\text{pH} \approx 4$).²¹

To understand the charge storage mechanism of NTCDA, we have recovered the electrodes from the NTCDA||Zn-(N) cell at the completely discharged (to $0.3 \text{ V vs. Zn|Zn}^{2+}$) and charged (to $1.4 \text{ V vs. Zn|Zn}^{2+}$) states. After recovering from the respective cells, the electrodes are carefully washed with water to remove the ZnOTf electrolyte salt from the electrode surface. The FTIR data (Fig. 4a) of the original electrode and that of the recovered electrodes from the discharged and charged cells were compared. In the pristine electrode, the strong peak at 1780 cm^{-1} corresponds to the anhydride functional group present in the NTCDA molecule.²² Upon the first discharge, we did not observe any significant change in the anhydride peak. However, a new peak at 1362 cm^{-1} appeared, which is attributed to the formation of enolate (C-O^-) from the carbonyl group (C=O) of the anhydride functionalities.^{21,23} Additionally, a few other peaks at 1260 , 1182 , 772 , and 647 cm^{-1} were found to evolve after the discharge. These additional peaks indicate the structural changes that occurred due to the interaction of NTCDA with the H^+ / Zn^{2+} ions. Moreover, the intensity of the peaks mentioned above diminishes upon complete charging, which confirms the reversibility of the electrochemical reactions occurring at the electrode.

Later, the NTCDA electrodes (original and recovered electrodes from the charged and discharged cells) were subjected to elemental mapping analysis and SEM imaging. Fig. S6† dis-

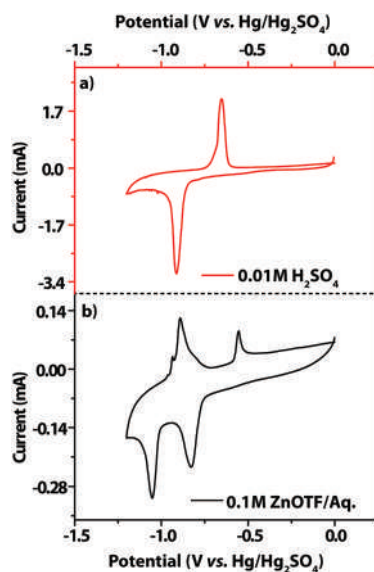


Fig. 2 CV profiles for NTCDA electrode characterized in a three-electrode cell with respect to a $\text{Hg/Hg}_2\text{SO}_4$ reference electrode in (a) $0.01 \text{ M H}_2\text{SO}_4$ and (b) 0.1 M ZnOTf/Aq. electrolytes.

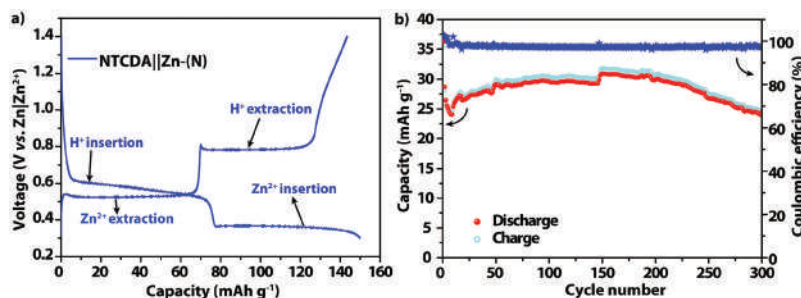


Fig. 3 (a) GCD plot for the NTCDA||Zn-(N) cell (at 0.1 A g⁻¹ current rate) showing the potential region for predominant Zn²⁺ and/or H⁺ coordination with NTCDA and (b) cycling stability data measured at a current rate of 2 A g⁻¹ for the NTCDA||Zn-(N) cell.

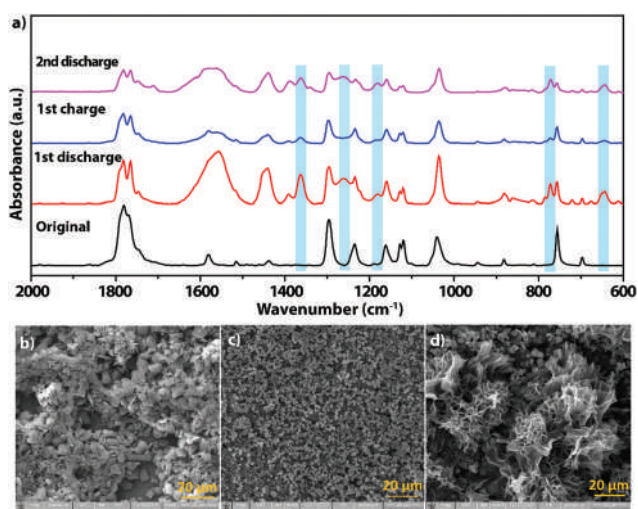


Fig. 4 (a) FTIR data of the NTCDA electrodes at the original state and after recovering from the NTCDA||Zn-(N) cells at discharged and charged states; SEM image of NTCDA electrodes at (b) the original state and after recovery from the NTCDA||Zn-(N) cell at (c) the discharge and (d) charge states.

plays the presence of C, O, and Zn in both the discharged and charged electrodes; however, the Zn content is found to be significantly higher in the former. The elemental compositions of the original and cycled electrodes obtained from the EDAX analysis (Table S2[†]) also show the higher content of Zn in the discharged electrode compared to that of the charged electrode. The presence of Zn in the charged electrode could be the result of the irreversibly consumed Zn²⁺ by the NTCDA electrode, which results in capacity loss during the first charging cycle (Fig. S2a and b[†]).

A significant change in the electrode morphology is also observed upon Zn²⁺-insertion and extraction. The original electrode (Fig. 4b) consists of micrometer-size block-like particles along with carbon nanofiber strands, which are used as the conducting additives for improving the electronic conductivity. Upon full discharge (Fig. 4c and Fig. S7a, b[†]), the particle morphology converts to small granules. Interestingly, after complete charging (Fig. 4d and Fig. S7c, d[†]), the morphology of the electrode does not return to the original state. Instead, a

non-uniform morphology is observed in the charged state containing aggregated nanosheets along with irregularly shaped particles. The remarkable morphological evolution of NTCDA at the discharge and charge states associates with the phase transition is evident from the sharp redox peak in the CV profile as well as the well-defined plateaus in the GCD curves of the NTCDA||Zn-(N) cell. A similar morphological change is also reported with other organic electrode materials (such as *p*-chloranil) for ZMBs.¹² However, further studies are required to understand the underlying mechanism for the observed structural changes in the NTCDA electrode.

The structural and morphological changes occurring in the electrode material after the cycling stability test are studied. From the XRD profiles of the original and cycled electrodes (Fig. S8a-e[†]), it is observed that some peaks match with that of the original electrode, as indicated in Fig. S8d and e[†]. Besides, the XRD data of the cycled electrode contain several new peaks with good intensities, which could be related to the structural changes associated with the electrode material and the residual electrolyte salt trapped in the electrode. The morphological evolution of the NTCDA electrode after the cycling is further evident from the SEM images shown in Fig. S9a and b[†]. Compared to the original NTCDA electrode possessing an irregular block-like morphology (Fig. 4b), the cycled electrode is observed to exhibit an aggregated nanosheet-like morphology, which resembles that of the charged electrode (Fig. 4d).

The performance of NTCDA as the insertion anode in the full-cell is investigated by pairing it with the electrodeposited MnO₂ cathode. We have chosen MnO₂ as the cathode because of its high average voltage and adequate capacity. The specific discharge capacity of the MnO₂||Zn-(N) half-cell is obtained from the GCD analysis, and the related plots are shown in Fig. S10.[†] Besides, the MnO₂ electrode was also characterized in a three-electrode cell assembly (Fig. S11[†]) using 0.005 M H₂SO₄ and 0.1 M ZnOTF/Aq. as the electrolytes. The broad redox peaks in the cathodic and anodic CV scans suggest the redox-assisted H⁺ storage/release in the MnO₂ electrode in the 0.005 M H₂SO₄ electrolyte. On the other hand, the CV data taken in the 0.1 M ZnOTF/Aq. electrolyte show more distinct oxidation and reduction peaks associated with the insertion/extraction of Zn²⁺ and H⁺ ions. Moreover, several earlier reports on the MnO₂ cathode have also confirmed the charge

storage behavior in the Zn^{2+} -conducting aqueous electrolytes involve co-insertion of Zn^{2+} and H^+ ions.^{24–26}

Later the $\text{MnO}_2||\text{NTCDA}$ full-cell was assembled, and the cell is schematically presented in Fig. 5a. The $\text{MnO}_2||\text{NTCDA}$ ZIB full-cell facilitated by the Zn^{2+} and H^+ insertion at both the anode and cathode (as discussed in the previous sections) can be called a $\text{Zn}^{2+}/\text{H}^+$ hybrid battery (or zinc–proton hybrid ion battery). The CV profile of the $\text{MnO}_2||\text{NTCDA}$ full-cell is shown in Fig. 5b, which displays the reversible redox processes occurring in the cell during the cathodic and anodic scans. The GCD profiles recorded at various current rates are given in Fig. 5c. The full-cell delivers the discharge capacities of 41, 33, 25, and 20 $\text{mA h g}_{\text{total}}^{-1}$ at the current rates of 0.17, 0.33, 0.67, and 1.0 $\text{A g}_{\text{total}}^{-1}$, respectively. The term ‘total’ in the units of capacity and current rates represents the cumulative mass-loading in both the positive and negative electrodes. The maximum energy density obtained for the full-cell is 32 $\text{W h kg}_{\text{total}}^{-1}$. For a better understanding of the average voltage of the full-cell, the GCD profiles of the $\text{MnO}_2||\text{NTCDA}$, $\text{MnO}_2||\text{Zn}-(\text{N})$, and $\text{NTCDA}||\text{Zn}-(\text{N})$ cells are summarized in Fig. S12.† As shown in the figure, the MnO_2 and NTCDA electrodes display an average voltage of 1.35 V and 0.46 V vs. $\text{Zn}| \text{Zn}^{2+}$, respectively. When NTCDA is paired with the MnO_2 cathode, the resulting full-cell shows an average voltage of 0.80 V (Fig. S12 and S13†). The cycling stability of the full-cell is investigated at a current rate of 0.33 $\text{A g}_{\text{total}}^{-1}$. Fig. 5d shows that the $\text{MnO}_2||\text{NTCDA}$ cell exhibits capacity fading in the first few cycles reaching a capacity of 22 $\text{mA h g}_{\text{total}}^{-1}$ at the 5th cycle. In the following cycles, the drop in the capacity value is found to be reduced, resulting in a capacity retention of 15 $\text{mA h g}_{\text{total}}^{-1}$ over 100 cycles. Moreover, the overall performance of the full-cell is also comparable to some of the previously reported ZIB full-cells (Table S3†).^{11,27–30} Therefore, the replacement of metallic Zn with an NTCDA anode shows a new

direction toward developing aqueous rechargeable batteries based on Zn-ion chemistry.

Conclusions

This work demonstrates that NTCDA exhibits adequate capacity (143 mA h g^{-1}) and cycling stability in aqueous 1 M ZnOTf/Aq. electrolyte. The electrochemical characterization studies reveal that both Zn^{2+} and H^+ present in aqueous electrolytes contribute to the charge storage performance of NTCDA . The suitable low-voltage plateau (vs. $\text{Zn}| \text{Zn}^{2+}$) of NTCDA allows its use as an anode material in combination with the MnO_2 cathode for assembling a *zinc–proton hybrid ion battery* full-cell ($\text{MnO}_2||\text{NTCDA}$). The prototype full-cell delivers a 41 $\text{mA h g}_{\text{total}}^{-1}$ initial capacity with an average voltage of 0.80 V higher than that of the $\text{NTCDA}||\text{Zn}-(\text{N})$ half-cell. Ultimately, in contrast to the previously reported inorganic materials, this work provides new insights into the designing of insertion anodes based on the environment-friendly organic molecules for aqueous ‘rocking chair’ ZIBs.

Conflicts of interest

There are no conflicts to declare.

Acknowledgements

M. G. acknowledges CSIR, India, for the research fellowship. S. D. and V. V. acknowledge UGC, India, for the research fellowship. K. S. and M. K. acknowledge the Department of Science and Technology, New Delhi, for the funding of the project (GAP328726).

References

- 1 C. Li, X. Zhang, W. He, G. Xu and R. Sun, *J. Power Sources*, 2020, **449**, 227596.
- 2 Q. Han, X. Chi, Y. Liu, L. Wang, Y. Du, Y. Ren and Y. Liu, *J. Mater. Chem. A*, 2019, **7**, 22287–22295.
- 3 J. Shin, J. Lee, Y. Park and J. W. Choi, *Chem. Sci.*, 2020, **11**, 2028–2044.
- 4 N. Zhang, F. Cheng, Y. Liu, Q. Zhao, K. Lei, C. Chen, X. Liu and J. Chen, *J. Am. Chem. Soc.*, 2016, **138**, 12894–12901.
- 5 K. Zhao, C. Wang, Y. Yu, M. Yan, Q. Wei, P. He, Y. Dong, Z. Zhang, X. Wang and L. Mai, *Adv. Mater. Interfaces*, 2018, **5**, 1800848.
- 6 W. Li, K. Wang, M. Zhou, H. Zhan, S. Cheng and K. Jiang, *ACS Appl. Mater. Interfaces*, 2018, **10**, 22059–22066.
- 7 B.-S. Lee, S. Cui, X. Xing, H. Liu, X. Yue, V. Petrova, H.-D. Lim, R. Chen and P. Liu, *ACS Appl. Mater. Interfaces*, 2018, **10**, 38928–38935.
- 8 X. Liu, F. Yang, W. Xu, Y. Zeng, J. He and X. Lu, *Adv. Sci.*, 2020, **7**, 2002173.

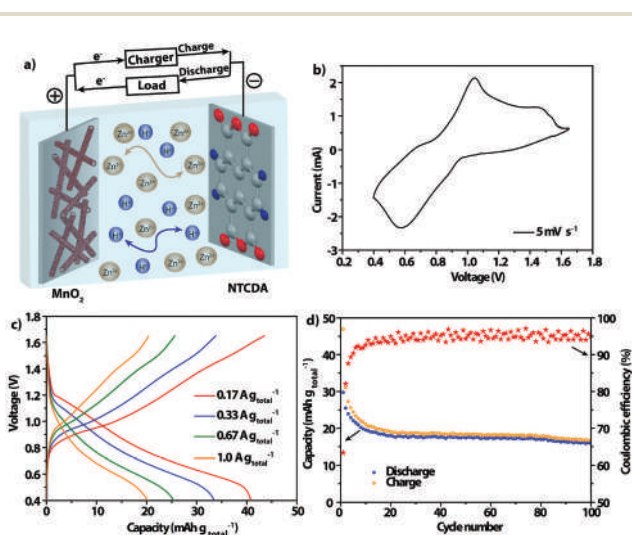


Fig. 5 (a) Schematic presentation of the $\text{MnO}_2||\text{NTCDA}$ full-cell; (b) CV profile, (c) GCD profiles at various current rates, and (d) cycling stability data recorded at the current rate of 0.33 $\text{A g}_{\text{total}}^{-1}$ for the $\text{MnO}_2||\text{NTCDA}$ full-cell.

- 9 Y. Cheng, L. Luo, L. Zhong, J. Chen, B. Li, W. Wang, S. X. Mao, C. Wang, V. L. Sprenkle and G. Li, *ACS Appl. Mater. Interfaces*, 2016, **8**, 13673–13677.
- 10 W. Kaveevivitchai and A. Manthiram, *J. Mater. Chem. A*, 2016, **4**, 18737–18741.
- 11 W. Li, K. Wang, S. Cheng and K. Jiang, *Adv. Energy Mater.*, 2019, **9**, 1900993.
- 12 D. Kundu, P. Oberholzer, C. Glaros, A. Bouzid, E. Tervoort, A. Pasquarello and M. Niederberger, *Chem. Mater.*, 2018, **30**, 3874–3881.
- 13 F. Wan and Z. Niu, *Angew. Chem., Int. Ed.*, 2019, **58**, 16358–16367.
- 14 X. Yue, H. Liu and P. Liu, *Chem. Commun.*, 2019, **55**, 1647–1650.
- 15 P. He, M. Yan, G. Zhang, R. Sun, L. Chen, Q. An and L. Mai, *Adv. Energy Mater.*, 2017, **7**, 1601920.
- 16 M. Ghosh, V. Vijayakumar, B. Anothumakkool and S. Kurungot, *ACS Sustainable Chem. Eng.*, 2020, **8**, 5040–5049.
- 17 J. Kasnatscheew, T. Placke, B. Streipert, S. Rothermel, R. Wagner, P. Meister, I. C. Laskovic and M. Winter, *J. Electrochem. Soc.*, 2017, **164**, A2479.
- 18 Z. Tie, L. Liu, S. Deng, D. Zhao and Z. Niu, *Angew. Chem.*, 2020, **59**, 4920–4924.
- 19 H. Zhang, Y. Fang, F. Yang, X. Liu and X. Lu, *Energy Environ. Sci.*, 2020, **13**, 2515–2523.
- 20 M. Na, Y. Oh and H. R. Byon, *Chem. Mater.*, 2020, **32**, 6990–6997.
- 21 I. A. Rodríguez-Pérez, Y. Yuan, C. Bommier, X. Wang, L. Ma, D. P. Leonard, M. M. Lerner, R. G. Carter, T. Wu and P. A. Greaney, *J. Am. Chem. Soc.*, 2017, **139**, 13031–13037.
- 22 V. Burtman, A. Zelichonok and A. V. Pakoulev, *Int. J. Mol. Sci.*, 2011, **12**, 173–225.
- 23 J. Wu, W. Xu, Y. Lin, X. Shi, F. Yang and X. Lu, *J. Power Sources*, 2021, **483**, 229114.
- 24 W. Sun, F. Wang, S. Hou, C. Yang, X. Fan, Z. Ma, T. Gao, F. Han, R. Hu and M. Zhu, *J. Am. Chem. Soc.*, 2017, **139**, 9775–9778.
- 25 M. J. Park, H. Yaghoobnejad Asl and A. Manthiram, *ACS Energy Lett.*, 2020, **5**, 2367–2375.
- 26 Q. Zhao, X. Huang, M. Zhou, Z. Ju, X. Sun, Y. Sun, Z. Huang, H. Li and T. Ma, *ACS Appl. Mater. Interfaces*, 2020, **12**, 36072–36081.
- 27 N. Liu, X. Wu, Y. Zhang, Y. Yin, C. Sun, Y. Mao, L. Fan and N. Zhang, *Adv. Sci.*, 2020, **7**, 2000146.
- 28 M. S. Chae and S.-T. Hong, *Batteries*, 2019, **5**, 3.
- 29 M. Yu, N. Chandrasekhar, R. K. M. Raghupathy, K. H. Ly, H. Zhang, E. Dmitrieva, C. Liang, X. Lu, T. D. Kühne and H. Mirhosseini, *J. Am. Chem. Soc.*, 2020, **142**(46), 19570–19578.
- 30 X. Wu, Y. Xu, C. Zhang, D. P. Leonard, A. Markir, J. Lu and X. Ji, *J. Am. Chem. Soc.*, 2019, **141**, 6338–6344.